Spring 2019

Defining historical earthquake rupture parameters and proposed slip distributions through tsunami modeling in south-central Chile

Alexander Dolcimascolo
Central Washington University, adolcimascolo31@gmail.com

DEFINING HISTORICAL EARTHQUAKE RUPTURE PARAMETERS AND PROPOSED SLIP DISTRIBUTIONS THROUGH TSUNAMI MODELING IN SOUTH-CENTRAL CHILE

A Thesis

Presented to

The Graduate Faculty

Central Washington University

In Partial Fulfillment

of the Requirements for the Degree

Master of Science

Geological Sciences

by

Alexander Ryan Dolcimascolo

May 2019

CENTRAL WASHINGTON UNIVERSITY

Graduate Studies

We hereby approve the thesis of

Alexander Ryan Dolcimascolo

Candidate for the degree of Master of Science

APPROVED FOR THE GRADUATE FACULTY

Dr. Breanyn MacInnes, Committee Chair

Dr. Lisa Ely

Dr. Walter Szeliga

Dean of Graduate Studies

ABSTRACT

DEFINING HISTORICAL EARTHQUAKE RUPTURE PARAMETERS AND PROPOSED SLIP DISTRIBUTIONS THROUGH TSUNAMI MODELING IN SOUTH-CENTRAL CHILE

by

Alexander Ryan Dolcimascolo

May 2019

Reliable tsunami early warning forecasts rely on accurate initial modeling conditions and interpretations of subduction zone behavior in a multi-century perspective. GPS and seismologic data were introduced this past century to study rupture dynamics in detail, however limited information is known about ruptures that pre-date the 20th century. I propose a methodology that uses statistics to better understand these pre-20th century ruptures. This methodology applies the historical and geologic tsunami record as a means to select a suite of tsunami simulations from earthquake source solutions. I chose south-central Chile (46°S to 30°S) to test this new methodology; it has an extensive earthquake historical record at 47 different coastal sites, some of which date to the 16th century. Between 1570 and 1960, this region experienced at least 17 tsunamigenic earthquakes. In addition to evaluating possible source solutions for these earthquakes, my methodology also allows the test of whether subducted fracture zones, like the Mocha fracture zone (MFZ) in south-central Chile, controls rupture propagation (as previously hypothesized). For this research, I used GeoClaw, a numerical tsunami modeling code, to simulate 423 forward-modeled M_w

8.7 - 9.5 earthquake scenarios with stochastic, variable slip distributions. I used Akaike's Information Criterion (AIC) to identify significant earthquake parameters (M_w and slip location) of 17 events by statistically selecting source models that had similar simulated wave heights to known observations in the historic and geologic record. For example, I concluded from AIC that the 1960 event was a M_w 9.3 rupture with high slip concentration (~ 30 m) at ~ 39-40ºS, and the 1730 event was a M_w 9.3 rupture with shallow maximum slip at ~ 36ºS; both solutions support the MFZ hypothesis. The AIC results generally agree with previously estimated magnitudes within the literature and were validated by using root mean square error RMSE values. I produced high resolution maps at three coastal sites with well-known tsunami observations for further refinement of potential rupture scenarios. Defining historical rupture characteristics gives insight regarding temporal and spatial variabilities of locking zones. This information may be useful for predicting future near-field tsunami wave heights for particularly vulnerable coastal regions.

ACKNOWLEDGMENTS

Before I get into my more personal acknowledgments, I first want to acknowledge the Central Washington University School of Graduate Studies and Research for providing me with my graduate assistantships for the past two years. Also, I would like to acknowledge the National Science Foundation for providing funding to this research with grant EAR-1624542 awarded to Dr. Lisa Ely and Dr. Breanyn MacInnes.

Now, I would like to give a big thank you to my advisor, Bre, for her guidance during the process of completing this project. I especially would like to acknowledge her patience and encouragement when it came to teaching me how to model tsunamis - this is a skill I am very grateful to have learned and one that I am very excited to apply towards my career. I could not have asked for a better advisor.

I would also like to thank my "co-advisor," Walter, for teaching me how to fish, rather than just giving me a fish. I now have an understanding of how to code in Python, which will prove to be useful when I enter the workforce. Also, thanks for talking sports with me whenever I needed a break from this project.

Additionally, my final committee member, Lisa, has been a tremendous help to me throughout this project - especially when it came to learning about the tsunami historical record of Chile. Traveling to Chile with you and the rest of the field team was a wonderful experience I will never forget. With that said, I'd also want to acknowledge Pachi for her absolutely extraordinary cooking during our field season. Those were an extra 10 pounds, I would be glad to get back.

Also, thank you Craig Scrivner, Catherine Jeffries, and Ben Norford: Craig for your help setting me up on the Linux machines and walking me through many UNIX commands/error messages. Catherine for your Linux help and answering all my calls to help me troubleshoot GeoClaw when I would accidentally crash it. And Ben for helping me with making my fault model.

Shout out to "the Fellas" at 14th Ave and the "Earthquakers" for all good times, memories, and making my CWU experience worthwhile. Lastly, thank you to Alec Melone for lending me your snowshoes that I used to summit Mt. St. Helens. Here is your acknowledgment that I promised.

TABLE OF CONTENTS

TABLE OF CONTENTS (CONTINUED)

LIST OF TABLES

LIST OF FIGURES

LIST OF FIGURES (CONTINUED)

LIST OF FIGURES (CONTINUED)

Figure Page

CHAPTER I

INTRODUCTION

Reliable forecasts are a necessary component of accurate advisory and warning messages in the case of an impending tsunami. Models can predict flooding in highly vulnerable areas along the coast, but models rely on accurate initial conditions, including the rupture dynamics of tsunamigenic earthquakes. Currently, little is known about the rupture characteristics of most pre-20th century events; the methods used today to study detailed rupture dynamics, such as GPS and seismologic data, are all inventions of the last century, and as such only work for modern events. To improve tsunami forecasts with a multi-century perspective of rupture dynamics, it is critical to understand how a subduction zone behaved during pre-20th century events. In some locations, written accounts provide enough evidence to estimate some earthquake details, such as magnitude (M_w) and the area of rupture (Lagos 2000; Lomnitz, 2004; Udias et al., 2012). With the addition of paleotsunami geological studies, these estimates can be refined to include better precision of magnitude and location, and potentially also estimates of location of high slip (Hirata et al., 2003; Nanayama et al., 2003; Satake et al., 2003; Satake and Atwater, 2007; MacInnes et al., 2010; Atwater et al., 2016).

In this research I plan to use observed historic and geologic tsunami evidence as a benchmark to define the inundating properties of known tsunamis, which I will link to the rupture properties of the earthquake that produced these tsunamis (MacInnes et al., 2010). The initial water disturbance by a subduction zone earthquake that generates a tsunami directly reflects the seafloor deformation pattern produced by the earthquake's rupture pattern. Many of these details of original rupture characteristics are preserved in the

tsunami as it propagates (Okal, 2009). For example, Geist (2002) suggests that tsunami flooding in the near-field is sensitive to the source parameters of an earthquake independent to seismic moment, such as the distribution of slip. Because a tsunami deposit on land is considered a good proxy for the horizontal distance of tsunami penetration (inundation) and the elevation above mean sea level (runup) (MacInnes et al., 2013), the overall deposit distribution in the near-field may preserve details of original rupture characteristics, such as details the earthquake's slip distribution (Satake et al., 2003; Satake et al., 2008; MacInnes et al., 2010; MacInnes et al., 2013).

The goal of my research was to create and evaluate a new methodology to statistically assess possible rupture parameters of known pre-instrumental earthquakes. First, I built a database of forward-modeled numerical tsunami simulations from hundreds of earthquake sources that defined realistic possible rupture patterns on a subduction zone. The earthquake sources had stochastic (i.e. randomly determined) variable finite-slip distributions. The detailed historical record and paleotsunami deposit database that I compiled provides a means identify a suite of earthquake source models and their associated simulated tsunamis that best replicate the known maximum wave heights from a specific historical event. Finally, I evaluated the suite of best earthquake models to estimate rupture characteristics for known earthquakes.

The method of statistically selecting earthquake models that I used for this study was Akaike's information criterion (AIC) statistical modeling (Burnham and Anderson, 2002). AIC provided a simple, effective, and objective way to analyze a large data set for the selection of an estimated "best approximating model" (Burnham and Anderson, 2002). AIC determined its model selection based on information theory and Bayesian

methods (Burnham and Anderson, 2002). This newer paradigm in the statistical sciences is an extension to R.A. Fisher's maximum likelihood principle (Kullback, 1959; Akaike, 1974). The process of model selection has new philosophical and computational advantages, which is different from previous methods based on null hypothesis testing (Akaike, 1974; Anderson et al., 2000; Breihman, 2001; Burnham and Anderson, 2002).

Chile was an excellent candidate for this new methodology because there is an extensive earthquake written record dating to the 1500s with previously estimated slip distributions for specific earthquake events (e.g. 1960; Barrientos and Ward, 1990; Moreno et al., 2009; NGDC/WGS, 2018). Recovered writings from Spanish conquistadors' supports evidence of Chile having one of the world's most active interplate margins (Cisternas et al., 2005). In south-central Chile (46°S to 30°S), at least 17 destructive tsunamigenic events occurred between AD 1570 and 1960; the 1960 earthquake (M_w 9.5) was instrumentally recorded as the largest earthquake in modern history (NGDC/WDS, 2018). Additionally, south-central Chile has nine localities with good preservation of the tsunami record studied in detail to date. South-central Chile's warm and temperate climate, in addition to its coastal geomorphology (many marshes and beach swales) allow for this preservation of geologic tsunami evidence. These 17 events all have rough estimates of M_w and general rupture position, but few solutions of rupture parameters have been defined with any confidence (Lagos, 2000; Lomnitz 2004; Udias et al., 2012; NGDC/WDS, 2018).

Although this study's goal is to interpret pre-20th century earthquakes, I include the 1960 earthquake as means to validate the statistical results of this new methodology. The 1960 event has two previously published slip distributions associated with it that

hypothesize a long rupture extent along strike (Barrientos and Ward, 1990; Moreno et al., 2009). The 1960 tsunami also has ~29 nearshore locations over ~ 1,120 km with historic or geologic tsunami evidence (Saint-Amand, 1963; Sievers et al., 1963; Weischet, 1963; Iida et al., 1967; Iida, 1984; Atwater et al., 1999; Lagos, 2000; Fritz et al., 2011; Atwater et al., 2013; Ely et al., 2014; Garrett et al, 2015; Carvajal et al., 2017; Cisternas et al. 2017; Dura et al., 2017; Hong et al. 2017; Kempf et al., 2017; L. Ely Pers. Comm., 2019; Matos-Llavona et al., 2019).

In addition to having a long record of known tsunamis, Chile's subduction zone also poses an interesting, yet simple test case to study whether this methodology can show subduction-zone dynamics over the centuries time scale. The south-central Chile subduction zone is proposed to be divided into two segments that rupture independently, separated by the Mocha fracture zone (MFZ; Contreras-Reyes and Carrizo, 2011). Because coastal marine terraces at this latitude reveal ~200 m of relief and demonstrate zones of rapid coastal uplift, the MFZ is hypothesized to continue as a subducted fracture zone under the Isla Mocha region at ~ 38.3°S (Contreras-Reyes et al., 2008; Melnick et al., 2009; Jara-Munoz et al., 2015). Whether or not fracture zones such as the MFZ control rupture propagation is an open question. The statistical analysis of hundreds of modeled earthquake scenarios should be able to test whether the MFZ may have inhibited rupture propagation in the past 500 years. Specific suites of earthquakes with a "good-fit" arising on one side of the MFZ, but not crossing the MFZ boundary would support this claim.

Earthquake source models that generate tsunami simulations that best match the paleotsunami and historical observations of past south-central Chile tsunamigenic events

have the potential to provide spatial and temporal information about the behavior of the Chilean subduction zone. The outcome of this research shows how current paleotsunami deposits can be used in the understanding of earthquake rupture characteristics from past events along the coast. This research may lead to applications for identifying coastal vulnerability, potential future tsunami forecasting, and hazard preparedness in coastal communities.

CHAPTER II

BACKGROUND

Geologic setting

Recovered historical writing and geologic paleotsunami studies show that Chile is one of the most seismically active locations in the world. Chile's entire 4,270-km long coastline sits alongside the Chilean subduction zone. Here, the Nazca Plate is subducting at ~15° underneath the South American at ~6.6 cm/yr (Angermann et al., 1999). Because of the fast rate of subduction in south-central Chile, there have been as many as 17 historical tsunamigenic earthquakes from 1570 AD to 1960 AD in south-central Chile (Figure 1; Table 1), between 46.2°S (the Chile Triple Junction) and 30.57°S (the Limari Province; FitzRoy, 1839; Milne 1900a; Milne, 1911; Davidson, 1936; Berninghausen, 1962; Sievers et al., 1963; Weischet, 1963; Iida et al., 1967; Lomnitz, 1970; Soloviev and Go, 1975; Instituto Hidrografico de la Armada, 1982; Iida, 1984; Lockridge, 1985; Van Dorn, 1987; Lander and Lockridge, 1989; Monge 1993; Atwater et al., 1999; Lagos, 2000; Lomnitz, 2004; Cisternas et al., 2005; Fritz et al., 2011; Udias et al., 2012; Valenuela, 2012; Wang et al., 2012; Atwater et al., 2013; Ely et al., 2014; Garrett et l., 2015; Urbina Carrasco et al., 2016; Carvajal et al., 2017; Cisternas et al., 2017; Dura et al., 2017; Hong et al., 2017; Kempf et al., 2017). Just within the last 60 years, two major earthquakes occurred in south-central Chile: the 1960 M_w 9.5 earthquake off the coast of Valdivia (Weischet, 1963), and the 2010 M_w 8.8 earthquake off the coast of Maule (Fritz et al., 2011).

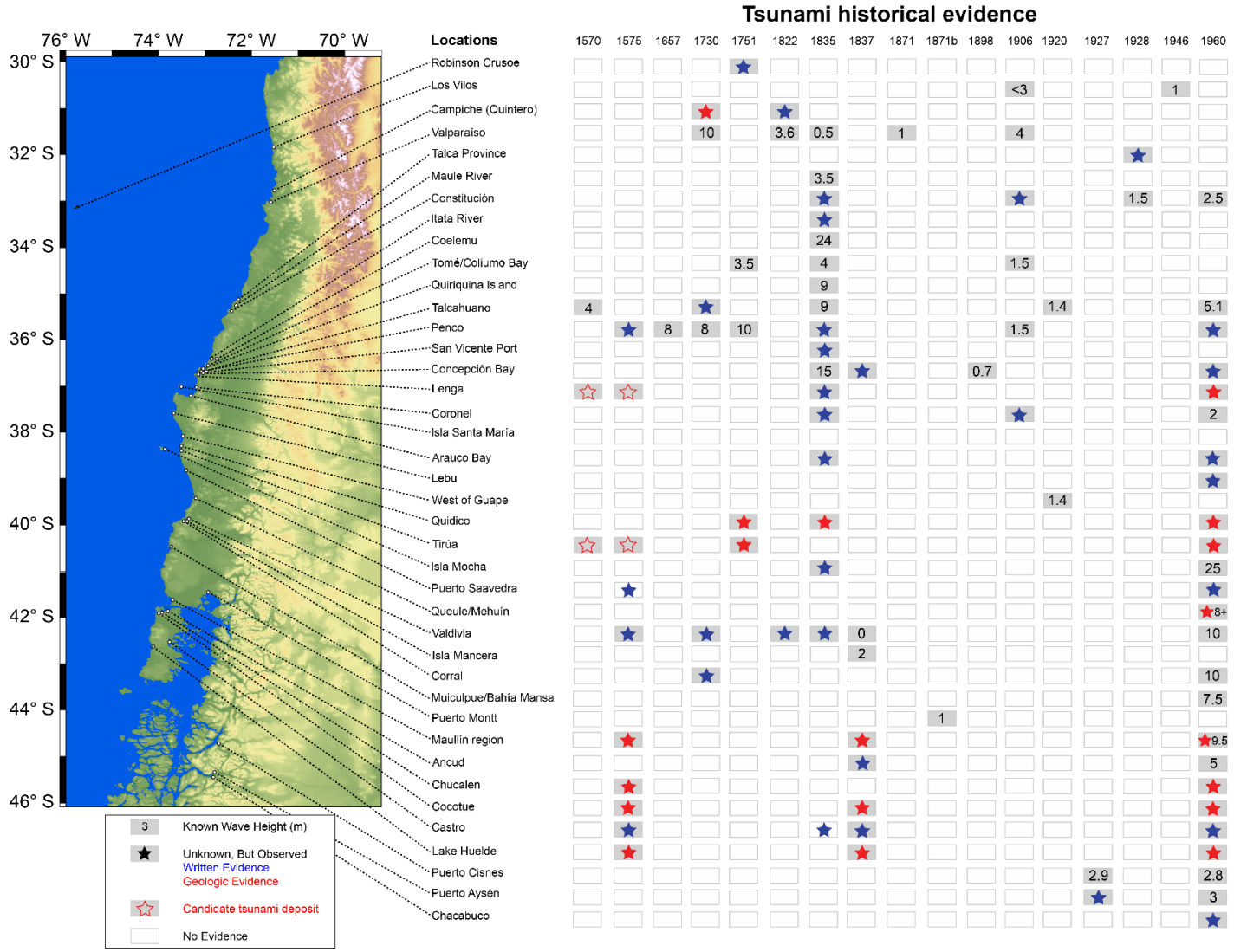

Figure 1: Location of tsunami historical evidence for 17 tsunamigenic earthquake events between 1570 and 1960. Numbers indicate maximum wave heights (m) recorded ("0" refers to documentation of no tsunami recording). Stars indicate unspecified maximum wave heights within the geologic record (red = geologic evidence, blue = written evidence, open red = candidate tsunami deposit) Refer to Table 1 for original sources of all data.

Table 1: Complete historical tsunami observation database between 1570 and 1960 in south-central Chile. "O" indicates unspecified maximum wave height within the historical record. "X" indicates documentation of no tsunami recording.

Year	Date	Estimated magnitude	Latitude (°S)	Longitude (°W)	Location	Maximum wave height (m)	Type of observation	Maximum wave height citation
1570	8-Feb	M 8.0 - 8.5	36.73617	72.99081	Penco	4	Written	Soloviev and Go, 1975
			36.77093	73.16522	Lenga	O**	Geologic	L. Ely Pers Comm., 2018
			38.34447	73.48758	Tirúa	O**	Geologic	L. Ely Pers. Comm., 2018
1575	17-Mar	Similar to 1960 M_w 9.5	36.73617	72.99081	Penco	O	Written	Soloviev and Go, 1975
			36.77093	73.16522	Lenga	O**	Geologic	L. Ely Pers Comm., 2018
			38.32930	73.48824	Tirúa	O	Geologic	Ely et al., 2014
			38.34447	73.48758	Tirúa	O**	Geologic	L. Ely Pers Comm., 2018
			38.78323*	73.40182	Puerto Saavedra	O	Written	Cisternas et al., 2005
			39.81743	73.26205	Valdivia	O	Written	Lomnitz, 2004
			41.63198	73.57816	Maullín	O	Geologic	Cisternas et al., 2017
			41.84600	74.00039	Chucalen	O	Geologic	Garrett et al., 2015
			41.92361	74.00299	Cocotue	O	Geologic	Cisternas et al., 2017
			42.48118*	73.75943*	Castro	O	Written	Lomnitz, 2004
			42.59949	74.11395	Lake Huelde	O	Geologic	Kempf et al., 2017
1657	15-Mar	M 8.0	36.73617	72.99081	Penco	8	Written	Lomnitz, 2004
1730 (cont. onto next page)	8-Jul	M 9.1 - 9.3	32.75595	71.46517	Campiche (Quintero)	O	Geologic	M. Carvajal Pers. Comm., 2019
			33.03948	71.62942	Valparaíso	10	Written	Carvajal et al., 2017
			36.72474*	73.10445*	Talcahuano	O	Written	Instituto Hidrografico de la Armada, 1982
			36.73617	72.99081	Penco	8	Written	Carvajal et al., 2017

Year	Date	Estimated magnitude	Latitude (°S)	Longitude (°W)	Location	Maximum wave height (m)	Type of observation	Maximum wave height citation
			39.81743	73.26206	Valdivia	O	Written	Soloviev and Go, 1975
			39.88387	73.42598	Corral	O	Written	Instituto Hidrografico de la Armada, 1982
1751	25-Mar	Similar to 2010 M_w 8.8	33.64150*	78.84610	Robinson Crusoe; Juan Fernandez Islands	O	Written	Lyell, 1875; Udias, 2012
			36.54621	72.93624	Coliumo Bay (Los Morros)	3.5	Written	Lagos, 2000
			36.73617	72.99081	Penco	10	Written	Udias et al., 2012
			38.25070	73.49290	Quidico	O	Geologic	Hong et al., 2017
			38.32930	73.48824	Tiráa	O	Geologic	Ely et al., 2014
1822	19-Nov	M 8.0 - 8.5	32.75595	71.46517	Quintero	O	Written	Soloviev and Go, 1975
			33.04271	71.69600	Valparaíso	3.6	Written	Soloviev and Go, 1975; Lomnitz, 2004
			39.81743	73.26205	Valdivia	O	Written	Soloviev and Go, 1975
1835 (cont. onto next page)	20-Feb	M 8.2 - 8.5	33.04271	71.69600	Valparaíso	0.5	Written	Lomnitz, 2004
			35.31632*	72.41130	Maule River	3.5	Written	Soloviev and Go, 1975
			35.32786*	72.42865	Constitución	O	Written	Soloviev and Go, 1975
			36.47846*	72.69542	Coelemu	24	Written	Soloviev and Go, 1975
			36.48430	72.90664	Itata River	O	Written	Soloviev and Go, 1975
			36.54621	72.93624*	Coliumo Bay (Los Morros)	4	Written	FitRoy, 1839
			36.61774	72.96333	Tomé	4	Written	Soloviev and Go, 1975
			36.63735	73.05999	Quiriquina Island	9	Written	Soloviev and Go, 1975
			36.72474*	73.10445*	Talcahuano	9	Written	Soloviev and Go, 1975

Year	Date	Estimated magnitude	Latitude (°S)	Longitude (°W)	Location	Maximum wave height (m)	Type of observation	Maximum wave height citation
			36.72917	73.13777	San Vicente Port (Concepción)	O	Written	Soloviev and Go, 1975
			36.73471	73.05561	Concepción Bay	15	Written	Lomnitz, 2004
			36.73617	72.99081	Penco	O	Written	Soloviev and Go, 1975
			36.77093	73.16522	Lenga	O	Written	FitzRoy, 1839
			37.04550	73.51033	Isla Santa María	O	Written	FitzRoy, 1839; Wesson et al., 2015
			37.23680	73.30788	Arauco	O	Written	Soloviev and Go, 1975
			38.25070	73.49290	Quidico	O	Geologic	Hong et al., 2017
			38.37465	73.86740	Isla Mocha	O	Written	FitRoy, 1839
			39.81743	73.262045*	Valdivia	O	Written	FitRoy, 1839
			42.481176*	73.75943*	Castro	O	Written	Soloviev and Go, 1975
1837	7-Nov	M 8.0 - 8.5	36.73471	73.05561	Concepción Bay	O	Written	Cisternas et al., 2005
			39.81743	73.26205	Valdivia	X	Written	Iida, 1984
			39.89045*	73.39495	Isla Mancera	2	Written	Lockridge, 1985
			41.59498	73.59854	Western Maullín	O	Geologic	Cisternas et al., 2005
			41.63198	73.57816	Maullín	O	Geologic	Cisternas et al., 2005
			41.86663	73.82977	Ancud	O	Written	Soloviev and Go, 1975
			41.92361	74.00299	Cocotue	O	Geologic	Cisternas et al., 2017
			42.48118*	73.75943*	Castro	O	Written	Berninghausen, 1962
			42.59949	74.11395	Lake Huelde	O	Geologic	Kempf et al., 2017
1871	25-Mar	M 7.5	33.04271	71.69600	Valparaíso	1	Written	Lockridge, 1985
1871b	28-Dec	n/a	41.486024*	72.96388	Puerto Montt	1	Written	Lockridge, 1985
1898	23-Jul	M 6.5	36.73471	73.05561	Concepción Bay	0.7	Written	Milne, 1900a; Lockridge, 1985

Year	Date	Estimated magnitude	Latitude (°S)	Longitude (°W)	Location	Maximum wave height (m)	Type of observation	Maximum wave height citation
1906	16-Aug	M 8.2 - 8.6	31.90929	71.51158*	Los Vilos	<3	Written	Lagos, 2000
			33.04271	71.69600	Valparaíso	4	Written	Lagos, 2000
			35.32786*	72.42865	Small settlements near Constitución	O	Written	Soloviev and Go, 1975
			36.61774	72.96333	Tomé	1.5	Written	Soloviev and Go, 1975
			36.73664	72.99600	Penco	1.5	Written	Soloviev and Go, 1975
			37.03602	73.14661*	Coronel	O	Written	Soloviev and Go, 1975
1920	20-Aug	M 7.0	36.72474*	73.10445*	Talcahuano	1.4	Written	Berninghausen, 1962; Lockride, 1985
			37.99779	73.47869	West of Guape	1.4	Written	Lagos, 2000
1927	21-Nov	M 7.1	44.73059	72.68421	West of Puerto Cisnes	2.9	Written	Iida et al., 1967; Soloviev and Go, 1975
			45.40257	72.82976	Puerto Aysen	O	Written	Lockridge, 1985
1928	1-Dec	M 7.6 to 8.4	35.03805*	72.16394	Talca Province	O	Written	Soloviev and Go, 1975
			35.32786*	72.42865	Constitución	1.5	Written	Lomnitz, 2004; Soloviev and Go, 1975
1943	6-Apr	M 8.3	31.90929*	71.51158	Los Vilos	1	Written	Lagos, 2000; Lomnitz, 2004
1960 (cont. onto next page)		M_w 9.5	35.32786*	72.42866	Constitución	2.5	Written	Iida et al., 1967
			36.72474*	73.10445*	Talcahuano	5.1	Written	Fritz et al., 2011
			36.73471	73.05561	Concepción Bay	O	Written	Iida, 1967
			36.73617	72.99081	Penco	O	Written	Carvajal et al., 2017
			36.77093	73.16522	Lenga	O	Geologic	L. Ely Pers. Comm, 2019
			37.03602	73.14661*	Coronel	2	Written	Iida et al., 1967
			37.23680	73.30788	Arauco	O	Written	Iida et al., 1967

Year	Date	Estimated magnitude	Latitude (°S)	Longitude (°W)	Location	Maximum wave height (m)	Type of observation	Maximum wave height citation
			37.59129	73.64870	Lebu	O	Written	Lagos, 2000
			38.25070	73.49290	Quidico	O	Geologic	Dura et al., 2017; Hong et al. 2017
			38.32930	73.48824	Tirúa	O	Geologic	Ely et al., 2014
			38.37465	73.86740	Isla Mocha	25	Written	Iida, 1984
			38.78323	73.40182	Puerto Saavedra	11.5	Written	Weischet, 1963
			39.39792	73.21172	Queule	O	Geologic	Matos-Llavona et al., 2019
			39.42997	73.21527	Mehuín	8 to 15	Written	Weischet, 1963; Iida, 1984
			39.81743	73.26204	Valdivia	10	Written	Iida, 1984
			39.88387	73.42598	Corral	10	Written	Iida, 1984
			40.58421	73.73598	Muiculpue/ Bahía Mansa	7.5	Written	Weischet, 1963
			73.6782	41.57341	Maullín region	9.5	Geologic	Atwater et al., 2013
			41.84600	74.00039	Chucalen	O	Geologic	Garrett et al., 2015
			41.84618	74.00065	Chucalen	O	Geologic	Garrett et al., 2015
			41.86663	73.82977	Ancud	5	Written	Saint-Amand, 1963; Weischet, 1963
			41.92361	74.00299	Cocotue	O	Geologic	Cisternas et al., 2017
			42.48118*	73.75943*	Castro	O	Written	Lagos, 2000; Lomnitz, 2004; Cisternas et al., 2005
			42.59949	74.11395	Lake Huelde	O	Geologic	Kempf et al., 2017
			44.73059	72.68421	West of Puerto Cisnes	2.8	Written	Sievers et al., 1963
			45.40258	72.82976	Puerto Aysen	3	Written	Sievers et al., 1963
			45.45655*	72.83443*	Chacabuco	O	Written	Sievers et al., 1963

* Estimated coordinate from Google Earth.

** Geologic tsunami deposit. Radiocarbon constraints suggest that this deposit could be from 1570 or 1575.

History of occupation and settlement in south-central Chile

The history and timeline of occupation by Spanish Conquistadors in south-central Chile may unfortunately bias the written tsunami historical record. Despite native Mapuche already settled in south-central Chile, only the Spanish kept a documented written record of tsunamigenic earthquake events, which were sent back to Spain in reports. Pre-1580, Spanish settlement was sparse, as there were only a few locations that were fortified and/or occupied. These locations within my study area were Concepción (referred to as Penco post-1843), Arauco, La Imperial (also known as Puerto Saavedra), Corral Bay (also known as Valdivia), and Castro (Guarda, 1970; Campos-Harriet, 1989; Burgos, 1990; Lane, 2015; Cisternas et al., 2012; Cisternas et al., 2017). By 1600, Spanish settlements occupied an outpost in Valparaíso as well, extending the written record to the north (Guarda, 1978). In the 17th century, native Huilliche and Mapuche joined the Dutch to attack the Spanish settlement at Castro and Valdivia, respectively (Lane, 2015). These forts were eventually overtaken, but abandoned by the Dutch due to financial burden. This sequence of events allowed native tribes to establish a stronghold in southern Chile and effectively block out new Spanish settlements between Valdivia and Castro (Lane, 2015). During the 18th century, the Spanish Bourbon dynasty came to power, resettling forts at Valdivia and Castro, and the historical record spatially expanded to also include Spanish coastal fortifications at Talcahuano, Coliumo Bay (also called Dichato), Ancud, Robinson Crusoe Island, and Tenquehuen (in the Aysen region, however abandoned after a couple years; Saavedra Villegas, 1984; Rodríguez, 2006;

Villanueva et al., 2010; Urbina Carrasco, 2014; Cisternas et al., 2017). Chile officially declared independence from Spain in 1818 and in this time of political changes leading up to the Parliamentary era at the end of the 19th century, settlement continued to expand to locations such as Los Vilos, Constitución, Coronel, Lebu, and Puerto Montt (Collier and Sater, 1996). In the 20th century, more settlements began to establish between the major cities, in addition to resettlement in the Puerto Aysen region, which expanded written records to the southern portion of Chile (Urbina Carrasco, 2014).

Geologic paleotsunami field studies in south-central Chile

Geologic paleostunami studies and dating methods in south-central Chile are helpful to limit bias in the historical record due to the lack of occupation and availability of writing. As of 2019, there are paleostunami field studies (Figure 1; Table 1) from Quintero (M. Carvajal Pers. Comm., 2019), Lenga (L. Ely Pers. Comm., 2019), Tirúa (Ely et al., 2014), Queule (Matos-Llavona et al., 2019), Quidico (Dura et al., 2017; Hong et al., 2017), Maullín (Cisternas et al., 2005; Atwater et al., 2013), Chucalen (Garrett et al., 2015), Cocotue (Cisternas et al., 2017), and Lake Huelde (on Chiloe Island; Kempf et al., 2017). These paleotsunami deposit studies generally consist of surveying a coastal landscape, identifying a potential tsunami deposit, mapping the extent of a tsunami deposit, and dating the deposit (Pinegina and Bourgeois, 2001; Ely et al., 2014). Tsunamis leave depositional sand layers on the landscape that get preserved with a sharp

contact over the previous modern soil in certain conditions when deposited in beach swales and marshes (Brill et al, 2011; Nelson et al., 2015). Paleotsunami studies use methods in which tsunami depositional sand layers are identified through the techniques of gouge-coring, pit-digging, trench-digging, lake sediment coring, and augering (Cisternas et al., 2005; Atwater et al., 2013; Ely et al., 2014; Kempf et al., 2017). These sand layers can be used as a proxy for large earthquake events as they provide recurrence histories within the stratigraphy (Pinegina and Bourgeois, 2001). The distribution of a tsunami deposit provides a minimum estimate of inundation distances and runup heights in a specific location (Fujiwara et al., 2000; Scheffers et al., 2008; Peterson et al., 2011).

Historical earthquakes and tsunamis in south-central Chile

Written accounts and paleotsunami sand deposits document 17 known tsunamigenic earthquakes between 1570 AD and 1960 AD (Figure 1; Table 1). These earthquake events, from earliest to most recent, consist of the: 1570, 1575, 1657, 1730, 1751, 1822, 1835, 1837, 1871, 1871b, 1898, 1906, 1920, 1927, 1928, 1943, and 1960 AD events (FitzRoy, 1839; Milne 1900a; Milne, 1911; Davidson, 1936; Berninghausen, 1962; Sievers et al., 1963; Weischet, 1963; Iida et al., 1967; Lomnitz, 1970; Soloviev and Go, 1975; Instituto Hidrografico de la Armada, 1982; Iida, 1984; Lockridge, 1985; Van Dorn, 1987; Lander and Lockridge, 1989; Monge 1993; Atwater et al., 1999; Lagos, 2000; Lomnitz, 2004; Cisternas et al., 2005; Fritz et al., 2011; Udias et al., 2012; Valenuela, 2012; Wang et al., 2012; Atwater et al., 2013; Ely et al., 2014; Garrett et l., 2015; Urbina Carrasco et al., 2016; Carvajal et al., 2017; Cisternas et al., 2017; Dura et

al., 2017; Hong et al., 2017; Kempf et al., 2017). The rupture location of these earthquakes can be defined to varying degrees of accuracy (Lagos, 2000; Lomnitz, 2004; Cisternas et al., 2005; Udias et al., 2012). What follows is a description of what is known about each of these events.

1570 Event

At 9:00 AM local time on February 8, 1570, an earthquake shook central Chile near from Concepción (present day location of Penco; Soloviev and Go, 1975). Based on the written record from Spanish conquistadors, this earthquake is associated with a major tsunami that was observed mainly in the Concepción Bay region. It was recorded that the ocean along the coast of present day Penco receded nearly ten kilometers before it completely inundated the town. Ships were transported onto dryland, settlements were completely washed away, and over 2000 people were killed in the tsunami (Soloviev and Go, 1975). Tsunami sand deposit candidates observed in Lenga and Tirúa have a radiocarbon age that is constrained within the time period of this earthquake; however, these deposits could be from the 1575 tsunami instead (Ely et al., 2014; Dura et al., 2017; L. Ely Pers. Comm., 2018). The magnitude of the earthquake was estimated to be between M 8.0 and 8.5, which is based on written reports of damages and shaking intensity (Lagos 2000; Lomnitz, 2004). Concepción Bay was the northernmost extent that was recorded as affected by the tsunami (Soloviev and Go, 1975). Tirúa may have been the southernmost extent based on a potential paleotsunami deposit; however, if the

deposit observed in Tirúa is from the 1575 event (L. Ely Pers Comm., 2018), the tsunami historical record is constrained to the Concepción Bay region.

1575 Event

At 10:00 AM local time on March 17, 1575, an earthquake caused a major tsunami that was recorded from Concepción (present day location of Penco) to Lake Huelde on Chiloe Island (Lagos, 2000; Lomnitz, 2004; Udias et al., 2012; Kempf et al., 2017). In Valdivia, the tsunami reversed the natural flow of the Valdivia River as it rushed in nearly 25 km from the mouth. This rise in water knocked down settlements and uprooted trees. In the Valdivia port, two galleon ships were sunk and washed onshore, and ~1500 deaths occurred, including ~100 native fisherman that drowned near the mouth of the Imperial River (Lomnitz, 1970; Soloviev and Go, 1975). Although the tsunami was observed around the Concepción Bay region, there was no reported information of damage from the tsunami (Soloviev and Go, 1975). Tsunami deposits with radiocarbon ages corresponding to the 1575 event are widespread and found at Maullín, and Cocotue (Cisternas et al., 2017), with two potential tsunami candidates found at Lenga and Tirúa (same deposits noted in the *1570 Event* section (L. Ely Pers Comm., 2018). Additionally, the lateral extent of shaking from this earthquake is interpreted as similar to the M_w 9.5 1960 earthquake off the coast of Valdivia (Cisternas et al., 2017). The large span of coastline that appears to have been inundated from both the 1575 and

1960 tsunami suggests that 1575 may have also been an earthquake with a long rupture of great magnitude.

1657 Event

On March 15, 1657 an earthquake occurred off the coast of Concepción around 8:00 PM local time (Berninghausen, 1962). A report written to Felipe IV in Spain on April 3rd, 1657, by Alonso de Solorzano y Velasco, the officer of the Royal Court of Santiago, regarding the state of the nation alludes to a large tsunami (Lomnitz, 2004). This report states that seawater had entered the streets and houses three times at Concepción (present day location of Penco; Lomnitz, 2004). Other written accounts from civilians in Concepción confirm that there were at least three large waves with the largest occurring at least two hours after the earthquake (Berninghausen, 1962; Soloviev and Go, 1975). Much of Concepción suffered heavy damage, especially areas along the river of the eastern part of the town, as there were fewer houses to protect the inner sections from the waves (Instituto Hidrografico de la Armada, 1982). The written documents also estimate the maximum wave height of this tsunami to be ~8 m high in what is now Penco (Lockridge, 1985). The earthquake was estimated as a M 8.0 based on written reports of damages and shaking intensity (Lockridge, 1985; Lomnitz, 2004; Lagos, 2000).

1730 Event

On July 8, 1730, at ~ 4:45 AM local time, an earthquake occurred near the Valparaíso area (Soloviev and Go, 1975). After the shaking, a disruptive tsunami quickly inundated the land with three large flows that "were said to have exceeded that of 1657" (Lomnitz, 2004). Many towns and fields were reportedly affected. In Concepción (present day location of Penco), nearly two-thirds of the town was destroyed, which consisted of more than 200 houses and buildings (Soloviev and Go, 1975). Only two or three people were killed in this tsunami, "since inhabitants, on first noting the receding sea, ran for the hills from where they watched the destruction of their houses and their property" (Soloviev and Go, 1975). This was the third major tsunami since the town's founding. Recovered documents from an anonymous Jesuit Father also noted flow depth values of ~8 m at the beach, ~1 m at the Jesuit convent, ~1.5 m at the Franciscan convent; unspecified flooding at the hospital, guard, plaza, palace, and cathedral; and that no flooding reached the Mercedarian convent that was situated on higher ground (Carvajal et al., 2017).

Other recovered religious records reported that the tsunami was 7 m high along the Valparaíso beach, and that flooding had occurred at the Valparaíso Augustinian convent, La Matriz Church, and the Mercedarian convent (Valenuela, 2012; Urbina et al., 2016; Carvajal et al., 2017). Carvajal et al. (2017) conducted a post-tsunami water mark survey three weeks after the 2010 M 8.8 Maule earthquake (which is assumed by Carvajal et al. (2017) to be smaller than 1730) in both Valparaíso and Penco. Correlating

water heights from the 2010 tsunami, their survey concluded that in Valparaíso, for water to reach Augustinians, La Mariz, and Mercedarians in 1730, the water had to be ~10 m, ~9 m, and ~9 m high, respectively. In Penco, the 1730 tsunami would be ~ 3 m high at the Guard, ~8 m high at the Jesuit and Mercedarian convents, ~5 m high at the Fransican and Augustinian convents, ~ 3 m high at the hospital, fort, and palace, and ~ 7 m high at the cathedral (Carvajal et al., 2017). Written accounts also suggest that the tsunami affected Talcahuano, Corral, and Valdivia (Soloviev and Go, 1975; Instituto Hidrografico de la Armada, 1982; Urbina Carrasco et al., 2016). Tsunami modeling to match the observations noted in these religious texts suggest that this earthquake may have been around M 9.1 to M 9.3 in size (Carvajal et al., 2017).

1751 Event

On March 25, a little after 1:00 AM local time, a large earthquake was felt near the Concepción area (Soloviev and Go, 1975). About 30 minutes following the shaking, Concepción experienced three large waves, occurring one after another "quite rapidly" (Soloviev and Go, 1975; Lomnitz, 2004). Historical accounts suggest that the main wave was ~10 m high, and recovered Spanish reports suggest that this event was at least the fourth time that Old Concepción was affected by tsunamis in its history and, perhaps the third time in 20 years (Udias, 2012). As a result, Concepción was rebuilt farther inland from the coast and the old site became the town of Penco (Soloviev and Go, 1975). The tsunami was also observed in Valparaíso. Udias (2012) suggests that the 1751 earthquake

was similar in size to the 2010 Maule M_w 8.8 earthquake based on the description of the damage, and the areal extent of the earthquake shaking and tsunami. The 1751 tsunami caused a total of 36 recorded deaths, including the governor of the Fernandez Islands (Udias, 2012). Radiocarbon dates constraining geologic tsunami deposit ages suggest this tsunami also inundated Quidico (Hong et al., 2017) and Tirúa (Ely et al., 2014).

1822 Event

At ~10:30 PM local time on November 19, 1822, the Valparaíso area felt a damaging earthquake with an epicenter about ~15 km north of Valparaíso (Berninghausen, 1962). The subsequent tsunami in Valparaíso was estimated to be ~ 3.6 m high, based on wave height recordings compared to the ordinary high tide mark on the morning of November 20, 1882 (Soloviev and Go, 1975; Lagos, 2000; Lomnitz, 2004). The sea suddenly rose with the initial wave, which thrust the admiral's ship up to the same level as the customs house, 3.5 m above the high tide mark, and then suddenly receded, which stranded other small vessels from the harbor inland (Davidson, 1936; Soloviev and Go, 1975). Additional waves also occurred, but never reached the height of the first, and eventually became unnoticeable after 15 minutes (Soloviev and Go, 1975). Near-field tsunami inundation was reported from Quintero in the north to Valdivia in the south; however no inundation accounts were reported in between (Soloviev and Go, 1975). In Quintero, dunes were washed away by the tsunami, numerous rocks were reported to be placed above the water level, and a sunken vessel that could previously

only be reached by boat (even in low tide) was now ~0.5 m above the water level due to uplift of the seafloor (Soloviev and Go, 1975). The magnitude of this earthquake was estimated between an M 8.0 and M 8.5 based on shaking intensity and land-level changes (Lagos, 2000; Lomnitz, 2004).

1835 Event

The February 20, 1835 earthquake occurred at ~11:30 AM local time off the coast of Concepción (Soloviev and Go, 1975). Based on shaking intensities derived from written reports, this earthquake was estimated to be M 8.2-8.5 (Lomnitz, 2004). During this event, the water in Concepción Bay darkened and let off an odor of hydrogen sulfide (Soloviev and Go., 1975). About 30 minutes after the initial earthquake, the water in the bay receded leaving the rocks and reefs bare before flooding the bay and transporting vessels to dry land (Soloviev and Go, 1795). Based on written reports, the maximum water height in Concepción Bay at Talcahuano and Quiriquina Island was suggested to be ~9 m high (Soloviev and Go., 1975; Lomnitz, 2004). The west shore of the bay experienced uprooted trees, shearing of houses, and movement of everything loose (Soloviev and Go, 1975). After this first wave, a second and third followed which were just as destructive as the first. The tsunami was noted as receding "suddenly" and carrying away many properties and belongings into the ocean (Soloviev and Go, 1975). The tsunami was reported for at least a 1000-km span in the written record from Valparaíso in the north to Castro on Chiloe Island in the south (Soloviev and Go, 1975).

The Coelemu shore experienced the largest recorded waves, ~24 m, with six inundating waves noted (Soloviev and Go, 1975). Soloviev and Go (1975) collected written evidence of inundation at the Maule River (~ 3.5 m), Constitución, Itata River, Coliumo Bay (~ 4 m), Tomé (~ 4 m), Penco, and Arauco, FitzRoy, (1839) noted inundation at Valdivia, San Vicente/Lenga, Coliumo, and Santa María (where uplift was 2.4-3 m (Wesson et al., 2015)). Inundation also occurred at Isla Mocha (Soloviev and Go., 1975; Lagos, 2000; Lomnitz, 2004; Wang et al., 2012; Dura et al., 2017), and there is geological evidence of tsunami deposits preserved in coastal environments in Quidico (Hong et al., 2017).

During Charles Darwin's voyage on the Beagle, Darwin and his crew experienced the shaking of the 1835 earthquake on land at Valdivia (FitzRoy, 1839; Lomnitz, 2004). In Valdivia, the river swelled up, the land subsided; and the sea flooded the shore to the high tide mark during low-tide—two people were reported deceased (Soloviev and Go, 1975). Overall, the sea never receded below the low tide mark and the river never fell below its usual level, but flood tides recurred one to two times an hour (Soloviev and Go, 1975).

1837 Event

In 1837, at ~8:05 AM local time on November 7, a large earthquake occurred off Chiloe Island near Ancud and Castro (Soloviev and Go, 1975). The earthquake was estimated from shaking intensities written in the historical record to be between M 8-8.5 (Lagos, 2000; Lomnitz, 2004). Accounts at Ancud suggest that the subsequent tsunami

caused both the Pudeto River and the strait that separates mainland Chile with Chiloe Island to experience large "tides" that migrated an "enormous" amount of seaweed and mollusks onto the shore (Soloviev and Go 1975). This tsunami largely affected the west side of Chiloe Island with no waves noted as inundating the east side, including at Castro (Berninghausen, 1962). Valdivia was also not affected by the tsunami, but was damaged from the earthquake (Iida, 1984). Additional written accounts in Chile indicate the tsunami inundated Concepción (Cisternas et al., 2005; Maullín (Cisternas et al., 2005), Cocotue (Cisternas et al., 2017), Lake Huelde (Kempf et al., 2017), and ~ 2m in Isla Mercera (Lockridge, 1985). The tsunami was also recorded as damaging in Hawaii, Samoa, the Tonga Islands, and Japan (Iida, 1984). Geological evidence of this tsunami has been found in Cocotue (Cisternas et al., 2017) and Lake Huelde (Kempf et al., 2017).

1871 Event

On March 25, 1871 at ~11:00 AM local time, a strong earthquake occurred north of Constitución at ~ 35°S (Soloviev and Go, 1975). At Valparaíso, the written accounts suggest a tsunami runup height of 1 m (Lockridge, 1985). This earthquake caused the sea off the coast of Valparaíso to also become "very agitated;" reports from ships in the Valparaíso harbor note they felt shaking (Soloviev and Go, 1975). The written accounts regarding shaking and the localized tsunami event in Valparaíso led to an estimate of M 7.5 for this earthquake (Lockridge, 1985).

1871b Event

Shortly after midnight local time on December 28, 1871, an earthquake was felt in the Puerto Montt region (Soloviev and Go, 1975). Written accounts suggest that the shaking from the earthquake caused a tent frame to fall, the hillsides to collapse, and the sea to become "very agitated" (Soloviev and Ho, 1975). The tsunami from this earthquake had a 1-m high wave runup in Puerto Montt (Lockridge, 1985).

1898 Event

At ~10:30 PM on July 23, 1898, a relatively small earthquake occurred near Concepción with a noticeable foreshock (Soloviev and Go, 1975). The earthquake was inferred to be M 6.5 (based on the degree of damages, shaking intensity, and where it was felt—Talcahuano, Valparaíso, Santiago (~ 100 km S-SE inland of Valparaíso), Coronel, Arauco, Lebu, Concepción, and small settlements inland between Constitución and Lebu (Soloviev and Go, 1975; Milne, 1911; Figure 1). The most serious destruction occurred in Concepción and Talcahuano; about 50 homes suffered some damages from cracked and warped walls, collapsed partitions, and fallen corinces (Soloviev and Go, 1975). Additionally, there was some small damage (no collapses) in Tomé, but three homes completely destroyed in Rere (small settlement SE of Concepción; Soloviev and Go, 1975). A M 6.5 earthquake typically is not large enough to generate a tsunami capable of inundation (Soloviev and Go, 1975). However, there are two conflicting written reports:

1) A report from the Mayor of Concepción at the time who mentions no activity in the sea and surrounding ports following the earthquake, and 2) a report from Milne (1900 a), suggesting the sea retreated off the coast of Concepción and Talcahuano, making inhabitants "terrified" of a tsunami (Soloviev and Go, 1975). Lockridge (1985) notes a tsunami 0.7 m high in the Concepción Bay area.

1906 Event

On August 16, 1906 at 8:40 PM local time, an earthquake with very strong and sudden shaking occurred near Valparaíso (Soloviev and Go, 1975). This earthquake was instrumentally recorded to be M 8.2 (Di Giacomo et al., 2015a; 2018). The shaking from this event was felt in Tacna Peru, Buenos Aires, Argentina, Chiloe Island, and the San Fernandez Islands (Soloviev and Go, 1975). Written accounts record that immediately following the earthquake, there were "strong surges" in the wave current in the bay near Coronel, with "not the slightest wind" (Soloviev and Go, 1975). At Penco and Tomé, the sea retreated 50-60 m and then rose ~1.5-m high to inundate the coastline sometime between 15 minutes to one hour after the initial earthquake (Soloviev and Go, 1975). Three to four tsunami waves flooded the land (Soloviev and Go, 1975). Also, nearby small coastal settlements around Constitución (such as Buchupureo, Putu, and Llico) reported that "the sea began to seethe or boil," disturbing the wave generation process (Soloviev and Go, 1975). The largest tsunami was recorded farther north than the

suggested source of the earthquake— written documents note a tsunami 3.6-m high west of Los Vilos (Lagos, 2000).

1920 Event

On August 20, 1920 at 11:30 AM local time, an earthquake occurred near 38.0 °S, 73.5 °W and was felt from the mouth of the Mataquito River in the north (36.0 °S) to Reloncavi Fjord in the south (41.1 °S; Iida et al., 1967; Soloviev and Go, 1975). The size of this earthquake is estimated to be a M 7.0 based on the extent of where it was felt and tsunami generation (Lockridge, 1985; Lagos, 2000). Historical records suggest that this earthquake caused a 1.4 m wave to inundate the coast west of Guape and at Talcahuano (Lockridge, 1985; Lagos, 2000). At the harbor at Talcahuano, anchored vessels were "violently thrown" by the harsh waves (Berninghausen, 1962).

1927 Event

On November 21, 1927 an earthquake occurred in southern Chile near Puerto Cisnes (Soloviev and Go, 1975). This earthquake was instrumentally recorded to be M 7.2 (Di Giacomo et al., 2015a; 2018). Reports suggest that large waves up to 2.8 m high formed around 44.6°S, 73º W near Puerto Aysen (Lockridge, 1985). Additional reports suggest that water inundated 100-150 m inland along 45 km along the coast of the Puerto Aysen region (the number of observations was not listed; Soloviev and Go, 1975; Iida et

al, 1967). One written account also suggests that a boat and crew were flung into the treetops from a large tsunami wave (Berninghausen, 1962).

1928 Event

At 12:07 AM local time on December 1, 1928 an earthquake sourced in central Chile nearly destroyed both Talca and Constitución: at Talca a fire broke out after the tsunami, which nearly burned down the town, causing 108 casualties, while many buildings collapsed at Constitución (and other neighboring settlements), causing 117 casualties (Soloviev and Go, 1975). This earthquake had an estimated magnitude of 7.7 (Di Giacomo et al., 2015a; 2018). This earthquake event caused waves up to 1.5 m above the diurnal high tide in Constitución (Soloviev and Go, 1975). Written accounts from sailors aboard the Santa Elisa and Poseidon steamships ~11-13 km off shore at Constitución observed the waves from considerable distance on a moonlit night. The sailors reported that unusually large waves moved in all directions on the surface for "no more than 112 minutes" (Soloviev and Go, 1975).

1943 Event

On April 6, 1943, a tsunamigenic earthquake, instrumentally recorded to be a M 8.1, occurred north of Los Vilos with an epicenter at ~ 30.6°S (Lomnitz, 2004; Di Giacomo et al., 2015a; 2018; Figure 1). This earthquake was felt inland at Santiago, Chile and Buenos Aires, Argentina where dishes were reported to break and liquids reported to

spill in tall buildings (Lomnitz, 2004). This earthquake caused a 1 m local tsunami at Los Vilos damaging fishing boats (Soloviev and Go, 1975; Lagos, 2000; Lomnitz, 2004; Lagos, 2000). It was recorded that the tsunami arrived at the tide gauge at Valparaíso 22.3 minutes after the initial earthquake (height of oscillations was 80 cm, average period was 10 cm, duration of oscillations was ~ 36 hours). This tsunami also registered at tide gauges in the far-field at Hawaii, California, and Japan (Kushimoto, Hanasaki, and Shimosato). It took approximately 23 hours and 25 minutes for this tsunami to reach the gauge at Kushimoto, Japan (25-cm oscillation amplitude; Soloviev and Go, 1975).

1960 Event

On May 22, 1960, at 3:12 PM local time, the largest instrumentally recorded earthquake in the world to date (M_w 9.5) ruptured in south-central Chile (Soloviev and Go., 1975; Van Dorn, 1987; Di Giacomo et al., 2015a; 2018). Written accounts from Maullín show that some citizens initially mistook the event for nuclear war (Atwater et al., 2013; Atwater et al., 1999). Both the earthquake and tsunami associated with this seismic event were catastrophic and devastated the land: Chile faced approximately $550 million in material damages and ~1000 deaths following this event (Instituto Hidrografico de la Armada, 1982; Lander and Lockridge, 1989). Also, the Hawaiian Islands, western U.S. coast, and Japan faced approximately $24 million in damages, $500,000 to $1,000,000, and $50 million in damages, respectively. There were 61

casualties in Hawaii, and 199 in Japan, where the wave was more than 6 m high (Lander and Lockridge, 1989).

Locally in Chile, there are countless geological and historical records of the event. Sediment deposits from this event can be found in Tirúa (Ely et al., 2014), Quidico (Dura et al., 2017; Hong et al. 2017), Chucalen (Garrett et al, 2015), Maullín (Atwater et al., 2013; Cisternas et al. 2017), Cocotue (Cisternas et al., 2017), Chiloe Island at Lake Huelde (Kempf et al., 2017), Queule (Matos-Llavona et al., 2019), and Lenga (L. Ely Pers. Comm., 2019). Additionally, written accounts indicate the tsunami had a wave height of: 2.5 m at Constitución (Iida et al., 1967); Maule River, 5.1 m at Talcahuano (Fritz et al., 2011), 2 m at Coronel (Iida et al., 1967), 25 m at Isla Mocha (Iida, 1984), 11.5 m at Puerto Saavedra (Weischet, 1963), 8 m or 15 m at Mehuín/Missisipi (Weischet, 1963; Iida, 1984), 10 m at Valdivia (Iida, 1984), 10 m at Corral (Iida, 1984), 7.5 m at Muiculpue/Bahía Mansa (Weischet, 1963), 5 m at Ancud (Saint-Amand, 1963; Weischet, 1963), 2.8 m west of Puerto Cisnes, and 3 m at Puerto Aysen (Sievers et al., 1963). The tsunami was also reported at Concepción (Iida, 1967), Penco (Carvajal et al., 2017), Arauco (Iida et al., 1967), Lebu (Lagos, 2000), and Chacabuco (Sievers et al., 1963), but specific values of wave height were not defined.

CHAPTER III

METHODOLOGY

Compiling observational values

To assess potential rupture scenarios, I first compiled a database of the tsunami historical record for my study area (Table 1) from a complete literature review of scientific papers and historical documents that described the effects from all 17 tsunamigenic earthquake events between 1570 and 1960 AD. The literature review is summarized in the *Background* chapter. The database of tsunami observations includes three types of data: 1) written observations of a tsunami with a known wave height recorded in historical documents, 2) written observations of a tsunami with no numerical value recorded in historical documents, and 3) geologic evidence of a buried tsunami sand deposit with no known wave height. How I used the database as a benchmark to compare against my simulated tsunami wave heights is described in more detail in the *AIC statistical analysis* section below.

GeoClaw simulations

I created earthquake and tsunami simulations with the open-source tsunami software, GeoClaw version 5.4.1 (http://www.clawpack.org/geoclaw). GeoClaw is a finite-difference model that solves the nonlinear shallow-water equations to calculate tsunami propagation and inundation given specific earthquake and bathymetric input parameters (George and LeVeque, 2006; MacInnes et al., 2013; Clawpack Development

Team, 2017). GeoClaw successfully predicts tsunami arrival times and runup heights and is approved by the US National Tsunami Hazard Mitigation Program (Gonzalez et al., 2011). GeoClaw utilizes the standard wave propagation algorithms of Clawpack for a rectangular grid with adaptive mesh refinement to increase the resolution of the simulation when the slope of the water surface exceeds a specific threshold (Berger and LeVeque, 1998; LeVeque et al., 2011). An explanation of the numerical and wave propagation algorithms used to solve the two-dimensional shallow-water equations can be found in LeVeque (2002) and Berger et al. (2011).

GeoClaw propagates a tsunami by solving for the nonlinear shallow water wave equations for a specific time step, while conserving mass and momentum in a Cartesian grid (LeVeque, 2002; LeVeque et al., 2011). Additionally, inundation in GeoClaw is determined by means of calculating water depth values for each cell per time step: dry land cells yield a value of zero, while wet cells yield positive values (LeVeque et al., 2011). In each time step, these water depth values may vary as radial momentum is also accounted for due to a radially symmetric ocean (LeVeque et al., 2011). The inputs necessary to initiate a tsunami in GeoClaw include a specific latitude and longitude domain used on a sphere (a pre-determined value), pre-loaded bathymetry of the coastal region with adjacent onshore topography (discussed in the *Bathymetry and topography* section below), and seafloor motion, such as from a generated earthquake (LeVeque et al., 2011), discussed in the *Seafloor deformation and earthquake generation* section below.

Bathymetry and topography

For the combined bathymetry and topography of south-central Chile in this research, I used the 30 arc-second resolution from the General Bathymetric Chart of the Oceans (GEBCO; Intergovernmental Oceanographic Commission et al., 2014). Other 30 arc-second data sets were available, such the Scripps Institution of Oceanography Shuttle Radar Topography Mission (SRTM+), and the Estimated Seafloor Topography (ETOPO1), however the GEBCO bathymetry is the most realistic for the Chilean continental shelf (Becerra, 2018).

Additionally, Pan et al. (2010), MacInnes et al. (2013), and Gusman et al. (2014) give examples of how high-resolution bathymetry and topography affect nearshore wave behavior, inundation and runup. For this research, I also simulated the nearshore wave behavior and inundation dynamics at three sites where there is either geological data (Quidico and Tirúa) or well-defined runup in the written record (Puerto Saavedra) of specifically the 1960 tsunami. I used 1/3 arc-second topography grids merged in Arc-GIS to bathymetry based on the existing GEBCO bathymetry from Becerra (2018) for these high resolution simulations. In the case for Tirúa, I modified the merged topography to remove a newly built bridge that acted as a physical seawall rather than a bridge in the river just south of the town. On its own, the GEBCO 30 arc-second bathymetry used elsewhere along the coast is considered too coarse for recreating wave inundation dynamics (c.f. Tang et al., 2009) so only sites with high-resolution topography could be used for my detailed inundation dynamics modeling.

Seafloor deformation and earthquake generation

Seafloor deformation is also a required input to initiate a tsunami in GeoClaw; in my study, this deformation is calculated from earthquake rupture scenarios. GeoClaw calculates seafloor motion from slip on discrete subfaults along a fault model of the Chilean subduction zone interface (from the USGS Slab 1.0 model (Hayes et al., 2012). GeoClaw applies the solutions of the Okada (1985) equations, which calculates the deformation of an elastic half-space due to dislocation of an internal rectangular fault element. The combined calculation of seafloor displacement is assumed to directly correspond to water displacement, and thus the initial tsunami (Borrero et al., 2015).

For my Chilean fault model, I created a grid of 76 along-strike by 5 down-dip subfaults, with each subfault corresponding to a 23 x 23 km area (Figure 2). Subfault row #1 is the southernmost subfault along strike and subfault row #76 is the northernmost subfault along strike. I chose to use 23x23 km subfaults to evenly subdivide the fault model between the boundaries of the Mocha Fracture Zone (MFZ) at ~ 38.3°S (between subfaults 39 and 40) and the Chile Triple Junction at subfault 1. The subfault grid extended ~900 km both north and south of the MFZ. The strike of each subfault changes abruptly at the MFZ from 12.5° in the north to 4.7° in the south. For each subfault, the rake was inferred to be 90° to represent a standard thrusting tectonic event (Hayes et al., 2014; Gusman et al., 2014). The dip angle and depth value of each subfault was based from the USGS Slab 1.0 Chilean subduction zone interface (top-center locations of each subfault; Appendix A).

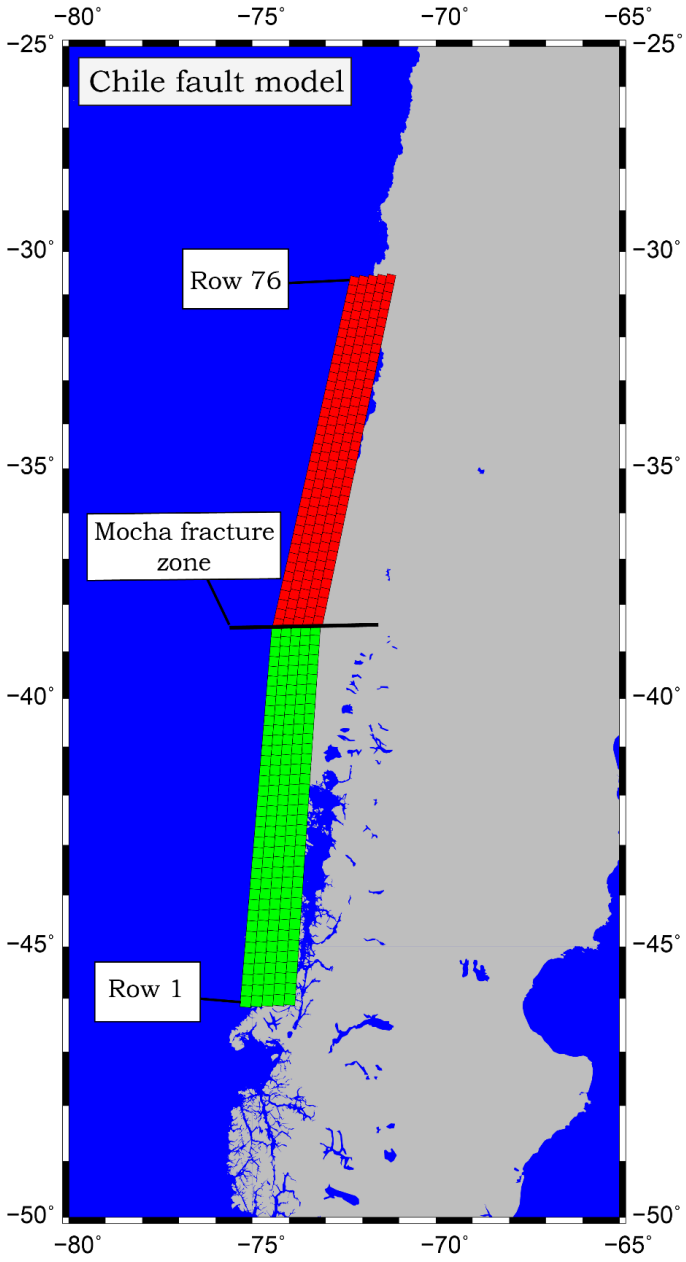

Figure 2: Chilean fault model consisting of 23 x 23 km subfaults (76 along-strike subfaults and 5 down-dip subfaults). The change from red subfaults to green subfaults indicates the hypothesized MFZ segment divide along with the change in strike from the northern to southern segment of the fault model (12.5° on the northern segment to 4.7° on the southern segment).

To generate a suite of hypothetical earthquake scenarios, I defined the width, length, and slip between source models, and changed the hypocenter location systematically from south to north. The width of all earthquake scenarios was kept constant at 115 km despite the full width of the seismogenic subduction zone being closer to ~145-150 km (Comte et al., 1994; Haberland et al., 2009; Moreno et al., 2010). I chose this width because Leonard et al. (2010) inferred from the geodetic and thermal data that Chilean subduction zone ruptures are ~25% less than the full width locked zone. Also, because a deeper part of the rupture zone does not significantly contribute to tsunami generation (Geist, 2002), a 25% width decrease, representing the upper ~115 km rupture width, will not confine tsunami generation.

I chose values for length and slip of my earthquake scenarios to represent a range of earthquake magnitudes from M_w 8.7, M_w 8.9, M_w 9.1, M_w 9.3, and M_w 9.5 (Table 2). The range of earthquake magnitudes was chosen to focus on the largest events that would generate the most pervasive tsunami records (Gusiakov, 2007). I constrained the along-strike length of rupture by limiting the stress drop to 10-100 bars, a typical stress drop for megathrust earthquakes (Kanamori, 1977). Realistic stochastic (or randomly determined) slip distributions were generated using the von Karman autocorrelation function (ACF) values from Mai and Beroza (2002) that model the stochastic characterizations of the distribution of slip as a spatial random field. I used 3 slip distributions for each M_w 8.7 and 8.9 earthquake location, and 10 variable slip distributions for each M_w 9.1, 9.3, and 9.5 earthquake location (Appendix B). These slip distributions were shifted around the

fault model systematically from south to north, which generated multiple earthquake scenarios at different segments along strike. It is important to note that the total distance in kilometers ruptured along strike for each earthquake size includes significant slip tapering from the areas of high slip.

By incrementally shifting the central subfault of each slip distribution latitudinally, I created 423 hypothetical earthquake source models. The naming scheme for these models contains three variables: 1) the along-strike subfault number of the central subfault, 2) the moment magnitude of the earthquake, and 3) the random slip distribution number (1-3 or 1-10). For example, earthquake model 09_87_1 represents a M_w 8.7 earthquake corresponding with slip distribution #1 with subfault row 9 at its center. Because M_w 9.5 earthquakes rupture the entire fault model area, all have a central subfault number of 38.

In addition to the random slip distributions, I created other earthquake models for comparison. These include centrally located uniform slip models for each earthquake magnitude (38_87_X, 38_89_X, 38_91_X, 38_93_X, and 38_95_X). I determined slip for these models by averaging the slip values for all rupturing subfaults within the fault model. I also created a source model from the solution for the 1960 earthquake event based off surface deformation from Barrientos and Ward (1990). Despite the Barrientos and Ward (1990) solution having a seismic moment equivalent to a M_w 9.3 earthquake, my "Barrientos slip" earthquake has a seismic moment equivalent to a M_w 9.0 event. This is because I determined slip for this source by contouring and scaling their values of

proposed slip to my fault model. This method caused a portion of slip from the Barrientos and Ward (1990) solution to be omitted in my earthquake source since the proposed slip was situated too deep in the subduction zone, and beyond my fault model, to contribute to tsunami generation (Geist, 2002).

Table 2: Characteristics of hypothetical earthquake simulations.

Magnitude	Subfaults ruptured along strike	Subfaults ruptured along dip	Total subfaults ruptured	Distance along strike ruptured (km)	Distance ruptured down dip (km)	Stress drop (bars)
8.7	18	5	90	414	115	15.33
8.9	36	5	180	828	115	15.29
9.1	72	5	360	1656	115	15.25
9.3	72	5	360	1656	115	30.43
9.5	76	5	380	1748	115	57.53

Simulated tide gauge locations

Using my literature review of all historical tsunami-producing earthquakes between 1570 and 1960, I created 47 tide gauges as locations to record waveforms in tsunami simulations (Table 3). Each tide gauge position corresponds to either observations in the historical record or geologic deposits of buried sands, although tide gauges are located offshore of those points, near the shoreline, at a water depth of 0 to -10 m. Because the resolution of the GEBCO bathymetry/topography was only 30 arc-seconds, I placed all tide gauges in the ocean for three reasons: (1) the oversimplification (i.e. averaging) of topography to 30 arc-second resolution meant that many observation sites were higher elevation in the simulations than reality and rivers or valleys narrower

than 30" were often missing from simulations, (2) a gauge on land could not record a simulated wave height lower than the gauge elevation, and (3) 30 arc-second resolution is considered too coarse for reliable modeling of coastal inundation processes (Pan et al., 2010). To insure the bathymetric/topographic grid resolution stayed consistent at each tide gauge over the duration of the simulation, I used 15 arc-second boxes of refinement around clusters of gauges (20 boxes total), subdivided from the 30 arc-second GEBCO bathymetry (Appendix C).

Table 3: Tide gauge location information for GeoClaw models. Shoreline longitude/latitude is the position used in simulations.

Gauge number	General location	Observation longitude	Observation latitude	Shoreline longitude	Shoreline latitude
1000	Valparaíso Region	-71.63205	-33.03631	-33.04365	-33.03631
1001	Valparaíso Region	-71.62942	-33.03948	-71.62859	-33.04365
1002	Valparaíso Region	-71.61034	-33.04254	-71.61034	-33.04254
1003	Valparaíso Region	-71.60727	-33.04879	-71.59477	-33.03254
1004	N of Constitución	-72.21120	-35.10968	-72.21120	-35.10968
1005	Maule River Mouth	-72.42500	-35.31588	-72.42500	-35.31588
1006	Constitución	-72.41130	-35.31632	-72.41963	-35.31215
1008	Dichato/ Coliumu Bay	-72.93624	-36.54621	-72.94457	-36.53788
1009	Tomé	-72.96333	-36.61774	-72.96708	-36.63024
1010	S of Tomé	-73.05999	-36.63735	-73.05687	-36.63735
1011	Talcahuano	-73.10445	-36.72474	-73.10445	-36.72057
1012	Concepción Bay	-73.05561	-36.73471	-73.05561	-36.73054
1013	San Vicente Bay	-73.16166	-36.73471	-73.15708	-36.72638

Gauge number	General location	Observation longitude	Observation latitude	Shoreline longitude	Shoreline latitude
1014	Penco	-72.99081	-36.73617	-72.99914	-36.72784
1015	Lenga	-73.17249	-36.76566	-73.16522	-36.77093
1022	Coronel	-73.14661	-37.03602	-73.15494	-37.03602
1023	Arauco Bay	-73.42752	-37.23425	-73.42335	-37.23425
1024	Arauco Province	-73.54026	-37.89854	-73.54026	-37.89854
1025	Arauco Province	-73.47869	-37.99779	-73.48369	-37.99779
1026	Arauco Province	-73.48082	-38.01159	-73.48082	-38.01159
1027	Arauco Province	-73.46170	-38.08409	-73.46170	-38.08409
1028	Quidico	-73.47727	-38.22961	-73.47727	-38.23294
1029	Quidico	-73.49290	-38.25070	-73.49290	-38.24237
1052	Quidico	-73.49333	-38.25364	-73.49333	-38.24531
1053	Tirúa	-73.53700	-38.32806	-73.53908	-38.32806
1054	Tirúa	-73.48758	-38.34447	-73.54591	-38.34447
1055	Isla Mocha	-73.86740	-38.37465	-73.87052	-38.37882
1056	Puerto Saavedra	-73.47045	-38.71792	-73.46712	-38.71792
1058	Puerto Saavedra	-73.42675	-38.78532	-73.42258	-38.78532
1059	North of Tolten	-73.28660	-39.12751	-73.28660	-39.12751
1060	Tolten	-73.24019	-39.28183	-73.23603	-39.28183
1061	Queule	-73.23197	-39.35852	-73.22780	-39.35852
1062	Mehuín	-73.24635	-39.42700	-73.24635	-39.42700
1066	Valdivia Region	-73.42598	-39.88387	-73.41765	-39.88387
1067	Valdivia Region	-73.39495	-39.89045	-73.39912	-39.89045
1068	Valdivia Region	-73.59558	-39.94386	-73.59558	-39.94386
1069	Bahía Mansa	-73.71390	-40.53544	-73.74307	-40.53544
1070	Puerto Montt	-72.96388	-41.48602	-72.95222	-41.48602
1072	Maullín	-73.67817	-41.57341	-73.67817	-41.53591
1100	Cocotue Region	-74.00065	-41.84618	-74.01731	-41.88785
1101	N Chiloe Island	-74.04832	-42.06002	-74.04832	-42.06002
1102	Lake Huelde	-74.12694	-42.63499	-74.12694	-42.63499
1103	S Chiloe Island	-74.19680	-42.86273	-74.19680	-42.86273
1104	West of Puerto Cisnes	-72.68421	-44.73059	-72.70921	-44.72976
1105	Puerto Aysen	-72.82976	-45.40258	-72.84226	-45.40258
1106	Campiche	-71.49623	-32.75048	-71.46517	-32.75595

Gauge number	General location	Observation longitude	Observation latitude	Shoreline longitude	Shoreline latitude
1107	Los Vilos	-71.51217	-31.91211	-71.51158	-31.90929

AIC statistical analysis

To determine how well each simulation matched observed historical tsunamis, I compared the maximum wave heights simulated at each tide gauge with my tsunami observation database using the Akaike Information Criterion (AIC) statistical equations (Burnham and Anderson, 2002). This analytical method uses the known historical observation and paleotsunami deposit database to select tsunami simulations that correlate better with what is known in the historical record. AIC allows for the comparison between simulations by analyzing the residual sum of squares (RSS) between the modeled and observed wave heights for each simulation at every tide gauge (Burnham and Anderson, 2002). Earthquake source models that have different rupture characteristics (e.g. position along strike and distribution of slip) will generate different waveform data with varying RSS. The AIC equations enable me to identify a suite of statistically significant simulations based on how closely modeled wave heights match the inputted known wave heights at all locations (Burnham and Anderson, 2002). AIC provides an effective, yet simple method for selecting an estimated best approximating model and set of "good models" through this concept of variable selection and marrying information theory with mathematical statistics, as opposed to hypothesis testing (Burnham and Anderson, 2002).

The equations used in the analysis are after Burnham and Anderson (2002):

$\sigma^2 \frac{\Sigma \epsilon i^2}{n}$(RSS, Residual sum of Squares)

$$AIC = n * log_{10}(\sigma^2) + 2k$$

where n is the number of observations and k is the number of subfaults plus one (total number of estimated regression parameters). The AIC equation accounts for the differences in rupture lengths (k) in the different earthquake source models (e.g. M_w 8.7 source models rupture 90 subfaults while M_w 9.5 rupture 380 subfaults). However, to account for the small sample sizes of observations, a second order correction to the AIC formula, AIC_c, is needed:

$$AIC_c = AIC + \frac{2k(k+1)}{n-k-1}$$

The AIC equations require definitive wave height values from the historical and geologic record to be used for comparison of simulated wave heights. This requirement poses a problem when conclusive wave height data are absent within the written record. Thus, to solve the AIC equations, I interpolated probable wave heights for coastal sites with undefined wave heights (defined in Appendix D) by averaging the range of potential wave heights to that could produce observation records. These wave heights were defined on a site-specific and event-specific basis. I used a combination of strategies to estimate the minimum and maximum wave height needed for a tsunami to be observed at a site before the observation description would have likely changed how the tsunami was described: 1) elevation profiles from Google Earth, 2) previous literature on paleotsunami studies, which told me locations that should have been inundated (Ely et al., 2014;

Garrett et al., 2015; Cisternas et al., 2017; Dura et al., 2017; Hong et al., 2017; Kempf et al., 2017; Carvajal Pers. Comm., 2019; Matos-Llavona et al., 2019), 3) written reports of damages (and locations) associated with each respective event, and 4) comparisons to other recorded wave heights that occurred at the relatively same location in other historical tsunamis. The resulting range of inferred average wave heights are uncertain, but I accounted for this by calculating the standard deviation between the possible maximum and minimum wave heights and weighting the averages by each respective standard deviation. For example, coastal sites with large differences between a possible maximum and minimum wave height have less weight in the RSS calculation than sites that have smaller ranges. To make sure that coastal sites with documented wave heights were weighted the strongest in the statistical analysis, I considered these heights to have the minimum amount of uncertainty (standard deviation of 0.5 m) of all observations.

Determining a "good fit"

AIC_c values are typically positive, although can range from large negative numbers (due to computing AIC from regression statistics) to numbers as high as 340,000 (Burnham and Anderson, 2002). In this statistical analysis, the AIC_c values can be shifted negative depending on the number of observations present for each earthquake scenario. However, to assess whether a model is fits well or not, it is not the absolute size of the AIC value, but rather the difference between the relative AIC_c values from the $AIC_{c\,min}$, known as Δ_i ($\Delta_i = AIC_{c\,i} - AIC_{c\,min}$), that is important (Burnham and Anderson, 2002).

Therefore, AIC_c values are only comparable relative to other AIC_c values in the same model set. An individual AIC_c value is not interpretable or useful; Burnham and Anderson (2002) suggest that following levels of empirical support based on the Δ_i for $AIC_{c\,i}$:

- 0-2 = Substantial
- 4-7 = Considerably less
- > 10 = Essentially none

Because models with Δ_i >10 fail to describe substantial explainable variation within the wave height data, I can omit source models that have Δ_i values greater than 10 as not being a reasonable solution for the rupture characteristics of a historically observed event.

The accuracy of the AIC statistical analysis is evaluated through calculating the root mean square error (RMSE) value of the statistically significant earthquake solutions. The RMSE value uses the same weighted values from the RSS and AIC equations and declares an absolute measure of fit with lower values indicating better fit (e.g. a RMSE value of 1 m indicates that the mean modeled wave height is either 1 m higher or lower than the observed wave height in the historical record). This RMSE equation acts as a validity check within the AIC model selection process:

$$RMSE = \sqrt{\frac{\sum_{i=1}^{n}(Xobs,i - Xmo,i)^2}{n}}$$

where *Xobs* is the observed wave height, *Xmo* is the modeled wave height, and *n* is the number of tide gauges. Theoretically, the spread of AIC_c values should yield both low and high RMSE values. Therefore, the RMSE values validate the overall pool of

earthquake source models and define both "good-fitting" and "poor-fitting" solutions in the AIC analysis.

For a tsunami simulation to be listed as properly matching 1960 tsunami inundation at Tirúa, Quidico, and Puerto Saavedra, I required simulated inundation to match previously documented inundated areas (Figure 3). The inundated areas at Quidico were based on Hong et al. (2017), and those at Tirúa were based on Ely et al. (2014). Since no geologic evidence has been measured to date at Puerto Saavedra, wave height accounts recorded in the historical record were used to match tsunami simulations: maximum tsunami height inundating the village was measured to be 7-8 m (Sievers et al., 1963) and 11.5 m was recorded at the southern corner of the bay (Weischet, 1963).

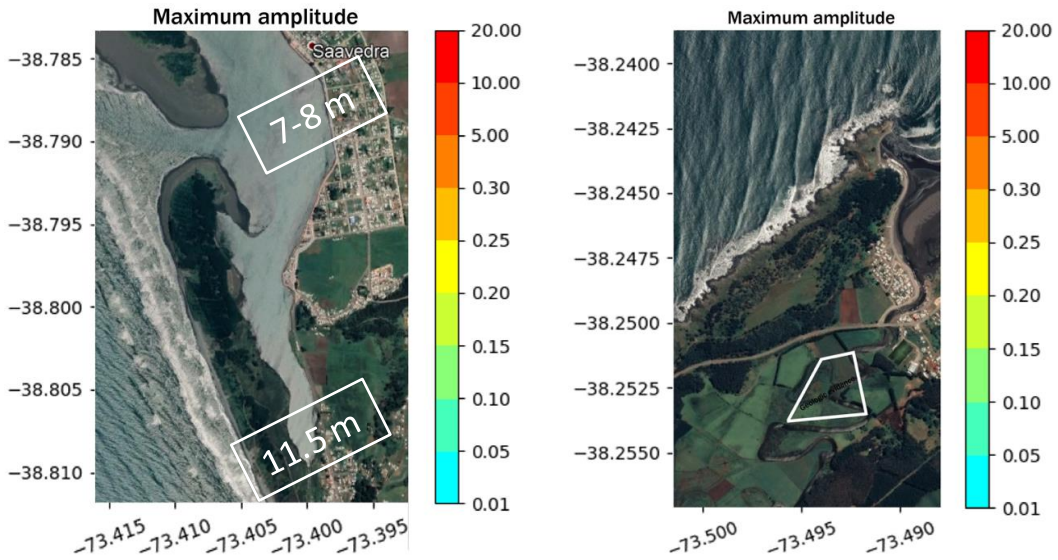

Figure 3: The three locations where 1/3 arc-second bathymetry was used to simulate inundation dynamics: left) Puerto Saavedra, right) Quidico, and bottom) Tirúa. White boxes indicate areas where geologic evidence was found for the 1960 tsunami. No geologic evidence has been studied at Puerto Saavedra.

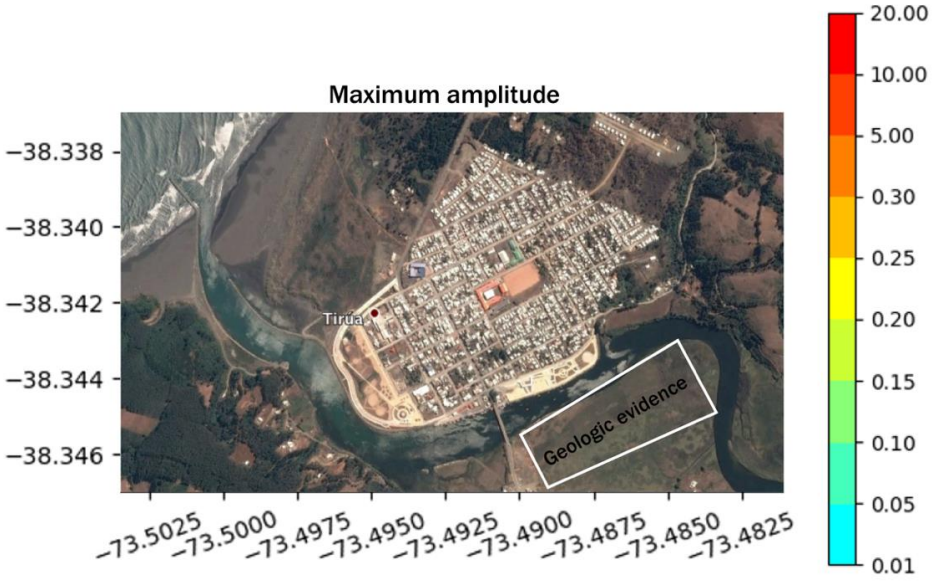

Figure 3: Continued.

Using seafloor deformation to refine "best-fit" model selection

The AIC equations can be used as a great method for eliminating source models, however additional methods are needed to improve the suite of models to determine more geologically probable fits. One of these methods available is the seafloor deformation data. Because we assume that the water column moves as an incompressible fluid based on Newtonian physics (Berger et al., 2011), seafloor deformation correlates directly to displaced water. Therefore, the absolute values of seafloor deformation for each cell in the subfault model equals the volume of water displaced. I calculated the area of water displacement in degrees from the seafloor deformation of all earthquakes with AIC_c values <10 for the 1960 earthquake, then converted degrees to meters using Haversine

equations. I then determined the total volume displaced by multiplying this value (m^2) by the water displacement each cell in the source model. Knowing the volume of displaced water in each source model allows for greater insight towards how each slip distribution influences different waveform and inundation patterns.

CHAPTER IV

HISTORICAL RESULTS

1570 tsunami simulations

The 1570 event AIC_c analysis used three tide gauges (Appendix D); one correlating to an observation in the written record (Penco), and two possible accounts within the geologic record that cannot be ruled out, but either correspond to the tsunami from this event or the 1575 event (Tirúa and Lenga; Table 1). Based on the AIC_c statistical analysis of the three gauges, the Δ_i of all ranged from 0 to 29.23 values and 39 models yielded a Δ_i value less than 7 (Appendix E_1). Of these 39 earthquake models, four yielded a Δ_i value less than 2.0, indicating "substantial fits" (Figure 4). Better fitting earthquake source models for the 1570 event appear to rupture a greater area on the northern segment of the Chilean subduction zone (e.g. 46_87_3). The top four earthquake source models, 38_91_3, 39_91_3, 43_89_3, and 46_87_3, all had an average root mean square error (RMSE) value less than 0.31 m. The M_w 9.3 and M_w 9.1 earthquake source models showed similar concentrations of high slip located at ~ 36°S and ~ 40°S, while the smaller M_w 8.7 source model showed a single high slip concentration at ~ 37.5°S (Figure 5).

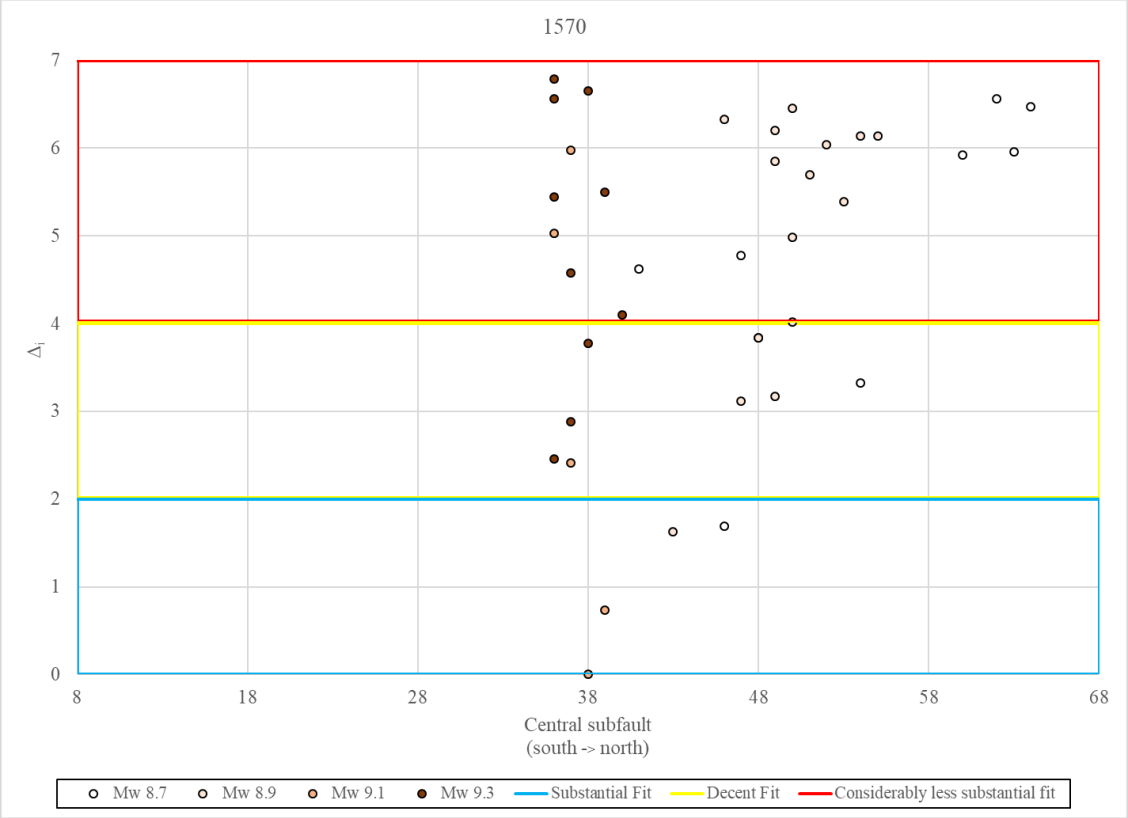

Figure 4: The 39 earthquake source models that yielded a $\Delta_i < 7.0$ when compared against the 1570 historical data. Tsunami simulations from the earthquake source models 38_91_3, 39_91_3, 43_89_3, and 46_87_3 represent a statistically substantial fit based on the historical tsunami data available for the 1570 event.

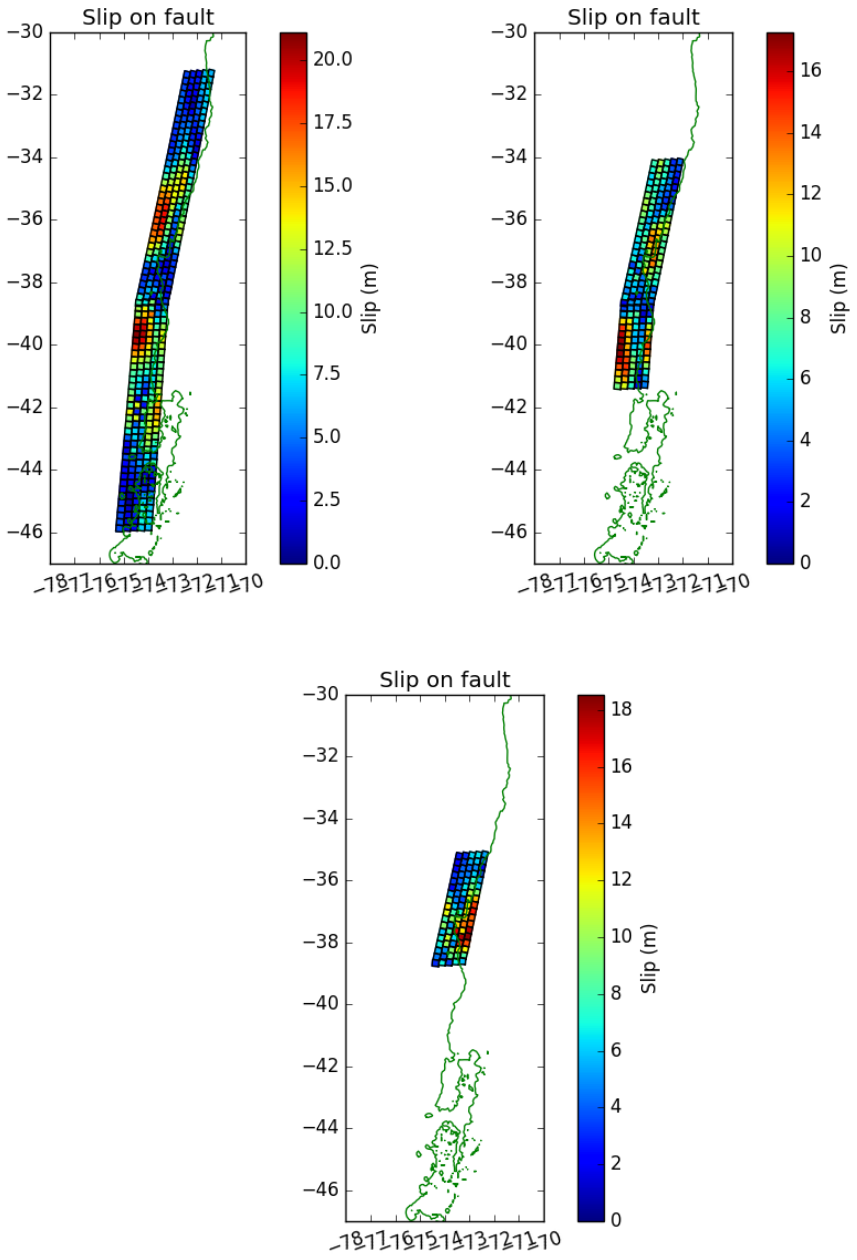

Figure 5: Potential rupture scenarios of three statistically significant source models, which yielded Δ_i values that suggest a substantial fit based on the AIC equations for the 1570 event: left) model 38_91_3, right) 43_89_3, and bottom) model 46_87_3.

1575 tsunami simulations

The 1575 AIC_c analysis used 12 tide gauges (Appendix D). Five tide gauges correlated to observations in the written record (Penco, two around Puerto Saavedra, Valdivia, Chucalen), while the other seven gauges correlated to accounts within the geologic record (Lenga, two around Tirúa, Maullín, Cocotue, Castro, and Lake Huelde; Table 1). Similar to 1570, the gauges at Lenga and Tirúa are included in this analysis as they cannot be ruled out for this event. Based on the AIC_c statistical analysis with these gauges, the Δ_i of all earthquake source models ranged from 0 to 72.36 and two yielded a Δ_i value less than 7 (Appendix E_2). These models were 39_93_8 and 40_93_8 and both yielded a "substantially" significant Δ_i value (less than 2.0; Figure 6). These top two models also had a RMSE value less than 0.12 m, however, all models had a RMSE within 1.83 m. The region of high slip concentration for the top two models were similar as they were only offset by 23 km. Both models had a maximum, deep slip at ~ 39°S (Figure 7).

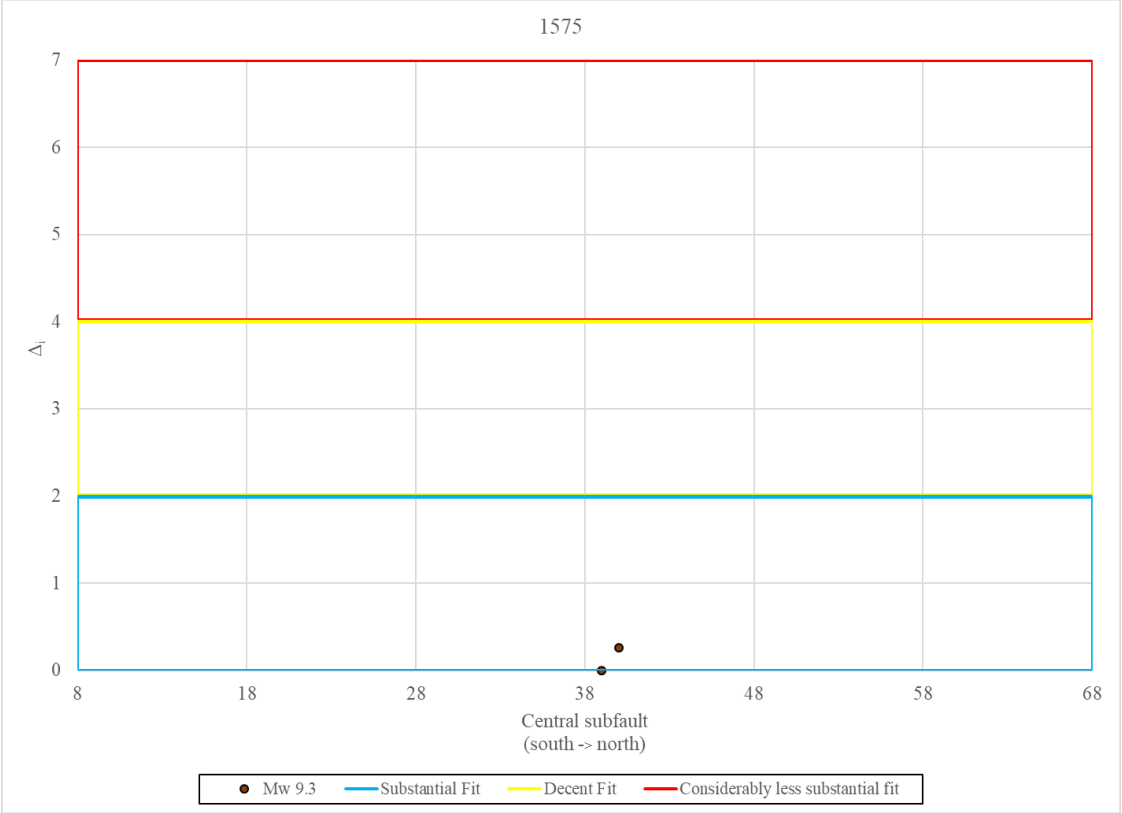

Figure 6: The two earthquake source models that yielded a $\Delta_i < 7.0$ when compared against the 1575 historical data. Tsunami simulations from the earthquake source model 39_93_8 and 40_93_8 represent statistically substantial fits based on the historical tsunami data available for the 1575 event.

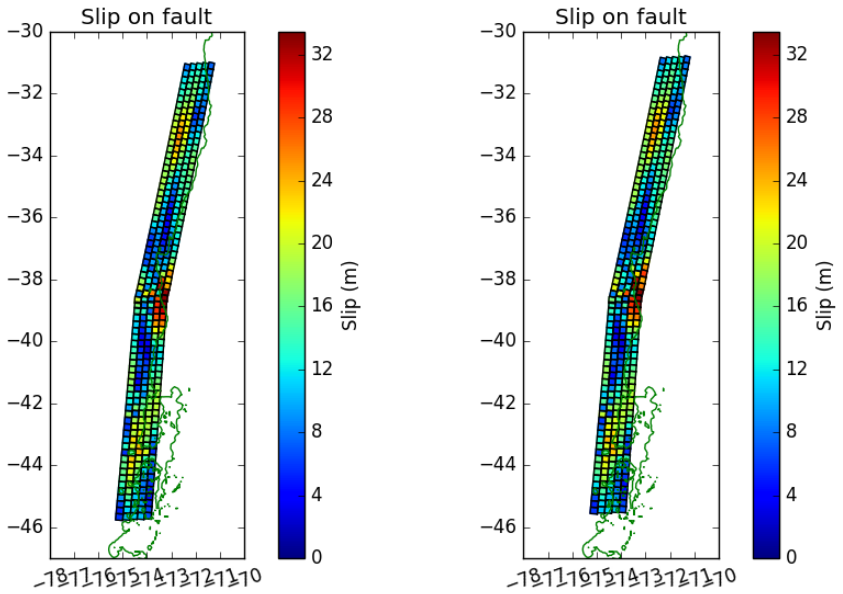

Figure 7: Potential rupture scenarios that were statistically significant, which yielded Δ_i values that suggest a substantial fit based on the AIC equations for the 1575 event: left) model 39_93_8, right) model 40_93_8.

1657 tsunami simulations

There was only one observation for the 1657 event (a written record in Penco), therefore only one tide gauge could be used for the AIC_c statistical analysis (Appendix D; Table 1). The Δ_i of all 423 earthquake source models at this one gauge ranged from 0 to 5.61. Thus, all 423 earthquake source models yielded a Δ_i value less than 7 (Figure 8; Appendix E_3), 11 of which gave a Δ_i value less than 2.0, indicating "substantial fits". These models were 36_93_3, 40_93_10, 40_93_9, 38_95_1, 37_93_3, 39_93_10, 39_93_9, 51_87_1, 38_95_4, 36_93_10, and 38_93_9. The earthquake source models with a Δ_i value less than 2.0 had RMSE values that ranged from 1.84 m to 4.95 m. The

region of high slip for these models vary greatly (Figure 9). See the *Discussion* chapter for the interpretation of all results having such close Δ_i values and only using one tide gauge.

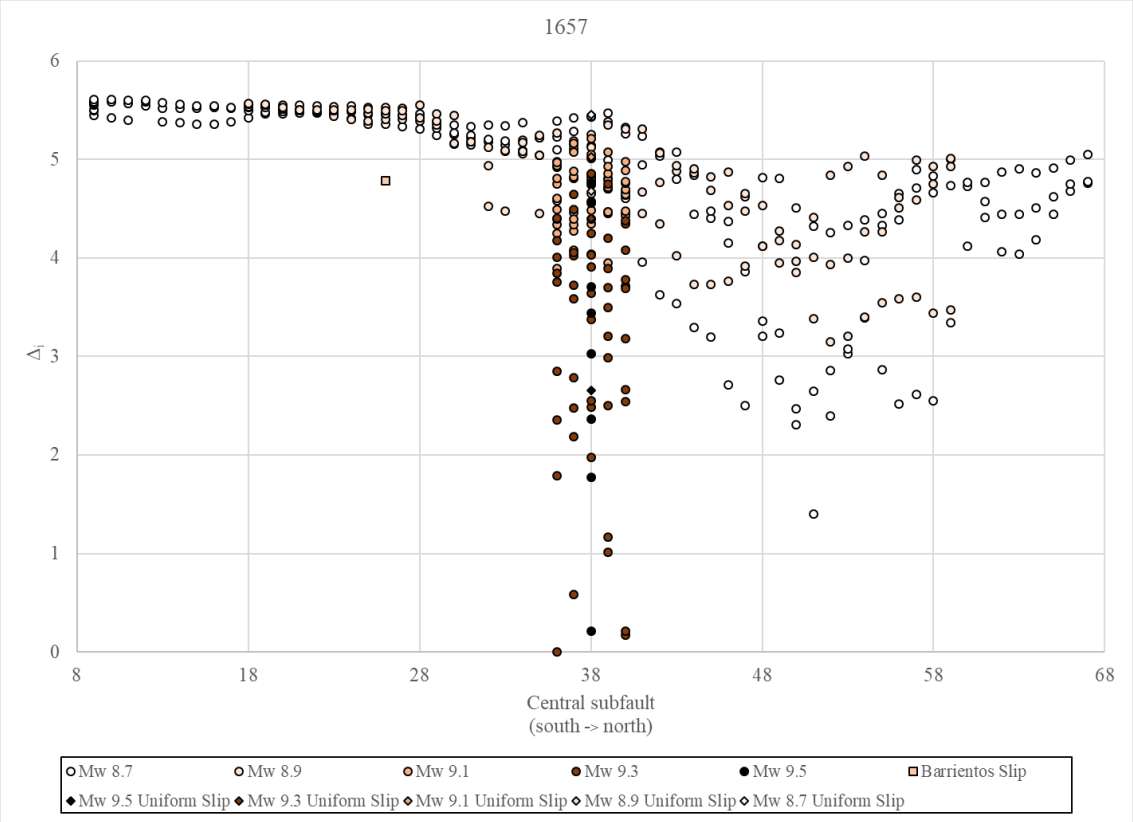

Figure 8: The Δ_i versus central subfault of rupture for all tsunami simulations relative to the lowest AIC value calculated from observations of the 1657 historical tsunami. Earthquake magnitude positively correlates to darker colored data points.

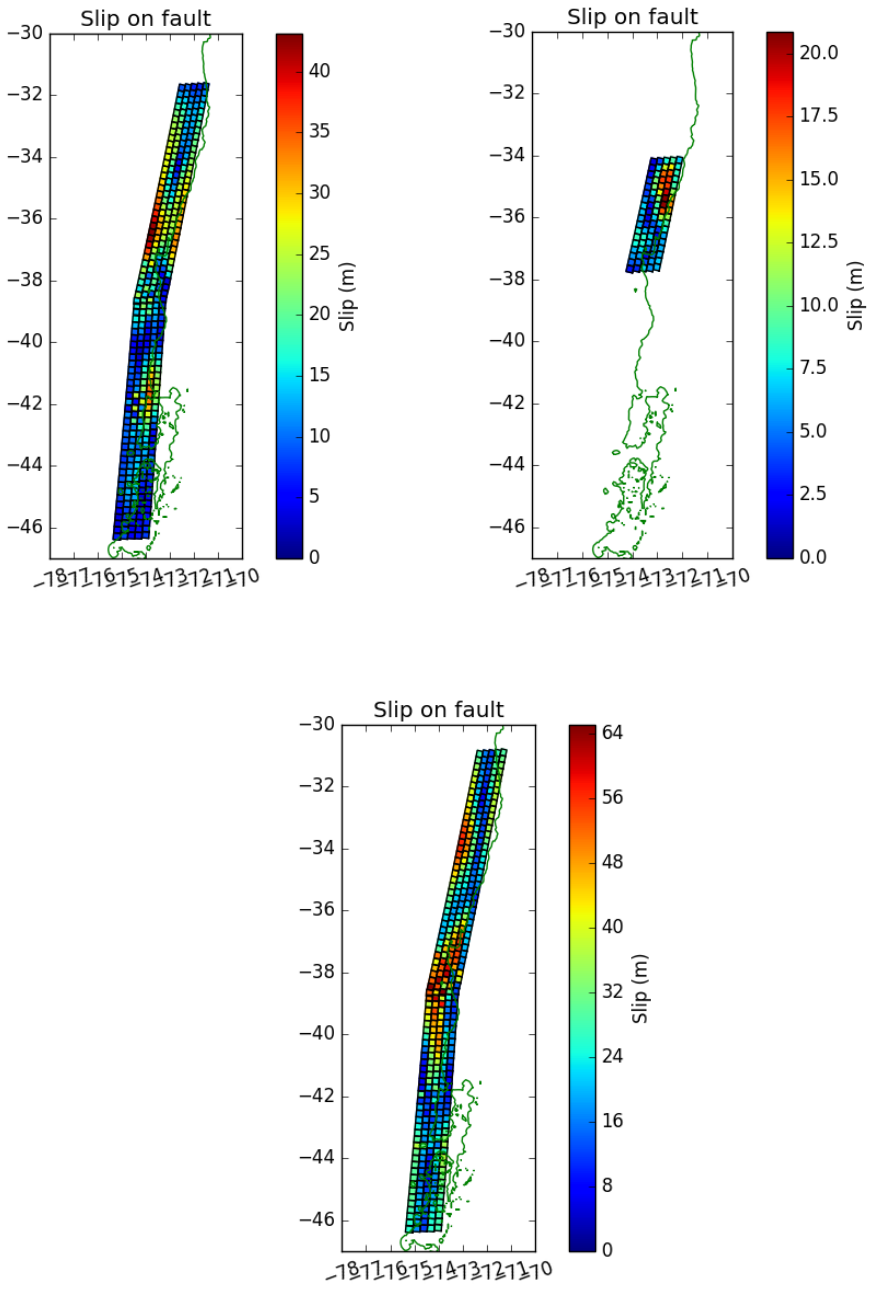

Figure 9: Potential rupture scenarios that were statistically significant, which yielded Δ_i values that suggest a substantial fit based on the AIC equations for the 1657 event: left) model 36_93_3 and right) model 51_87_1, and bottom) model 38_95_1.

1730 tsunami simulations

The 1730 AIC_c analysis used seven tide gauges (Appendix D). Six tide gauges correlated to observations in the written record (Penco, Talcahuano, three around Valparaíso, and Valdivia), while the other one gauge correlated to an account within the geologic record at Campiche (Table 1). Based on the AIC_c statistical analysis with these gauges, the Δ_i of all 423 earthquake source models ranged from 0 to 58.60 and five yielded a Δ_i value less than 7 (Appendix E_4). These five earthquake source models had a RMSE value between 0.72 m and 1.18 m, with four being a M_w 9.3 in size. Model 39_93_10 was the only "substantial fit" as no other solutions had a Δ_i value less than 2.0 (Figure 10). The region of high slip concentration for this lone "substantially" significant model was located on the northern segment of the fault model at ~ 34°S (Figure 11). Additionally, although not statistically significant, the M_w 8.9 and M_w 8.7 earthquake source models that ruptured the northern segment of the Chilean subduction zone had lower Δ_i values than the earthquake source models that ruptured the southern segment (Appendix E_4).

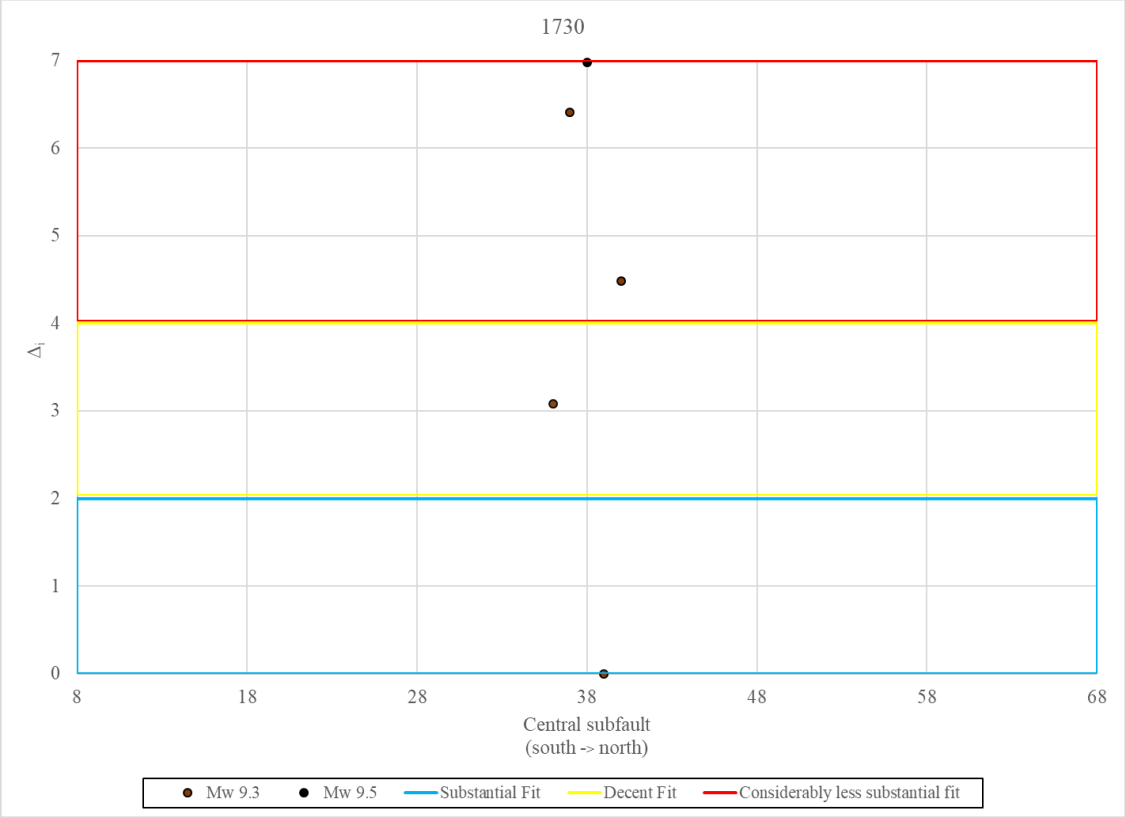

Figure 10: The five earthquake source models that yielded a $\Delta_i < 7.0$ when compared against the 1730 historical data. The tsunami simulations from earthquake source model 39_93_10 represents a statistically substantial fit based on the historical tsunami data available for the 1730 event.

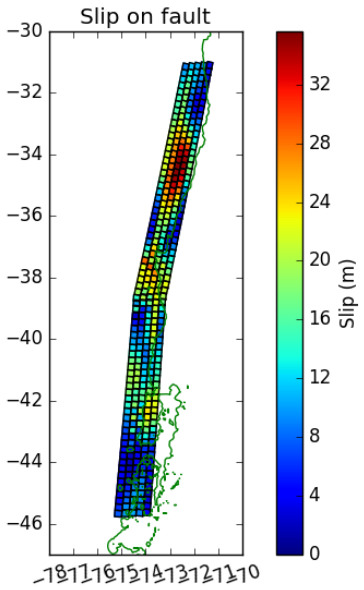

Figure 11: Potential rupture scenario that was a statistically significant, which yielded a Δ_i value that suggests a substantial fit based on the AIC equations for the 1730 event: model 39_93_10.

1751 tsunami simulations

The 1751 event used seven tide gauges in the AIC_c analysis (Appendix D). Two tide gauges correlated to observations in the written record (Los Morros/Coliumu Bay), while five gauges correlated to accounts within the geologic record (three around Quidico and two around Tirúa; Table 1). Based on the AIC_c statistical analysis with these gauges, the Δ_i of all 423 earthquake source models ranged from 0 to 33.75, with 96 solutions yielding a Δ_i value less than 7 (Appendix E_5). Ten of these 96 earthquake models were "substantial fits" with Δ_i values less than 2.0 (Figure 12). These models, 57_87_3, 56_87_3, 58_87_3, 52_87_3, 52_89_2, 51_87_3, 49_87_3, 53_89_2, 40_93_5, and

51_87_1, had RMSE values ranging from 2.24 m to 2.57 m. The region of high slip concentration for the M_w 8.7 and M_w 8.9 earthquake source models was generally located at ~ 35°S and ~ 37 °S, respectively, while the statistically significant-fitting M_w 9.3 model, 40_93_5, suggests that the region of high slip was at ~ 40 °S to ~ 43°S (Figure 13).

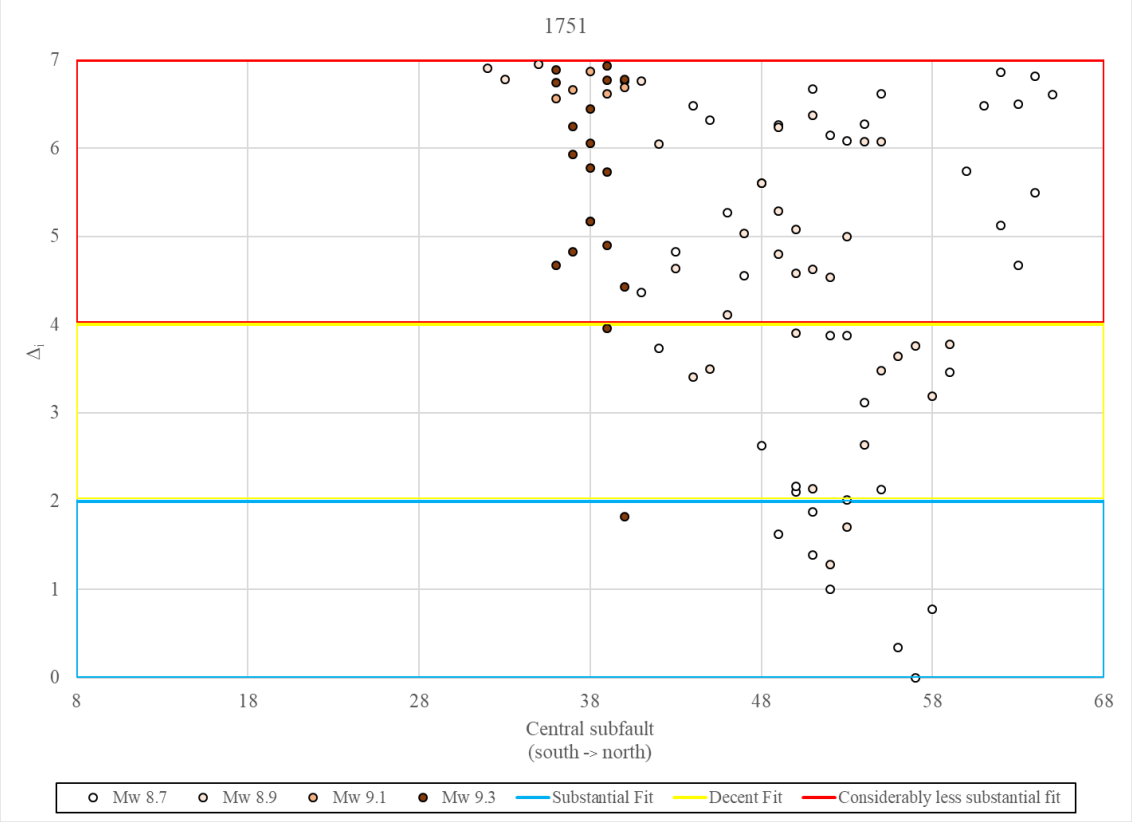

Figure 12: The 96 earthquake source models that yielded a $\Delta_i < 7.0$ when compared against the 1751 historical data. The tsunami simulations from earthquake source models 57_87_3, 56_87_3, 58_87_3, 52_87_3, 52_89_2, 51_87_3, 49_87_3, 53_89_2, 40_93_5, and 51_87_1 represent statistically substantial fits based on the historical tsunami data available for the 1751 event.

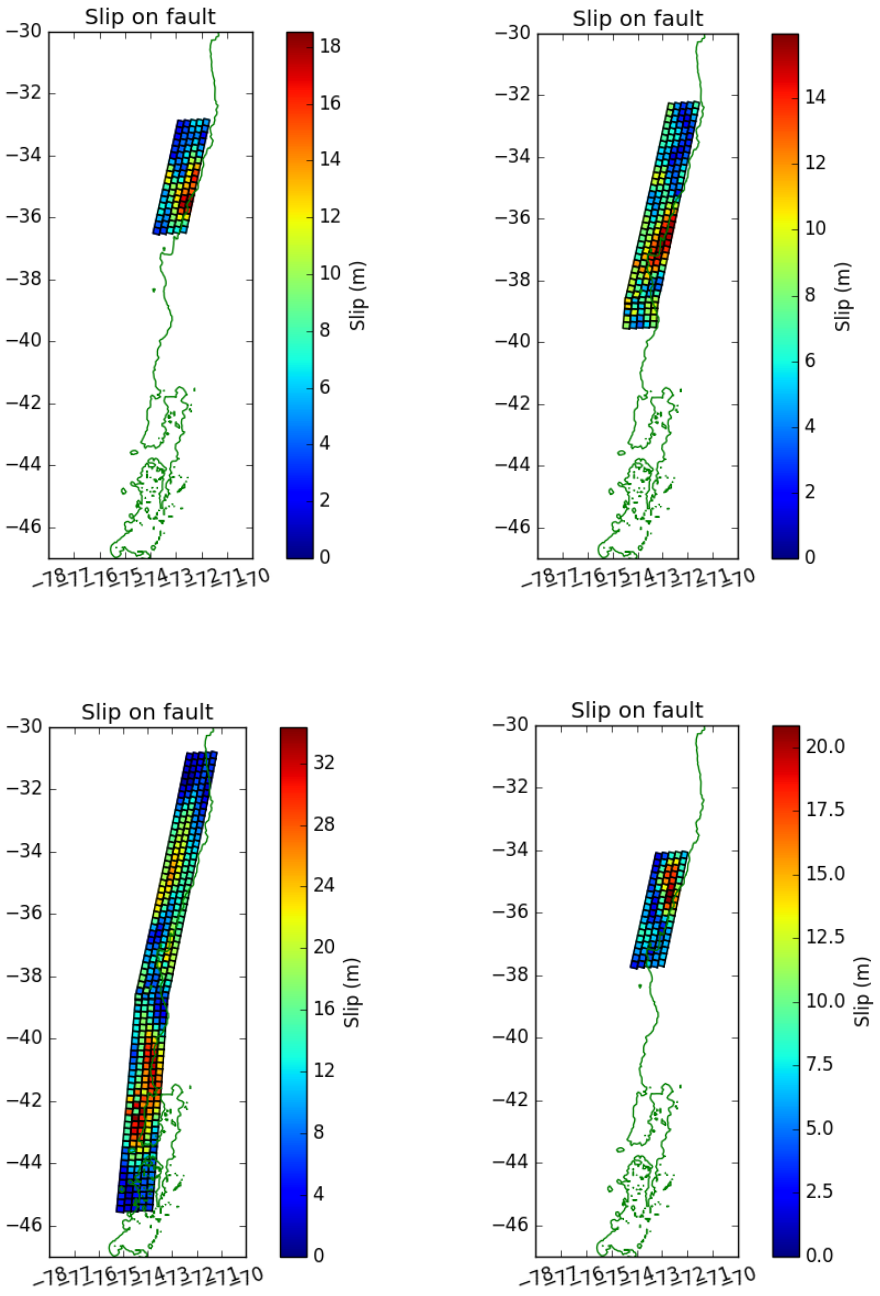

Figure 13: Potential rupture scenarios that were statistically significant, which yielded Δ_i values that suggest a substantial fit based on the AIC equations for the 1751 event: top left) model 57_87_3, top right) 52_89_2, bottom left) model 40_93_5, bottom right 51_87_1.

1822 tsunami simulations

Three tide gauges used for the 1822 event analysis correlated to observations in the written record (Campiche, Valparaíso, and the Valdivia region; Appendix D; Table 1). The Δ_i of all 423 earthquake source models within this statistical analysis ranged from 0 to 31.01 and 35 yielded a Δ_i value less than 7 (Appendix E_6). Four of these 35 earthquake models had a Δ_i value less than 2.0, indicating "substantial fits" (Figure 14). These models, 59_87_2, 51_89_2, 52_89_2, and 56_89_2, had RMSE values that ranged between 0.72 m and 1.00 m. The region of high slip concentration for these model was either shallow at ~ 34°S to ~ 35°S (M_w 8.7 source models) or deep at ~ 37°S (M_w 8.9 source models; Figure 15).

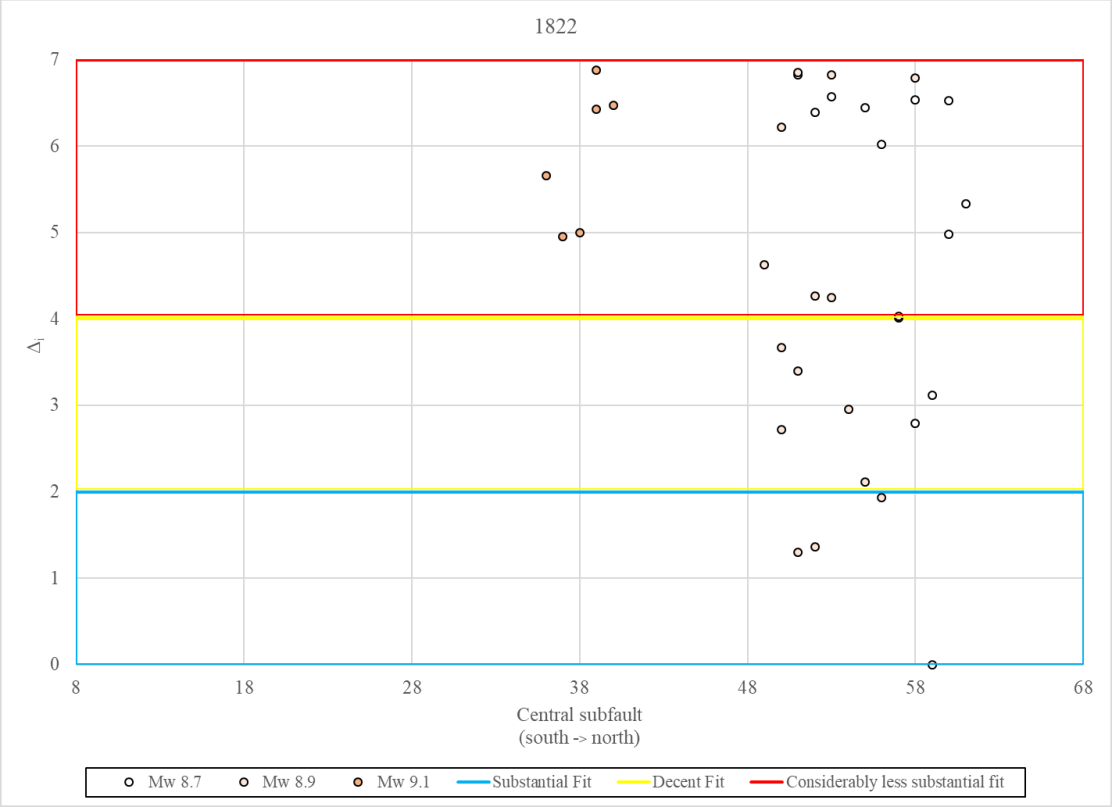

Figure 14: The 35 earthquake source models that yielded a $\Delta_i < 7.0$ when compared against the 1822 historical data. The tsunami simulations from earthquake source models 59_87_2, 51_89_2, 52_89_2, and 56_89_2 represent statistically substantial fits based on the historical tsunami data available for the 1822 event.

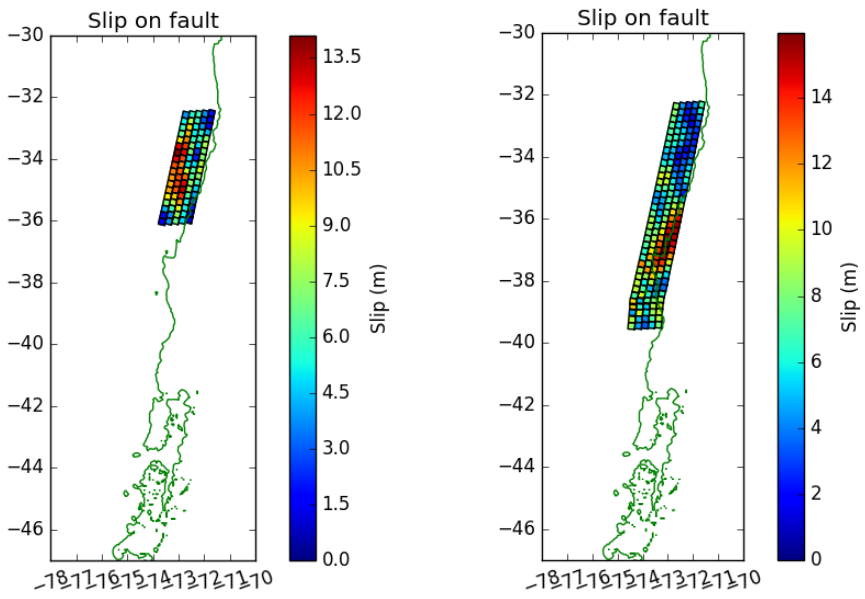

Figure 15: Potential rupture scenarios that were statistically significant, which yielded Δ_i values that suggest a substantial fit based on the AIC equations for the 1822 event: left) model 59_87_2 and right) model 52_89_2.

1835 tsunami simulations

Of the 17 tide gauges used for the 1835 event analysis (Appendix D), 14 gauges were from observations in the written record (Valparaíso, two north of Constitución, Tomé, south of Tomé, Talcahuano, Concepción Bay, San Vicente Bay, Penco, Coronel, Arauco Bay, Isla Mocha, Valdivia region, and northern Chiloe Island), and three from the geologic record (three around Quidico; Table 1). Based on the AIC_c statistical analysis with these gauges, the Δ_i of all 423 earthquake source models ranged from 0 to 66.54 and eight yielded a Δ_i value less than 7 (Appendix E_7). Two of these eight earthquake models were "substantial fits" with Δ_i values less than 2.0 (Figure 17). These models, 46_87_1

and 45_87_1, had RMSE values of 3.59 m and 3.77 m. The area of high slip concentration for these M_w 8.7 source models were located on the northern segment of the fault model at ~ 36.5°S (Figure 16). However, the M_w 9.3 and M_w 9.5 source models with Δ_i values less than 7 (40_93_9, 39_93_9, and 38_95_8) yielded slightly lower RMSE values (3.52 to 3.57 m) than the M_w 8.7 source models. The main concentrations of slip for the larger source models are different from the smaller M_w 8.7 source models: the high slip for the two M_w 9.3 source models occurred at ~ 39°S, and the M_w 9.5 source model had high slip between ~ 40°S to ~ 44°S in the deeper portion of the fault model (Figure 17).

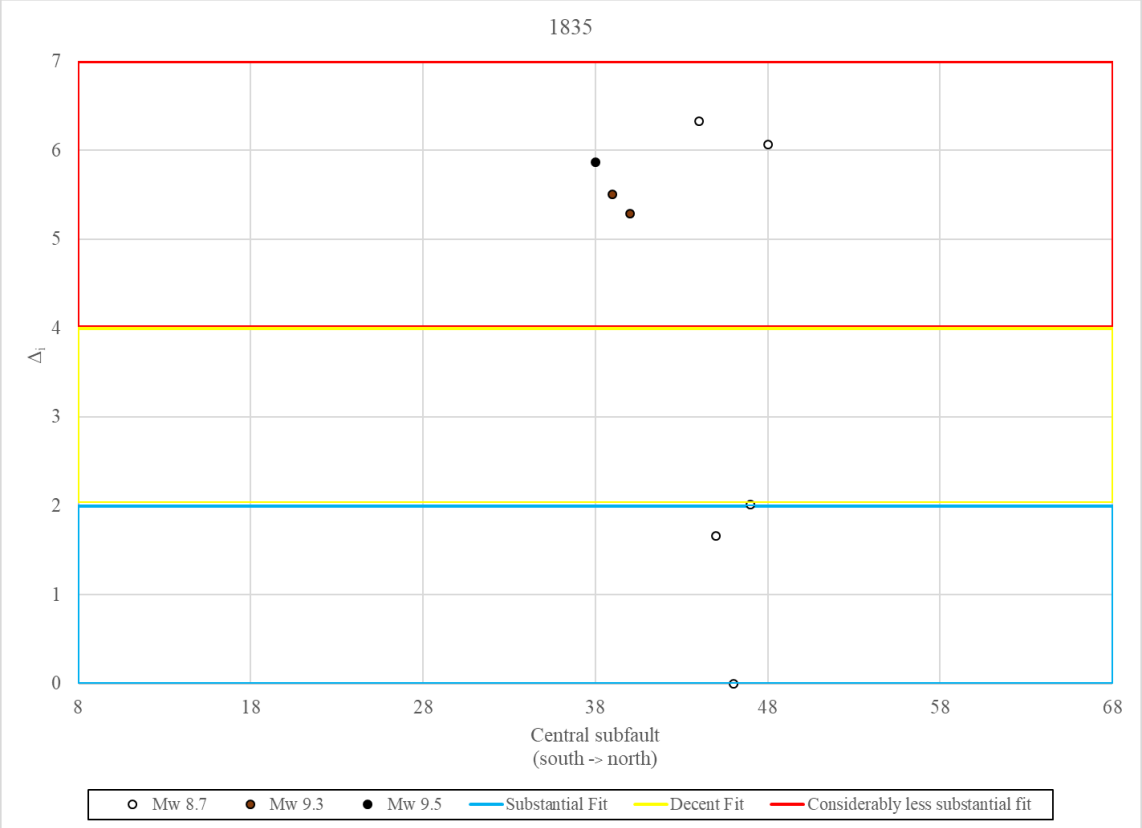

Figure 16: The eight earthquake source models that yielded a $\Delta_i < 7.0$ when compared against the 1835 historical data. The tsunami simulations from earthquake source models 46_87_1 and 45_87_1 represent statistically substantial fits based on the historical tsunami data available for the 1835 event.

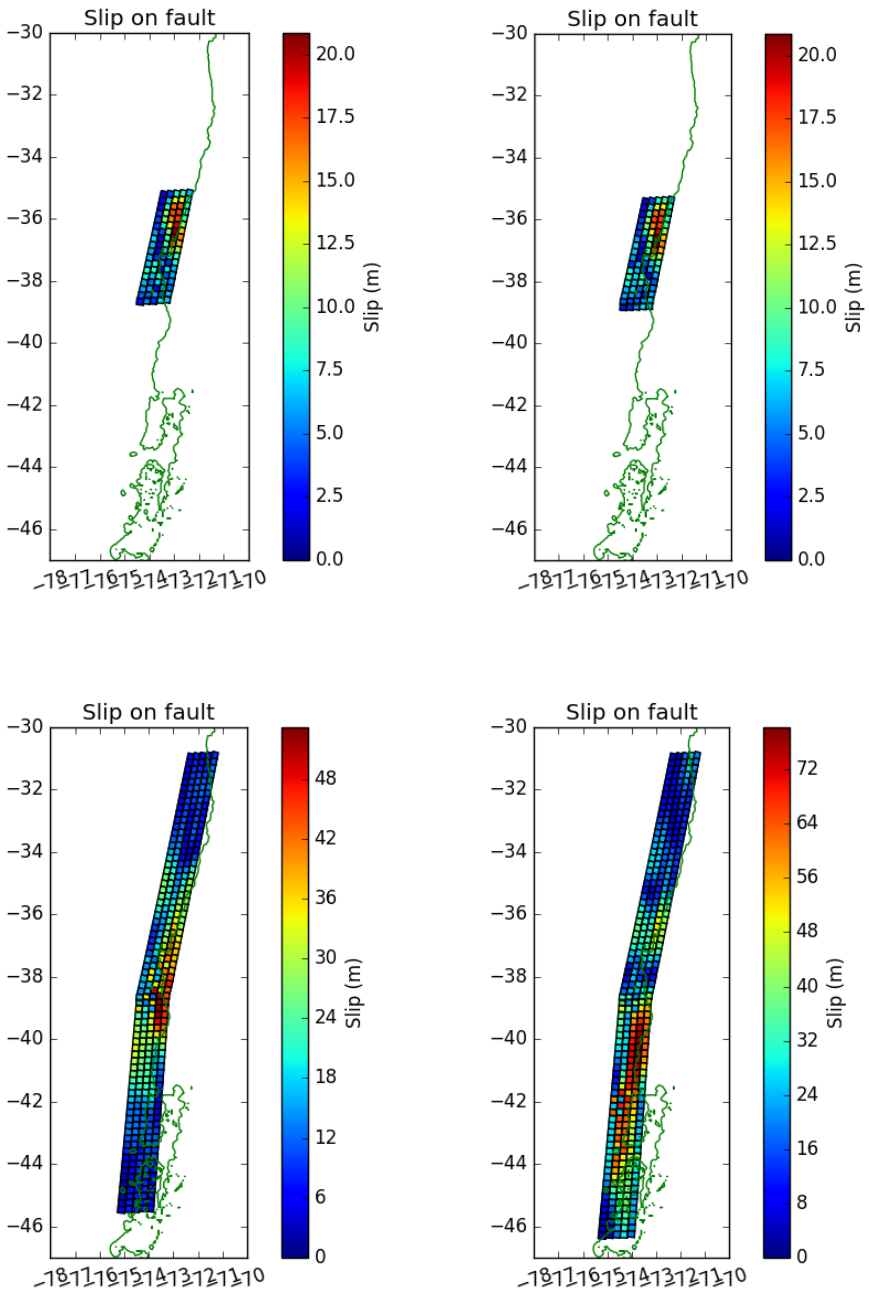

Figure 17: Potential rupture scenario that was statistically significant, which yielded Δ_i values that suggest a substantial fit based on the AIC equations for the 1835 event: top left) model 46_87_1, top right right) model 45_87_1, bottom left) 40_93_9, and bottom right) 38_95_8.

1837 tsunami simulations

Of the eight tide gauges used for the 1837 event analysis (Appendix D), six tide gauges correlated to observations in the written record (Valparaíso, Concepción Bay, the Valdivia region, Maullín, and north Chiloe Island), while the two gauges correlated to accounts within the geologic record (Cocotue and Lake Huelde; Table 1). Based on the AIC_c statistical analysis with these gauges, the Δ_i of all 423 earthquake source models ranged from 0 to 64.88 (Appendix E_8) and 55 yielded a Δ_i value less than 7 (Figure 18). All 56 earthquake source models with a Δ_i less than 7 had a RMSE value between 0.84 m and 1.29 m. The position of these earthquake source models varied significantly along strike, with a cluster of models with high slip on the southern segment of the fault model (e.g. 11_87_3) and a cluster of models with high slip on the northern segment (e.g. 52_87_2 and 50_87_3; Figure 19). Fifteen of these 56 earthquake models yielded a Δ_i value less than 2.0, indicating "substantial fits" (Figure 18). These "substantial fits" corresponded to having high slip on the northern segment of the fault model, as opposed to the southern segment.

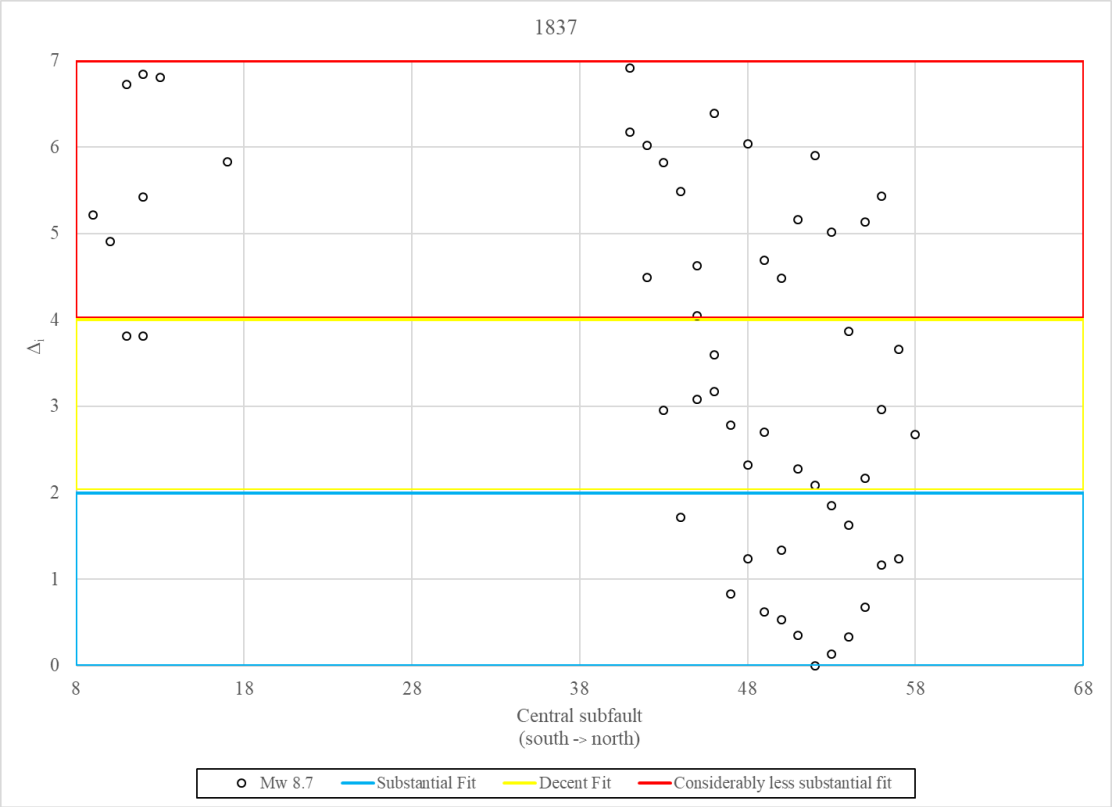

Figure 18: The 56 earthquake source models that yielded a $\Delta_i < 7.0$ when compared against the 1837 historical data. There were two spatial clusters of earthquake point source models in the south and north. These clusters may be a result from tsunami simulations over fitting two regions of spatially adjacent wave height data in the south and north that was data available for the 1837 event.

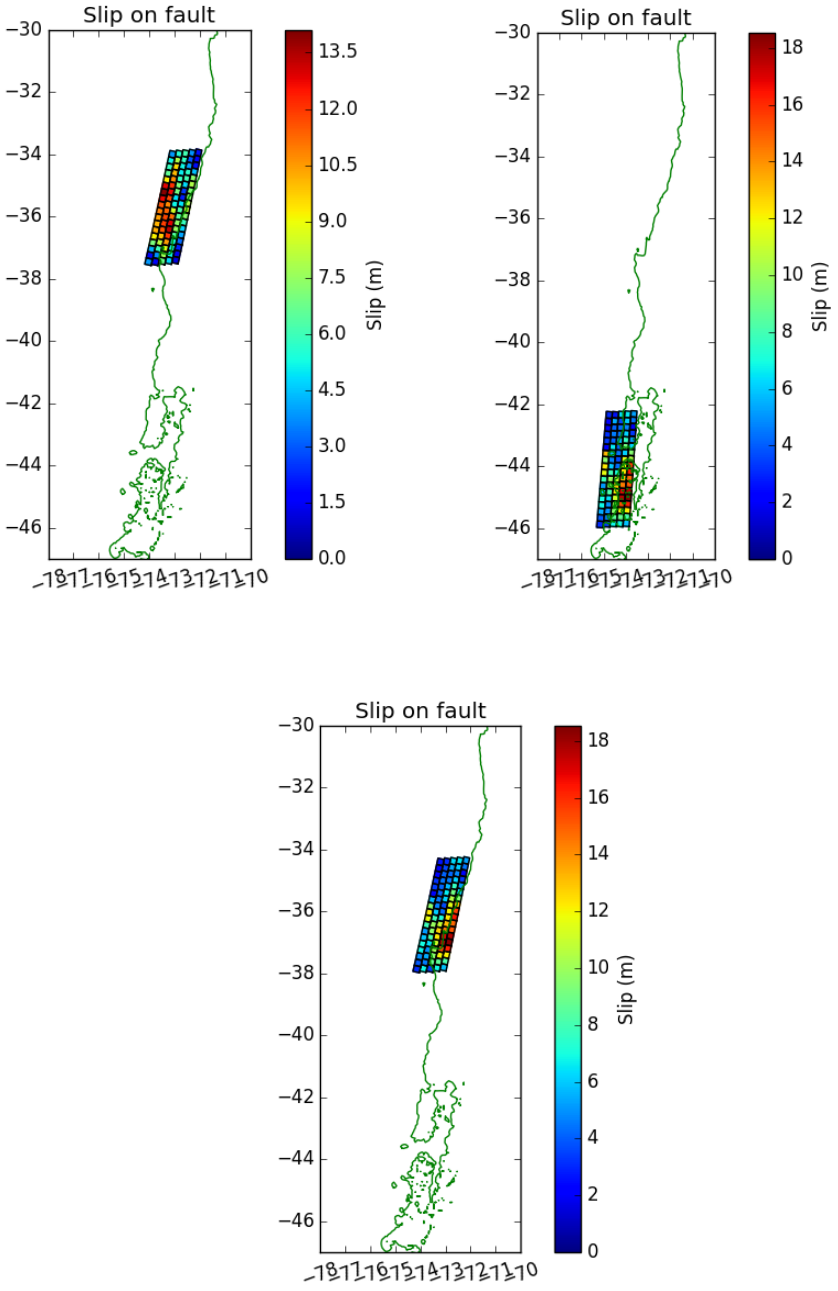

Figure 19: Potential rupture scenarios that were statistically significant, which yielded Δ_i values that suggest a substantial fit based on the AIC equations for the 1837 event: left) model 52_87_2, right) model 11_87_3, and bottom) 50_87_3.

1871 tsunami simulations

There was only one observation for 1871 event (a written record in Valparaíso), therefore only one tide gauge was used for the AIC_c statistical analysis (Appendix D; Table 1). The Δ_i of all 423 earthquake source models at this one tide gauge ranged from 0 to 16.08 with 29 yielding a Δ_i value less than 7 (Appendix E_9). Five of these 29 earthquake models had a Δ_i value less than 2.0, indicating "substantial fits" (Figure 20). These models, 52_87_2, 53_87_2, 56_87_3, 54_87_3, and 51_87_3, had an RMSE value between 0.02 m and 0.07 m. The region of high slip for all of these models was either located on deeper or shallower portion of the northern segment of the fault model at ~ 35.5°S (Figure 21).

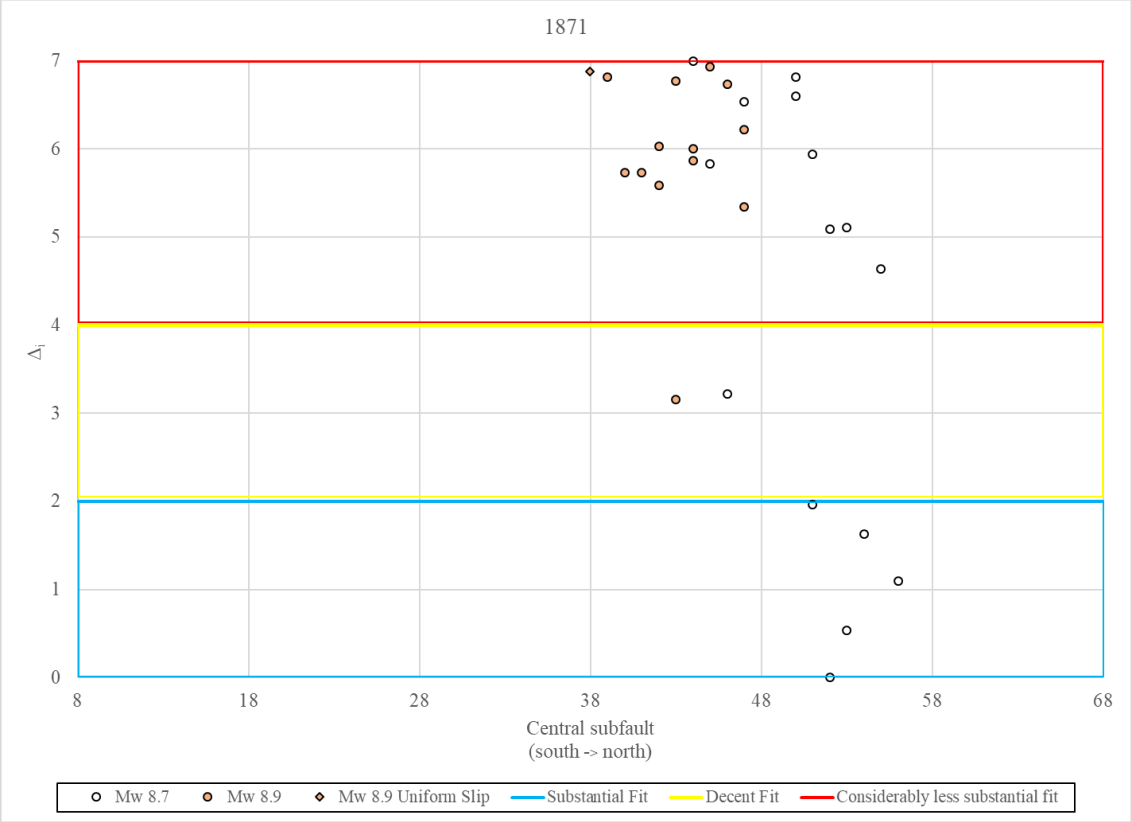

Figure 20: The 29 earthquake source models that yielded a $\Delta_i < 7.0$ when compared against the 1871 historical data. The tsunami simulations from earthquake source models 52_87_2, 53_87_2, 56_87_3, 54_87_3, and 51_87_3 represent statistically substantial fits based on the historical tsunami data available for the 1871 event.

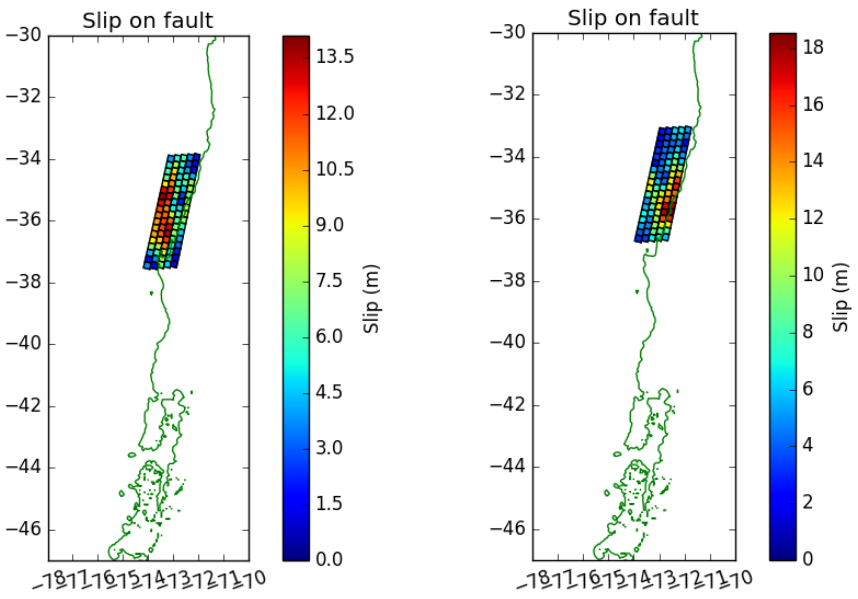

Figure 21: Potential rupture scenarios that were statistically significant, which yielded Δ_i values that suggest a substantial fit based on the AIC equations for the 1871 event: left) model 52_87_2 and right) model 56_87_3.

1871b tsunami simulations

The 1871b event was associated with one tsunami observation (at Puerto Montt), and therefore only tide gauge was used for the AIC_c statistical analysis (Appendix D; Table 1). The Δ_i of all 423 earthquake source models from the gauge at Puerto Montt ranged from 0 to 12.31 and 42 yielded a Δ_i value less than 7 (Appendix E_{10}). Of these 42 earthquake models, three had a Δ_i value less than 2.0, indicating "substantial fits" (Figure 22). These models, 37_93_9, 36_91_3, and 40_93_10, had a RMSE value between 0.02 m and 0.03 m. Additionally, some M_w 8.7 earthquakes that ruptured on the southern segment should be considered as potential fits as well (e.g. model 15_87_3 with Δ_i value

of 2.88; see *Discussion* chapter regarding localized tsunami accounts with only one observation). The region of maximum of slip for these earthquake source models were either located at ~ 40°S or ~ 34°S for the M_w 9.3 models, ~ 40°S and ~ 36°S for the M_w 9.1 model, and at ~ 44°S for the smaller M_w 8.7 models (Figure 23).

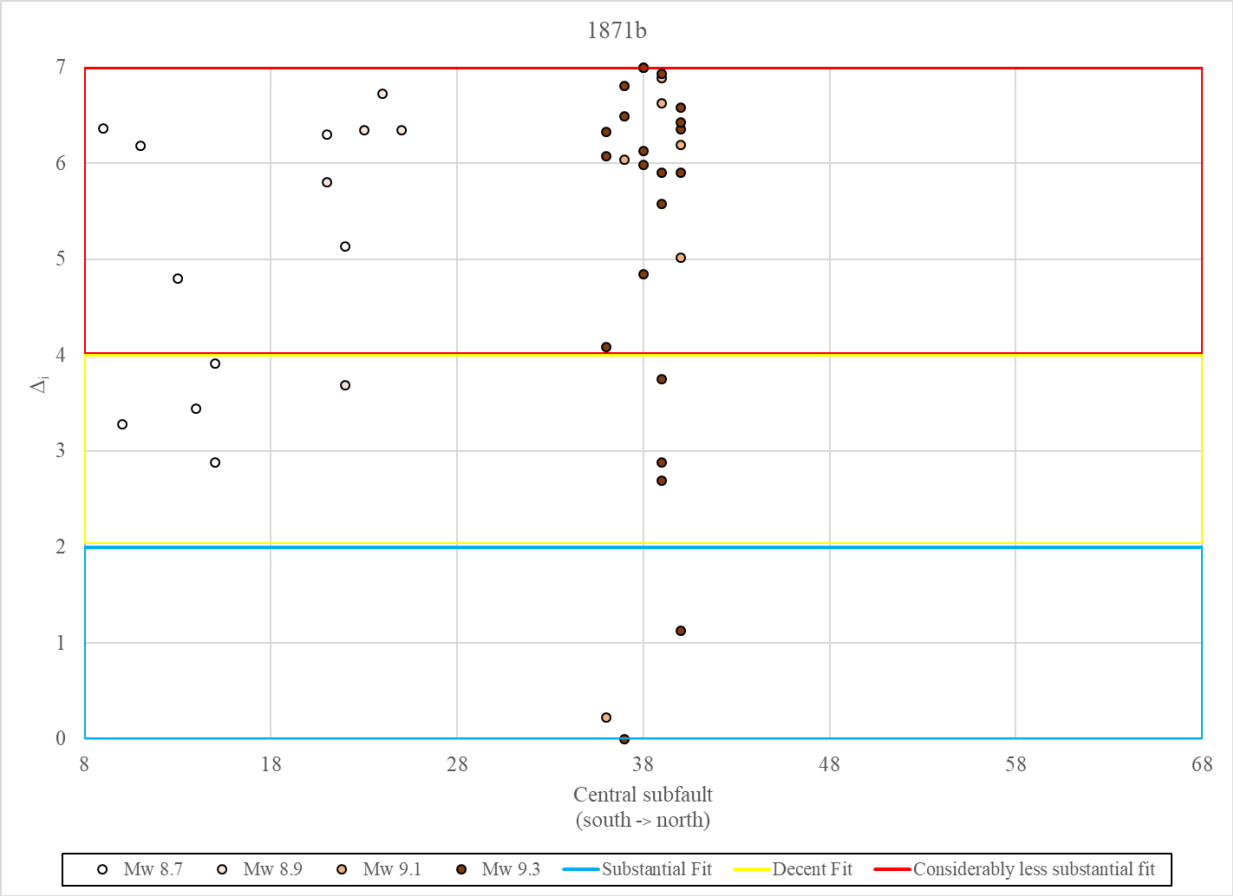

Figure 22: The 42 earthquake source models that yielded a $\Delta_i < 7.0$ when compared against the 1871b historical data. The tsunami simulations from earthquake source models 37_93_9, 36_91_3, and 40_93_10 represent statistically substantial fits based on the historical tsunami data available for the 1871b event.

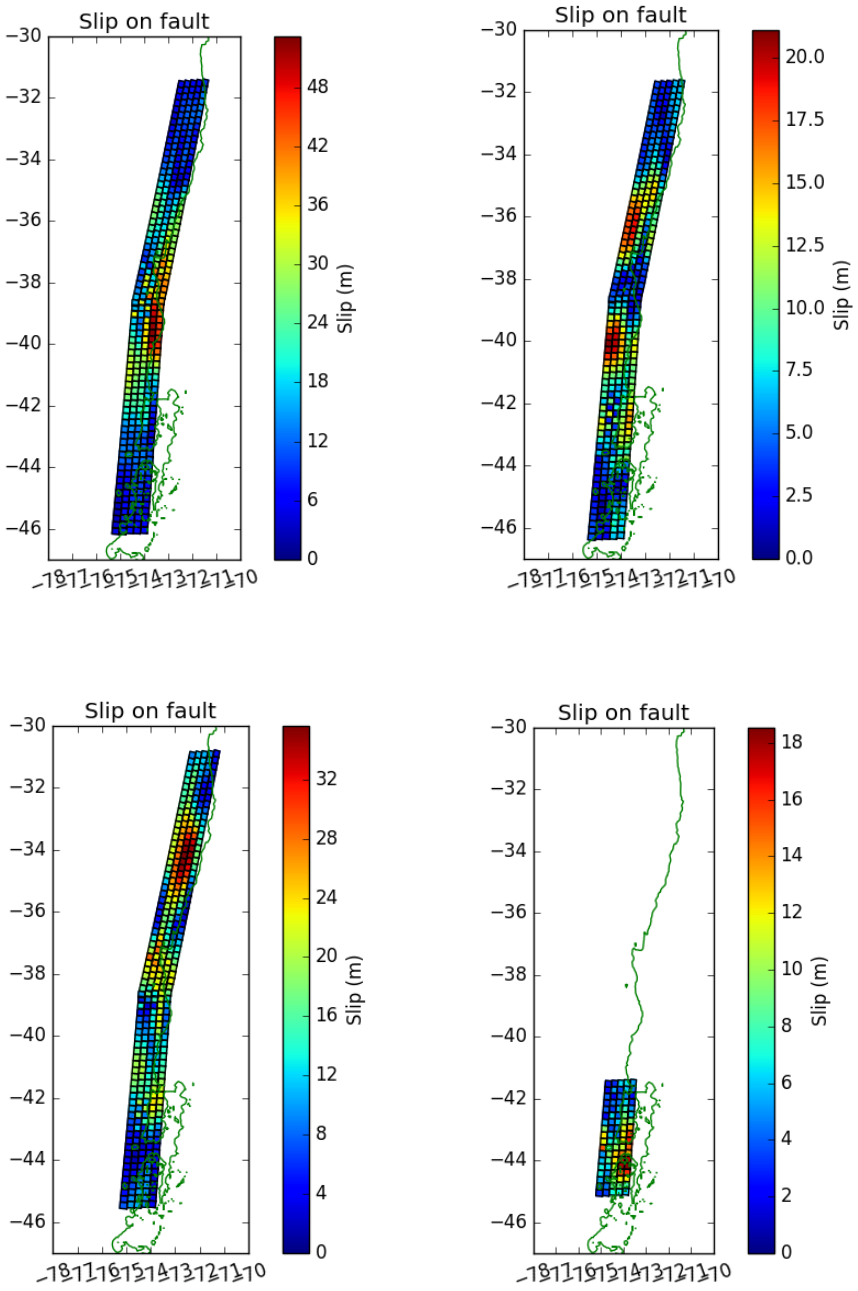

Figure 23: Potential rupture scenarios that were statistically significant for the 1871b event: top left) model 37_93_9, top right) 36_91_3, bottom left) model 40_93_10, and bottom right) model 15_87_3.

1898 tsunami simulations

The 1898 AIC_c analysis used only one tide gauge to account for the individual observation in the written record at Concepción Bay (Appendix D; Table 1). The Δ_i of all 423 earthquake source models ranged from 0 to 18.48 and 15 yielded a Δ_i value less than 7. All 15 of these statistically significant solutions ruptured on the southern segment of the Chilean subduction zone (Appendix E_{11}). However, none of these 15 earthquake models were within a Δ_i value of 2.0 from the best model, 17_87_2 (Figure 24). Model 17_87_2 had a RMSE of 0.01 m and a region of high slip located in the shallow part of the fault model between ~ 42.5°S and ~ 43.5°S (Figure 25).

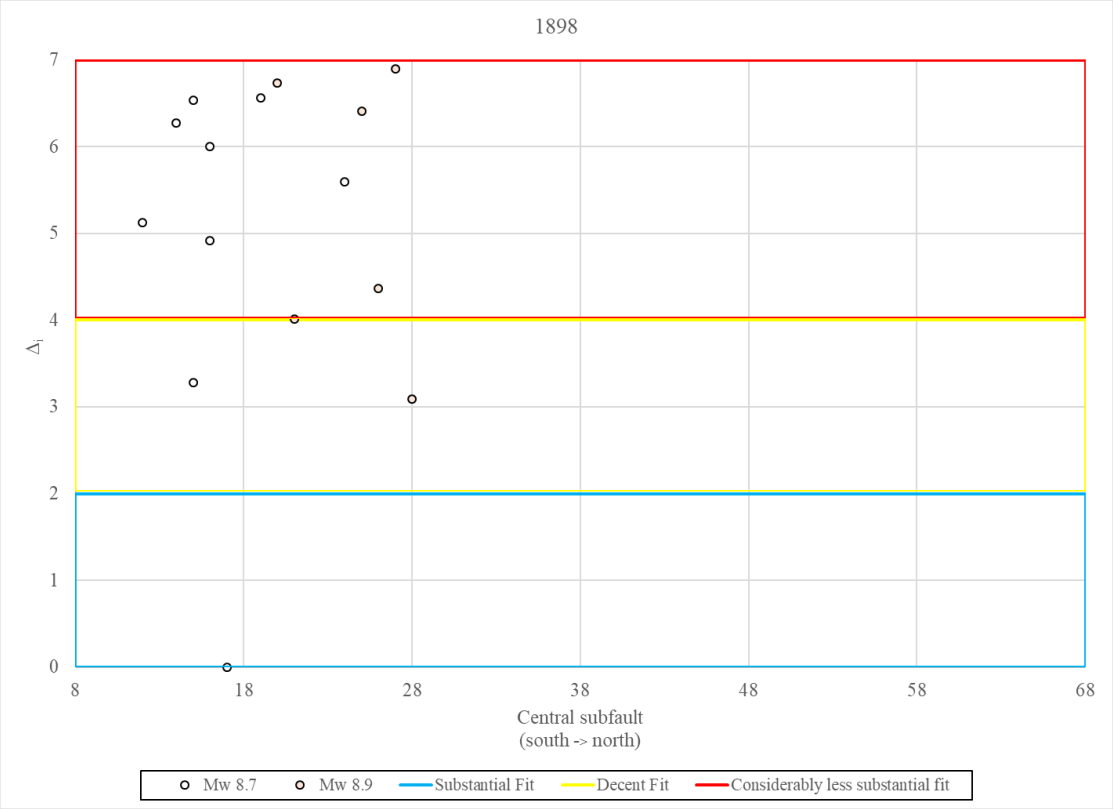

Figure 24: The 15 earthquake source models that yielded a $\Delta_i < 7.0$ when compared against the 1898 historical data. The tsunami simulation from earthquake source models 17_87_2 represents a statistically substantial fits based on the historical tsunami data available for the 1898 event.

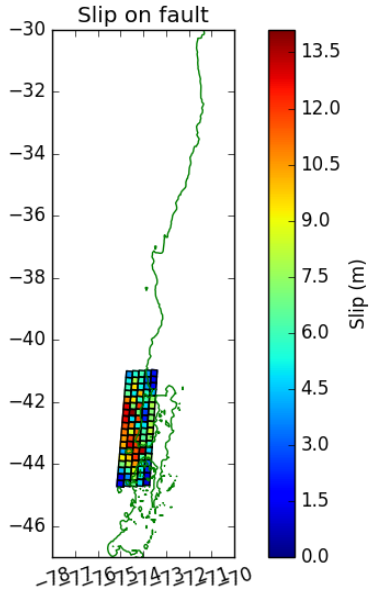

Figure 25: Potential rupture scenario that was statistically significant, which yielded a Δ_i value that suggests a substantial fit based on the AIC equations for the 1898 event: model 17_87_2.

1906 tsunami simulations

Nine tide gauges were used for the 1906 AIC_c analysis to account for all observations within the written record (Los Vilos, Valparaíso, three north of Constitución, Tomé, south of Tomé, Talcahuano, Penco, and Coronel; Appendix D; Table 1). The Δ_i of all 423 earthquake source models in this analysis ranged from 0 to 59.37 and 175 yielded a Δ_i value less than 7 (Appendix E_{12}). 68 of these 175 earthquake models, had a Δ_i value less than 2.0, indicating "substantial fits" (Figure 26). These 68 earthquake source models have a small range in RMSE with values from 1.45 m to 1.62 m. The majority of these top 68 models were M_w 8.7 in size and ruptured the south-

central area of the Chilean subduction zone. The region of high slip for these models was located near the Mocha fracture zone at ~ 39°S (Figure 27).

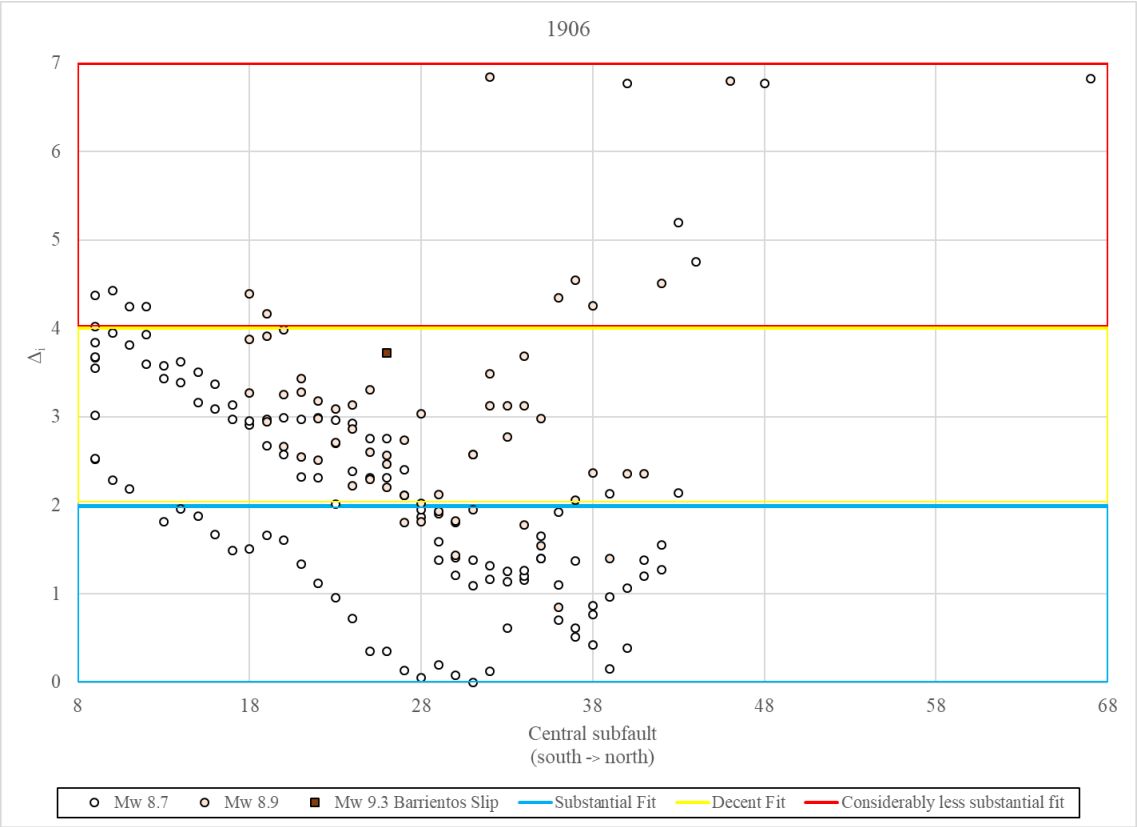

Figure 26: The 175 earthquake source models that yielded a $\Delta_i < 7.0$ when compared against the 1906 historical data. The statistically substantial fit tsunami simulations were generally derived from M_w 8.7 earthquake source models that ruptured the south-central segment of the subduction zone.

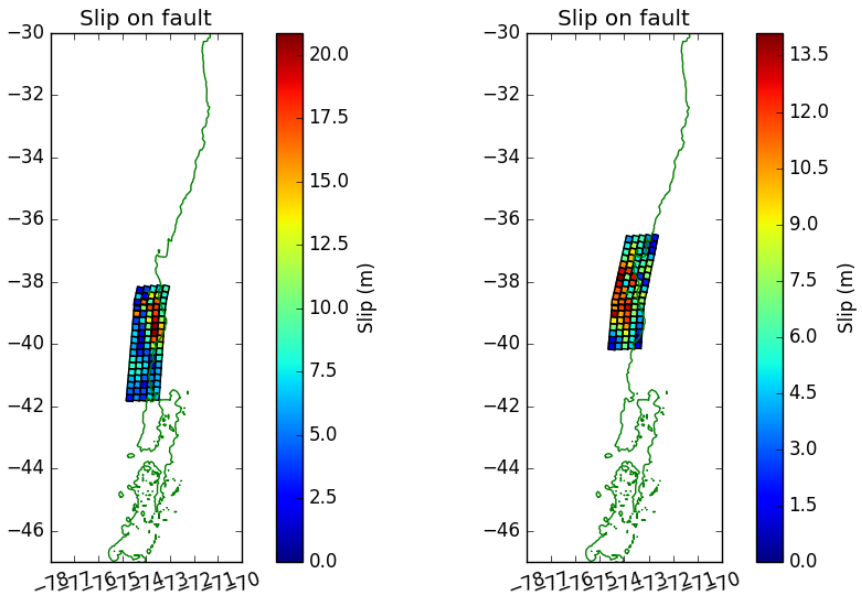

Figure 27: Potential rupture scenarios that were statistically significant, which yielded a Δ_i value that suggests a substantial fit based on the AIC equations for the 1906 event: left) model 31_87_1 and right) model 39_87_2.

1920 tsunami simulations

The 1920 AIC_c analysis used four tide gauges that corresponded to four observations within the written record (one at Talcahuano and three from the Arauco Province; Appendix D; Table 1). Based on the AIC_c statistical analysis with these gauges, the Δ_i of all 423 earthquake source models ranged from 0 to 57.05 and 17 yielded a Δ_i value less than 7 (Appendix E_{13}). Three of these 17 earthquake models, had a Δ_i value less than 2.0, indicating "substantial fits" (Figure 28). These models, 24_87_1, 29_87_2, and 23_87_1, had RMSE values that ranged from 0.29 m to 0.36 m. The region of high

slip for these models was located on the southern segment of the fault model between ~ 40°S and ~ 41°S (Figure 29).

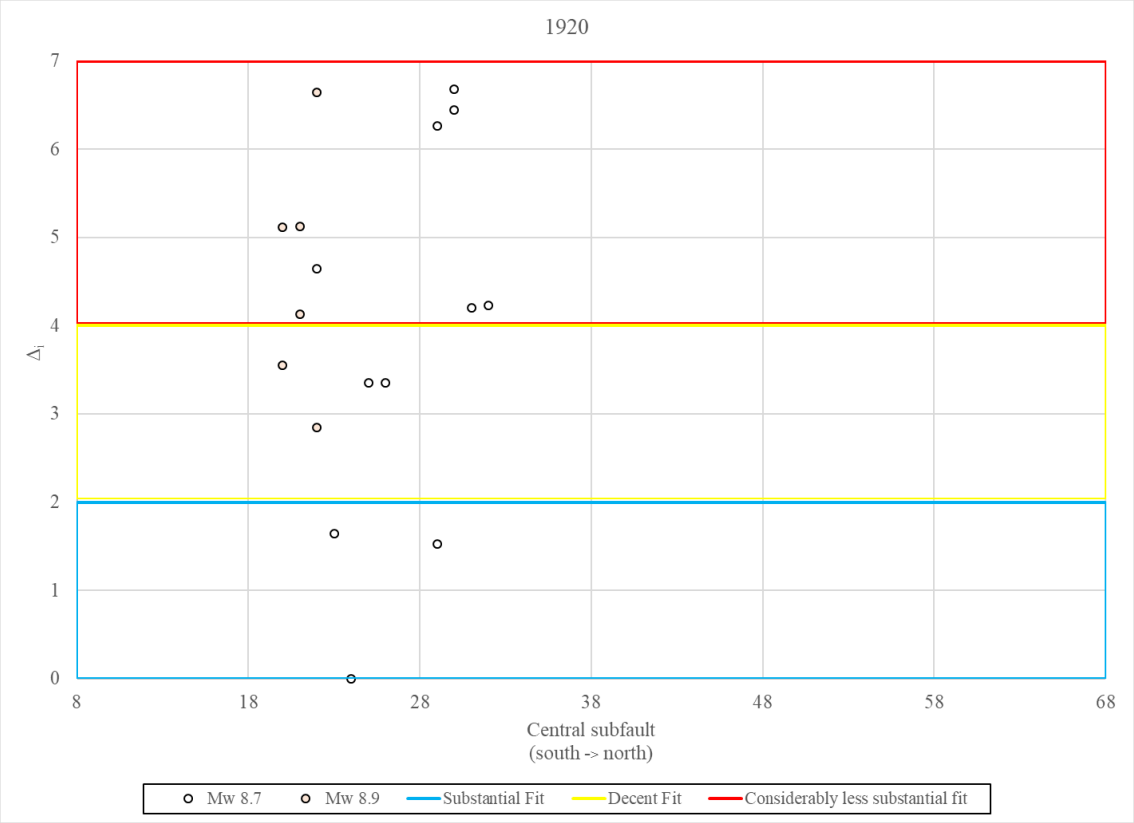

Figure 28: The 17 earthquake source models that yielded a $\Delta_i < 7.0$ when compared against the 1920 historical data. The tsunami simulations from earthquake source models 24_87_1, 29_87_2, and 23_87_1 represent statistically substantial fits based on the historical tsunami data available for the 1920 event.

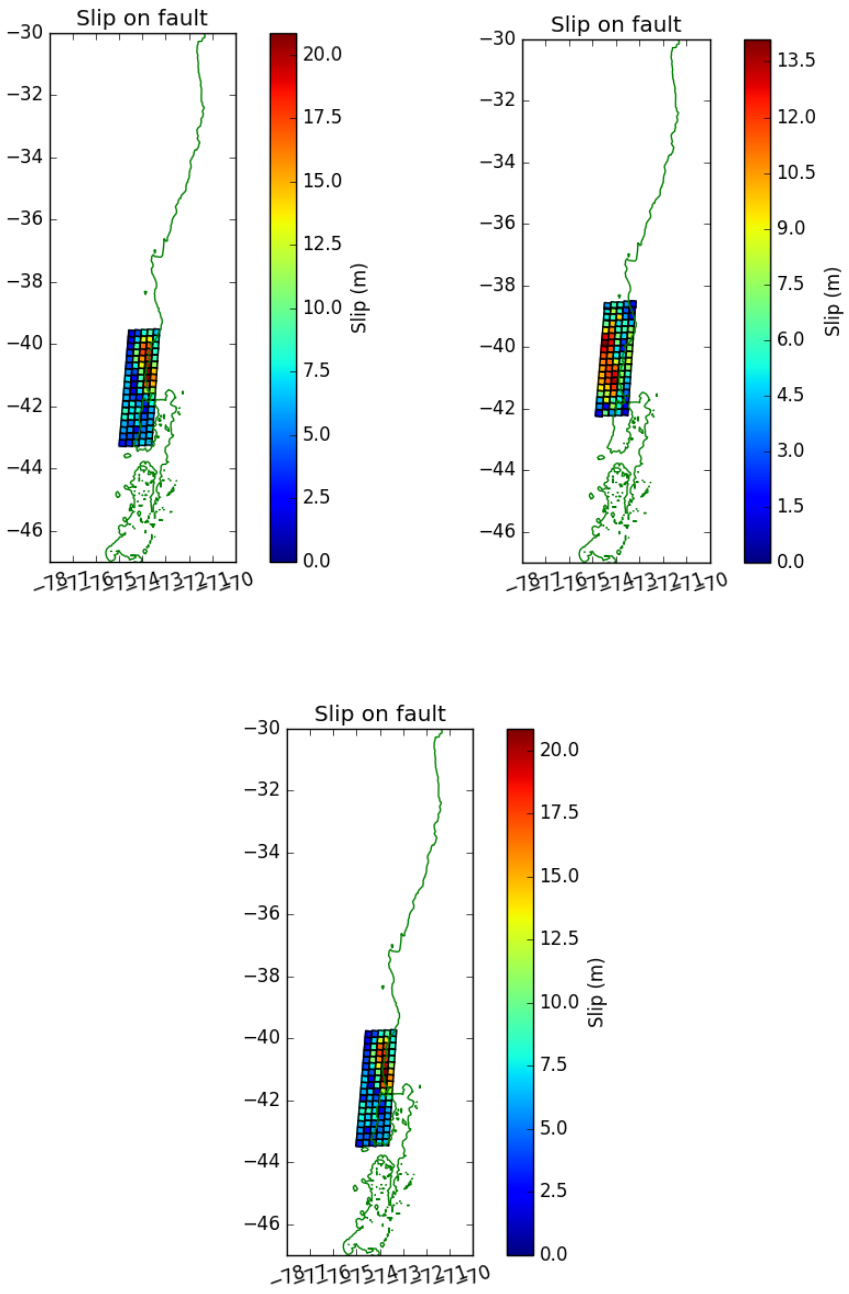

Figure 29: Potential rupture scenarios that were statistically significant, which yielded a Δ_i value that suggests a substantial fit based on the AIC equations for the 1920 event: left) model 24_87_1, right) model 29_87_2, and bottom) model 23_87_1.

1927 tsunami simulations

The 1927 AIC_c analysis used two tide gauges corresponding to observations in the written record at Puerto Aysen and Puerto Cisnes (Appendix D; Table 1). Based on the AIC_c statistical analysis with these gauges, the Δ_i of all 423 earthquake source models all appear to have the same result (Figure 30; Appendix E_{14}). By definition of the AIC equations, one model must receive a Δ_i of 0. However, all models had an RMSE value of 5.95 m, which confirms that water did not reach the tide gauges in any models. Puerto Asyen and Puerto Cisnes are located in southern Chile within fjords ~ 140 km from the open ocean.

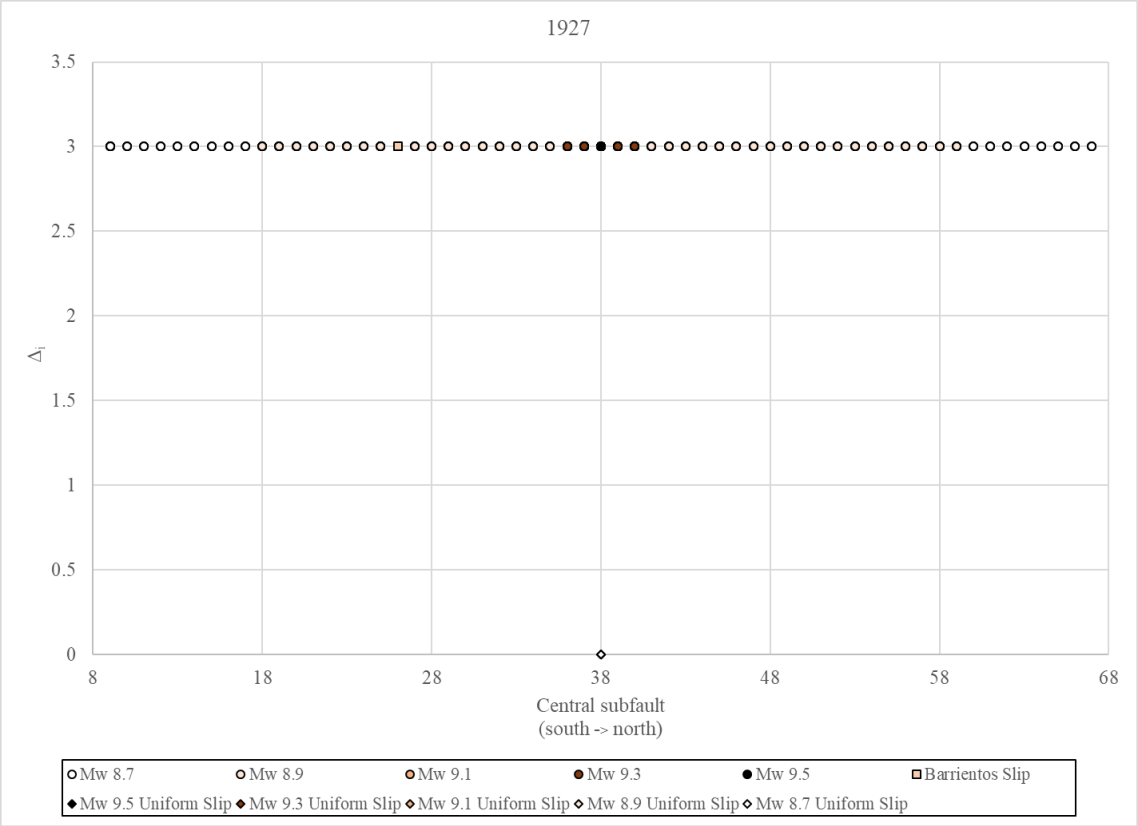

Figure 30: The Δ_i versus central subfault of rupture for all tsunami simulations relative to the lowest AIC value calculated from observations of the 1927 historical tsunami. Earthquake magnitude positively correlates to darker colored data points.

1928 tsunami simulations

The 1928 AIC_c analysis used two tide gauges that corresponded to observations in the written record just north of Constitución (Appendix D; Table 1). The Δ_i of all 423 earthquake source models ranged from 0 to 22.77 and 33 yielded a Δ_i value less than 7 (Appendix E_{15}). Four of these 33 earthquake models had a Δ_i value less than 2.0, indicating "substantial fits" (Figure 31). These models, 39_87_1, 44_87_2, 43_87_1, and 32_89_3, had RMSE values ranging from 0.11 m to 0.14 m. The region of high slip for

39_87_1, 44_87_2, and 43_87_1 were generally located on the northern segment of the fault model at ~ 37°S to ~ 38°S just north of the Mocha fracture zone at ~ 38°S to ~ 38.5°S (Figure 32). Earthquake source model 39_89_3 was a rupture on the southern segment of the fault model with high slip occurring at ~ 42°S (Figure 32).

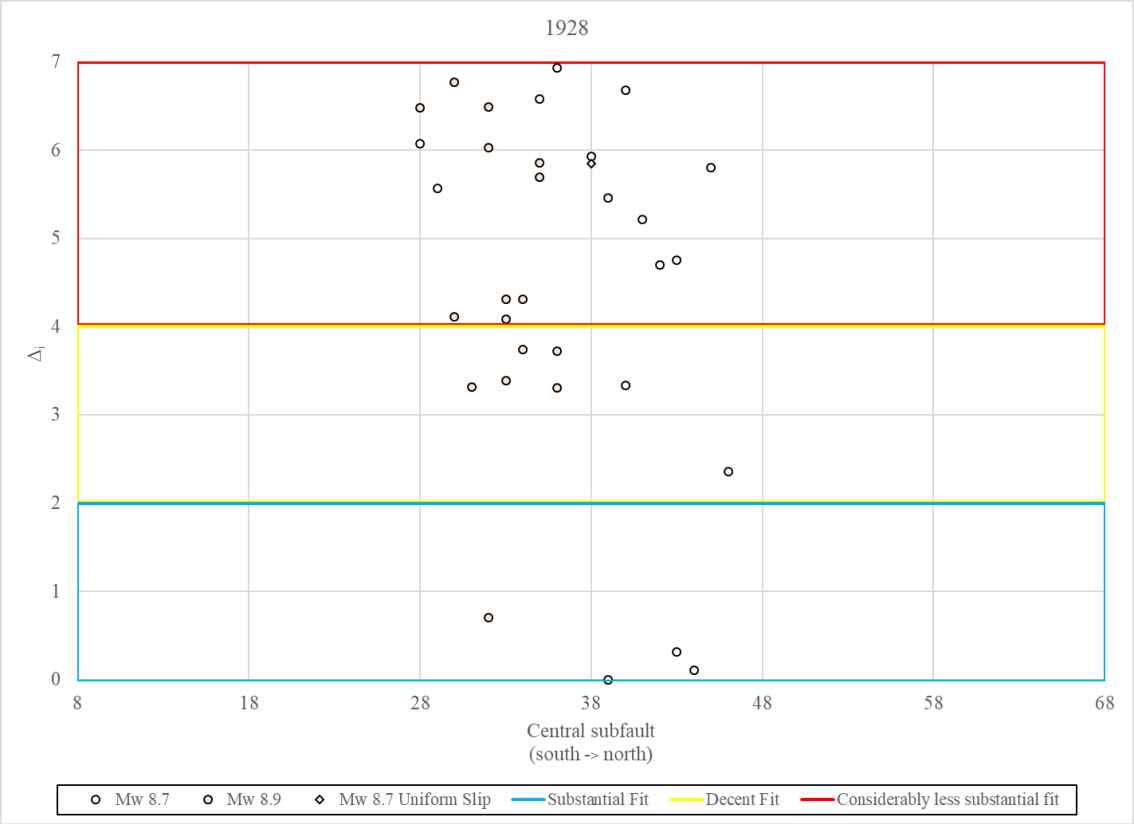

Figure 31: The 33 earthquake source models that yielded a $\Delta_i < 7.0$ when compared against the 1928 historical data. The tsunami simulations from earthquake source models 39_87_1, 44_87_2, 43_87_1, and 32_89_3 represent statistically substantial fits based on the historical tsunami data available for the 1928 event.

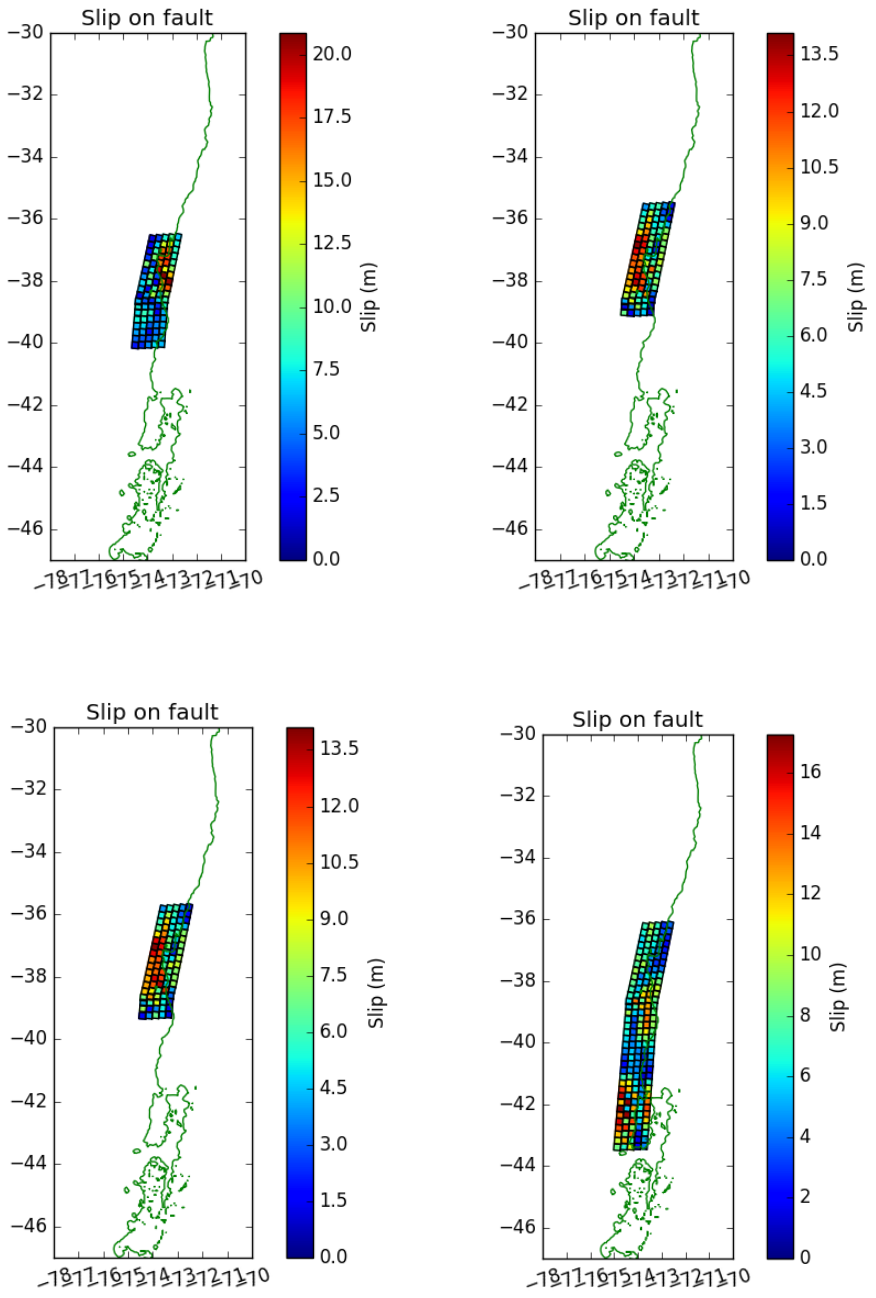

Figure 32: Potential rupture scenarios that were statistically significant, which yielded a Δ_i value that suggests a substantial fit based on the AIC equations for the 1928 event: top left) model 39_87_1, top right) model 44_87_2, bottom left) 43_87_2, and bottom right) 32_89_3.

1943 tsunami simulations

The 1943 AIC_c analysis used only one tide gauge based on a single observation in the written record at Los Vilos (Appendix D; Table 1). The Δ_i of all 423 earthquake source models ranged from 0 to 15.87 and 26 yielded a Δ_i value less than 7 (Appendix E_{16}). Three of these 26 earthquake models, had a Δ_i value less than 2.0, indicating "substantial fits" (Figure 33). These models, 44_87_1, 40_89_3, and 41_89_3, had an RMSE value ranging between 0.03 m to 0.08 m. The region of high slip for all three models are in the deeper part of the southern segment of the fault model at ~ 37°S, despite them varying in magnitudes. However, the M_w 8.9 source models also showed a region of greater shallow slip farther south between ~ 40°S and ~ 41°S (Figure 34).

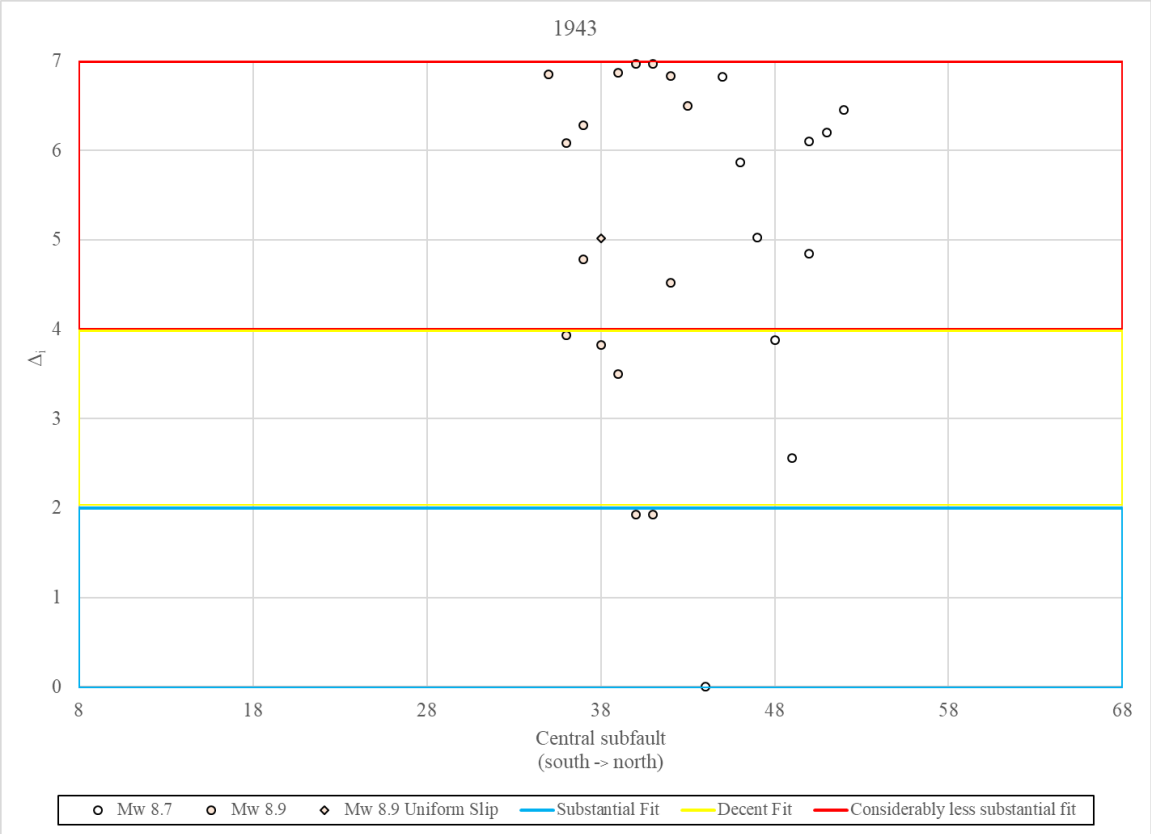

Figure 33: The 26 earthquake source models that yielded a $\Delta_i < 7.0$ when compared against the 1943 historical data. The tsunami simulations from earthquake source models 44_87_1, 40_89_3, and 41_89_3 represent statistically substantial fits based on the historical tsunami data available for the 1943 event.

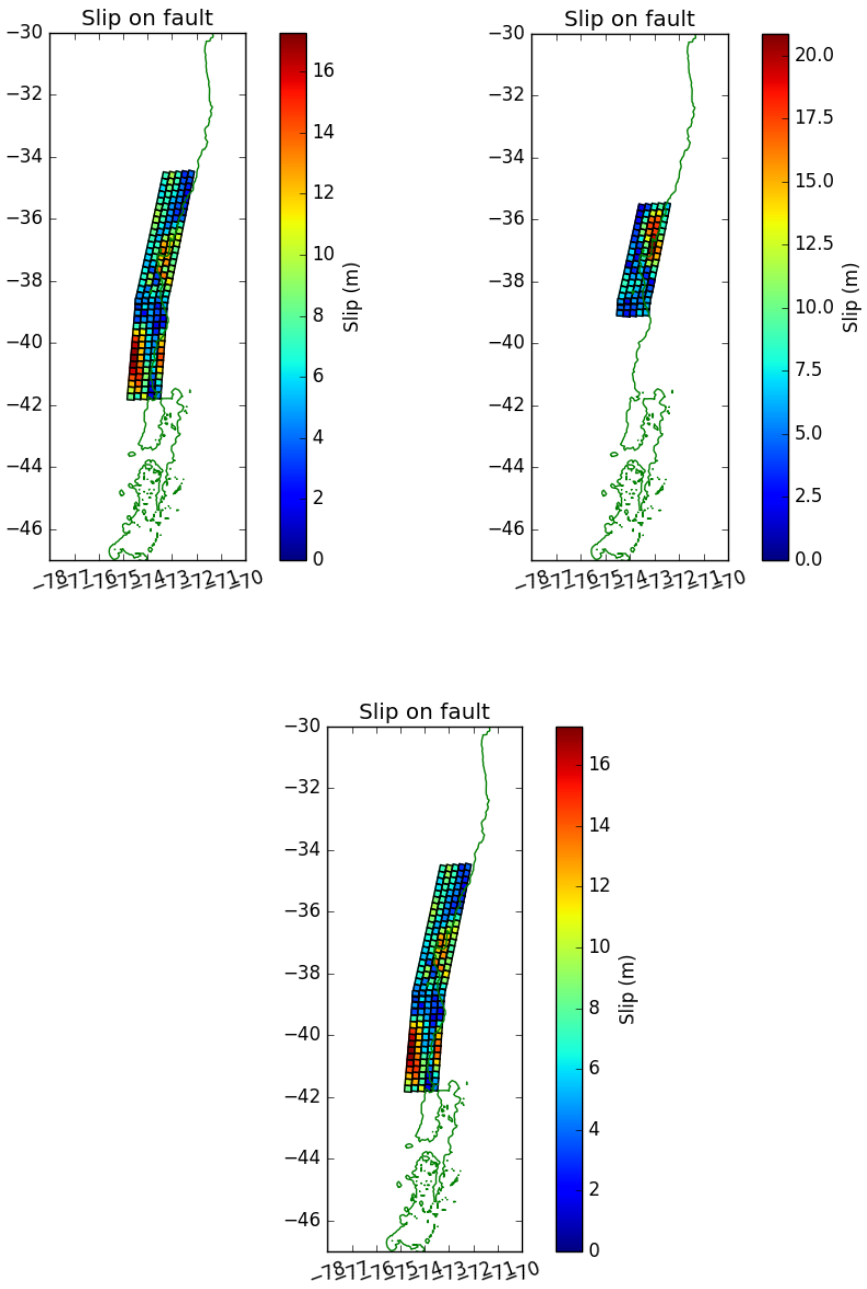

Figure 34: Potential rupture scenarios that were statistically significant, which yielded a Δ_i value that suggests a substantial fit based on the AIC equations for the 1943 event: left) model 44_87_1, right) model 40_89_3, and bottom) model 41_89_3

CHAPTER V
1960 RESULTS

1960 Tsunami Simulations

The 1960 AIC_c analysis used 30 tide gauges (Appendix D), of which 19 gauges were based on observations in the written record, while 11 gauges correlated to accounts within the geologic record (Table 1). The Δ_i of all 423 earthquake source models ranged from 0 to 102.86 and 58 yielded a Δ_i value less than 7 (Appendix E_{17}). 16 out of the 58 statistically significant models had a Δ_i value less than 2.0, indicating "substantial fits" (Figure 35). Two of these 16 substantial fits were from M_w 9.3 earthquake source models (39_93_1 and 37_93_1), while 14 were from M_w 8.7 earthquake source models. The center of rupture for the M_w 8.7 earthquakes varied 299 km along strike and included slip distributions #1, #2, and #3. The RMSE values of these 16 substantial fits ranged from 2.54 m to 3.84 m, with the M_w 9.3 earthquake source numbers being more than a meter less than the M_w 8.7 earthquake source models. The main region of high slip for the M_w 9.3 source models and the majority of M_w 8.7 models were located similarly at ~ 39°S. However, the M_w 9.3 earthquake source models also suggested there was shallow, high slip in the north or south at ~ 33°S and ~ 41°S, respectively (Figure 36). The published earthquake source model by Barrientos and Ward (1990) (refer to *Similarities of the "Barrientos slip" to AIC selected models* in the *Discussion* chapter) had a Δ_i value of 17.25, suggesting that this model had essentially no statistical significance.

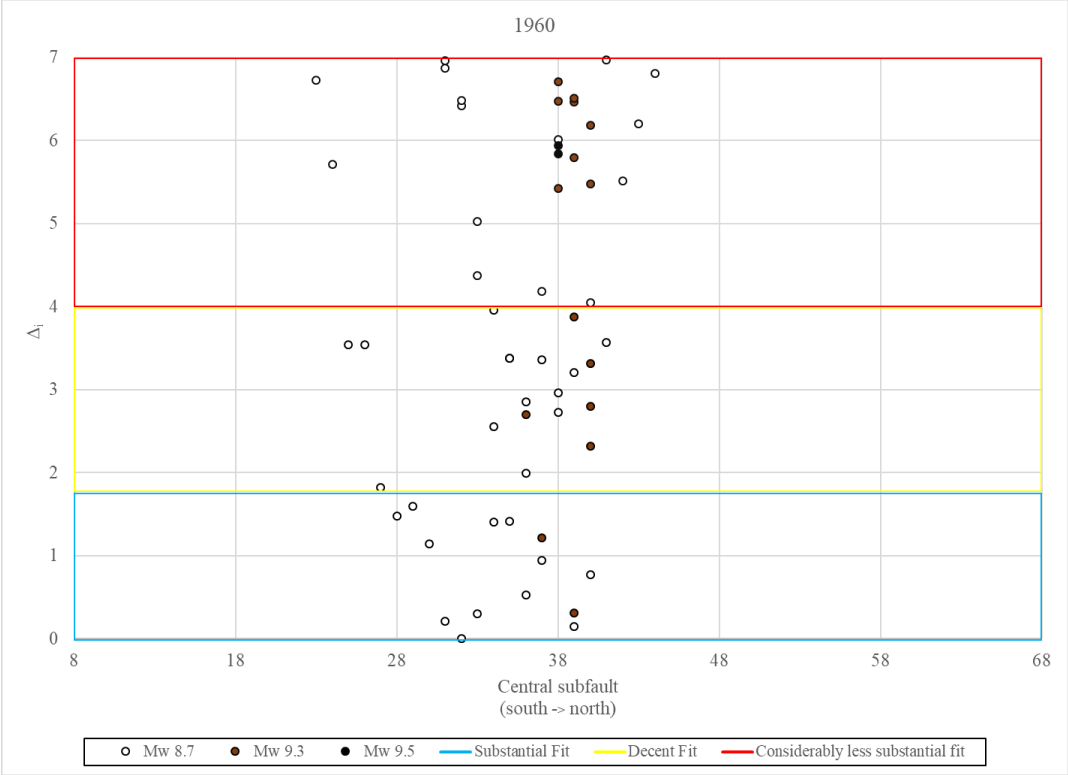

Figure 35: The 58 earthquake source models that yielded a $\Delta_i < 7.0$ when compared against the 1960 historical data. The two tsunami simulations from M_w 9.3 earthquake source models and 14 tsunami simulations from M_w 8.7 earthquake source models represent statistically substantial fits based on the historical tsunami data available for the 1960 event.

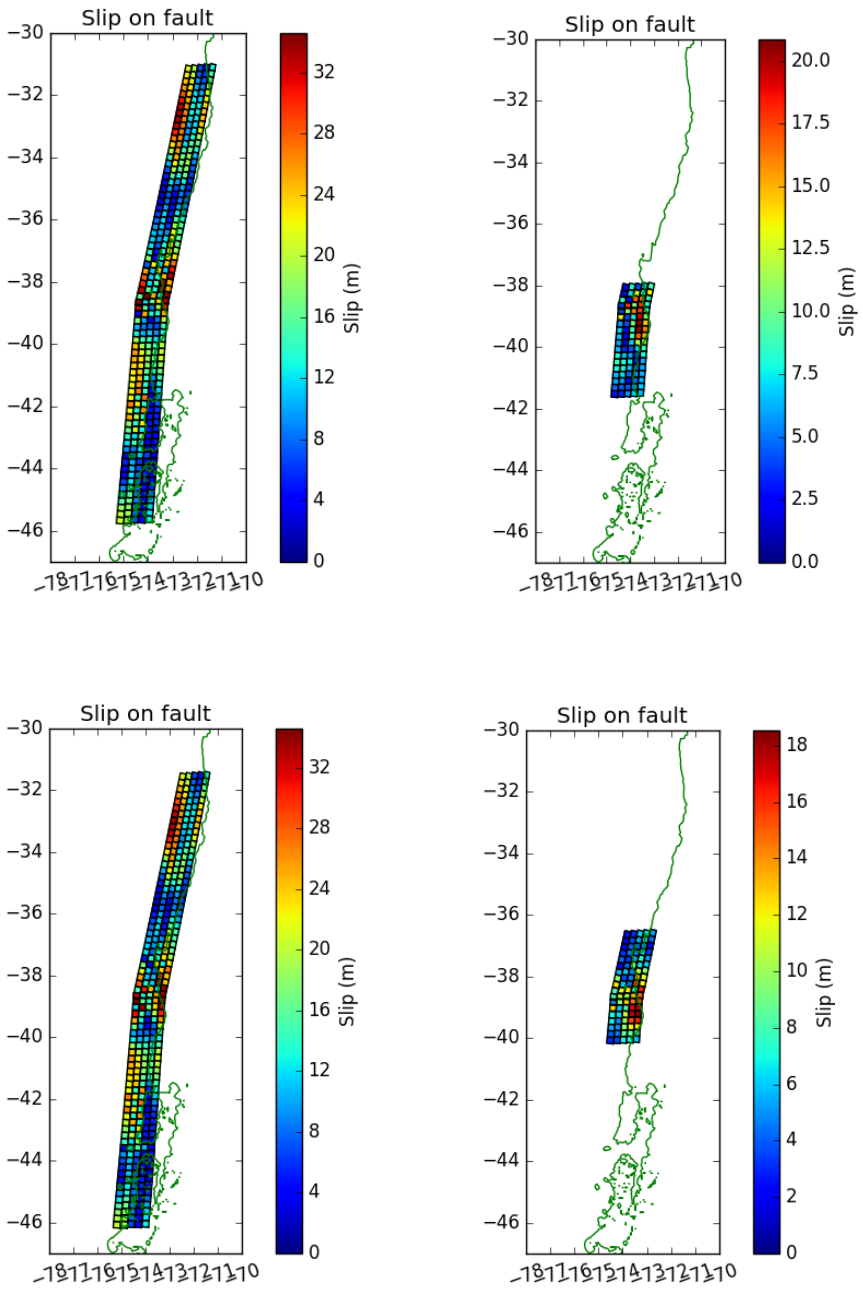

Figure 36: Potential rupture scenarios that were statistically significant, which yielded a Δ_i value that suggests a substantial fit based on the AIC equations for the 1960 event: top left) model 39_93_1, top right) 32_87_1, bottom left) model 37_93_1, and bottom right) model 39_87_3.

High-resolution bathymetry for 1960 analysis

The 1960 AIC analysis showed that 33 earthquake source models had a Δ_i less than 4.0, which can be narrowed down further using high resolution bathymetry by simulating on-land inundation using 1/3 arc-second high resolution topography at three locations (Tirúa, Quidico, and Puerto Saavedra). Out of the top 33 models determined by the AIC analysis, 16 simulations successfully inundated Tirúa, 21 in Quidico, and 2 in Puerto Saavedra. The two models that matched the data from Puerto Saavedra (40_93_7 and 39_93_7; Table 4) were both in the group of models that matched observations at Tirúa and Quidico. These two source models are of the same slip distribution only offset by 23 km along strike (Figure 37; Figure 38).

Table 4: Inundation comparison for three locations using earthquake source models that yielded a Δ_i value less than 4.0 for the 1960 event. 'O' shows models with inundation at tsunami observation/deposit sites, while an 'X' shows water stopping short of those sites.

Source model	Δ_i	Tirúa	Quidico	Puerto Saavedra
32_87_1	<2	X	O	X
39_87_3	<2	X	X	X
31_87_1	<2	X	O	X
33_87_1	<2	O	O	X
39_93_1	<2	X	O	X
36_87_2	<2	O	O	X
40_87_3	<2	X	X	X
37_87_2	<2	O	O	X
30_87_1	<2	X	O	X
37_93_1	<2	X	X	X
34_87_1	<2	O	O	X
35_87_1	<2	O	O	X

Model	Δ_i	Δ_i Rank	RMSE (m)	RMSE Rank
29_87_1	<2	O	O	X
27_87_1	<2	O	O	X
36_87_1	<2	O	O	X
40_93_1	<4	O	O	X
34_87_2	<4	O	O	X
36_93_1	<4	X	O	X
38_87_3	<4	X	X	X
40_93_2	<4	O	O	X
36_87_3	<4	X	O	X
38_87_2	<4	O	O	X
39_87_2	<4	O	X	X
40_93_7	<4	**O**	**O**	**O**
37_87_3	<4	X	X	X
35_87_3	<4	X	X	X
35_87_2	<4	X	X	X
25_87_1	<4	X	X	X
26_87_1	<4	X	X	X
41_87_3	<4	X	X	X
39_93_7	<4	**O**	**O**	**O**
34_87_3	<4	X	X	X
Total	**-**	**16**	**21**	**2**

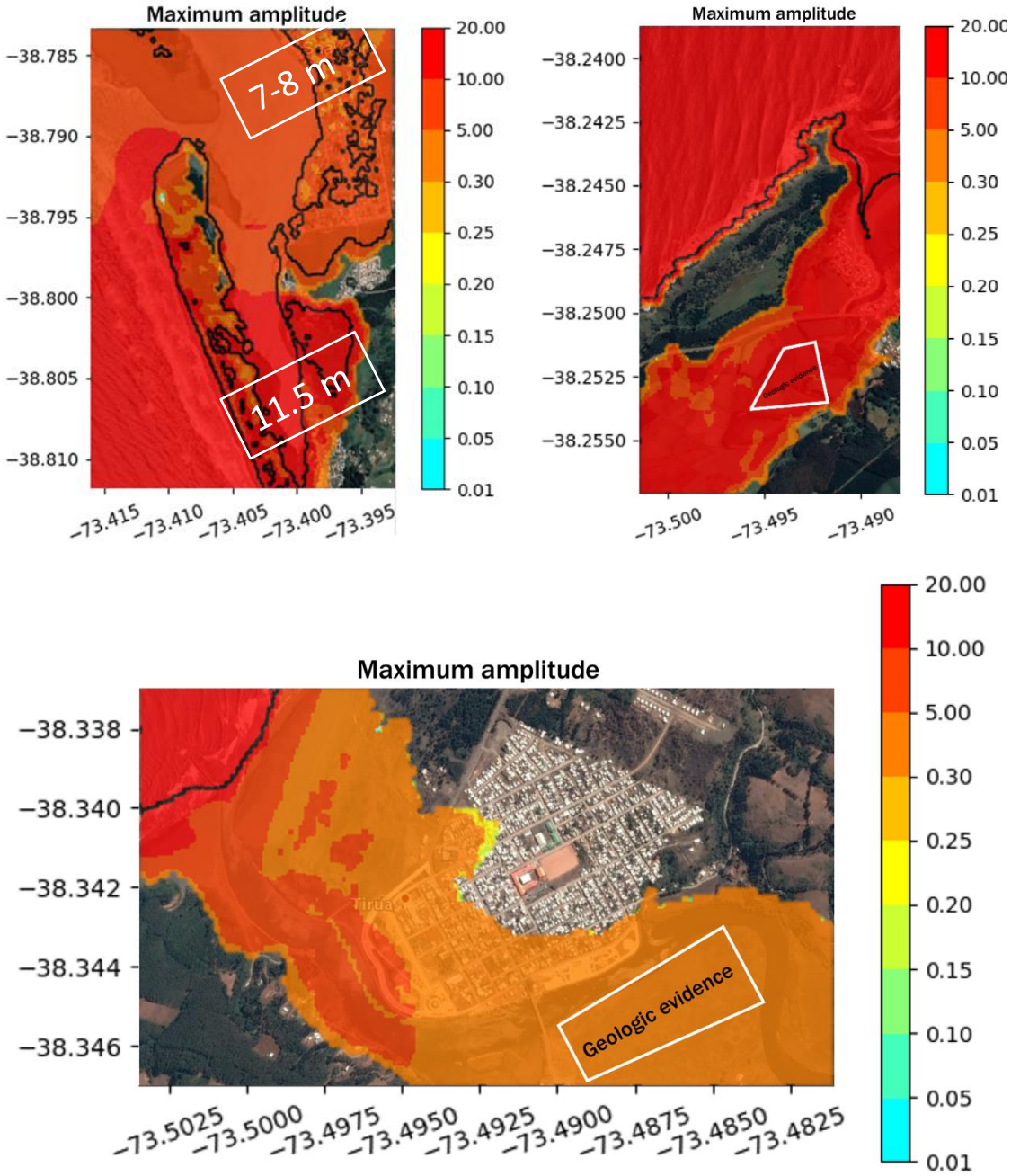

Figure 37: Maximum tsunami elevationat Puerto Saavedra (left), Quidico (right), and Tirúa (bottom) from earthquake source model 40_93_7. The scale bar is in meters. The tsunami simulation from this source model matched the geologic evidence recorded at Quidico and Tirúa, in addition to matching the 7-8 m wave height in the village of Puerto Saavedra and an 11.5 m wave height in the southern portion of the bay.

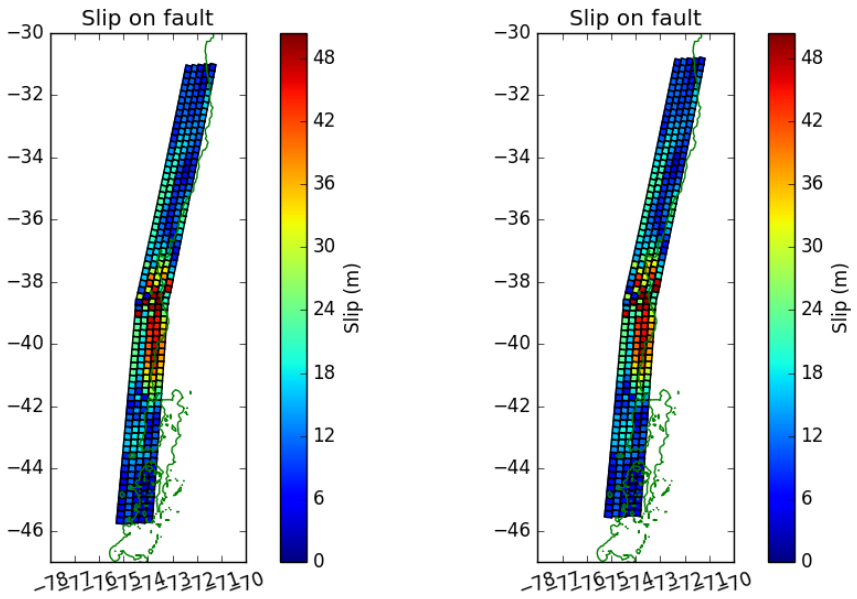

Figure 38: Potential rupture scenarios for earthquake source models 39_93_7 (left) and 40_93_7 (right), which successfully matched the inundation dynamics at Puerto Saavedra, Quidico, and Tirúa.

Total water displacement of "best-fitting" 1960 models

The total volume of water displaced from a tsunami was correlative to the magnitude of the earthquake source model. Out of the top 33 best-fitting earthquake source models for the 1960 event and the top two M_w 9.5 source models (AIC_c ranks #43 and #44), the tsunami simulations derived from the M_w 9.5 source models displaced the most amount of water (Table 5). Following the M_w 9.5 tsunami simulations, the M_w 9.3 tsunami simulations all displaced a greater volume of water than the M_w 8.7 tsunami simulations by an order of magnitude, and the (M_w 9.0) Barrientos and Ward (1990) source model (Table 5).

Table 5: The amount of total water displaced for all 1960 tsunami simulations with a Δ_i <4, the two best-fitting M_w 9.5 tsunami simulations, and the tsunami simulation derived from the Barrientos and Ward (1990) M_w 9.0 earthquake source model.

Displaced water rank	**Earthquake model**	**Volume of total water displaced (m^3)**	**Δ_i**	**AIC_c rank**
1	38_95_3	2.34 X 10^{15}	5.94	44
2	38_95_7	2.07 X 10^{15}	5.84	43
3	39_93_7	1.27 X 10^{15}	3.87	32
4	40_93_7	1.27 X 10^{15}	2.80	25
5	40_93_2	1.03 X 10^{15}	2.32	21
6	36_93_1	1.02 X 10^{15}	2.70	19
7	37_93_1	1.02 X 10^{15}	1.21	10
8	39_93_1	1.01 X 10^{15}	0.31	5
9	40_93_1	1.01 X 10^{15}	2.32	17
10	Barrientos_Slip	5.79 X 10^{14}	15.37	155
11	27_87_1	2.05 X 10^{14}	1.82	15
12	28_87_1	2.05 X 10^{14}	1.48	13
13	29_87_1	2.03 X 10^{14}	1.60	14
14	30_87_1	2.02 X 10^{14}	1.14	9
15	32_87_1	2.01 X 10^{14}	0.00	1
16	31_87_1	2.01 X 10^{14}	0.21	3
17	34_87_3	2.01 X 10^{14}	3.95	33
18	33_87_1	2.00 X 10^{14}	0.30	4
19	36_87_3	2.00 X 10^{14}	2.85	22
20	35_87_3	2.00 X 10^{14}	3.38	27
21	35_87_2	2.00 X 10^{14}	3.38	28
22	37_87_3	2.00 X 10^{14}	3.35	26
23	34_87_1	2.00 X 10^{14}	1.41	11
24	40_87_3	1.99 X 10^{14}	0.77	7
25	38_87_3	1.98 X 10^{14}	2.73	20
26	39_87_3	1.98 X 10^{14}	0.15	2
27	41_87_3	1.98 X 10^{14}	3.57	31
28	35_87_1	1.97 X 10^{14}	1.42	12
29	36_87_1	1.97 X 10^{14}	1.99	16

Displaced water rank	Earthquake model	Volume of total water displaced (m^3)	Δ_i	AIC_c rank
30	34_87_2	1.39×10^{14}	2.56	18
31	36_87_2	1.38×10^{14}	0.52	6
32	39_87_2	1.37×10^{14}	3.21	24
33	37_87_2	1.37×10^{14}	0.94	8
34	38_87_2	1.36×10^{14}	2.96	23
35	25_87_1	1.20×10^{14}	3.54	29
36	26_87_1	1.20×10^{14}	3.54	30

In general, tsunami simulations derived from the same magnitudes displace a similar volume of water. Within the top AIC_c source models for the 1960 event, the M_w 8.7 and M_w 9.3 tsunami simulations can each be grouped into two clusters of total volume of water displaced (Figure 39). Models 40_93_7 and 39_93_7—the only simulations within the top AIC_c 33 that generated large enough waves to match the wave heights at Puerto Saavedra—stand out as having a greater volume of displaced water than the rest of the M_w 9.3 source models as they fit into a higher cluster (Figure 39).

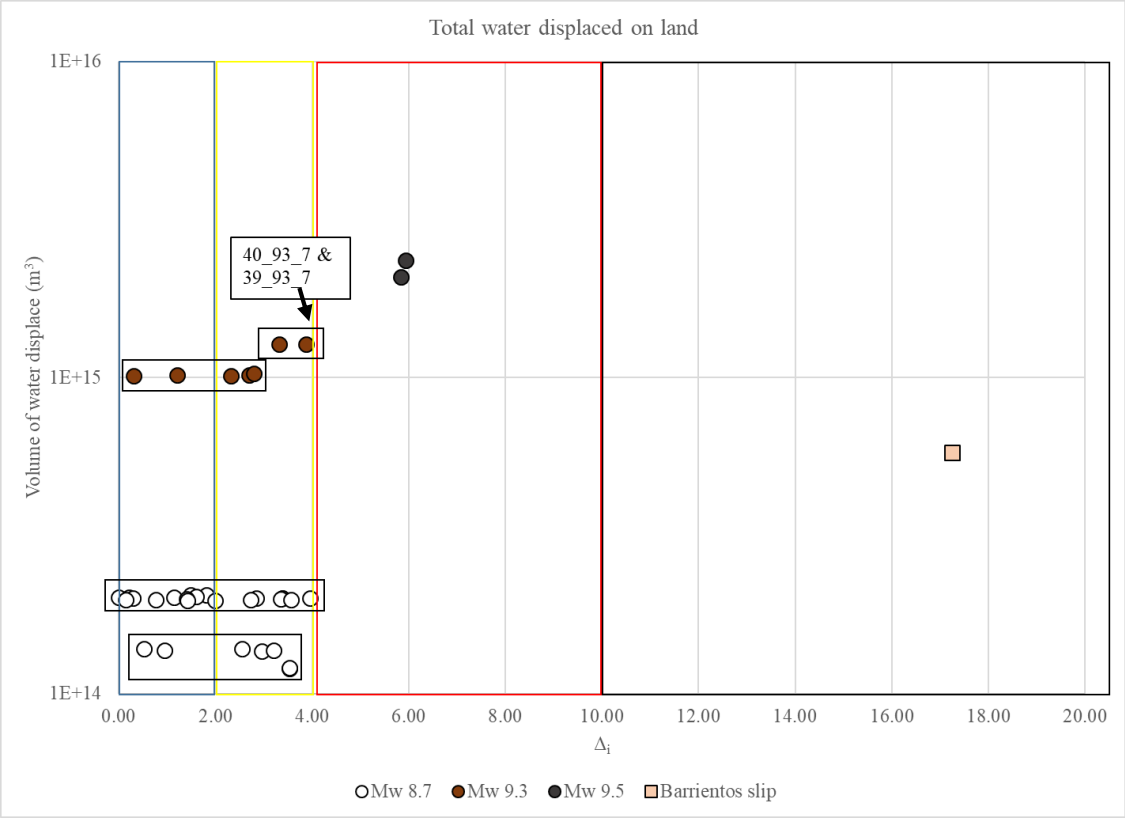

Figure 39: The volume of water displaced from the top 33 "best-fitting" tsunami simulations to the 1960 event, in addition to two M_w 9.5 tsunami simulations and the tsunami simulation derived from the Barrientos and Ward (1990) M_w 9.3 earthquake source model. The colored boxes represent the Δ_i zones of significance (0-2 = substantial significance, 3-4 = decent significance, 4-6 = considerably less significance, > 10 = essentially no significance).

CHAPTER VI

DISCUSSION

Variable slip models are better than uniform slip models

The earthquake source models in this research use stochastic variable slip solutions. However, to test whether stochastic variable slip solutions were more valuable than other solutions, a few centrally located uniform slip solutions on the same fault model as the variable slip solutions were also analyzed. In almost all earthquake analyses, the uniform slip scenarios plotted in the Δ_i category of having "essentially no" statistical significance and typically the uniform slip sources plotted worse than the variable earthquake source models that ruptured the same areas (Appendix E). Some exceptions include the 1657 analysis where all earthquake sources yielded Δ_i values less than 6.0, both 1871 and 1943 where the M_w 8.9 uniform slip source was one of those in the "considerably less substantial fit" category, and the 1928 event where the M_w 8.7 uniform slip source was one of the "considerably less substantial fit" sources. The last exception was the 1927 analysis, which showed all earthquake source models having the same result (this special case is addressed in the following section, *AIC statistical analyses are effective)*. These results are not surprising considering that earthquakes are known to not rupture uniformly across a fault area (Mikumo and Miyatake, 1978; Mai and Beroza, 2002; Moreno et al., 2010; Wang et al., 2013). Thus, when evaluating potential rupture characteristics for historical events, earthquakes with uniform slip are too simple and if possible, should not be considered.

AIC statistical analyses are effective

To evaluate the accuracy of using AIC_c as a method to determine "good-fitting" earthquake source models for a given earthquake event, I also analyzed the weighted root mean square error (RMSE) average of all tide gauges for each earthquake source model. The RMSE value declares an absolute measure of fit with lower values indicating better fit (e.g. a RMSE value of 1 m indicates that the modeled wave height is on average either 1 m higher or lower than the observed wave height in the historical record). The mean RMSE value in all model solutions, with the exception to 1570, 1575, 1837, 1871b, and 1906, was above 4.00 m with a standard deviation between 0.59 m to 16.01 m. This indicates that the majority of models have a range of "good-fitting" solutions as well as "poor fitting" solutions (Table 6). In the case of the listed exceptions, other than 1575, the locations of observations are not sensitive (yield too similar simulated values) enough to differentiate the majority of the earthquake source solutions. Disregarding the unusual 1927 earthquake event (Table 6), the RMSE value of the lowest Δ_i earthquake source model is small, which supports that the AIC analysis is valid in ranking models out of the dataset with "good-fitting" and "poor-fitting" models. This agreement between both low RMSE and Δ_i values suggests that the models that correspond to the best absolute measure of fit for all observations is being selected. However, in two earthquake analyses, the source model with the lowest Δ_i value was not the same model with the lowest RMSE value. In those two cases, 1835 and 1960 earthquakes, the larger M_w 9.3 and M_w 9.5 earthquake source model had a worse Δ_i value, but better RMSE value than

the smaller M_w 8.7 models. This discrepancy may either have to do with these smaller earthquake source models overfitting the main bulk of historical wave height data for each respective analysis (this issue is discussed further in the *Why do smaller earthquake solutions fit well for 1960?* section of this chapter), or because the larger earthquake source models rupture a greater number of subfaults. Larger source models that rupture a greater number of subfaults have more sensitively associated with its Δ_i value than the smaller source models as there are more parameters (number of subfaults) being analyzed in the AIC equations (Burnham and Anderson, 2002).

Table 6: RMSE values (m) of the "best-fitting" earthquake solution for each historical event based on the AIC equations, in addition to the mean RMSE and standard deviation of all solutions for a given historical event.

Earthquake event	Top Δ_i model	Top RMSE value (m)	Mean RMSE ± standard deviation (m)
1570	38_90_3	0.23	2.96 ± 1.88
1575	39_93_8	0.12	0.59 ± 0.19
1657	36_93_3	1.84	19.97 ± 7.34
1730	39_93_10	0.72	7.48 ± 2.68
1751	57_87_3	2.24	4.46 ± 1.08
1822	59_87_2	0.72	5.28 ± 3.54
1835	46_87_1	3.59	6.04 ± 0.82
1837	52_87_2	0.84	3.43 ± 2.89
1871	52_87_2	0.02	11.75 ± 14.63
1871b	37_93_9	0.02	2.49 ± 1.37
1898	17_87_2	0.01	10.21 ± 9.07
1906	31_87_1	1.45	3.11 ± 2.01
1920	24_87_1	0.29	5.48 ± 5.22
1927	89_uniform_slip	5.95	$5.95 \pm 7.95 \times 10^{-07}$
1928	39_87_1	0.11	5.82 ± 5.29
1943	44_87_1	0.03	12.31 ± 16.01
1960	32_87_1	3.71	4.13 ± 0.59

Overall, many of the earthquakes have few (< 3) historical wave height observations (e.g. 1657, 1871, 1871b, 1898, 1927, 1928, and 1943), which inherently biases the RMSE value because wave heights are compared against fewer data points. This becomes evident when analyzing the standard deviation of values; events with less than three observations have higher standard deviations than events with greater than three observations. Additionally, for events with only one observation (e.g. 1657, 1871, 1871b, 1898, and 1943), it does not make sense to analyze a weighted RMSE analysis.

For example, the mean RMSE and standard deviation for the 1657 event was 19.97 ± 7.34 m. These values disagree with the range of Δ_i values and suggests that there were large differences in maximum wave heights from varying source models. This inconsistency between the ranges of the Δ_i and RMSE values is partly a result of the scaling factor in the AIC_c equation (the AIC_c result may be indicating that RMSE is not a good method to use when only one observation is available). Another issue resides with using a weighted RMSE values for analyses with one gauge. The original weighted values from the residual sum of squares (RSS) in the AIC equations are not standardized to 1.0 when only one observation is involved. Thus, the large RMSE and standard deviation values, such as 19. 97 ± 7.34 m, are not representing an absolute measure of fit in these cases. Instead, it is necessary to analyze other factors, like residuals or the range of Δ_i values when only one observation is used for an event.

Analyzing the Δ_i values in detail helps to test the validity of these models results. Events with higher statistical analyses confidence should have an overall Δ_i range that is greater than 10.0 and few simulations yielding a Δ_i less than 2.0. The Δ_i value is dependent upon the lowest AIC_c model within the set of simulated earthquake source models. A Δ_i value cannot be intrinsically evaluated for goodness of fit within the AIC equations alone. However, if the range in overall Δ_i is too small (< 10.0), it suggests that all earthquake source models are too similar to be selected as truly substantially significant.

As such, two earthquakes, 1657 and 1927 can therefore be ruled out as having invalid results. The small range of Δ_i values for the 1657 and 1927 events suggest that the corresponding wave heights at the relevant tide gauges in each tsunami simulation were too similar to truly select statistically significant earthquake source scenarios. In part, the statistical failure of 1927 has to do with the resolution of bathymetry and topography. The 1927 event relied on placed tide gauges near Puerto Aysen and Puerto Cisnes. The 30 arc-second bathymetry used in these simulations interpreted the narrow fjords of the Puerto Aysen region as land, which restricted any tsunami propagation. Therefore, no tsunami simulation could inundate these tide gauges; if a finer bathymetric grid was available and used, inundation could be possible to properly evaluate the observations from these fjords.

The 1657 event's failure is due to the lack of historical data available; only one wave height at Penco was used in the AIC statistical analysis. However, the 1871, 1871b, 1898, and 1943 events also had only one historical data point at other tide gauge locations. Therefore, I assume that the tide gauge location at Penco (eastern part of Concepción Bay) is less sensitive to different rupture characteristics within the earthquake source models than other gauges (located at Valparaíso, Puerto Montt, the southern end of Concepción Bay, and Los Vilos, respectively). The geometry of eastern part of Concepción Bay, which is adjacent to Penco, may play a role in limiting the ability to differentiate waves from various tsunami simulations. However, out of all the earthquake events with one data point, the 1898 event also was analyzed with a gauge

placed in a portion of this bay. The 1898 Δ_i range was 18.48, perhaps indicating a greater sensitivity at the southern portion of Concepción Bay than the eastern portion adjacent to Penco.

Historical magnitudes match simulated estimations

The AIC equations identified suites of earthquake source models, compared to all source models in this study, that most-closely match observations of 17 known earthquake events. An important caveat is that the selected earthquake source models do not directly determine earthquake magnitude. This is because only localized historical tsunami wave heights were used as a variable in the selection process within this method. An accurate moment magnitude interpreted from only tsunami observations requires modeling additional data that this research does not address (e.g. observed land level changes and shaking intensities). There are also many tsunami modeling assumptions in these calculations, such as the process of correlating slip to seafloor deformation and whether horizontal deformation plays a role in tsunami generation. Instead, the suite of best source models defined probable locations of greatest sea surface disturbance during an earthquake responsible for producing accurate tsunami runup and inundation observations along the coast. Because water moves as an incompressible fluid, seafloor deformation within the fault model directly influences generation of a tsunami (Berger et al., 2011).

Model selection from the AIC statistical equations have made it apparent that slip distribution matters greatly. Earthquake sources of the same magnitude rupturing the same subfault area, but with different slip distributions showed wide AIC_c ranges. For example, when evaluating the validity of the source models for the 1960 event, model 39_93_1 yielded a Δ_i value of 0.31, suggesting a statistically substantial fit, while model 39_93_10, a different slip distribution, yielded a Δ_i value of 22.66, suggesting no statistical significance, despite rupturing the same area. Therefore, the position of where slip concentrations occur along the subduction zone appears to be the most critical factor for determining potential matches to historic ruptures.

That being said, the estimated magnitudes for these events in the literature still generally match well with the earthquake source model magnitudes chosen in the AIC model selection process (Table 7: Comparison table). For instance, the earthquake source simulations of the 1575, 1730, 1751, and 1960 events agree with the previously estimated magnitudes. For the cases where the estimated magnitude of an event was less than a M 8.7 rupture, it would make sense that a M_w 8.7 source model would most-closely match as they were the smallest models simulated (e.g. 1835, 1837, 1871, 1898, 1906, 1920, and 1928). However, the results of these events are inherently overestimates and smaller earthquake source models should be analyzed.

Table 7: Estimated magnitudes in the historical record (from the literature) versus estimated magnitudes from simulations.

Event	Historical record estimation of magnitude (M)	Estimated magnitude from simulations (M_w)
1570	8.0 – 8.5	8.9 and 9.1
1575	Similar to 1960	9.3
1657	8.0	8.7 and 9.3
1730	9.1 -9.3	9.3
1751	8.8	8.7, 8.9, and 9.3
1822	8.0 – 8.5	8.7 and 8.9
1835	8.2 – 8.5	8.7
1837	8.0 – 8.5	8.7
1871	7.5	8.7
1871b	n/a	8.7, 9.1, and 9.3
1898	6.5	8.7
1906	8.2	8.7
1920	7.0	8.7
1927	7.2	n/a
1928	7.7	8.7
1943	8.1	8.7 and 8.9
1960	9.5	9.3 and 8.7

For the 1570 1822, 1871b, and 1943 events, the AIC analysis overestimates the magnitudes relative to the historical estimations (Table 7: Comparison table), likely because these earthquakes have a large wave height in a localized region. The AIC analysis does not include gauges in locations with no observed wave height. However, a quick analysis of including "0's" for wave heights at tide gauges with no observations in all four of these analyses showed the M_w 8.7 earthquake source models yielded the best Δ_i. This result more closely resembles the estimated magnitudes from the historical

record. Additionally, earthquakes larger than M_w 8.7 should have observed wave heights at multiple locations along the coast in the historical record because the tsunamis would cover a broad area. The largest historical tsunami events in Chile (e.g. 1575, 1730, 1835, and 1960) all had observed tsunami runup in multiple areas along the coast or paleotsunami evidence as opposed to runup in one localized region. Therefore, earthquakes > M_w 8.7 should be unlikely fits for tsunami events with only one observation of runup. Because the 1570, 1822, 1871b, and 1943 events only have localized recorded wave heights in the historical record (< 3 observations; although 1570 may be limited due to settlement history), any source model greater than M_w 8.7 seems unlikely. The earthquake source models assume "standard" large subduction zone earthquakes and do not account for more complex scenarios in smaller magnitude events that could potentially mimic locations of high runup (e.g. earthquakes with co-seismic submarine landslides, or "tsunami earthquakes;" Kanamori, 1972; Kanamori and Kikuchi, 1993; Papadopoulos and Kortekaas, 2003). Thus, analyses for the events with limited wave heights at few (< 3) regional tide gauges may not be reliable, especially if the AIC_c analysis results in a solution > M_w 8.7.

Why do smaller earthquake solutions fit well for 1960?

The AIC analysis for the 1960 earthquake event shows that a M_w 8.7 source model is the best fit (32_87_1). This result disagrees with the literature, which interprets the 1960 earthquake as M_w 9.5 from instrumental records (Soloviev and Go., 1975; Dorn,

1987). However, according to the RMSE of the 1960 tsunami simulations, the statistically significant M_w 8.7 source models do not best match the maximum wave heights recorded at all tide gauges on average. Instead, the M_w 9.3 and M_w 9.5 have the lowest RMSE values (Table 8 1960 RMSE), better agreeing with the literature.

Table 8: RMSE values of source models ranked as statistically significant from the AIC equations.

Model	Δ_i	Δ_i Rank	RMSE (m)	RMSE Rank
39_93_1	0.31	5	2.54	1
37_93_1	1.21	10	2.58	2
40_93_1	2.32	17	2.63	3
36_93_1	2.70	19	2.65	4
40_93_2	2.80	21	2.65	5
40_93_7	3.32	25	2.68	6
39_93_7	3.87	32	2.70	7
38_95_7	5.84	43	2.74	8
38_95_3	5.94	44	2.75	9
38_93_1	5.43	38	2.77	10
40_93_8	5.48	39	2.77	11
39_93_8	5.79	42	2.79	12
40_93_9	6.18	46	2.81	13
39_93_9	6.46	49	2.82	14
38_93_7	6.47	50	2.82	15
39_93_2	6.50	52	2.82	16
38_93_9	6.71	53	2.83	17
32_87_1	0.00	1	3.71	18
39_87_3	0.15	2	3.72	19
31_87_1	0.21	3	3.73	20
33_87_1	0.30	4	3.73	21
36_87_2	0.52	6	3.75	22
40_87_3	0.77	7	3.76	23
37_87_2	0.94	8	3.77	24

Model	Δ_i	Δ_i Rank	RMSE (m)	RMSE Rank
30_87_1	1.14	9	3.79	25
34_87_1	1.41	11	3.80	26
35_87_1	1.42	12	3.80	27
28_87_1	1.48	13	3.81	28
29_87_1	1.60	14	3.82	29
27_87_1	1.82	15	3.83	30
36_87_1	1.99	16	3.84	31
34_87_2	2.56	18	3.88	32
38_87_3	2.73	20	3.89	33
36_87_3	2.85	22	3.90	34
38_87_2	2.96	23	3.90	35
39_87_2	3.21	24	3.92	36
37_87_3	3.35	26	3.93	37
35_87_3	3.38	27	3.93	38
35_87_2	3.38	28	3.93	39
25_87_1	3.54	29	3.94	40
26_87_1	3.54	30	3.94	41
41_87_3	3.57	31	3.94	42
34_87_3	3.95	33	3.97	43
40_87_2	4.05	34	3.97	44
37_87_1	4.19	35	3.98	45
33_87_2	4.37	36	4.00	46
33_87_3	5.02	37	4.04	47
42_87_3	5.51	40	4.07	48
24_87_1	5.72	41	4.09	49
38_87_1	6.01	45	4.11	50
43_87_3	6.20	47	4.12	51
32_87_2	6.42	48	4.13	52
32_87_3	6.48	51	4.14	53
23_87_1	6.72	54	4.16	54
44_87_3	6.80	55	4.16	55
31_87_2	6.87	56	4.17	56
31_87_3	6.96	57	4.17	57
41_87_2	6.97	58	4.17	58

Conceptually, it is at first puzzling to see that the AIC_c analysis selects some of the M_w 8.7 source models as more statistically significant than the M_w 9.3 and M_w 9.5 source models, despite the M_w 8.7 ruptures not being long enough along strike to match the entirety of observed wave heights in the historical record. However, these M_w 8.7 source models perform well in the AIC analysis because they overfit (i.e. fitting the bulk of the data more closely) the main concentration of historical wave height data between ~ 38.5°S and 39.5°S (Figure 40). The rupture positions of the better-fitting M_w 8.7 events are nearly parallel along strike to the main concentration of historical data (Figure 40). This overfitting of the bulk of the observed data in the "significant" M_w 8.7 source models offset the underestimation of large observational wave heights at more distal tide gauges from the historical record that match more closely with the M_w 9.3 (and M_w 9.5) source models (Figure 40).

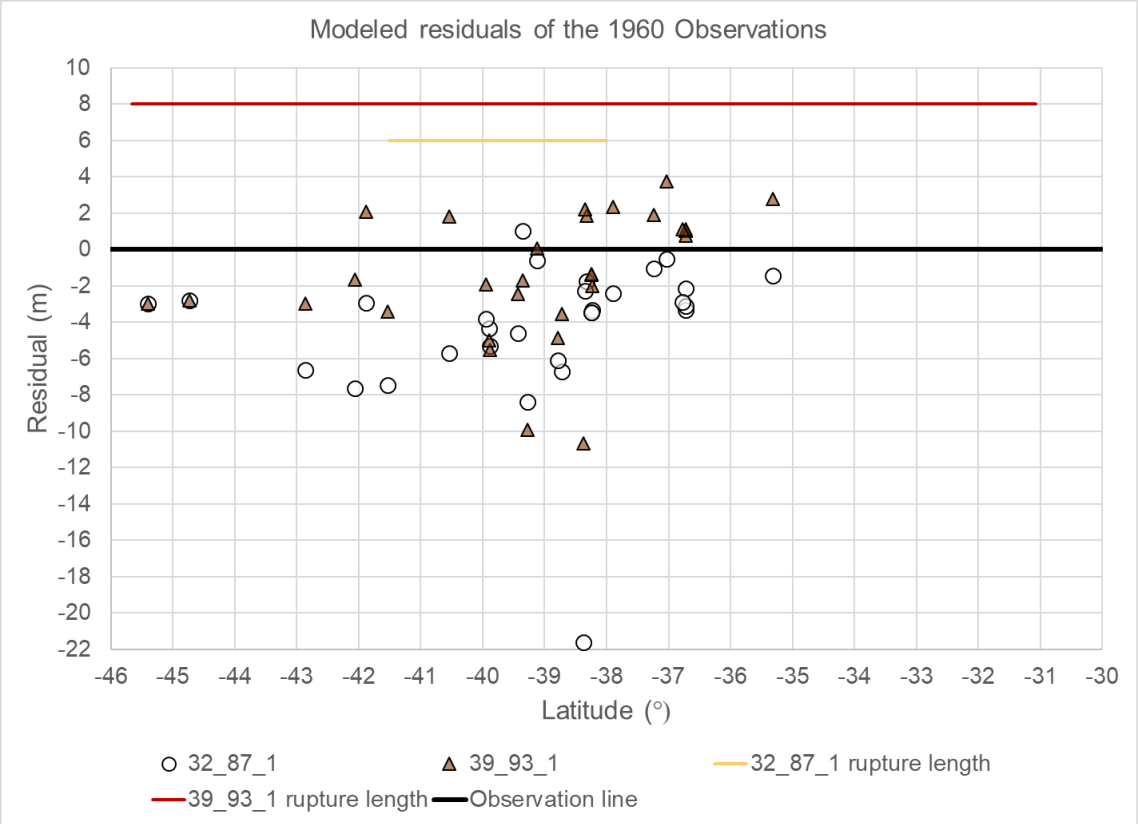

Figure 40: Residuals (simulated wave heights – observed wave heights) and rupture positions of two statistically significant earthquake source models for the 1960 event: 32_87_1 and 39_93_1. Calculated residual points closest to 0 indicate better agreement with the historical record; residual > 0 overestimates the observed wave height while < 0 underestimates the wave height.

The 1960 source model solutions support the interpretation that the AIC_c analysis does not necessarily suggest a potential magnitude of an historical event, but rather propose where the main concentration of seafloor deformation occurred in the fault model. For example, the M_w 9.3 and M_w 8.7 earthquake source models that were deemed statistically significant fits by the AIC methods share a commonality, despite the large difference in rupture lengths. This commonality is that the region of maximum seafloor deformation occurred at ~ 39°S. The lack of consistent and evenly spaced wave height

data along the coastline in the historical record within the area of study poses an uncertainty for identifying magnitudes, which was seen with the 1960 results. However, the AIC_c analysis was able to suggest the area of where the majority of the seafloor deformation would have occurred to match the historical wave height data in lieu of overall rupture lengths. This outcome was supported with multiple historical events. For instance, the 1570, 1657, 1752, 1822, 1871, 1871b, 1906, 1920, 1928, and 1943 events are all examples where differently sized earthquakes shared a common region of high slip in spite of varying rupture lengths and positions along strike.

The AIC range support the Mocha Fracture Zone hypothesis

Previous studies have hypothesized that the buoyancy of subducting high oceanic features (like the MFZ) caused by crustal thickening and mantle serpentinization is the reason for the increase in normal stress at the subduction interface, which has a strong relation to earthquake rupture segmentation along the Chile-Peru margin (Contreras-Reyes and Carrizo, 2011). However, other megathrust earthquake rupture propagations around the world, perhaps, cross segments that are similar to the MFZ in a subduction zone (Udias et al., 2012; Briggs et al., 2014). In this research, the smaller M_w 8.7 and M_w 8.9 earthquake source models allow me to assess the hypothesis of whether the Mocha fracture zone (MFZ) acts as a boundary at 38.3°S between southern and northern ruptures. This is because the rupture lengths for these sized events are able to be bounded by the MFZ on one end of the rupture extent. Solutions that support the MFZ hypothesis

must either correspond to a substantially significant rupture based on the AIC equations that was bounded by the MFZ, or had a high concentration of slip that taper to the MFZ.

The AIC overview graphs from *Appendix E* generally support the hypothesis that the MFZ controls earthquake rupture propagation and segmentation. The analyses of the 1575, 1871b, 1898, 1906, 1920, and 1960 events show that the M_w 8.7 and M_w 8.9 earthquake source models are statistically significant on the southern side of the MFZ (i.e. south of central subfault #38), but not on the northern side of the MFZ (Appendix E). On the other hand, the 1570, 1657, 1730, 1751, 1822, 1835, 1871, and 1943 events show that M_w 8.7 and M_w 8.9 earthquake source models are statistically significant on the northern side of the MFZ, but not the southern side (Appendix E). With the exception of the 1927 event, which was not modeled accurately due to coarse bathymetry, only the 1837 and 1928 events have the potential to cross the MFZ. However, the 1837 analysis could be interpreted that ruptures on either side of the MFZ are better than ruptures that cross the MFZ (Appendix E). In the 1928 analysis, the "good-fitting" M_w 8.7 earthquake source models display an area of high slip on the northern segment, which then terminates to the south at approximately the MFZ. Since these statistically significant models that best match the nearshore tsunami historical data had a termination of slip at the MFZ, the two segments within the Chilean subduction zone may rupture independently.

In some cases, the hypothesis that the MFZ is a barrier to rupture also appears to be supported with the larger statistically significant "good-fitting" M_w 9.1 and M_w 9.3

earthquake source models. Despite the rupture of these higher magnitude models extending beyond the boundary of the MFZ, many of the statistically significant source models had evident tapering of slip occurring at the MFZ in some of the statistical analyses. For example, source model 38_91_3 within the 1570 statistical analysis had high slip on the southern segment near the MFZ that then tapers to the north. Source models 30_93_10 for the 1730 analysis and 51_89_2 for the 1928 analysis also depict this tapering at the MFZ, but from north to south. Although the tapering of slip that is present in these models is just a reflection of the stochastic slip models and not proof of the existence of the MFZ, the models that have this tapering appear to be better matches to the historical record than models that do not. Thus, the hypothesis of the MFZ has some validity based on the analysis of these events. However, to further assess the legitimacy of the proposed MFZ hypothesis, tsunami simulations derived from smaller earthquake source models (M_w 8.0 to M_w 8.7) with additional variations of slip should be simulated to evaluate the historical earthquakes that appear to have high amounts of slip near the MFZ.

Analysis of the 1960 event using high-resolution bathymetry

The high resolution inundation maps generated at Tirúa, Quidico, and Puerto Saavedra were helpful to further refine the suite of best-fitting source models for the 1960 event. Out of the 33 earthquake source models that corresponded to a Δ_i less than 4.0 from the AIC_c analysis, two models, 40_93_7, and 39_93_7, matched the historic

inundation dynamics at Tirúa, Quidico, and Puerto Saavedra. These models are similar, only offset by 23 km along strike, and show a high concentration of slip around ~ 38.5°S to 40°S, as do many other "good-fitting" M_w 9.3 and M_w 8.7 source models from the AIC analysis.

Despite the 40_93_7 and 39_93_7 earthquake source models not having the lowest Δ_i values from the statistical analysis (Δ_i values between 3.0 – 4.0), they did have low RMSE values ranked in the top eight for the 1960 analysis (2.70 – 2.74 m). Thus, earthquake source models 40_93_7 and 39_93_7 should be considered as part of the suite of most-likely slip scenarios for the 1960 event because of the high-resolution modeling results and RMSE values. A possible explanation for why these models did not yield the absolute lowest AIC_c and Δ_i values could be due to testing only a subset of the complete observation record. These solutions may only match the historic and geologic tsunami evidence the best at the three locations where higher resolution bathymetry is available, and not the other locations along the coast (main concentration of high slip for these models is adjacent to Puerto Saavedra; refer to Figure 38). Also, it is possible that this difference in the Δ_i ranking is because the higher resolution and lower resolution source models are not simulated in the same model-space. If all source models were simulated with the high-resolution bathymetry, the AIC distribution may have varied.

When the AIC equations are calculated with just wave height data from Tirúa, Quidico, and Puerto Saavedra, earthquake source models 40_93_7 and 39_93_7 move up in the Δ_i ranking from #25 and #32 to #6 and #4, respectively. Additionally, the RMSE of

these earthquake source models were 1.07 m and 1.03 m when just comparing to the tide gauges at Tirúa, Quidico, and Puerto Saavedra. When evaluating just these tide gauges, models 40_93_9, 39_93_9, and 38_93_9 yielded the three lowest Δ_i values and are the best fits, followed by 39_93_7 and then 40_93_7. However, when the all of the tide gauges are evaluated in the 1960 data set, models 40_93_9, 39_93_9, and 38_93_9 showed worse results with Δ_i rankings of #46, #49, and #50, respectively, and fall into the "considerably less substantial fit" category. Thus, despite models 40_93_9, 39_93_9, and 38_93_9 fitting Tirúa, Quidico, and Puerto Saavedra the best, they should not be considered in the statistical analysis, whereas 40_93_7 and 39_93_7 still should. Thus, using high-resolution bathymetry to match known inundation dynamics in the written record has demonstrated to be a useful tool to further refine "good-fitting" source models from the initial AIC model selection process with the lower resolution bathymetry.

Model selection at Puerto Saavedra is the most constrained

The high-resolution inundation maps allowed for testing model selection constraints at three sites (Tirúa, Quidico, and Puerto Saavedra). At Tirúa 16 out of the top 33 earthquake source models for the 1960 event generated a tsunami that matched estimated inundation dynamics, while 21 matched at Quidico and only 2 at Puerto Saavedra. Although many of the top 33 earthquake source models had solutions that inundated the correct areas at Puerto Saavedra, the majority did not have large enough wave heights at the village (7-8 m) and at the southern end of the bay (11.5 m).

Therefore, Puerto Saavedra yielded the most constrained model selectivity of the three, followed by Tirúa and Quidico. This is partly because the bay of Puerto Saavedra is situated behind two large spits, and partly because of biases in the modeling dynamics. The inlet between the spits in front of Puerto Saavedra is narrow (~170 m). GeoClaw does not account for erosional bathymetric/topographic change during simulations, thus the inlet cannot be widened by the tsunami. The 1960 tsunami most likely did widen the opening, although these kinds of details are not preserved in the written record. The two source models that matched inundation patterns in Puerto Saavedra (40_93_7 and 39_93_7) both had deep slip, which created 1 - 2 m of subsidence at the site, therefore artificially widening the inlet prior to tsunami inundation. Therefore, due to the geometry of this bay, results favor the selection of larger earthquake solutions with high, deep slip concentration near Puerto Saavedra that can induce land level changes.

Additionally, analyzing the total volume of displaced water also supports the conclusion that Puerto Saavedra requires precise seafloor deformation as opposed to solutions with broader regions of slip. The two best-fitting earthquake source models at Puerto Saavedra in the top 33 AIC analysis (40_93_7 and 39_93_7) had concentrated areas of highest slip compared to slightly broader slip along the fault plane in other M_w 9.3 solutions, and therefore displaced a greater volume of water than the rest of the M_w 9.3 earthquake solutions adjacent to Puerto Saavedra. This additional volume of displaced water in the source models 40_93_7 and 39_93_7 is also an important contributing factor in addition to the land-level change at Puerto Saavedra to help match

observations there. Likewise, it should also be noted that the M_w 9.5 solutions of the sample slip model (Δ_i <7) displaced even more water than the solutions from models 40_93_7 and 39_93_7, and also accurately inundated Puerto Saavedra.

Similarities of the "Barrientos slip" to AIC selected models

The "Barrientos slip" source model derived from the published earthquake slip solution by Barrientos and Ward (1990) did not produce a statistically significant solution for the 1960 event. However, their high concentration of slip at ~ 39°S to 40°S is in the same location as the "good-fitting" earthquake source solutions from the AIC analyses, except deeper in the subduction zone (Figure 41). This general location of high slip at ~ 39°S to 40°S also agrees with the published slip distribution by Moreno et al. (2009). The Barrientos and Ward (1990) earthquake slip solution was equivalent to a M_w 9.3 event and was derived from coastal land-level changes. However, because deeper portions of a subduction zone do not significantly contribute to tsunami generation (Geist, 2002), the tsunami simulated from the "Barrientos slip" solution was equivalent to a M_w 9.0, because slip that was too deep for this fault model was trimmed. Still the "Barrientos slip" solution had a main concentration of slip in the deepest part of the fault model, closest to land, suggesting smaller contribution to tsunami generation (Geist, 2002). This deeper slip suggested by Barrientos and Ward (1990) may be a product of simplified, planar fault geometry (Moreno et al., 2009). The total volume of displaced water from the "Barrientos slip" source model was not large enough to correctly inundate the three

locations where high-resolution bathymetry was available (Tirúa, Quidico, and Puerto Saavedra). Similarly, the "Barrientos slip" source model displaced a lesser volume of water than all M_w 9.3 source models within my top 33 Δ_i (refer to Figure 39). Therefore, the tsunami solution derived from the Barrientos and Ward (1990) earthquake source model was not large enough to match the tsunami record.

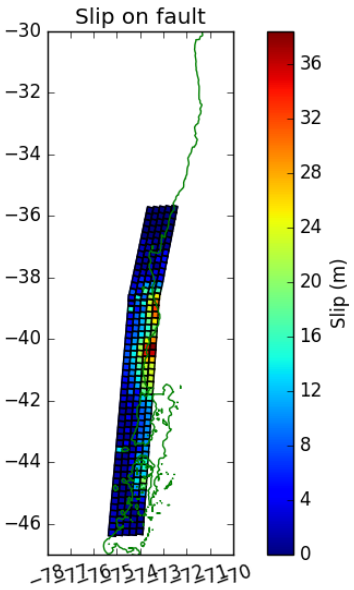

Figure 41: The M_w 9.0 earthquake source model based on land level changes from Barrientos and Ward (1990)

CHAPTER VII

SOURCES OF ERROR

Each step within the methodology of this research involves uncertainties, which can lead to error within the modeled results. The following sections will explain implications of the assumptions and sources of error for all interpretations.

The historic and geologic maximum wave height database

The historical observation database only included the average maximum wave height value that occurred in a specific location. Only focusing on the maximum wave heights oversimplifies the complex inundation dynamics that actually occurred at a location. For example, in Penco and Valparaíso during the 1730 event, Carvajal et al. (2010) noted a range of water heights at different historical buildings. Similarly during the 1960 event, Maullín experienced a range of maximum wave heights across different parts of the estuary (Cisternas et al., 2005; Atwater et al., 2013). However, because the bathymetry used in this study is itself quite simplified (only 30" resolution), using an average singular maximum wave height to represent an entire location could allow the modeling space and results to be equally a generalization of wave dynamics. However, if the absolute overall maximum wave height was used for a larger simplified location, such as Maullín, instead of the average maximum wave height, the modeled results in the AIC analysis are expected to be typically underfit. Additionally, highest wave runup can reflect amplification from small-scale local bathymetric or topographic features or wave dynamics that are not accounted for using the coarse bathymetry available.

Subfault model

The fault model had a consistent width rupture, independent of magnitude, from north to south for all simulated earthquakes. However, earthquakes are known to have variable rupture width along strike or with magnitude (Cande et al., 1987; Wang et al 2007). According to GPS data, the width of the Chilean seismogenic zone narrows to the south by ~ 1º in longitude, while retaining the same dipping angle (Wang et al., 2007). By not accounting for this narrowing and maintaining a constant width in the fault model for this research, the cosesimic slip on the southern segment within my earthquake source models may be smaller than what is realistic.

The dip values used for this fault model are derived from the USGS Slab 1.0 model; using slightly different depths and dip angles of subfaults would affect the tsunami simulations. For example, a more shallowly dipping fault model would widen the wavelength of a tsunami and result in less seafloor deformation for the same amount of slip. Vice-versa, a steeper dipping fault model would lead to shorter wavelengths and an increase in maximum wave heights in the near-field (Melnick et al., 2012). However, all tsunami simulations are exposed to the same kind of error associated with the fault model. Thus, I assume that this fault model error has a lesser impact in the overall variation of results.

Numerical modeling

The primary sources of error associated with the numerical modeling methods can be categorized into 1) bathymetry and topography or 2) mathematical approximations in GeoClaw. Errors regarding the coarseness of the 30 arc-second bathymetric resolution has been previously discussed in the *Methodology* chapter. In addition, because the 30 arc-second GEBCO bathymetry and topography focuses on the deep ocean, the quality of coverage on the shallow shelf is highly variable (Intergovernmental Oceanographic Commission, 2014). The potential lack of detailed bathymetry can cause many aspects of waveform propagation, such as wave diffraction, refraction, resonance, and shoaling, to be less accurate in shallow water regions. Because these kinds of propagation properties play a significant role in affecting overall wave heights and wave velocities (Pan et al., 2010), high resolution bathymetry (1/3 arc-second) is necessary to model coastal inundation (MacInnes et al., 2013). If more high-resolution bathymetry grids were used at different locations along the coast, inundation characteristics would be better assessed when comparing to historic tsunami events. Having higher resolution bathymetry could eliminate a greater number of earthquake source models from being a "good-fit," in the AIC analyses.

An additional bathymetric/topographic issue in this study was the lack of accounting for bathymetric/topographic changes throughout the historical record between 1570 and 1960 (except for removing a post-1960 bridge in the high-resolution topography for Tirúa). Some of these bathymetric and topographic differences that

change over time include beach progradation, estuary filling, spit-growth, and relative sea-level rise. A specific tsunami waveform that may have been able to inundate a certain area in 1570 may not be able to inundate that same area in the present because of these dynamic coastal processes. By not using historic coastlines when modeling maximum wave heights at each tide gauge, there is uncertainty regarding the accuracy of the "good-fitting" source models for historical earthquakes.

Within the category of mathematical approximations in GeoClaw, there are many complex processes that are numerically simplified when simulating a tsunami. For instance, the steps from converting slip on the fault model from seafloor deformation to sea-surface deformation and the generation of a tsunami are overgeneralized when compared to reality (Tanioka and Satake, 1996). GeoClaw converts slip to seafloor deformation with the Okada (1985) equations and approximations. These equations and approximations assume a two-dimensional flat seafloor made up of homogeneous elastic material for each subfault within the fault model, which is used to calculate only the vertical component of slip, assuming an instantaneous rupture. However, in real life examples, megathrust earthquake ruptures are three-dimensional and tend to propagate slip in all directions along the fault plane, releasing most of the energy over a 90-second period (Yamazaki, and Cheung, 2011). Seafloor deformation occurring on a steep slope with large horizontal displacement relative to vertical displacement is also an important contribution to sea-surface deformation and tsunami generation (Tanioka and Satake, 1996). The simplifications regarding the role of rise time, rupture velocity, and horizontal

motion within the GeoClaw application are an inherent source of error that affect the timing of tsunami generation, and therefore wave propagation, and maximum runup (Fuentes et al., 2018).

Validation of models (through AIC)

There are a considerable amount of uncertainties within the AIC statistical analysis in terms of selecting a "good-fitting" approximating model (Burnham and Anderson, 2003). Through the mathematical equations, by definition, one earthquake source model will automatically be considered the "best-fitting model" (with a $\Delta_i 0$) relative to the others. Despite this selection, the "best-fitting model" may not be best when evaluated in context. For example, in the 1960 analysis, a M_w 8.7 earthquake source model was chosen by the AIC analysis as "best-fitting", yet it was instrumentally recorded that the 1960 event was a M_w 9.5 event. Knowing the context of the historical rupture, such as extent of destruction and damages, should be used as a qualitative validity check. Thus, understanding the data set prior to the analysis will help identify any biases within the model selection process, like the results of the 1960 analysis. Once a biased source model is established as a "good-fitting" model, other analyses, such as the method used in this research of evaluating the root mean square error (RMSE), can help in explaining the initial selection process. Also, examining the data before the formal AIC analysis allows for the detection of obvious outliers and outright errors (Burnham and Anderson, 2003). Burnham and Anderson (2003) claim that the model selection

within AIC has a tendency to select models that are too simple (underfitted). This claim is seen in many of my results, especially the 1960 event where the M_w 8.7 earthquake source models appeared significant. To deal with this bias, one method is to examine the residuals from the modeled and observed data to potentially uncover any patterns in the candidate models during the selection process.

There are additional computer-intensive resampling methods that may improve the AIC assessment, such as the bootstrap method (a type of Monte Carlo method; Efron, 1979; Efron and Tibshirani, 1993; Mooney and Duval, 1993). A major purpose of the bootstrap method deals with robust estimation of sampling variances (standard errors) and confidence intervals in model selection applications (Burnham and Anderson, 2003). To limit model selection uncertainty, 1,000 bootstrap samples may be needed, which would consist of systematically removing different tide gauge data points to estimate confidence intervals, sampling variances (or standard errors), and potentially single out any data point outliers (Burnham and Anderson, 2003). Also ~10,000 earthquake source models for the model selection may be needed to limit selection uncertainty (Burnham and Anderson, 2003).

CHAPTER VII

SUMMARY AND CONCLUSIONS

The purpose of this research was to define a new methodology to characterize the unknown rupture parameters of known pre-instrumental earthquakes. If successful, this methodology can be implemented for all subduction zones with either a geologic and/or historical record. South-central Chile was an excellent candidate for this research because of its well documented tsunami record. Portions of south-central Chile have been inundated by destructive tsunamis from at least 17 near-field sources between 1570 and 1960. These earthquakes have been documented at localized regions within the historical record and through limited paleotsunami studies. Thus, the rupture dynamics of these pre-instrumental earthquakes are not well constrained and pose a major problem in terms of reliable forecasting. To improve tsunami forecasting in the future, it is crucial to understand how the Chilean subduction zone behaved during these 17 earthquake events.

To define the historical earthquake rupture parameters of south-central Chile, I forward modeled tsunami simulations from 423 different ruptures source models. These source models ranged from M_w 8.7 to M_w 9.5 and had stochastic slip distributions. I evaluated the validity of these tsunami simulations by comparing the maximum wave heights at 47 strategically placed tide gauges along the coast to the recorded wave heights from each tsunami event from historical record and tsunami field observations. Through this analysis, my goal was to suggest a suite of possible earthquake rupture scenarios that

may have been similar to each past event in the Chilean historical record. The following summarizes the key results and interpretations of each earthquake:

1570 earthquake

- Four "substantial fit" source models that range from M_w 8.7 to M_w 9.1 and rupture the northern segment of the fault model.
- High slip located at ~ 36°S and/or ~ 40°S (M_w 8.7 solutions had high slip only at ~ 37.5°S).
- Supports Mocha fracture zone (MFZ) segmentation; northern rupture if smaller earthquake, both southern and northern ruptures if larger earthquake.

1575 earthquake

- Two M_w 9.3 "substantial fit" source models that ruptured the deepest portion of the fault model at ~ 39°S.
- Supports MFZ segmentation; southern rupture.

1657 earthquake

- All 423 models calculate as being statistically significant, so conclusions below are not robust.
- Eleven "substantially fitting" models consisting of M_w 8.7 (one), M_w 9.3 (nine), and M_w 9.5 (one).

- Larger "substantially fitting" models (M_w 9.3 and M_w 9.5) most likely a result from a few observations of high wave heights
- Smaller "substantially fitting" source model (M_w 8.7) most likely a result of limited observations in the historical record in 1657.
- Supports MFZ segmentation; northern rupture.

1730 earthquake

- Five statistically significant M_w 9.3 (four) to M_w 9.5 (one) source models with one M_w 9.3 "substantial fit" better than the rest.
- High slip located at ~ 34°S.
- Supports MFZ segmentation; northern rupture.

1751 earthquake

- Ten "substantially fitting" models consisting of M_w 8.7 (seven), M_w 8.9 (one) and M_w 9.3 (one).
- High slip of M_w 8.7 and 8.9 at ~ 35°S and ~ 37 °S, while high slip for M_w 9.3 at ~ 40°S to ~ 43°S.
- Supports MFZ segmentation; could be northern or southern rupture.

1822 earthquake

- Four "substantial fit" source models that range from M_w 8.7 to M_w 8.9.
- High shallow slip at ~ 34°S to ~ 35°S (M_w 8.7) or high deep slip at ~ 37°S (M_w 8.9).
- Supports MFZ segmentation; northern rupture.

1835 earthquake

- Two M_w 8.7 "substantial fit" source models with high slip at ~ 36.5°S.
- RMSE analysis suggests that two "considerably less significant" M_w 9.3 solutions and one "considerably less significant" M_w 9.5 solution match mean maximum wave heights for all gauges better than the selected "substantial fit" solutions.
- The larger "considerably less significant" solutions rupture the deeper portion of the southern segment within the fault model between ~ 39°S to ~ 44°S.
- Supports MFZ segmentation; northern rupture if smaller; southern if larger.

1837 earthquake

- 15 M_w 8.7 "substantial fit" source models that ruptured on the northern segment of the fault model.
- Nine other less statistically significant source models that ruptured on the southern segment of the fault model.
- Rupture may cross MFZ segmentation or ruptures on either side of the MFZ are better fits than ruptures that cross the MFZ.

1871 earthquake

- Five M_w 8.7 "substantial fit" source models with high slip either deep or shallow at ~ 35.5 °S.
- Supports MFZ segmentation; northern rupture

1871b earthquake

- Three "substantially fitting" models, M_w 9.1 (one) and M_w 9.3 (two), in addition to some smaller statistically significant Mw 8.7 source models
- High slip at ~ 40°S or ~ 34°S for the M_w 9.3 models, 40°S and 36°S for the M_w 9.1 model, and ~ 44°S for the smaller M_w 8.7 models
- Larger "substantially fitting" models (M_w 9.3) most-likely a result from a high localized observed wave height
- M_w 8.7 are more plausible due to lack of observations in the historical record.
- Supports MFZ segmentation; northern if small, either northern or southern if larger earthquake.

1898 earthquake

- 15 statistically significant M_w 8.7 (nine) to M_w 8.9 (six) source models with one M_w 8.7 "substantial fit" better than the rest.
- High slip on the shallow portion of the fault model between ~42.5°S and ~43.5°S.
- Supports MFZ segmentation; southern rupture.

1906 earthquake

- 68 "substantially fitting" models consisting of M_w 8.7 (58) and M_w 8.9 (ten) that ruptured on the south-central segment of the fault model.
- Majority had high slip near the MFZ at ~39°S.
- Supports MFZ segmentation; southern rupture.

1920 earthquake

- Three M_w 8.7 "substantial fit" source models with high slip between ~ 40°S and ~41°S.
- Supports MFZ segmentation; southern rupture.

1927 earthquake

- All earthquake source models had approximately the same Δ_i value.
- Bathymetry was too coarse for water to inundate tide gauges at Puerto Asyen and Puerto Cisnes (located within fjords ~ 140 km from the open ocean).
- Insufficient model results.

1928 earthquake

- Four "substantially fitting" models consisting of M_w 8.7 (three rupturing on northern segment) and M_w 8.9 (one rupturing on southern segment).
- High slip in both the north and south at ~ 38°S to ~ 38.5°S and ~ 42°S, respectively.
- Rupture may cross MFZ segmentation.

1943 earthquake

- Three "substantially fitting" models consisting of M_w 8.7 (one) and M_w 8.9 (two) with high slip between ~ 40°S and ~ 41°S in the deeper portion of the fault model.
- Supports MFZ segmentation; southern rupture.

1960 earthquake

- 16 "substantially fitting" source models consisting of M_w 8.7 (14) and M_w 9.3 (two).

- High slip at ~ 39°S. M_w 9.3 solutions also had shallow high slip in the north or south at either ~ 33°S or ~ 41°S.
- RMSE analysis and high-resolution bathymetric inundation at Tirúa, Quidico, and Puerto Saavedra support that the larger M_w 9.3 solutions are better fits than the smaller M_w 8.7 solutions.
- Published slip model "Barrientos slip" derived from Barrientos and Ward (1990) was not statistically significant, however had similar location of high slip at ~39°S to 40°S (except in the deepest portion of the fault model). The slip distribution published by Moreno et al. (2009) agrees with high shallow slip at ~39°S to 40°S.
- Supports MFZ segmentation; southern rupture.

Through using the AIC statistical application, it appears that variable slip patterns play a crucial part in matching good-fitting rupture models. All earthquake statistical analyses suggest that significant source-models are derived from the models with variable slip rather than uniform slip. Often times, the uniform slip models yielded Δ_i values amongst the worst of all earthquake source model solutions. This supports the widespread understanding that earthquakes do not rupture uniformly along strike (Mikumo and Miyatake, 1978; Mai and Beroza, 2002; Moreno et al., 2010; Wang et al., 2013). Future modeling applications should not use uniform slip solutions when assessing potential rupture parameters.

Similarly, the location of high sea surface deformation in the slip distribution is also a critical parameter for model selection, rather than overall magnitude. This is seen in the 1960 statistical analysis where the AIC application showed that M_w 8.7 source models were just as significant at M_w 9.3 source models. This result is due to an uneven distribution of sampling along strike, thus signifying the importance of additional geologic studies where possible. The currently available tsunami historic record is unevenly distributed and concentrated in the major populated areas. In terms of the 1960 statistical analysis, the "good-fitting" M_w 8.7 earthquake source models appeared to match the bulk of the recorded wave heights in a specific area where there were many spatially-close observations, but underestimated the recorded maximum wave heights. This differs from the M_w 9.3 statistically significant earthquake source models that matched the maximum recorded wave height extents better, but overestimated the bulk of the recorded wave heights in the regions with a high concentration of placed tide gauges. However, the commonality between these statistically significant models of different sizes is the location of the concentration of maximum slip in each respective fault model.

The 1/3 arc-second high-resolution bathymetry was a helpful tool to further analyze some of the statistically significant source models and as an overall check of the AIC application. By having previous knowledge of the inundation dynamics that occurred at specific locations during the 1960 tsunami (e.g. Tirúa, Quidicio, and Puerto Saavedra), I was able to pinpoint a rupture along strike, specific magnitude, and slip distribution within the top Δ_i models that best match the known inundation dynamics at

these three sites. According to the models, the source model that best matched the inundation dynamics for where we had data (Tirúa, Quidico, and Puerto Saavedra) were models 40_93_7, and 39_93_7 (offset by 23 km along strike).

Using the known inundation dynamics for further model selection refinement also allowed me to hypothesize which locations have greater model selection constraints to different modeling inputs. For example, Tirúa appears to have more model selection constraints than Quidico as 16 of the top 33 Δ_i source models for the 1960 analysis correctly inundated Tirúa, while 22 source models correctly inundated Quidico. Additionally, Puerto Saavedra may have the most constrained model selectivity as 40_93_7, and 39_93_7 were the only two out of the top 33 source models for the 1960 analysis that correctly matched inundation. However, the few correct matches at Puerto Saavedra is more likely the result of the geomorphology around Puerto Saavedra limiting inundation in GeoClaw; the code does not change the bathymetry due to erosion from the tsunami. Puerto Saavedra is situated behind two spits with a narrow inlet to a bay that most likely widened during the 1960 tsunami. Therefore, favorable source models at Puerto Saavedra required high deep slip to create subsidence and artificially widen the inlet to allow for full tsunami inundation. Earthquake source models 40_93_7 and 39_93_7 both had a slip distribution pattern (relating to seafloor deformation) that caused land level change to generate enough water to inundate this coastal site.

Supplementary evaluations of validity, like inundation matching with high-resolution bathymetry, is useful in refining potential suites of best-fitting solutions,

especially when the overall bathymetry used in the tsunami simulations is too coarse to be considered useful for modeling inundation dynamics (e.g. 30 arc-second resolution). Other useful evaluations of validity include root mean square error (RMSE) analysis. RMSE evaluates the mean differences in wave heights at all tide gauges for a given earthquake source model. In almost all cases, the model with the best Δ_i value also had the lowest RMSE value.

This research provides a new methodology, which applies tsunami modeling in regions with a long historical record and paleotsunami histories, to learn about past earthquake rupture characteristics and tsunami behavior. The tsunami historical record is a valid dataset for revealing suites of most-likely earthquake parameters, such as region of high slip and potential magnitudes for these pre-instrumental earthquakes. Therefore, this methodology can be applied to better understand rupture dynamics of other subduction zones as well.

Future Research

Future studies in south-central Chile should prioritize finding new geologic tsunami evidence to allow for a more even distribution of sampling for tsunami modeling comparisons. Additionally, using far-field deposits (e.g. Japan) may also be helpful to refine the rupture characteristics of a given earthquake. For example, the far-field tsunami records may eliminate the M_w 8.7 earthquake source solutions as "good-fitting" scenarios

for the 1960 event as they probably are not large enough to displace enough water to correctly inundate Japan.

From a modeling standpoint, more models with additional stochastic slip distributions should be simulated to increase the model selection space. The validity of the AIC statistical analysis is correlative to the number of models inputted into the analysis (Burnham and Anderson, 2003) and will be improved with more models. However, assessments should not solely rely on the outputs from the AIC application. Additional methods like simulating the inundation dynamics at more locations with high-resolution bathymetry (e.g. Maullín) will be useful in assessing the validity of the AIC statistical analyses. It should likewise be prioritized to simulate smaller earthquake source models (M_w 8.7 and smaller). Assessing the slip distributions of these shorter rupture events will be required to assess some of the smaller historical earthquakes in this study with magnitude estimations less than M 8.7. By analyzing smaller source models, a greater understanding regarding the important question of segmentation at the Mocha fracture zone is also possible. Simulating more earthquake source models will ultimately allow for greater insight in relation to the spatial variability of locking zones through time and provide clues to the recurrence of locations with high slip.

REFERENCES

Akaike, H., 1974, A new look at the statistical model identification: Institute of Electrical and Electronic Engineers, Transactions on Automatic Control, Vol. 19 No. 6, p. 716-723.

Anderson, D.R., Burnham, K.P., and Thompson, W.L., 2000, Null hypothesis testing: problems, prevalence, and an alternative: Journal of Wildlife Management 64, p. 912–923.

Angermann, D., Klotz, J., & Reigber, C., 1999, Space-geodetic estimation of the Nazca-South America Euler vector: Earth and Planetary Science Letters, Vol. 171, No. 3, p. 329-334.

Atwater, B. F., 1999, Surviving a tsunami--lessons from Chile, Hawaii, and Japan (No. 1187): Geological Survey (USGS).

Atwater, B. F., Cisternas, M., Yulianto, E., Prendergast, A. L., Jankaew, K., Eipert, A. A., Starin-Fernando, W.I., Tejakusuma, I., Schiappacasse, I., & Sawai, Y., 2013, The 1960 tsunami on beach-ridge plains near Maullín, Chile: Landward descent, renewed breaches, aggraded fans, multiple predecessors: Andean Geology, Vol. 40, No. 3, p. 393-418.

Atwater, B. F., Musumi-Rokkaku, S., Satake, K., Tsuji, Y., Ueda, K., & Yamaguchi, D. K., 2016, The orphan tsunami of 1700: Japanese clues to a parent earthquake in North America: University of Washington Press, p. 144.

Barrientos, S. E., & Ward, S. N., 1990, The 1960 Chile earthquake: inversion for slip distribution from surface deformation: Geophysical Journal International, Vol. 103, No.3, p. 589-598.

Becerra, R., 2018, Assessing the use of tsunami simulations as a tool to predict source magnitudes and locations of paleoearthquakes in chile, [Master's thesis]: Central Washington University, p. 130.

Berger, M. J., & LeVeque, R. J., 1998, Adaptive mesh refinement using wave-propagation algorithms for hyperbolic systems: SIAM Journal on Numerical Analysis, Vol. 35, No. 6, p. 2298-2316.

Berger, M. J., D. L. George, R. J. LeVeque, and K. T. Mandli, 2011, The GeoClaw software for depth-averaged flows with adaptive refinement, Adv: Water Resour. Vol. 34, p. 1195-1206.

Berninghausen, W. H., 1962, Tsunamis reported from the west coast of South America 1562-1960: Bulletin of the Seismological Society of America, Vol. 52, No.4, p. 915-921.

Borrero, J.C., LeVeque R.J., Greer, S.D., O'Neill, S., and Davis, B.N., 2015, Observations and modelling of tsunami currents at the port of Tauranga, New Zealand: Australasian Coasts and Ports Conference 2015: 22nd Australasian Coastal and Engineering Conference and the 15th Australasian Port and Harbour Conference, p. 90.

Breiman, L., 2001, Statistical modeling: the two cultures (with discussion): Statistical Science, Vol. 16, p. 199–231.

Briggs, R. W., Engelhart, S. E., Nelson, A. R., Dura, T., Kemp, A. C., Haeussler, P. J., Corbett, D.R., Angster, S.J., & Bradley, L. A., 2014, Uplift and subsidence reveal a nonpersistent megathrust rupture boundary (Sitkinak Island, Alaska): Geophysical Research Letters, Vol. 41, No. 7, p. 2289-2296.

Brill, D., Brückner, H., Jankaew, K., Kelletat, D., Scheffers, A., & Scheffers, S., 2011, Potential predecessors of the 2004 Indian Ocean Tsunami—Sedimentary evidence of extreme wave events at Ban Bang Sak, SW Thailand: Sedimentary Geology, Vol. 239, No. 3-4, p. 146-161.

Burgos, R. U., 1990, La rebelión indígena de 1712: los tributarios de Chiloé contra la encomienda. Tiempo y espacio, (1), 73-86.Urbina Carrasco, M. X., 2014, El frustrado fuerte de Tenquehuén en el archipiélago de los Chonos, 1750: dimensión chilota de un conflicto hispano-británico: Historia (Santiago), Vol. 47, No. 1, p. 133-155.

Burnham, K. P., & Anderson, D. R., 2002, Model selection and multimodel inference - 2nd ed.: A practical information-theoretic approach: New York, NY, Springer-verlag New York pp. 488.

Campos-Harriet, F., 1989, Historia de Concepción 1550-1988: Editorial Universitaria, Santiago, pp. 438.

Cande, S. C., Leslie, R. B., Parra, J. C., & Hobart, M., 1987, Interaction between the Chile Ridge and Chile Trench: geophysical and geothermal evidence: Journal of Geophysical Research: Solid Earth, Vol. 92, No. B1, p. 495-520.

Carvajal, M., Cisternas, M., & Catalán, P. A., 2017, Source of the 1730 Chilean earthquake from historical records: Implications for the future tsunami hazard on the coast of Metropolitan Chile: Journal of Geophysical Research: Solid Earth, Vol. 122, No.5, p. 3648-3660.

Cisternas, M., Atwater, B.F., Torrejón, F., Sawai, Y., Machuca, G., Lagos, M., Eipert, A., Youlton, C., Salgado, I., Kamataki, T., Shishikura, M., Rajendran, C.P., Malik, J.K., Rizal, Y., and Husni, M., 2005, Predecessors of the giant 1960 Chile earthquake: Nature, Vol. 437, p. 404–407.

Cisternas, M., Torrejón, F., & Gorigoitía, N., 2012, Amending and complicating Chile's seismic catalog with the Santiago earthquake of 7 August 1580: Journal of South American Earth Sciences, Vol. 33, No. 1, p. 102-109.

Cisternas, M., Garrett, E., Wesson, R., Dura, T., & Ely, L. L., 2017, Unusual geologic evidence of coeval seismic shaking and tsunamis shows variability in earthquake size and recurrence in the area of the giant 1960 Chile earthquake: Marine Geology, Vol. 385, p. 101-113.

Clawpack Development Team, 2017, Clawpack Version 5.4.1: http://www.clawpack.org (assessed 2018), doi:10.5281/zenodo.262111.

Collier, S., & Sater, W. F., 1996, A history of Chile, 1808-1994: Cambridge Latin American Studies, Vol. 82, Cambridge, New York, University Press.

Comte, D., & Suárez, G., 1994, An inverted double seismic zone in Chile: Evidence of phase transformation in the subducted slab: Science, Vol. 263 No. 5144, p. 212-215.

Contreras-Reyes, E., Grevemeyer, I., Flueh, E. R., & Reichert, C., 2008, Upper lithospheric structure of the subduction zone offshore of southern Arauco peninsula, Chile, at~ 38 S: Journal of Geophysical Research: Solid Earth, Vol. 113, No. B07303.

Contreras-Reyes, E., & Carrizo, D., 2011, Control of high oceanic features and subduction channel on earthquake ruptures along the Chile–Peru subduction zone: Physics of the Earth and Planetary Interiors, Vol. 186, No. 1-2, p. 49-58.

Davidson, C. 1936. Great Earthquakes: T. Hurby and Co.: Myrby, London pp. 286.

Di Giacomo, D., I. Bondár, D.A. Storchak, E.R. Engdahl, P. Bormann and J. Harris, 2015a, ISC-GEM: Global Instrumental Earthquake Catalogue (1900-2009): III. Re-computed MS and mb, proxy MW, final magnitude composition and completeness assessment: Phys. Earth Planet. Int., Vol. 239, p. 33-47.

Di Giacomo, D., E.R. Engdahl and D.A. Storchak, 2018, The ISC-GEM Earthquake Catalogue (1904–2014): status after the Extension Project: Earth System Science Data, Vol. 10, p. 1877-1899.

Dura, T., Horton, B. P., Cisternas, M., Ely, L. L., Hong, I., Nelson, A. R., Wesson, R.L., Pilarczyk, J.E., Parnell, A.C., & Nikitina, D., 2017, Subduction zone slip variability during the last millennium, south-central Chile: Quaternary Science Reviews, Vol. 175, p. 112-137.

Efron, B., 1979, Computers and the theory of statistics: thinking the unthinkable: Society for Industrial and Applied Mathematics review, Vol. 21, No. 4, p. 460-480.

Efron, B. and Tibshirani, R.J., 1993, An Introduction to the Bootstrap: Monographs on Statistics and Applied Probability, Vol. 57, Chapman & Hall, New York, New York, pp. 456.

Ely, L. L., Cisternas, M., Wesson, R. L., & Dura, T., 2014, Five centuries of tsunamis and land-level changes in the overlapping rupture area of the 1960 and 2010 Chilean earthquakes: Geology, Vol. 42, No. 11, p. 995-998.

FitzRoy, R., 1839, Narrative of the Surveying Voyages of His Majesty's Ships Adventure and Beagle, between the Years 1826 and 1836: Describing Their Examination of the Southern Shores of South America, and the Beagle's Circumnavigation of the Globe, Vol. 2: Proceedings of the Second Expedition, 1831-1836, under the Command of Captain Robert FitzRoy, R.N., with Appendix, London: Henry Colbum, Great Marlborough Street, pp. 693.

Fritz, H.M., Petroff, C.M., Catalán, P.A., Cienfuegos, R., Winckler, P., Kalligeris, N., Weiss, R., Barrientos, S.E., Meneses, G., Valderas-Bermejo, C., Ebeling, C., Papadopoulos, A., Contreras, M., Almar, R., Dominguez, J.C., and Synolakis, C.E., 2011, Field Survey of the 27 February 2010 Chile Tsunami: Pure and Applied Geophysics, Vol. 168, p. 1989-2010.

Fuentes, M., Riquelme, S., Ruiz, J., & Campos, J., 2018, Implications on 1+ 1 D Tsunami runup modeling due to time features of the earthquake source: Pure and Applied Geophysics, Vol. 175, No.4, p. 1393-1404.

Fujiwara, O., Masuda, F., Sakai, T., Irizuki, T., Fuse, K., Daiyoni, K., 1999, Holocene tsunami deposits detected by drilling in drowned valleys of Boso and Miura peninsulas: Quaternary Research, Vol. 38, p. 41-58.

Garrett, E., Shennan, I., Woodroffe, S. A., Cisternas, M., Hocking, E. P., & Gulliver, P., 2015, Reconstructing paleoseismic deformation, 2: 1000 years of great earthquakes at Chucalén, south central Chile: Quaternary Science Reviews, Vol. 113, p. 112-122.

Geist, E.L., 2002, Complex earthquake rupture and local tsunamis: Journal of Geophysical Research, Vol. 107, p. 1-6.

George, D. L., & LeVeque, R. J., 2006, Finite volume methods and adaptive refinement for global tsunami propagation and local inundation. Science of Tsunami Hazards, Vol. 24, No.5, p. 319–328, 2006.

Gonzalez, F., R. J. LeVeque, P. Chamberlain, B. Hirai, J. Varkovitzky, and D.L. George, 2011, GeoClaw Results for the NTHMP Tsunami Benchmark Problems, [NTHMP] National Tsunami Hazard Mitigation Program: Proceedings and Results of the 2011 NTHMP Model Benchmarking Workshop, Boulder: U.S. Department of Commerce/NOAA/NTHMP (NOAA Special Report), pp. 436.

Guarda, G, 1978, Historia urbana del Reino de Chile: Editorial Andrés Bello, Santiago, Chile, pp. 509.

Gusiakov, V. K., 2007, Tsunami as a destructive aftermath of oceanic impacts: In Comet/asteroid impacts and human society, Springer, Berlin, Heidelberg, p. 247-263.

Gusman, A. R., Tanioka, Y., MacInnes, B. T., & Tsushima, H., 2014, A methodology for near-field tsunami inundation forecasting: Application to the 2011 Tohoku tsunami: Journal of Geophysical Research: Solid Earth, Vol. 119, No. 11, p. 8186-8206.

Haberland, C., Rietbrock, A., Lange, D., Bataille, K., & Dahm, T., 2009, Structure of the seismogenic zone of the southcentral Chilean margin revealed by local earthquake traveltime tomography: Journal of Geophysical Research: Solid Earth, Vol. 114, No. B01317.

Hayes, G. P., Wald, D. J., & Johnson, R. L., 2012, Slab1.0: A three-dimensional model of global subduction zone geometries: Journal of Geophysical Research: Solid Earth, Vol. 117, No. B01302.

Hirata, K., Geist, E., Satake, K., Tanioka, Y., & Yamaki, S., 2003, Slip distribution of the 1952 Tokachi-Oki earthquake (M 8.1) along the Kuril trench deduced from tsunami waveform inversion: Journal of Geophysical Research: Solid Earth, Vol. 108, No. 101029/2002JB001976.

Hong, I., Dura, T., Ely, L. L., Horton, B. P., Nelson, A. R., Cisternas, M., Nikitina, D., & Wesson, R. L., 2017, A 600-year-long stratigraphic record of tsunamis in south-central Chile: The Holocene, Vol. 27, No. 1, p. 39-51.

Iida, K., Cox, D. C., & Pararas-Carayannis, G., 1967, Preliminary catalog of tsunamis occurring in the Pacific Ocean: Data Repository, Vol 5, No. HIG-67-10, Hawaii Institute of Geophysics, University of Hawaii, Honolulu, pp. 131.

Iida, K., 1984, Catalog of tsunamis in Japan and its neighboring countries: Department of Civil Engineering, Aichi Institute of Technology, Special Report, Japan pp. 52.

Instituto Hidrográfico de la Armada, 1982, Atlas Hidrográfico de Chile: Derrotero de la Costa de Chile Volumen III, El Instituto, Mapoteca/SHOA, Valparaiso, Chile.

Intergovernmental Oceanographic Commission, 2014, The GEBCO_2014 Grid: International Hydrographic Organization and Intergovernmental Oceanic Commission of UNESCO, [Accessed: 2014].

Jara-Munoz, J., Melnick, D., Brill, D., & Strecker, M. R., 2015, Segmentation of the 2010 Maule Chile earthquake rupture from a joint analysis of uplifted marine terraces and seismic-cycle deformation patterns: Quaternary Science Reviews, Vol. 113, p. 171-192.

Kanamori, H, 1972, Mechanism of tsunami earthquakes: Physics of the earth and planetary interiors, Vol. 6, No. 5, p. 346-359.

Kanamori, H., 1977, The energy release in great earthquakes: Journal of geophysical research, Vol. 82, No. 20, p. 2981-2987.

Kanamori, H., & Kikuchi, M, 1993, The 1992 Nicaragua earthquake: a slow tsunami earthquake associated with subducted sediments: Nature, Vol. 361, No. 6414, p. 714.

Kempf, P., Moernaut, J., Van Daele, M., Vandoorne, W., Pino, M., Urrutia, R., & De Batist, M., 2017, Coastal lake sediments reveal 5500 years of tsunami history in south central Chile: Quaternary Science Reviews, Vol. 161, p. 99-116.

Kullback, S., 1959, Information theory and statistics: John Wiley and Sons, New York, New York.

Lagos, M., 2000, Near-source-generated tsunamis at the coasts of Chile (Tsunamis de origen cercano a las costas de Chile), Revista de Geografia Norte Grande, Vol. 27, p. 93-102.

Lander, J. F., & Lockridge, P. A., 1989, United States Tsunamis (including United States Possessions): *1690-1988*: US Department of Commerce, National Oceanic and Atmospheric Administration, National Environmental Satellite, Data, and Information Service, National Geophysical Data Center, Vol 41, No. 2, Boulder, Colorado.

Lane, K. E., & Levine, R. M., 2015, Pillaging the Empire: Piracy in the Americas, 1500-1750: Routledge, p. 88-92.

Leonard, L. J., Currie, C. A., Mazzotti, S., & Hyndman, R. D., 2010, Rupture area and displacement of past Cascadia great earthquakes from coastal coseismic subsidence: Bulletin, Vol. 122, No. 11-12, p. 2079-2096.

LeVeque, R. J., 2002, Finite volume methods for hyperbolic problems, Vol. 31, Cambridge university press, pp 558.

LeVeque, R. J., George, D. L., & Berger, M. J., 2011, Tsunami modelling with adaptively refined finite volume methods: Acta Numerica, Vol. 20, p. 211-289.

Lockridge, P. A., 1985, Tsunamis in Peru-Chile, Report SE-39: World Data Center for Solid Earth Geophysics, Boulder, CO, pp. 97.

Lomnitz, C., 2004, Major earthquakes of Chile: a historical survey, 1535-1960: Seismological Research Letters, Vol. 75, No., 3, 368-378.

MacInnes, B. T., Weiss, R., Bourgeois, J., & Pinegina, T. K., 2010, Slip distribution of the 1952 Kamchatka great earthquake based on near-field tsunami deposits and historical records: Bulletin of the Seismological Society of America, Vol. 100, No. 4, p. 1695-1709.

MacInnes, B. T., Gusman, A. R., LeVeque, R. J., & Tanioka, Y., 2013, Comparison of earthquake source models for the 2011 Tohoku event using tsunami simulations and near-field observations: Bulletin of the Seismological Society of America, Vol. 103, No. 2B, p. 1256-1274.

Mai, P. M., & Beroza, G. C., 2002, A spatial random field model to characterize complexity in earthquake slip: Journal of Geophysical Research: Solid Earth, Vol. 107, No. B11, 2308, ESE-10, p. 1-27.

Matos-Llavona, P., Ely L.L., MacInnes, B., Dura, T., Cisternas, M., Tang, H., Dolcimascolo, A., Bruce, D., 2019, Mapping and reconstructing the paleostunami record in a new site in Queule, South-central Chile, Geological Society of America Abstracts with Programs. Vol. 41, No. 4, p. 28.

Melnick, D., Bookhagen, B., Strecker, M. R., & Echtler, H. P., 2009, Segmentation of megathrust rupture zones from fore-arc deformation patterns over hundreds to millions of years, Arauco peninsula, Chile: Journal of Geophysical Research: Solid Earth, Vol. 114, No. B01407.

Melnick, D., Moreno, M., Motagh, M., Cisternas, M., & Wesson, R. L., 2012, Splay fault slip during the Mw 8.8 2010 Maule Chile earthquake: Geology, Vol 40, No.3, p. 251-254.

Mikumo, T., & Miyatake, T., 1978, Dynamical rupture process on a three-dimensional fault with non-uniform frictions and near-field seismic waves: Geophysical Journal International, Vol. 54, No. 2, p. 417-438.

Milne, J., 1900a, Discussion of the preceding registers, Seismological investigations: Fourth report CSI, p. 161-238: Report 69th Meeting. British Association for the Advancement of Science, held at Dover in 1899, p. 203.

Milne, J., 1911. Catalogue of destructive earthquakes: Report of the 81st meeting of the British Association for the Advancement of Science, Portsmouth, London, United Kingdom, p. 649–740.

Monge, J., 1993, Estudios de riesgo de tsunami en costas chilenas: Santiago, Chile. Jornadas chilenas de Sismología en ingeniería antisísmica, Vol. 2, p. 3-22.

Mooney, C. Z., Duval, R. D., & Duvall, R., 1993, Bootstrapping: A nonparametric approach to statistical inference: Sage Publications, No. 95, Newbury Park, California.

Moreno, M. S., Bolte, J., Klotz, J., & Melnick, D., 2009, Impact of megathrust geometry on inversion of coseismic slip from geodetic data: Application to the 1960 Chile earthquake: Geophysical Research Letters, Vol. 36, No. L16310, doi: 10.1029/2009GL039276.

Moreno, M., Rosenau, M., & Oncken, O., 2010, 2010 Maule earthquake slip correlates with pre-seismic locking of Andean subduction zone: Nature, Vol. 467, No. 7312, p. 198.

Morton, R. A., Gelfenbaum, G., & Jaffe, B. E., 2007, Physical criteria for distinguishing sandy tsunami and storm deposits using modern examples: Sedimentary Geology, Vol. 200, No. 3-4, p. 184-207.

Nanayama, F., Satake, K., Furukawa, R., Shimokawa, K., Atwater, B. F., Shigeno, K., & Yamaki, S., 2003, Unusually large earthquakes inferred from tsunami deposits along the Kuril trench: Nature, Vol. 424, No. 6949, p. 660.

National Geophysical Data Center / World Data Service (NGDC/WDS), 2018, Global Historical Tsunami Database: National Geophysical Data Center, NOAA, doi:10.7289/V5PN93H7 [Accessed: 2018].

Nelson, A. R., Briggs, R. W., Dura, T., Engelhart, S. E., Gelfenbaum, G., Bradley, L. A., Forman, S.L., Vane, C.H., & Kelley, K. A., 2015, Tsunami recurrence in the eastern Alaska-Aleutian arc: A Holocene stratigraphic record from Chirikof Island, Alaska: Geosphere, Vol. 11, No. 4, p. 1172-1203.

Okada, Y., 1985, Surface deformation due to shear and tensile faults in a half-space: Bulletin of the seismological society of America, Vol. 75, No. 4, p. 1135-1154.

Okal, E. A., 2009, Excitation of tsunamis by earthquakes, in The Sea: Tsunamis E. N. Bernard and A. R. Robinson (Editors), Harvard University Press, Cambridge, Massachusetts, Vol. 15, p. 137–177.

Pan, W., Wang, S. A., & Cai, S., 2010, Numerical simulations of the coastal effects of tsunami waves caused by the 1993 Hokkaido-Nansei-Oki earthquake: Chinese Journal of Oceanology and Limnology, Vol. 28, No. 5, p. 1029-1039.

Papadopoulos, G. A., & Kortekaas, S., 2003, Characteristics of landslide generated tsunamis from observational data: In Submarine Mass Movements and Their Consequences, Springer, Dordrecht. p. 367-374.

Peterson, C.D., Carver, G.A., Cruikshank, K.M., Abramson, H.F., Garrison-Laney, C.E., Dengler, L.A., 2011, Evaluation of the use of paleotsunami deposits to reconstruct inundation distance and runup heights associated with prehistoric inundation events, Crescent City, southern Cascadia margin: Earth Surface Processes and Landforms, Vol. 36, p. 967-980.

Pinegina, T. K., & Bourgeois, J., 2001, Historical and paleo-tsunami deposits on Kamchatka, Russia: long-term chronologies and long-distance correlations: Natural Hazards and Earth System Sciences, Vol. 1, No. 4, p. 177-185.

Rodríguez, J. A. S., 2006, La defensa hispana del Reino de Chile: Tiempo y espacio, No. 16. SSN 0716-9671.

Saint-Amand, P., 1963, Special issue: Oceanographic, geologic, and engineering studies of the Chilean earthquakes of May 1960: Seismological Society of America Bulletin, Vol. 53, No. 6, Special issue, p. 1123-1436.

Satake, K., Wang, K., & Atwater, B. F., 2003, Fault slip and seismic moment of the 1700 Cascadia earthquake inferred from Japanese tsunami descriptions: Journal of Geophysical Research: Solid Earth, Vol. 108, No. 2545.

Satake, K., & Atwater, B. F., 2007, Long-term perspectives on giant earthquakes and tsunamis at subduction zones: Annual. Reviews of Earth and Planetary Sciences, Vol. 35, p. 349-374.

Satake, K., F. Nanayama, and S. Yamaki, 2008, Fault models of unusual tsunamis in the 17th century: Earth Planets Space, Vol. 60, p. 925–935.

Saavedra Villegas, R, 1984, Panorama histórico de Tomé. Siglos XVI a XIX: Antecedentes geográficos y miscelánea communal: Ediciones Perpelén, pp. 69.

Scheffers, A., Kelletat, D., Vött, A., May, S. M., & Scheffers, S., 2008, Late Holocene tsunami traces on the western and southern coastlines of the Peloponnesus (Greece): Earth and Planetary Science Letters, Vol. 269, No. 1-2, p. 271-279.

Sievers, H., Villegas, G., & Barros, G, 1963, The seismic sea wave of 22 May 1960 along the Chilean Coast: Seismological Society of America, Bulletin, Vol. 53, p. 1125-1190.

Soloviev, S. L., and Go, C. N., 1975, A Catalogue of Tsunamis on the Eastern Shore of the Pacific Ocean [Dates Include 1513–1968]. Moscow: Academy of Sciences of the USSR, Nauka Publishing House, pp. 204. (Canadian Translation of Fisheries and Aquatic Sciences No. 5078, 1984).

Tang, L., Titov, V.V., and Chamberlin, C.D., 2009, Development, testing, and applications of site-specific tsunami inundation models for real-time forecasting: Journal of Geophysical Research, Vol. 114, p. 1-22.

Tanioka, Y., & Satake, K., 1996, Tsunami generation by horizontal displacement of ocean bottom: Geophysical Research Letters, Vol. 23, No. 8, p. 861-864.

Udías, A., Madariaga, R., Buforn, E., Muñoz, D., & Ros, M., 2012, The large Chilean historical earthquakes of 1647, 1657, 1730, and 1751 from contemporary documents: Bulletin of the Seismological Society of America, Vol. 102, No. 4, p. 1639-1653.

Urbina Carrasco, M.X., 2014, El frustrado fuerte de Tenquehuén en el archipiélago de los Chonos, 1750: dimensión chilota de un conflicto hispano-británico. Historia (Santiago), Vol. 47, No. 1, p. 133-155.

Urbina Carrasco, M. X., Abbott, N. G., & Vega, M. C., 2016, Aportes a la historia sísmica de Chile: el caso del gran terremoto de 1730: Anuario de Estudios Americanos, Vol. 73, No. 2, p. 657-687.

Valenzuela, J., 2012, Relaciones jesuitas del terremoto de 1730: Santiago, Valparaíso y Concepción: Cuadernos de Historia, Vol. 37, Santiago, p. 195–224.

Van Dorn, W. G., 1987, Tide gage response to tsunamis. Part II: Other oceans and smaller seas: Journal of physical oceanography, Vol. 17, No. 9, p. 1507-1516.

Villanueva, A. S., Sánchez, J. B., & Rubio, C. Q., 2010, Flandes Indiano Chiloense: un patrimonio invencible en el tiempo: Revista de Urbanismo, No. 23, pp. 27.

Wang, K., Hu, Y., Bevis, M., Kendrick, E., Smalley Jr, R., Vargas, R. B., & Lauría, E., 2007, Crustal motion in the zone of the 1960 Chile earthquake: Detangling earthquake-cycle deformation and forearc-sliver translation: Geochemistry, Geophysics, Geosystems, Vol. 8, No. 10.

Weischet, W., 1963, Further observations of geologic and geomorphic changes resulting from the catastrophic earthquake of May 1960, in Chile: Bulletin of the Seismological Society of America, Vol. 53, No. 6, p. 1237-1257.

Yamazaki, Y., Cheung, K. F., & Kowalik, Z., 2011, Depth-integrated, non-hydrostatic model with grid nesting for tsunami generation, propagation, and run-up: International Journal for Numerical Methods in Fluids, Vol. 67, No. 12, p. 2081-2107

APPENDICES

APPENDIX A

Fault model

Table A1: Fault model template used to create earthquake source models. Row 1 at depth A corresponds to the southwest corner of the fault model. Stochastic variable slip distributions were inputted into the "slip" column to generate each individual source model.

Row	Depth	Longitude (°S)	Latitude (°W)	Depth 2	Dip	Strike	Rake	Length	Width	Slip
1	A	75.35808	46.28350	6.00	6	4.68	90	23	23	
1	B	75.05473	46.25957	8.40	10	4.68	90	23	23	
1	C	74.75450	46.24952	12.40	14	4.68	90	23	23	
1	D	74.45740	46.25334	17.96	18	4.68	90	23	23	
1	E	74.15421	46.22942	25.07	22	4.68	90	23	23	
2	A	75.32980	46.06232	6.00	6	4.68	90	23	23	
2	B	75.03371	46.06614	8.40	10	4.68	90	23	23	
2	C	74.73154	46.04221	12.40	14	4.68	90	23	23	
2	D	74.43555	46.04603	17.96	18	4.68	90	23	23	
2	E	74.13655	46.03598	25.07	22	4.68	90	23	23	
3	A	75.30775	45.86888	6.00	6	4.68	90	23	23	
3	B	75.00665	45.84495	8.40	10	4.68	90	23	23	
3	C	74.70866	45.83490	12.40	14	4.68	90	23	23	
3	D	74.41377	45.83872	17.96	18	4.68	90	23	23	
3	E	74.11588	45.82867	25.07	22	4.68	90	23	23	
4	A	75.28273	45.66157	6.00	6	4.68	90	23	23	
4	B	74.98579	45.65152	8.40	10	4.68	90	23	23	
4	C	74.68585	45.62759	12.40	14	4.68	90	23	23	
4	D	74.39205	45.63141	17.96	18	4.68	90	23	23	
4	E	74.09526	45.62136	25.07	22	4.68	90	23	23	
5	A	75.25781	45.45426	6.00	6	4.68	90	23	23	
5	B	74.95893	45.43033	8.40	10	4.68	90	23	23	
5	C	74.66615	45.43416	12.40	14	4.68	90	23	23	
5	D	74.36736	45.41023	17.96	18	4.68	90	23	23	
5	E	74.07469	45.41405	25.07	22	4.68	90	23	23	
6	A	75.23299	45.24695	6.00	6	4.68	90	23	23	
6	B	74.93519	45.22302	8.40	10	4.68	90	23	23	

Row	Depth	Longitude (°S)	Latitude (°W)	Depth 2	Dip	Strike	Rake	Length	Width	Slip
6	C	74.64348	45.22685	12.40	14	4.68	90	23	23	
6	D	74.34880	45.21679	17.96	18	4.68	90	23	23	
6	E	74.05417	45.20674	25.07	22	4.68	90	23	23	
7	A	75.20827	45.03964	6.00	6	4.68	90	23	23	
7	B	74.91455	45.02959	8.40	10	4.68	90	23	23	
7	C	74.61788	45.00566	12.40	14	4.68	90	23	23	
7	D	74.32726	45.00948	17.96	18	4.68	90	23	23	
7	E	74.03370	44.99943	25.07	22	4.68	90	23	23	
8	A	75.18364	44.83233	6.00	6	4.68	90	23	23	
8	B	74.89097	44.82228	8.40	10	4.68	90	23	23	
8	C	74.59836	44.81223	12.40	14	4.68	90	23	23	
8	D	74.30579	44.80217	17.96	18	4.68	90	23	23	
8	E	74.01028	44.77825	25.07	22	4.68	90	23	23	
9	A	75.15910	44.62502	6.00	6	4.68	90	23	23	
9	B	74.86450	44.60109	8.40	10	4.68	90	23	23	
9	C	74.57590	44.60492	12.40	14	4.68	90	23	23	
9	D	74.28438	44.59486	17.96	18	4.68	90	23	23	
9	E	73.98992	44.57094	25.07	22	4.68	90	23	23	
10	A	75.13466	44.41771	6.00	6	4.68	90	23	23	
10	B	74.84407	44.40766	8.40	10	4.68	90	23	23	
10	C	74.55352	44.39761	12.40	14	4.68	90	23	23	
10	D	74.26005	44.37368	17.96	18	4.68	90	23	23	
10	E	73.97258	44.37750	25.07	22	4.68	90	23	23	
11	A	75.10735	44.19653	6.00	6	4.68	90	23	23	
11	B	74.82074	44.20035	8.40	10	4.68	90	23	23	
11	C	74.53121	44.19030	12.40	14	4.68	90	23	23	
11	D	74.23877	44.16637	17.96	18	4.68	90	23	23	
11	E	73.95230	44.17019	25.07	22	4.68	90	23	23	
12	A	75.08605	44.00309	6.00	6	4.68	90	23	23	
12	B	74.79748	43.99304	8.40	10	4.68	90	23	23	
12	C	74.50896	43.98299	12.40	14	4.68	90	23	23	
12	D	74.21754	43.95906	17.96	18	4.68	90	23	23	
12	E	73.93207	43.96288	25.07	22	4.68	90	23	23	
13	A	75.05894	43.78191	6.00	6	4.68	90	23	23	
13	B	74.77431	43.78573	8.40	10	4.68	90	23	23	
13	C	74.48385	43.76180	12.40	14	4.68	90	23	23	

Row	Depth	Longitude (°S)	Latitude (°W)	Depth 2	Dip	Strike	Rake	Length	Width	Slip
13	D	74.19931	43.76562	17.96	18	4.68	90	23	23	
13	E	75.03487	43.57460	25.07	22	4.68	90	23	23	
14	A	74.75122	43.57842	6.00	6	4.68	90	23	23	
14	B	74.46468	43.56837	8.40	10	4.68	90	23	23	
14	C	74.17819	43.55831	12.40	14	4.68	90	23	23	
14	D	73.90895	43.74170	17.96	18	4.68	90	23	23	
14	E	73.89175	43.54826	25.07	22	4.68	90	23	23	
15	A	75.01381	43.38116	6.00	6	4.68	90	23	23	
15	B	74.44264	43.36106	8.40	10	4.68	90	23	23	
15	C	74.72528	43.35723	12.40	14	4.68	90	23	23	
15	D	74.15713	43.35100	17.96	18	4.68	90	23	23	
15	E	73.87166	43.34095	25.07	22	4.68	90	23	23	
16	A	74.98991	43.17385	6.00	6	4.68	90	23	23	
16	B	74.70527	43.16380	8.40	10	4.68	90	23	23	
16	C	74.42067	43.15375	12.40	14	4.68	90	23	23	
16	D	74.13612	43.14369	17.96	18	4.68	90	23	23	
16	E	73.85162	43.13364	25.07	22	4.68	90	23	23	
17	A	74.96609	42.96654	6.00	6	4.68	90	23	23	
17	B	74.39876	42.94644	8.40	10	4.68	90	23	23	
17	C	74.67950	42.94261	12.40	14	4.68	90	23	23	
17	D	74.11517	42.93638	17.96	18	4.68	90	23	23	
17	E	73.82872	42.91246	25.07	22	4.68	90	23	23	
18	A	74.94236	42.75923	6.00	6	4.68	90	23	23	
18	B	74.65962	42.74918	8.40	10	4.68	90	23	23	
18	C	74.37692	42.73913	12.40	14	4.68	90	23	23	
18	D	74.09427	42.72907	17.96	18	4.68	90	23	23	
18	E	73.81167	42.71902	25.07	22	4.68	90	23	23	
19	A	74.91871	42.55192	6.00	6	4.68	90	23	23	
19	B	74.35514	42.53182	8.40	10	4.68	90	23	23	
19	C	74.63402	42.52799	12.40	14	4.68	90	23	23	
19	D	74.07343	42.52176	17.96	18	4.68	90	23	23	
19	E	73.78888	42.49784	25.07	22	4.68	90	23	23	
20	A	74.61427	42.33456	6.00	6	4.68	90	23	23	
20	B	74.89227	42.33074	8.40	10	4.68	90	23	23	
20	C	74.33343	42.32451	12.40	14	4.68	90	23	23	
20	D	74.05264	42.31445	17.96	18	4.68	90	23	23	

Row	Depth	Longitude (°S)	Latitude (°W)	Depth 2	Dip	Strike	Rake	Length	Width	Slip
20	E	73.77190	42.30440	25.07	22	4.68	90	23	23	
21	A	74.87166	42.13730	6.00	6	4.68	90	23	23	
21	B	74.31178	42.11720	8.40	10	4.68	90	23	23	
21	C	74.58884	42.11337	12.40	14	4.68	90	23	23	
21	D	74.03191	42.10714	17.96	18	4.68	90	23	23	
21	E	73.75208	42.09709	25.07	22	4.68	90	23	23	
22	A	74.56920	41.91994	6.00	6	4.68	90	23	23	
22	B	74.84541	41.91612	8.40	10	4.68	90	23	23	
22	C	74.29019	41.90989	12.40	14	4.68	90	23	23	
22	D	74.01122	41.89983	17.96	18	4.68	90	23	23	
22	E	73.73230	41.88978	25.07	22	4.68	90	23	23	
23	A	74.82494	41.72268	6.00	6	4.68	90	23	23	
23	B	74.26867	41.70258	8.40	10	4.68	90	23	23	
23	C	74.54394	41.69875	12.40	14	4.68	90	23	23	
23	D	73.99059	41.69252	17.96	18	4.68	90	23	23	
23	E	73.71256	41.68247	25.07	22	4.68	90	23	23	
24	A	74.80170	41.51537	6.00	6	4.68	90	23	23	
24	B	74.52443	41.50532	8.40	10	4.68	90	23	23	
24	C	74.24720	41.49527	12.40	14	4.68	90	23	23	
24	D	73.97002	41.48521	17.96	18	4.68	90	23	23	
24	E	73.69287	41.47516	25.07	22	4.68	90	23	23	
25	A	74.77854	41.30806	6.00	6	4.68	90	23	23	
25	B	74.50215	41.29801	8.40	10	4.68	90	23	23	
25	C	74.22580	41.28796	12.40	14	4.68	90	23	23	
25	D	73.94949	41.27790	17.96	18	4.68	90	23	23	
25	E	73.67322	41.26785	25.07	22	4.68	90	23	23	
26	A	74.75546	41.10075	6.00	6	4.68	90	23	23	
26	B	74.47993	41.09070	8.40	10	4.68	90	23	23	
26	C	74.20445	41.08065	12.40	14	4.68	90	23	23	
26	D	73.92901	41.07059	17.96	18	4.68	90	23	23	
26	E	73.65362	41.06054	25.07	22	4.68	90	23	23	
27	A	74.73245	40.89344	6.00	6	4.68	90	23	23	
27	B	74.45779	40.88339	8.40	10	4.68	90	23	23	
27	C	74.18317	40.87334	12.40	14	4.68	90	23	23	
27	D	73.90859	40.86328	17.96	18	4.68	90	23	23	
27	E	73.63405	40.85323	25.07	22	4.68	90	23	23	

Row	Depth	Longitude (°S)	Latitude (°W)	Depth 2	Dip	Strike	Rake	Length	Width	Slip
28	A	74.70952	40.68613	6.00	6	4.68	90	23	23	
28	B	74.43571	40.67608	8.40	10	4.68	90	23	23	
28	C	74.16194	40.66603	12.40	14	4.68	90	23	23	
28	D	73.88821	40.65597	17.96	18	4.68	90	23	23	
28	E	73.61453	40.64592	25.07	22	4.68	90	23	23	
29	A	74.68667	40.47882	6.00	6	4.68	90	23	23	
29	B	74.41370	40.46877	8.40	10	4.68	90	23	23	
29	C	74.14078	40.45872	12.40	14	4.68	90	23	23	
29	D	73.86789	40.44866	17.96	18	4.68	90	23	23	
29	E	73.59504	40.43861	25.07	22	4.68	90	23	23	
30	A	74.66390	40.27151	6.00	6	4.68	90	23	23	
30	B	74.39176	40.26146	8.40	10	4.68	90	23	23	
30	C	74.11967	40.25141	12.40	14	4.68	90	23	23	
30	D	73.84761	40.24135	17.96	18	4.68	90	23	23	
30	E	73.57560	40.23130	25.07	22	4.68	90	23	23	
31	A	74.64119	40.06420	6.00	6	4.68	90	23	23	
31	B	74.36988	40.05415	8.40	10	4.68	90	23	23	
31	C	74.09861	40.04410	12.40	14	4.68	90	23	23	
31	D	73.82738	40.03404	17.96	18	4.68	90	23	23	
31	E	73.55619	40.02399	25.07	22	4.68	90	23	23	
32	A	74.61856	39.85689	6.00	6	4.68	90	23	23	
32	B	74.34807	39.84684	8.40	10	4.68	90	23	23	
32	C	74.07762	39.83679	12.40	14	4.68	90	23	23	
32	D	73.80720	39.82673	17.96	18	4.68	90	23	23	
32	E	73.53683	39.81668	25.07	22	4.68	90	23	23	
33	A	74.59601	39.64958	6.00	6	4.68	90	23	23	
33	B	74.32632	39.63953	8.40	10	4.68	90	23	23	
33	C	74.05668	39.62948	12.40	14	4.68	90	23	23	
33	D	73.78707	39.61942	17.96	18	4.68	90	23	23	
33	E	73.51750	39.60937	25.07	22	4.68	90	23	23	
34	A	74.57352	39.44227	6.00	6	4.68	90	23	23	
34	B	74.30464	39.43222	8.40	10	4.68	90	23	23	
34	C	74.03579	39.42217	12.40	14	4.68	90	23	23	
34	D	73.76698	39.41211	17.96	18	4.68	90	23	23	
34	E	73.49821	39.40206	25.07	22	4.68	90	23	23	
35	A	74.55111	39.23496	6.00	6	4.68	90	23	23	

Row	Depth	Longitude (°S)	Latitude (°W)	Depth 2	Dip	Strike	Rake	Length	Width	Slip
35	B	74.28301	39.22491	8.40	10	4.68	90	23	23	
35	C	74.01496	39.21486	12.40	14	4.68	90	23	23	
35	D	73.74694	39.20480	17.96	18	4.68	90	23	23	
35	E	73.47896	39.19475	25.07	22	4.68	90	23	23	
36	A	74.26146	39.01760	6.00	6	4.68	90	23	23	
36	B	73.99418	39.00755	8.40	10	4.68	90	23	23	
36	C	74.52589	39.00061	12.40	14	4.68	90	23	23	
36	D	73.72695	38.99749	17.96	18	4.68	90	23	23	
36	E	73.45975	38.98744	25.07	22	4.68	90	23	23	
37	A	74.50649	38.82034	6.00	6	4.68	90	23	23	
37	B	74.23996	38.81029	8.40	10	4.68	90	23	23	
37	C	73.97346	38.80024	12.40	14	4.68	90	23	23	
37	D	73.70700	38.79018	17.96	18	4.68	90	23	23	
37	E	73.44058	38.78013	25.07	22	4.68	90	23	23	
38	A	74.50348	38.65588	6.00	6	4.68	90	23	23	
38	B	73.95582	38.63091	8.40	10	4.68	90	23	23	
38	C	74.22691	38.62952	12.40	14	4.68	90	23	23	
38	D	73.67935	38.60454	17.96	18	4.68	90	23	23	
38	E	73.40563	38.59206	25.07	22	4.68	90	23	23	
39	A	74.17278	38.44030	6.00	6	12.47	90	23	23	
39	B	74.44316	38.43891	8.40	10	12.47	90	23	23	
39	C	73.62675	38.41532	12.40	14	12.47	90	23	23	
39	D	73.89703	38.41393	17.96	18	12.47	90	23	23	
39	E	73.35110	38.38896	25.07	22	12.47	90	23	23	
40	A	74.38842	38.24968	6.00	6	12.47	90	23	23	
40	B	74.11339	38.22332	8.40	10	12.47	90	23	23	
40	C	73.84111	38.21083	12.40	14	12.47	90	23	23	
40	D	73.29939	38.19974	17.96	18	12.47	90	23	23	
40	E	73.56888	38.19835	25.07	22	12.47	90	23	23	
41	A	74.32844	38.03271	6.00	6	12.47	90	23	23	
41	B	73.78803	38.02161	8.40	10	12.47	90	23	23	
41	C	74.05687	38.02022	12.40	14	12.47	90	23	23	
41	D	73.24511	37.99664	17.96	18	12.47	90	23	23	
41	E	73.51386	37.99525	25.07	22	12.47	90	23	23	
42	A	74.27133	37.82961	6.00	6	12.47	90	23	23	
42	B	73.73240	37.81851	8.40	10	12.47	90	23	23	

Row	Depth	Longitude (°S)	Latitude (°W)	Depth 2	Dip	Strike	Rake	Length	Width	Slip
42	C	74.00050	37.81712	12.40	14	12.47	90	23	23	
42	D	73.45898	37.79215	17.96	18	12.47	90	23	23	
42	E	73.18829	37.77966	25.07	22	12.47	90	23	23	
43	A	74.21705	37.64039	6.00	6	12.47	90	23	23	
43	B	73.94429	37.61402	8.40	10	12.47	90	23	23	
43	C	73.40692	37.60293	12.40	14	12.47	90	23	23	
43	D	73.67424	37.60154	17.96	18	12.47	90	23	23	
43	E	73.13429	37.57656	25.07	22	12.47	90	23	23	
44	A	73.89089	37.42480	6.00	6	12.47	90	23	23	
44	B	74.15759	37.42341	8.40	10	12.47	90	23	23	
44	C	73.61891	37.39844	12.40	14	12.47	90	23	23	
44	D	73.34964	37.38595	17.96	18	12.47	90	23	23	
44	E	73.08041	37.37346	25.07	22	12.47	90	23	23	
45	A	74.10095	37.22031	6.00	6	12.47	90	23	23	
45	B	73.83231	37.20783	8.40	10	12.47	90	23	23	
45	C	73.56372	37.19534	12.40	14	12.47	90	23	23	
45	D	73.29517	37.18285	17.96	18	12.47	90	23	23	
45	E	73.02667	37.17037	25.07	22	12.47	90	23	23	
46	A	74.04447	37.01722	6.00	6	12.47	90	23	23	
46	B	73.77655	37.00473	8.40	10	12.47	90	23	23	
46	C	73.50867	36.99224	12.40	14	12.47	90	23	23	
46	D	73.24084	36.97975	17.96	18	12.47	90	23	23	
46	E	72.97305	36.96727	25.07	22	12.47	90	23	23	
47	A	73.98815	36.81412	6.00	6	12.47	90	23	23	
47	B	73.72093	36.80163	8.40	10	12.47	90	23	23	
47	C	73.45376	36.78914	12.40	14	12.47	90	23	23	
47	D	73.18664	36.77666	17.96	18	12.47	90	23	23	
47	E	72.91955	36.76417	25.07	22	12.47	90	23	23	
48	A	73.93198	36.61102	6.00	6	12.47	90	23	23	
48	B	73.66546	36.59853	8.40	10	12.47	90	23	23	
48	C	73.39900	36.58604	12.40	14	12.47	90	23	23	
48	D	73.13257	36.57356	17.96	18	12.47	90	23	23	
48	E	72.86619	36.56107	25.07	22	12.47	90	23	23	
49	A	73.87596	36.40792	6.00	6	12.47	90	23	23	
49	B	73.61014	36.39543	8.40	10	12.47	90	23	23	
49	C	73.34437	36.38294	12.40	14	12.47	90	23	23	

Row	Depth	Longitude (°S)	Latitude (°W)	Depth 2	Dip	Strike	Rake	Length	Width	Slip
49	D	73.07863	36.37046	17.96	18	12.47	90	23	23	
49	E	72.81294	36.35797	25.07	22	12.47	90	23	23	
50	A	73.82009	36.20482	6.00	6	12.47	90	23	23	
50	B	73.55496	36.19233	8.40	10	12.47	90	23	23	
50	C	73.28987	36.17985	12.40	14	12.47	90	23	23	
50	D	73.02483	36.16736	17.96	18	12.47	90	23	23	
50	E	72.75982	36.15487	25.07	22	12.47	90	23	23	
51	A	73.76437	36.00172	6.00	6	12.47	90	23	23	
51	B	73.49992	35.98923	8.40	10	12.47	90	23	23	
51	C	73.23551	35.97675	12.40	14	12.47	90	23	23	
51	D	72.97115	35.96426	17.96	18	12.47	90	23	23	
51	E	72.70682	35.95177	25.07	22	12.47	90	23	23	
52	A	73.70879	35.79862	6.00	6	12.47	90	23	23	
52	B	73.44502	35.78614	8.40	10	12.47	90	23	23	
52	C	73.18128	35.77365	12.40	14	12.47	90	23	23	
52	D	72.91759	35.76116	17.96	18	12.47	90	23	23	
52	E	72.65394	35.74867	25.07	22	12.47	90	23	23	
53	A	73.65336	35.59552	6.00	6	12.47	90	23	23	
53	B	73.39026	35.58304	8.40	10	12.47	90	23	23	
53	C	73.12719	35.57055	12.40	14	12.47	90	23	23	
53	D	72.86416	35.55806	17.96	18	12.47	90	23	23	
53	E	72.60118	35.54558	25.07	22	12.47	90	23	23	
54	A	73.59808	35.39242	6.00	6	12.47	90	23	23	
54	B	73.33563	35.37994	8.40	10	12.47	90	23	23	
54	C	73.07323	35.36745	12.40	14	12.47	90	23	23	
54	D	72.81086	35.35496	17.96	18	12.47	90	23	23	
54	E	72.54854	35.34248	25.07	22	12.47	90	23	23	
55	A	73.54294	35.18933	6.00	6	12.47	90	23	23	
55	B	73.28115	35.17684	8.40	10	12.47	90	23	23	
55	C	73.01939	35.16435	12.40	14	12.47	90	23	23	
55	D	72.75768	35.15186	17.96	18	12.47	90	23	23	
55	E	72.49601	35.13938	25.07	22	12.47	90	23	23	
56	A	73.48794	34.98623	6.00	6	12.47	90	23	23	
56	B	73.22679	34.97374	8.40	10	12.47	90	23	23	
56	C	72.96569	34.96125	12.40	14	12.47	90	23	23	
56	D	72.70462	34.94877	17.96	18	12.47	90	23	23	

Row	Depth	Longitude (°S)	Latitude (°W)	Depth 2	Dip	Strike	Rake	Length	Width	Slip
56	E	72.44360	34.93628	25.07	22	12.47	90	23	23	
57	A	73.43308	34.78313	6.00	6	12.47	90	23	23	
57	B	73.17257	34.77064	8.40	10	12.47	90	23	23	
57	C	72.91211	34.75815	12.40	14	12.47	90	23	23	
57	D	72.65168	34.74567	17.96	18	12.47	90	23	23	
57	E	72.39130	34.73318	25.07	22	12.47	90	23	23	
58	A	73.37836	34.58003	6.00	6	12.47	90	23	23	
58	B	73.11849	34.56754	8.40	10	12.47	90	23	23	
58	C	72.85866	34.55506	12.40	14	12.47	90	23	23	
58	D	72.59886	34.54257	17.96	18	12.47	90	23	23	
58	E	72.33911	34.53008	25.07	22	12.47	90	23	23	
59	A	73.32377	34.37693	6.00	6	12.47	90	23	23	
59	B	73.06453	34.36444	8.40	10	12.47	90	23	23	
59	C	72.80533	34.35196	12.40	14	12.47	90	23	23	
59	D	72.54616	34.33947	17.96	18	12.47	90	23	23	
59	E	72.28704	34.32698	25.07	22	12.47	90	23	23	
60	A	73.26932	34.17383	6.00	6	12.47	90	23	23	
60	B	73.01070	34.16134	8.40	10	12.47	90	23	23	
60	C	72.75212	34.14886	12.40	14	12.47	90	23	23	
60	D	72.49358	34.13637	17.96	18	12.47	90	23	23	
60	E	72.23507	34.12388	25.07	22	12.47	90	23	23	
61	A	73.21501	33.97073	6.00	6	12.47	90	23	23	
61	B	72.95701	33.95825	8.40	10	12.47	90	23	23	
61	C	72.69904	33.94576	12.40	14	12.47	90	23	23	
61	D	72.44111	33.93327	17.96	18	12.47	90	23	23	
61	E	72.18322	33.92078	25.07	22	12.47	90	23	23	
62	A	73.16083	33.76763	6.00	6	12.47	90	23	23	
62	B	72.90343	33.75515	8.40	10	12.47	90	23	23	
62	C	72.64608	33.74266	12.40	14	12.47	90	23	23	
62	D	72.38876	33.73017	17.96	18	12.47	90	23	23	
62	E	72.13148	33.71769	25.07	22	12.47	90	23	23	
63	A	73.10678	33.56453	6.00	6	12.47	90	23	23	
63	B	72.84999	33.55205	8.40	10	12.47	90	23	23	
63	C	72.59323	33.53956	12.40	14	12.47	90	23	23	
63	D	72.33652	33.52707	17.96	18	12.47	90	23	23	
63	E	72.07984	33.51459	25.07	22	12.47	90	23	23	

Row	Depth	Longitude (°S)	Latitude (°W)	Depth 2	Dip	Strike	Rake	Length	Width	Slip
64	A	73.05286	33.36144	6.00	6	12.47	90	23	23	
64	B	72.79667	33.34895	8.40	10	12.47	90	23	23	
64	C	72.54051	33.33646	12.40	14	12.47	90	23	23	
64	D	72.28439	33.32397	17.96	18	12.47	90	23	23	
64	E	72.02831	33.31149	25.07	22	12.47	90	23	23	
65	A	72.99907	33.15834	6.00	6	12.47	90	23	23	
65	B	72.74347	33.14585	8.40	10	12.47	90	23	23	
65	C	72.48790	33.13336	12.40	14	12.47	90	23	23	
65	D	72.23237	33.12088	17.96	18	12.47	90	23	23	
65	E	71.97688	33.10839	25.07	22	12.47	90	23	23	
66	A	72.94541	32.95524	6.00	6	12.47	90	23	23	
66	B	72.69039	32.94275	8.40	10	12.47	90	23	23	
66	C	72.43541	32.93026	12.40	14	12.47	90	23	23	
66	D	72.18047	32.91778	17.96	18	12.47	90	23	23	
66	E	71.92556	32.90529	25.07	22	12.47	90	23	23	
67	A	72.89187	32.75214	6.00	6	12.47	90	23	23	
67	B	72.63744	32.73965	8.40	10	12.47	90	23	23	
67	C	72.38303	32.72717	12.40	14	12.47	90	23	23	
67	D	72.12867	32.71468	17.96	18	12.47	90	23	23	
67	E	71.87434	32.70219	25.07	22	12.47	90	23	23	
68	A	72.83846	32.54904	6.00	6	12.47	90	23	23	
68	B	72.58460	32.53655	8.40	10	12.47	90	23	23	
68	C	72.33077	32.52407	12.40	14	12.47	90	23	23	
68	D	72.07698	32.51158	17.96	18	12.47	90	23	23	
68	E	71.82322	32.49909	25.07	22	12.47	90	23	23	
69	A	72.78517	32.34594	6.00	6	12.47	90	23	23	
69	B	72.53188	32.33345	8.40	10	12.47	90	23	23	
69	C	72.27862	32.32097	12.40	14	12.47	90	23	23	
69	D	72.02540	32.30848	17.96	18	12.47	90	23	23	
69	E	71.77221	32.29599	25.07	22	12.47	90	23	23	
70	A	72.73201	32.14284	6.00	6	12.47	90	23	23	
70	B	72.47928	32.13036	8.40	10	12.47	90	23	23	
70	C	72.22658	32.11787	12.40	14	12.47	90	23	23	
70	D	71.97392	32.10538	17.96	18	12.47	90	23	23	
70	E	71.72129	32.09289	25.07	22	12.47	90	23	23	
71	A	72.67897	31.93974	6.00	6	12.47	90	23	23	

Row	Depth	Longitude (°S)	Latitude (°W)	Depth 2	Dip	Strike	Rake	Length	Width	Slip
71	B	72.42679	31.92726	8.40	10	12.47	90	23	23	
71	C	72.17465	31.91477	12.40	14	12.47	90	23	23	
71	D	71.92255	31.90228	17.96	18	12.47	90	23	23	
71	E	71.67048	31.88980	25.07	22	12.47	90	23	23	
72	A	72.62605	31.73665	6.00	6	12.47	90	23	23	
72	B	72.37442	31.72416	8.40	10	12.47	90	23	23	
72	C	72.12283	31.71167	12.40	14	12.47	90	23	23	
72	D	71.87128	31.69918	17.96	18	12.47	90	23	23	
72	E	71.61976	31.68670	25.07	22	12.47	90	23	23	
73	A	72.57324	31.53355	6.00	6	12.47	90	23	23	
73	B	72.32217	31.52106	8.40	10	12.47	90	23	23	
73	C	72.07112	31.50857	12.40	14	12.47	90	23	23	
73	D	71.82011	31.49609	17.96	18	12.47	90	23	23	
73	E	71.56913	31.48360	25.07	22	12.47	90	23	23	
74	A	72.52056	31.33045	6.00	6	12.47	90	23	23	
74	B	72.27002	31.31796	8.40	10	12.47	90	23	23	
74	C	72.01952	31.30547	12.40	14	12.47	90	23	23	
74	D	71.76905	31.29299	17.96	18	12.47	90	23	23	
74	E	71.51861	31.28050	25.07	22	12.47	90	23	23	
75	A	72.46799	31.12735	6.00	6	12.47	90	23	23	
75	B	72.21799	31.11486	8.40	10	12.47	90	23	23	
75	C	71.96802	31.10237	12.40	14	12.47	90	23	23	
75	D	71.71808	31.08989	17.96	18	12.47	90	23	23	
75	E	71.46818	31.07740	25.07	22	12.47	90	23	23	
76	A	72.41554	30.92425	6.00	6	12.47	90	23	23	
76	B	72.16607	30.91176	8.40	10	12.47	90	23	23	
76	C	71.91663	30.89928	12.40	14	12.47	90	23	23	
76	D	71.66722	30.88679	17.96	18	12.47	90	23	23	
76	E	71.41784	30.87430	25.07	22	12.47	90	23	23	

APPENDIX B

Stochastic variable slips

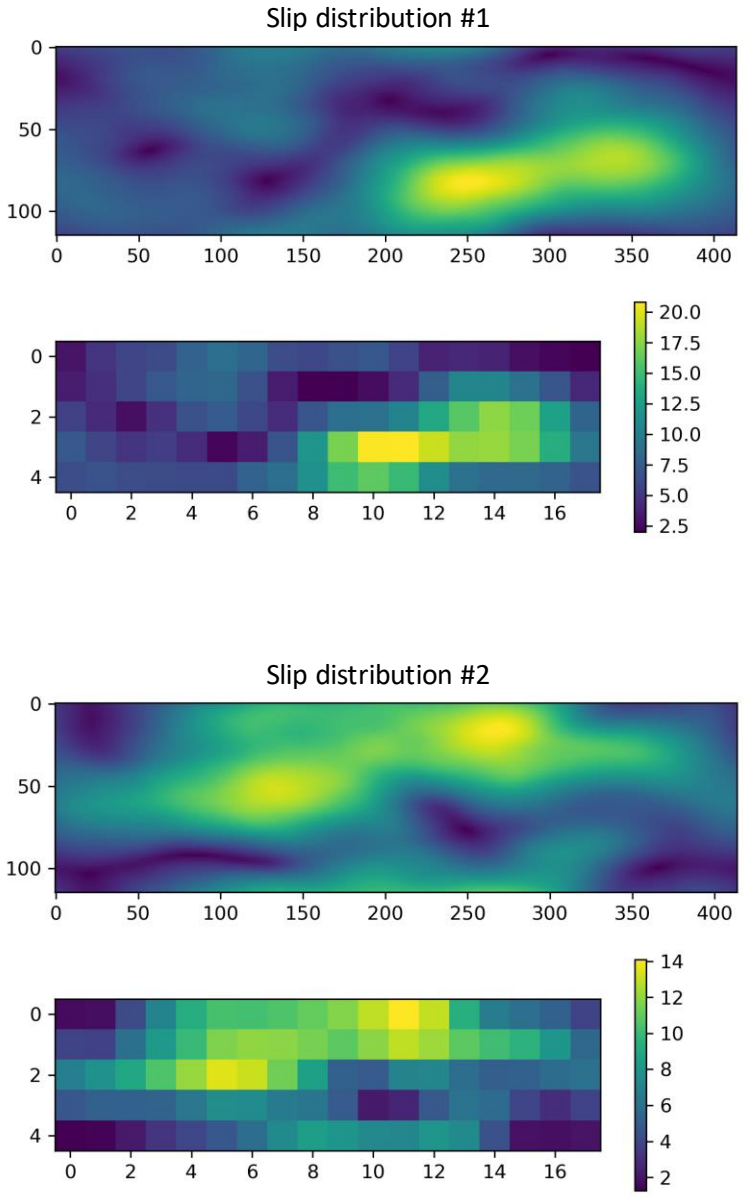

Figure B1: The three M_w 8.7 stochastic variable slip distributions in planar view (top) and cross-sectional view (bottom) used to generate earthquake source models. Brighter colors correspond to greater slip.

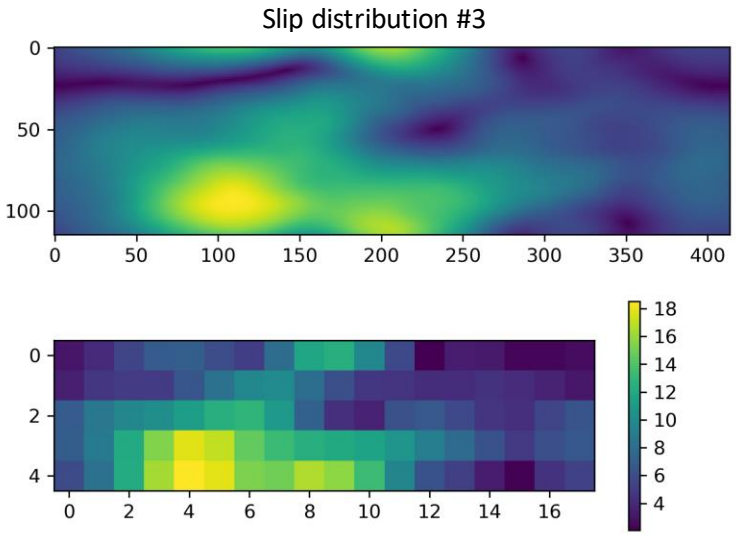

Figure B1: Continued.

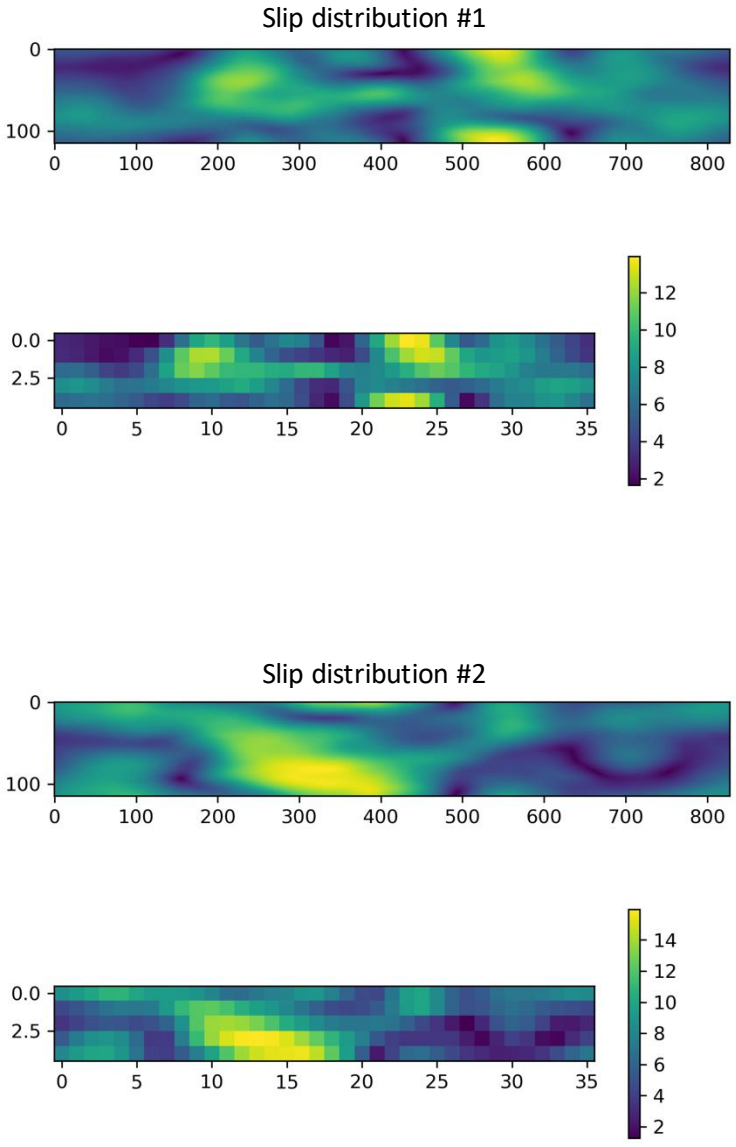

Figure B2: The three M_w 8.9 stochastic variable slip distributions in planar view (top) and cross-sectional view (bottom) used to generate earthquake source models. Brighter colors correspond to greater slip.

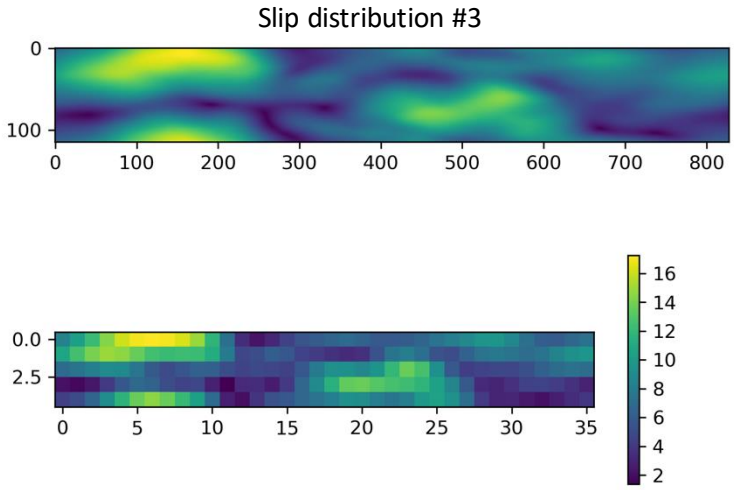

Figure B2: Continued.

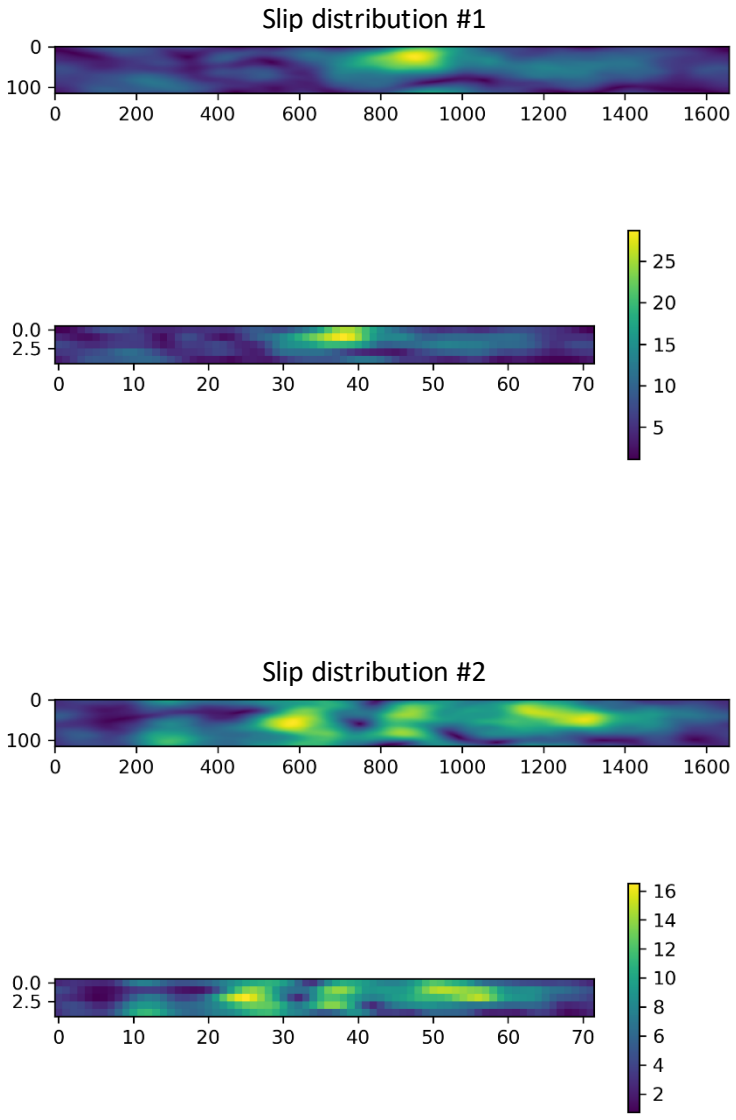

Figure B3: The ten M_w 9.1 stochastic variable slip distributions in planar view (top) and cross-sectional view (bottom) used to generate earthquake source models. Brighter colors correspond to greater slip.

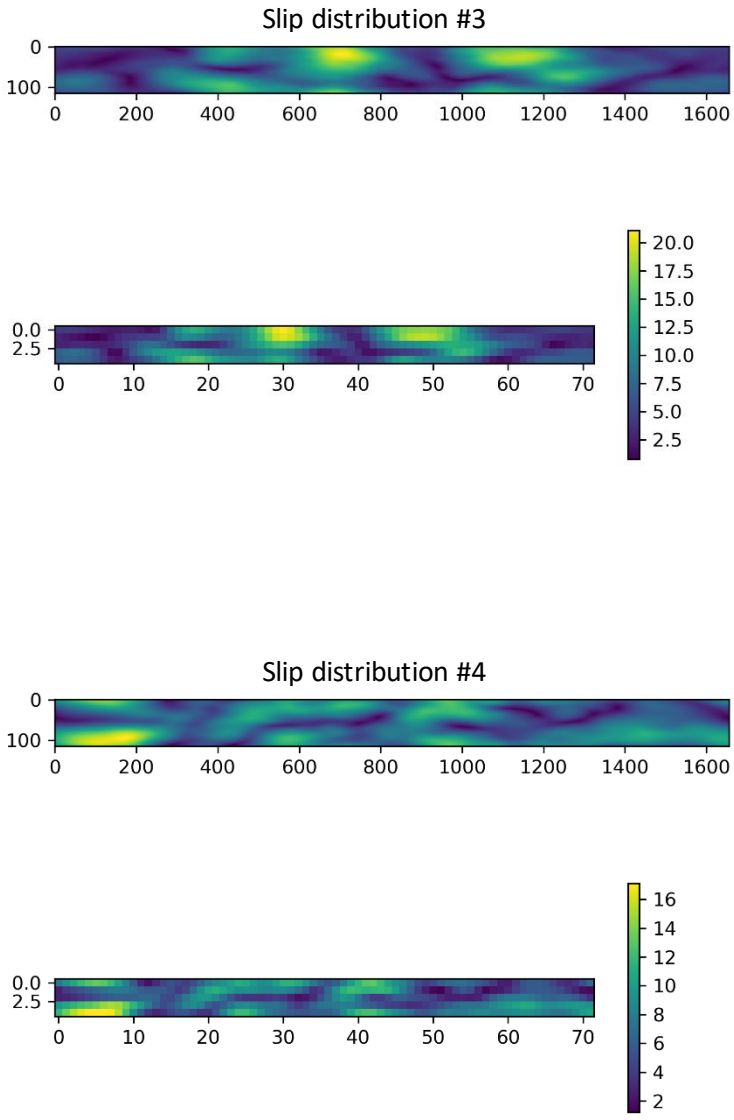

Figure B3: Continued.

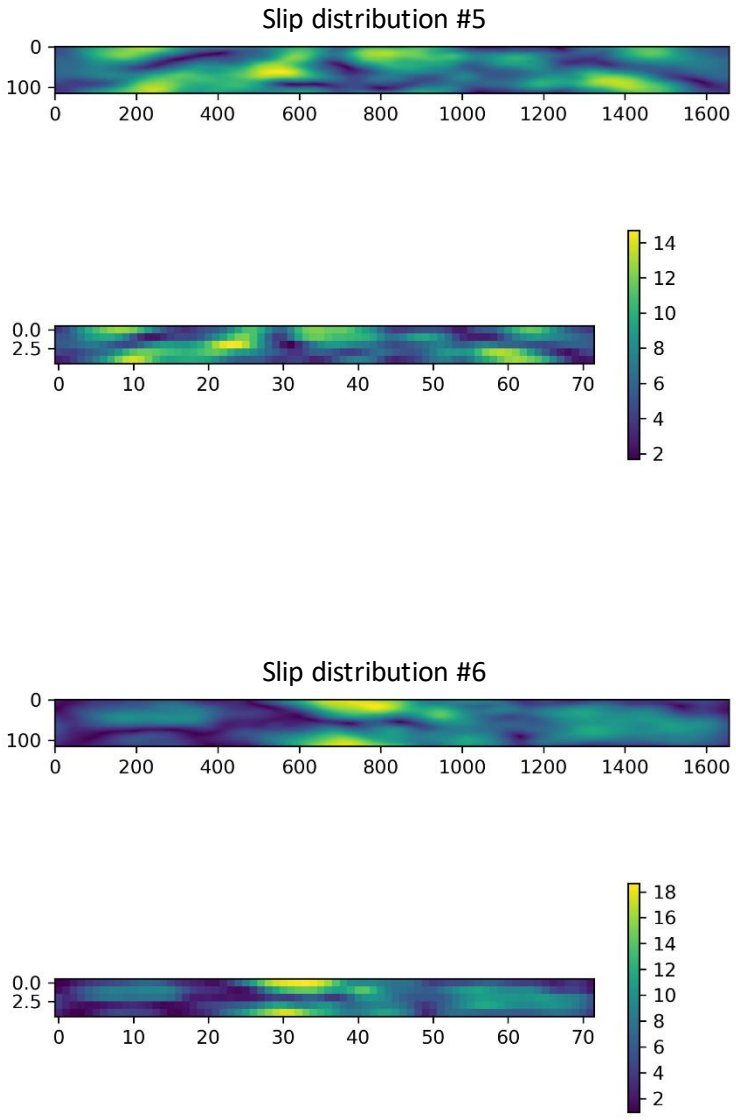

Figure B3: Continued.

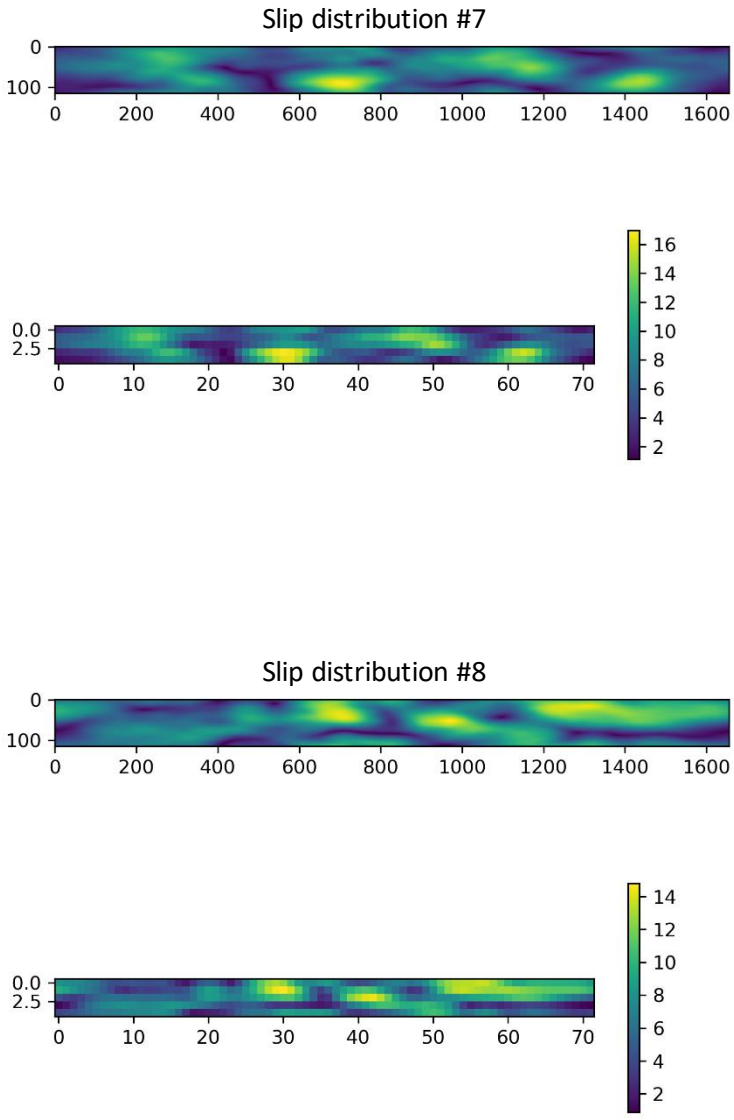

Figure B3: Continued.

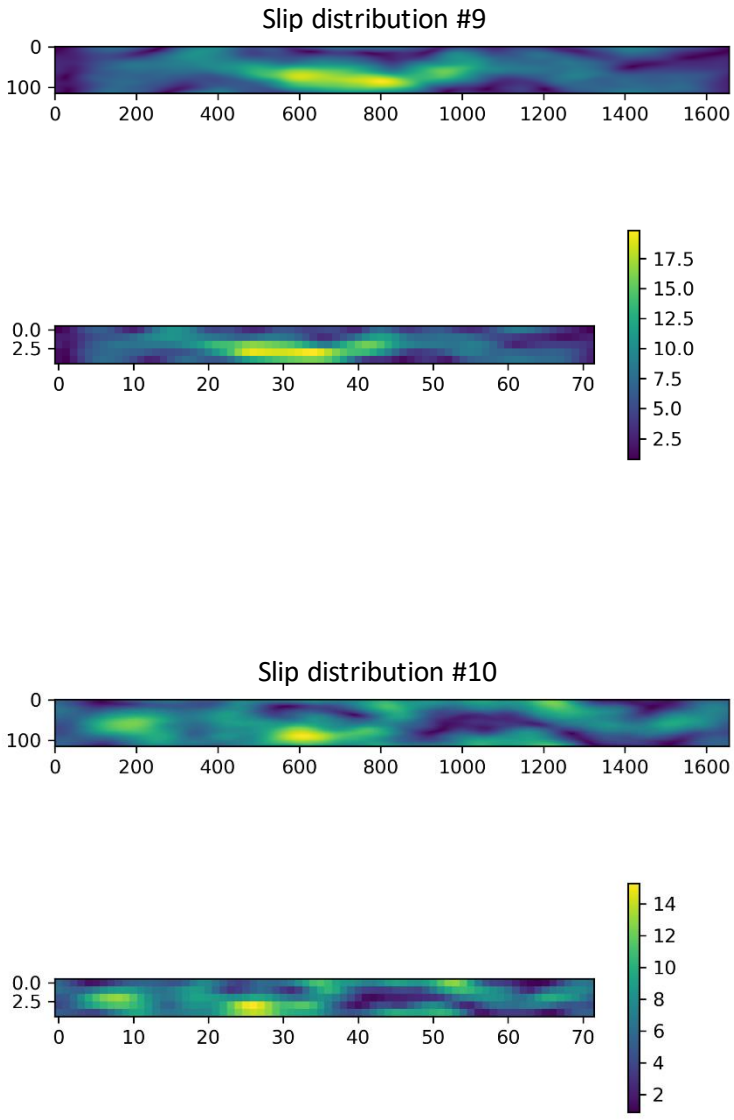

Figure B3: Continued.

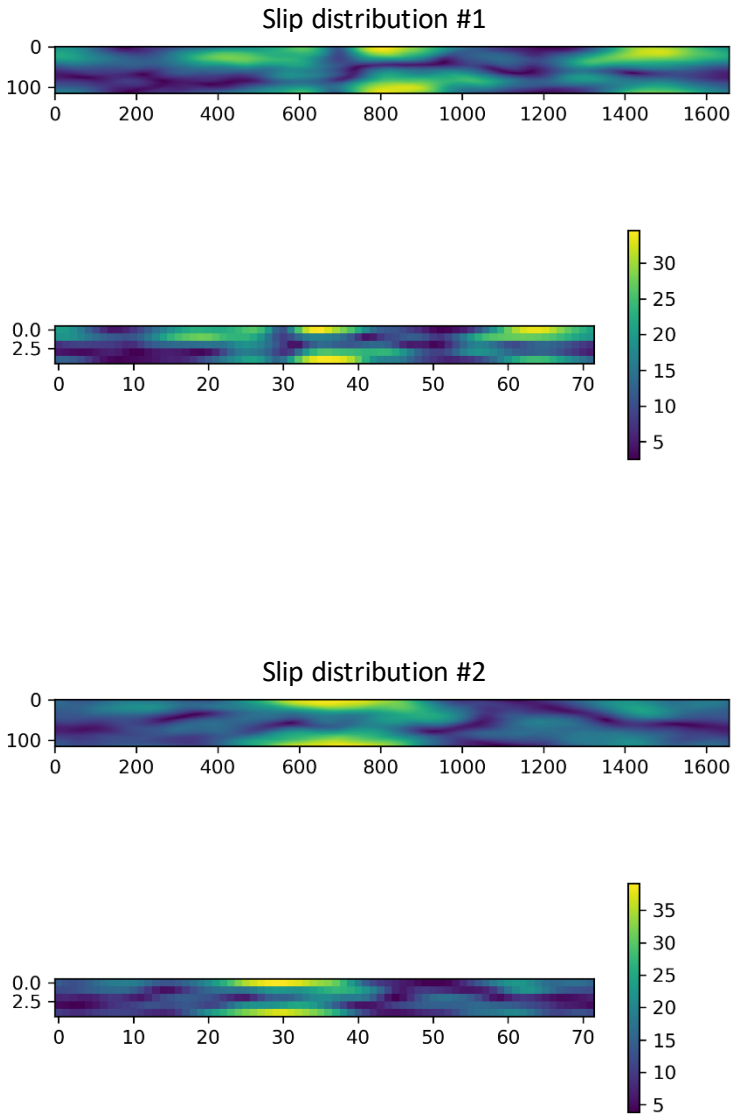

Figure B4: The ten M_w 9.3 stochastic variable slip distributions in planar view (top) and cross-sectional view (bottom) used to generate earthquake source models. Brighter colors correspond to greater slip.

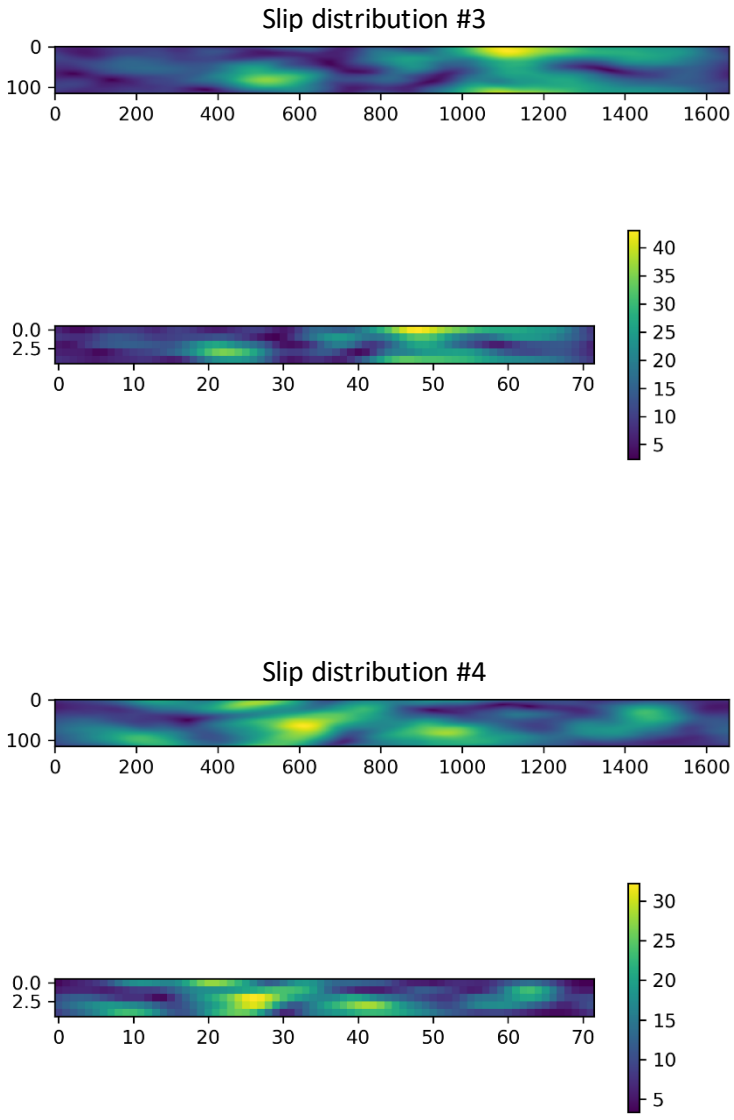

Figure B4: Continued.

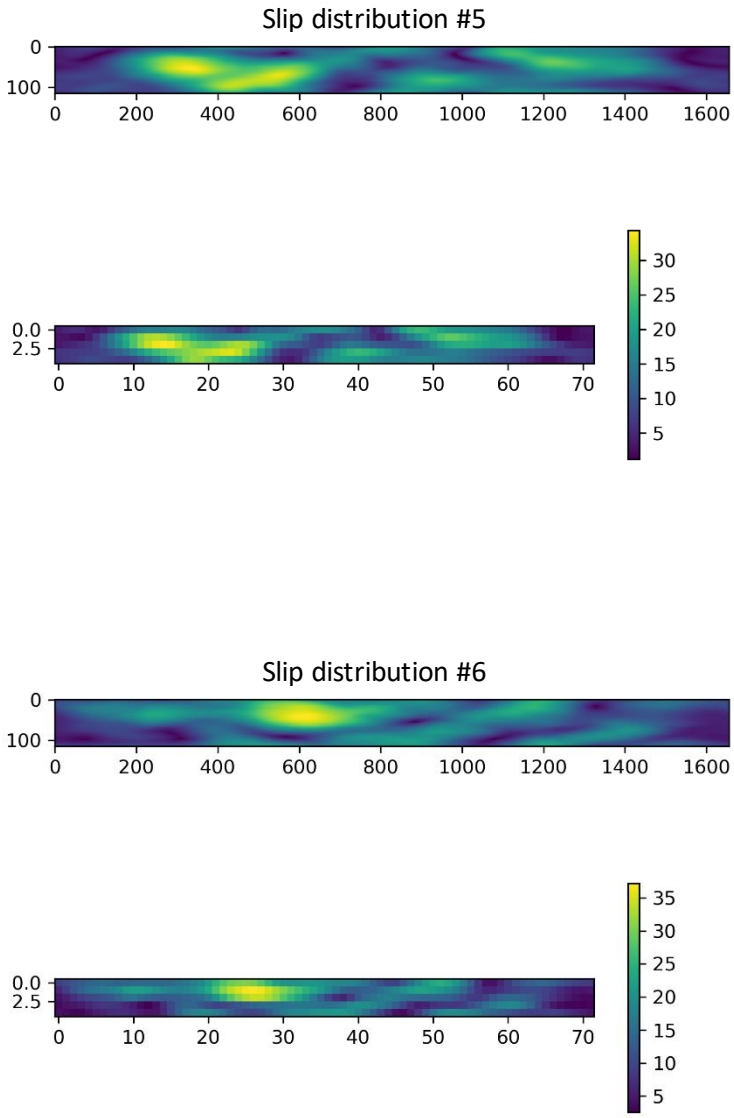

Figure B4: Continued.

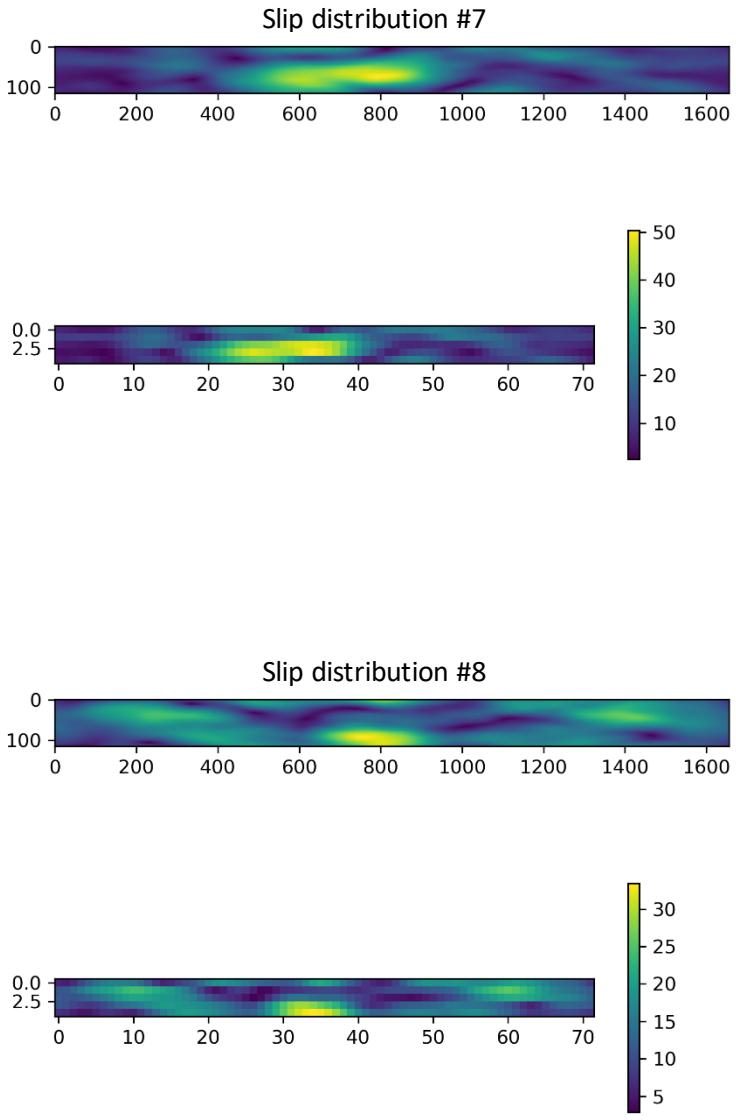

Figure B4: Continued.

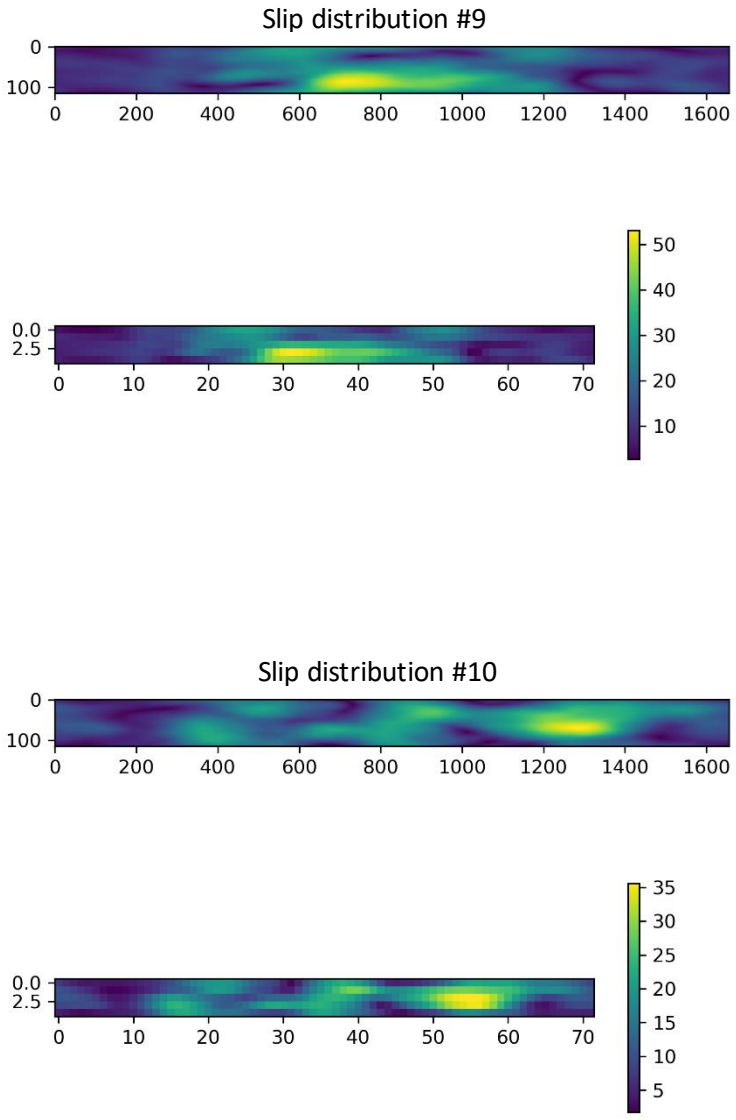

Figure B4: Continued.

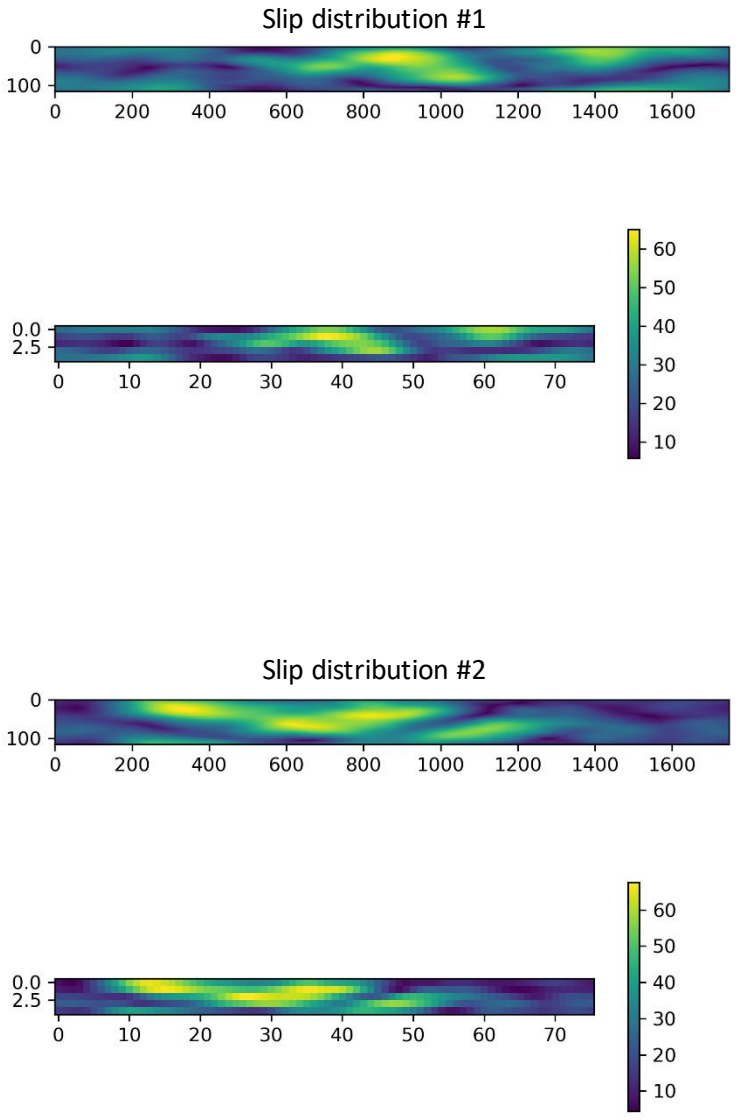

Figure B5: The ten M_w 9.5 stochastic variable slip distributions in planar view (top) and cross-sectional view (bottom) used to generate earthquake source models. Brighter colors correspond to greater slip.

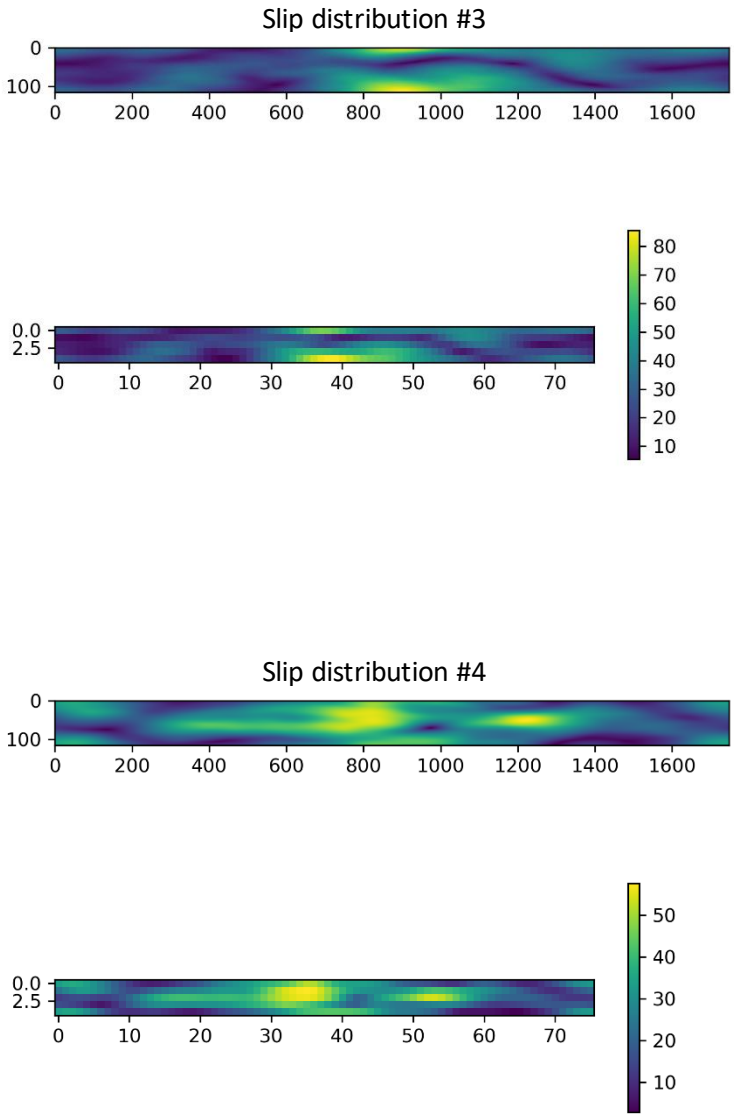

Figure B5: Continued.

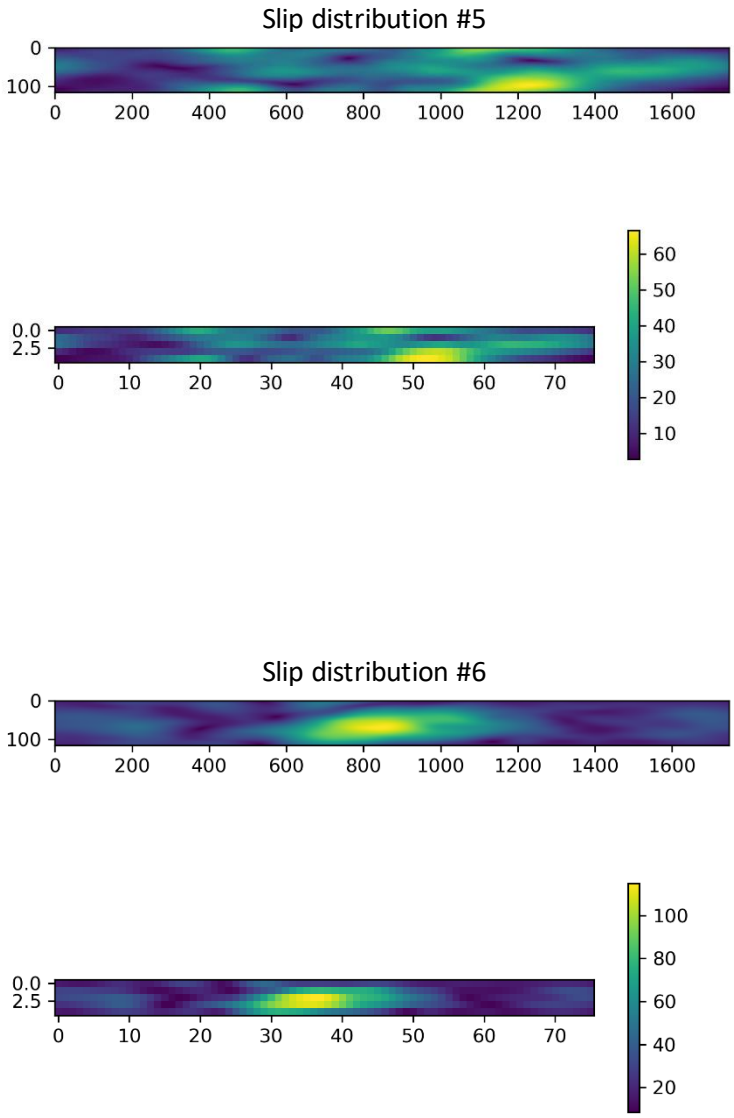

Figure B5: Continued.

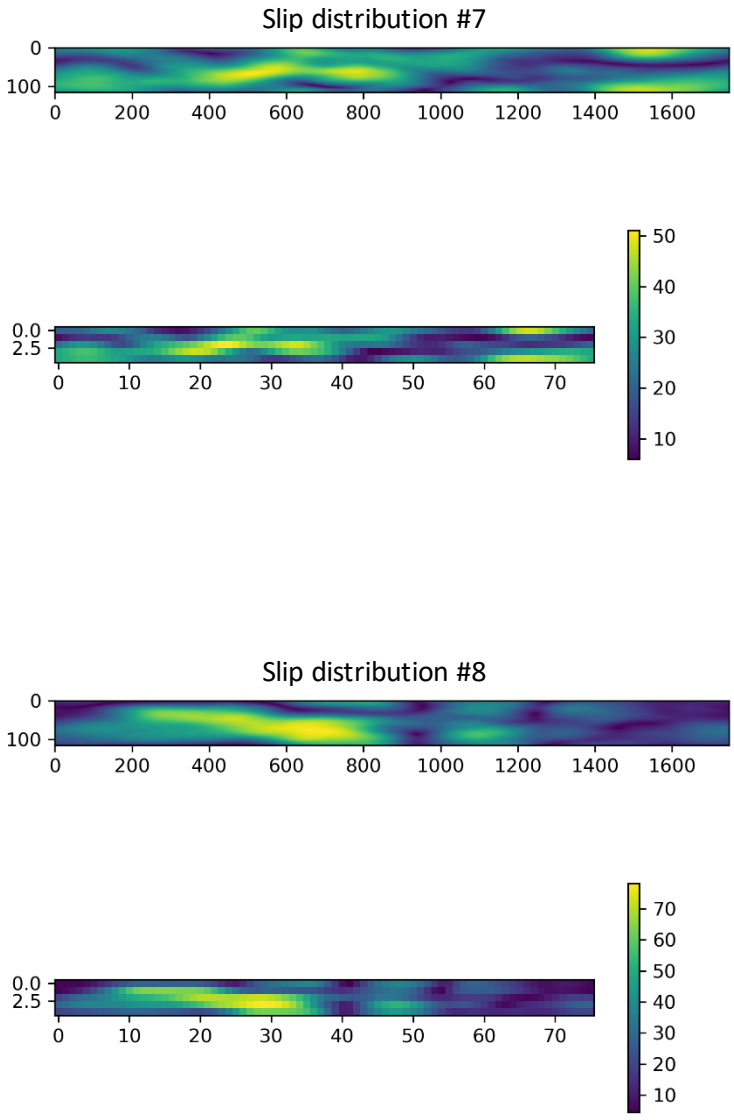

Figure B5: Continued.

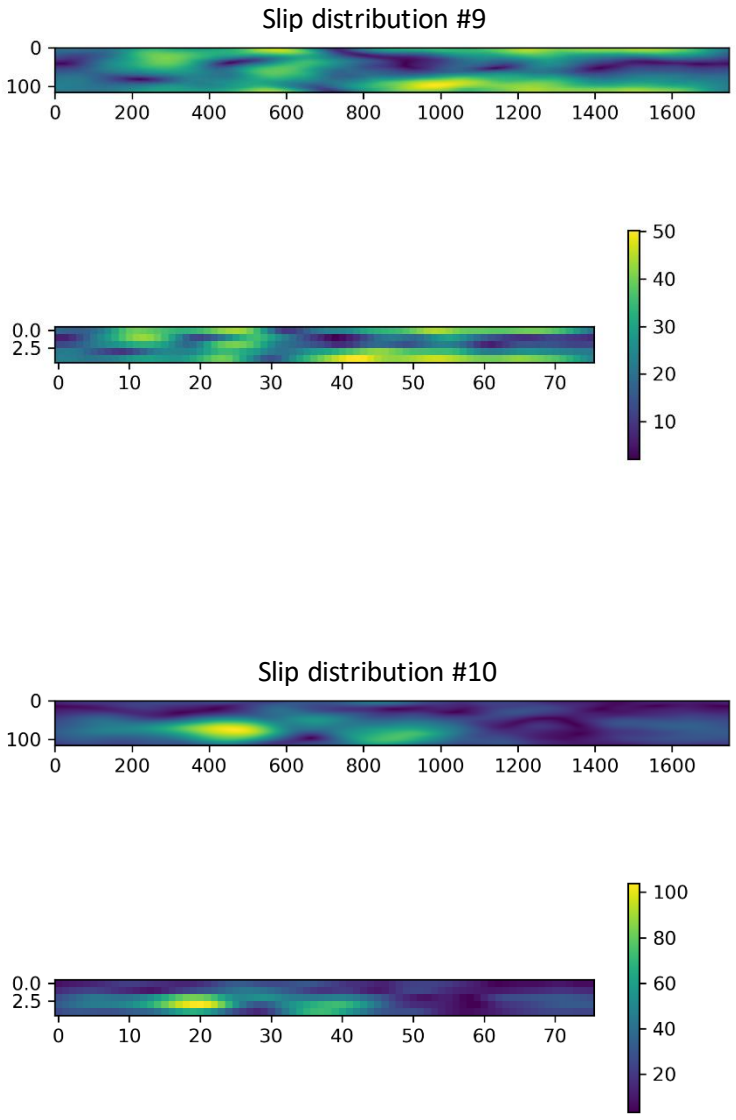

Figure B5: Continued

APPENDIX C
Setrun.py file for GeoClaw simulations

```
"""
Module to set up run time parameters for Clawpack.

The values set in the function setrun are then written out to data files
that will be read in by the Fortran code.

"""

from __future__ import absolute_import
from __future__ import print_function
import os
import numpy as np

try:
    CLAW = os.environ['CLAW']
except:
    raise Exception("*** Must first set CLAW enviornment variable")

# Scratch directory for storing topo and dtopo files:
scratch_dir = os.path.join(CLAW, 'geoclaw', 'scratch')


#------------------------------
def setrun(claw_pkg='geoclaw'):
#------------------------------

    """
    Define the parameters used for running Clawpack.

    INPUT:
        claw_pkg expected to be "geoclaw" for this setrun.

    OUTPUT:
        rundata - object of class ClawRunData

    """

    from clawpack.clawutil import data

    assert claw_pkg.lower() == 'geoclaw',  "Expected claw_pkg = 'geoclaw'"

    num_dim = 2
    rundata = data.ClawRunData(claw_pkg, num_dim)
```

```
#------------------------------------------------------
# Problem-specific parameters to be written to setprob.data:
#------------------------------------------------------

#probdata = rundata.new_UserData(name='probdata',fname='setprob.data')


#------------------------------------------------------
# GeoClaw specific parameters:
#------------------------------------------------------
rundata = setgeo(rundata)

#------------------------------------------------------
# Standard Clawpack parameters to be written to claw.data:
#   (or to amr2ez.data for AMR)
#------------------------------------------------------
clawdata = rundata.clawdata  # initialized when rundata instantiated


# Set single grid parameters first.
# See below for AMR parameters.


# ---------------
# Spatial domain:
# ---------------

# Number of space dimensions:
clawdata.num_dim = num_dim

# Lower and upper edge of computational domain:
clawdata.lower[0] = -80.0     # west longitude
clawdata.upper[0] = -60.0      # east longitude

clawdata.lower[1] = -48.0      # south latitude
clawdata.upper[1] = -28.0       # north latitude



# Number of grid cells: Coarsest grid
clawdata.num_cells[0] = 20
clawdata.num_cells[1] = 20

# ---------------
# Size of system:
# ---------------
```

```
# Number of equations in the system:
clawdata.num_eqn = 3

# Number of auxiliary variables in the aux array (initialized in setaux)
clawdata.num_aux = 3

# Index of aux array corresponding to capacity function, if there is one:
clawdata.capa_index = 2



# -------------
# Initial time:
# -------------

clawdata.t0 = 0.0


# Restart from checkpoint file of a previous run?
# If restarting, t0 above should be from original run, and the
# restart_file 'fort.chkNNNNN' specified below should be in
# the OUTDIR indicated in Makefile.

clawdata.restart = False               # True to restart from prior results
clawdata.restart_file = 'fort.chk00096'  # File to use for restart data

# -------------
# Output times:
#--------------

# Specify at what times the results should be written to fort.q files.
# Note that the time integration stops after the final output time.
# The solution at initial time t0 is always written in addition.

clawdata.output_style = 1

if clawdata.output_style==1:
    # Output nout frames at equally spaced times up to tfinal:
    clawdata.num_output_times = 24
    clawdata.tfinal = 4*3600.
    clawdata.output_t0 = True  # output at initial (or restart) time?

elif clawdata.output_style == 2:
    # Specify a list of output times.
    clawdata.output_times = [0.5, 1.0]

elif clawdata.output_style == 3:
    # Output every iout timesteps with a total of ntot time steps:
    clawdata.output_step_interval = 1
```

```
    clawdata.total_steps = 3
    clawdata.output_t0 = True


clawdata.output_format = 'ascii'      # 'ascii' or 'netcdf'

clawdata.output_q_components = 'all'   # need all
clawdata.output_aux_components = 'none'  # eta=h+B is in q
clawdata.output_aux_onlyonce = False    # output aux arrays each frame



# ---------------------------------------------
# Verbosity of messages to screen during integration:
# ---------------------------------------------

# The current t, dt, and cfl will be printed every time step
# at AMR levels <= verbosity.  Set verbosity = 0 for no printing.
#   (E.g. verbosity == 2 means print only on levels 1 and 2.)
clawdata.verbosity = 1



# --------------
# Time stepping:
# --------------

# if dt_variable==1: variable time steps used based on cfl_desired,
# if dt_variable==0: fixed time steps dt = dt_initial will always be used.
clawdata.dt_variable = True

# Initial time step for variable dt.
# If dt_variable==0 then dt=dt_initial for all steps:
clawdata.dt_initial = 0.2

# Max time step to be allowed if variable dt used:
clawdata.dt_max = 1 x 1099

# Desired Courant number if variable dt used, and max to allow without
# retaking step with a smaller dt:
clawdata.cfl_desired = 0.75
clawdata.cfl_max = 1.0

# Maximum number of time steps to allow between output times:
clawdata.steps_max = 5000
```

```
# ------------------
# Method to be used:
# ------------------

# Order of accuracy:  1 => Godunov,  2 => Lax-Wendroff plus limiters
clawdata.order = 2

# Use dimensional splitting? (not yet available for AMR)
clawdata.dimensional_split = 'unsplit'

# For unsplit method, transverse_waves can be
#  0 or 'none'      ==> donor cell (only normal solver used)
#  1 or 'increment' ==> corner transport of waves
#  2 or 'all'       ==> corner transport of 2nd order corrections too
clawdata.transverse_waves = 2

# Number of waves in the Riemann solution:
clawdata.num_waves = 3

# List of limiters to use for each wave family:
# Required:  len(limiter) == num_waves
# Some options:
#  0 or 'none'    ==> no limiter (Lax-Wendroff)
#  1 or 'minmod'  ==> minmod
#  2 or 'superbee' ==> superbee
#  3 or 'mc'      ==> MC limiter
#  4 or 'vanleer'  ==> van Leer
clawdata.limiter = ['mc', 'mc', 'mc']

clawdata.use_fwaves = True    # True ==> use f-wave version of algorithms

# Source terms splitting:
#  src_split == 0 or 'none'    ==> no source term (src routine never called)
#  src_split == 1 or 'godunov' ==> Godunov (1st order) splitting used,
#  src_split == 2 or 'strang'  ==> Strang (2nd order) splitting used,  not recommended.
clawdata.source_split = 'godunov'


# ------------------
# Boundary conditions:
# ------------------

# Number of ghost cells (usually 2)
clawdata.num_ghost = 2

# Choice of BCs at xlower and xupper:
#  0 => user specified (must modify bcN.f to use this option)
#  1 => extrapolation (non-reflecting outflow)
#  2 => periodic (must specify this at both boundaries)
```

```
#   3 => solid wall for systems where q(2) is normal velocity

clawdata.bc_lower[0] = 'extrap'
clawdata.bc_upper[0] = 'extrap'

clawdata.bc_lower[1] = 'extrap'
clawdata.bc_upper[1] = 'extrap'



# ---------------
# Checkpointing:
# ---------------

# Specify when checkpoint files should be created that can be
# used to restart a computation.

clawdata.checkpt_style = 0

if clawdata.checkpt_style == 0:
    # Do not checkpoint at all
    pass

elif clawdata.checkpt_style == 1:
    # Checkpoint only at tfinal.
    pass

elif clawdata.checkpt_style == 2:
    # Specify a list of checkpoint times.
    clawdata.checkpt_times = [0.1,0.15]

elif clawdata.checkpt_style == 3:
    # Checkpoint every checkpt_interval timesteps (on Level 1)
    # and at the final time.
    clawdata.checkpt_interval = 5



# ---------------
# AMR parameters:
# ---------------
amrdata = rundata.amrdata

# max number of refinement levels:
amrdata.amr_levels_max = 5

# List of refinement ratios at each level (length at least mxnest-1)
amrdata.refinement_ratios_x = [3,5,4,4]
amrdata.refinement_ratios_y = [3,5,4,4]
amrdata.refinement_ratios_t = [1,1,1,1]
```

```
# Specify type of each aux variable in amrdata.auxtype.
# This must be a list of length maux, each element of which is one of:
#   'center',  'capacity', 'xleft', or 'yleft'  (see documentation).

amrdata.aux_type = ['center','capacity','yleft']


# Flag using refinement routine flag2refine rather than richardson error
amrdata.flag_richardson = False    # use Richardson?
amrdata.flag2refine = True

# steps to take on each level L between regriddings of level L+1:
amrdata.regrid_interval = 3

# width of buffer zone around flagged points:
# (typically the same as regrid_interval so waves don't escape):
amrdata.regrid_buffer_width  = 2

# clustering alg. cutoff for (# flagged pts) / (total # of cells refined)
# (closer to 1.0 => more small grids may be needed to cover flagged cells)
amrdata.clustering_cutoff = 0.700000

# print info about each regridding up to this level:
amrdata.verbosity_regrid = 0

#  ----- For developers -----
# Toggle debugging  print statements:
amrdata.dprint = False      # print domain flags
amrdata.eprint = False      # print err est flags
amrdata.edebug  = False      # even more err est flags
amrdata.gprint = False      # grid bisection/clustering
amrdata.nprint = False      # proper nesting output
amrdata.pprint = False      # proj. of tagged points
amrdata.rprint = False      # print regridding summary
amrdata.sprint = False      # space/memory output
amrdata.tprint = True       # time step reporting each level
amrdata.uprint = False      # update/upbnd reporting

# More AMR parameters can be set -- see the defaults in pyclaw/data.py

# ------------------
# Regions:
# ------------------
rundata.regiondata.regions = []
# to specify regions of refinement append lines of the form
#  [minlevel,maxlevel,t1,t2,x1,x2,y1,y2]
```

```
    rundata.regiondata.regions.append([5,5,0,1e10,-71.64871767,-71.58226600,-33.05920767,-
33.01545867])#Valpraiso,7
    rundata.regiondata.regions.append([5,5,0,1e10,-72.44166167,-72.19453733,-35.33298667,-
35.09301133])#Constitucion,8
    rundata.regiondata.regions.append([5,5,0,1e10,-73.16999133,-72.92790667,-36.75318200,-
36.52120900])#Concepcion,9
    rundata.regiondata.regions.append([5,5,0,1e10,-73.44002000,-73.13827667,-37.25091467,-
37.01934833])#Arauco,10
    rundata.regiondata.regions.append([5,5,0,1e10,-73.55692967,-73.44502933,-38.09658800,-37.88187133])# North of
Tirua,11
    rundata.regiondata.regions.append([5,5,0,1e10,-73.51092067,-73.46477000,-38.26197233,-
38.21710700])#Quidico,12
    rundata.regiondata.regions.append([5,5,0,1e10,-73.56257800,-73.50366167,-38.36113267,-38.31139533])#Tirua,13
    rundata.regiondata.regions.append([5,5,0,1e10,-73.88406567,-73.85073233,-38.39548133,-38.36214800])#Isla
Mocha,14
    rundata.regiondata.regions.append([5,5,0,1e10,-73.48295400,-73.36848367,-38.80198667,-38.70124833])#Puerto
Saavedra,15
    rundata.regiondata.regions.append([5,5,0,1e10,-73.30326267,-73.21113467,-39.44663867,-
39.11084433])#Queule,16
    rundata.regiondata.regions.append([5,5,0,1e10,-73.61224667,-73.38245400,-39.96052567,-
39.86720733])#Valdivia,17
    rundata.regiondata.regions.append([5,5,0,1e10,-73.75973333,-73.72640000,-40.55210467,-
40.51877133])#Pucotrihue,18
    rundata.regiondata.regions.append([5,5,0,1e10,-72.97221633,-72.93888300,-41.50269067,-41.46935733])#Puerto
Montt,19
    rundata.regiondata.regions.append([5,5,0,1e10,-73.74162267,-73.70828933,-41.64843267,-
41.61509933])#Maullin,20
    rundata.regiondata.regions.append([5,5,0,1e10,-74.06498367,-73.99647933,-42.07668667,-41.87099900])#North
Chiloe ,21
    rundata.regiondata.regions.append([5,5,0,1e10,-74.21346667,-74.11026933,-42.87939867,-42.61832133])#South
Chiloe,22
    rundata.regiondata.regions.append([5,5,0,1e10,-72.72587467,-72.69254133,-44.74725567,-44.71392233])#Puerto
Aysen,23
    rundata.regiondata.regions.append([5,5,0,1e10,-72.85892967,-72.82559633,-45.41924367,-45.38591033])#Puerto
Aysen,24


    # ----------
    # Gauges:
    # ----------
    rundata.gaugedata.gauges  = []
    # for gauges  append lines of the form  [gaugeno, x, y, t1, t2]
    #rundata.gaugedata.gauges.append([32412, -86.392, -17.975, 0., 1.e10])
    rundata.gaugedata.gauges.append([1000,-71.632051,-33.036314,0,1e10])
    rundata.gaugedata.gauges.append([1001,-71.62858767,-33.04364967,0,1e10])
    rundata.gaugedata.gauges.append([1002,-71.610342,-33.042541,0,1e10])
    rundata.gaugedata.gauges.append([1003,-71.594766,-33.032542,0,1e10])
    rundata.gaugedata.gauges.append([1004,-72.211204,-35.109678,0,1e10])
    rundata.gaugedata.gauges.append([1005,-72.424995,-35.315883,0,1e10])
```

```
    rundata.gaugedata.gauges.append([1006,-72.41962833,-35.31215333,0,1e10])
    rundata.gaugedata.gauges.append([1008,-72.94457333,-36.53787567,0,1e10])
    rundata.gaugedata.gauges.append([1009,-72.967076,-36.630238,0,1e10])
    rundata.gaugedata.gauges.append([1010,-73.056865,-36.63735,0,1e10])
    rundata.gaugedata.gauges.append([1011,-73.10445,-36.72057333,0,1e10])
    rundata.gaugedata.gauges.append([1012,-73.055614,-36.73054133,0,1e10])
    rundata.gaugedata.gauges.append([1013,-73.15707467,-36.72637467,0,1e10])
    rundata.gaugedata.gauges.append([1014,-72.99914033,-36.72783767,0,1e10])
    rundata.gaugedata.gauges.append([1022,-73.15494333,-37.036015,0,1e10])
    rundata.gaugedata.gauges.append([1023,-73.42335333,-37.234248,0,1e10])
    rundata.gaugedata.gauges.append([1024,-73.540263,-37.898538,0,1e10])
    rundata.gaugedata.gauges.append([1025,-73.483688,-37.997792,0,1e10])
    rundata.gaugedata.gauges.append([1026,-73.480821,-38.011591,0,1e10])
    rundata.gaugedata.gauges.append([1027,-73.461696,-38.084088,0,1e10])
    rundata.gaugedata.gauges.append([1028,-73.47727,-38.23294033,0,1e10])
    rundata.gaugedata.gauges.append([1029,-73.492902,-38.24236567,0,1e10])
    rundata.gaugedata.gauges.append([1052,-73.49333,-38.24530567,0,1e10])
    rundata.gaugedata.gauges.append([1053,-73.53907833,-38.328062,0,1e10])
    rundata.gaugedata.gauges.append([1054,-73.54591133,-38.344466,0,1e10])
    rundata.gaugedata.gauges.append([1055,-73.870524,-38.37881467,0,1e10])
    rundata.gaugedata.gauges.append([1056,-73.46712067,-38.717915,0,1e10])
    rundata.gaugedata.gauges.append([1058,-73.42258433,-38.78532,0,1e10])
    rundata.gaugedata.gauges.append([1059,-73.286596,-39.127511,0,1e10])
    rundata.gaugedata.gauges.append([1060,-73.23602633,-39.281829,0,1e10])
    rundata.gaugedata.gauges.append([1061,-73.22780133,-39.358523,0,1e10])
    rundata.gaugedata.gauges.append([1062,-73.246352,-39.427001,0,1e10])
    rundata.gaugedata.gauges.append([1066,-73.41764867,-39.883874,0,1e10])
    rundata.gaugedata.gauges.append([1067,-73.39912067,-39.89045,0,1e10])
    rundata.gaugedata.gauges.append([1068,-73.59558,-39.943859,0,1e10])
    rundata.gaugedata.gauges.append([1069,-73.74306667,-40.535438,0,1e10])
    rundata.gaugedata.gauges.append([1070,-72.95221633,-41.486024,0,1e10])
    rundata.gaugedata.gauges.append([1072,-73.724956,-41.631766,0,1e10])
    rundata.gaugedata.gauges.append([1100,-74.01731267,-41.88784467,0,1e10])
    rundata.gaugedata.gauges.append([1101,-74.048317,-42.06002,0,1e10])
    rundata.gaugedata.gauges.append([1102,-74.126936,-42.634988,0,1e10])
    rundata.gaugedata.gauges.append([1103,-74.1968,-42.862732,0,1e10])
    rundata.gaugedata.gauges.append([1104,-72.709208,-44.72975567,0,1e10])
    rundata.gaugedata.gauges.append([1105,-72.842263,-45.402577,0,1e10])
    return rundata
    # end of function setrun
    # ----------------------


#-------------------
def setgeo(rundata):
#-------------------
    """
    Set GeoClaw  specific runtime parameters.
    For documentation see ....
```

```
"""

try:
    geo_data = rundata.geo_data
except:
    print("*** Error, this rundata has no geo_data attribute")
    raise AttributeError("Missing geo_data attribute")

# == Physics ==
geo_data.gravity = 9.81
geo_data.coordinate_system = 2
geo_data.earth_radius = 6367.5e3

# == Forcing Options
geo_data.coriolis_forcing = False

# == Algorithm and Initial Conditions ==
geo_data.sea_level = 0.0
geo_data.dry_tolerance = 1.e-3
geo_data.friction_forcing = True
geo_data.manning_coefficient =.025
geo_data.friction_depth = 1e6

# Refinement settings
refinement_data = rundata.refinement_data
refinement_data.variable_dt_refinement_ratios = True
refinement_data.wave_tolerance = 1.e-1
refinement_data.deep_depth = 1e2
refinement_data.max_level_deep = 3

# == settopo.data values ==
topo_data = rundata.topo_data
# for topography, append lines of the form
#    [topotype, minlevel, maxlevel, t1, t2, fname]
#topo_path = os.path.join(scratch_dir, 'etopo10min120W60W60S0S.asc')
topo_data.topofiles.append([3, 1, 5, 0., 1.e10, 'bathy/GEBCO2014.asc'])

# == setdtopo.data values ==
dtopo_data = rundata.dtopo_data
# for moving topography, append lines of the form :   (<= 1 allowed for now!)
#   [topotype, minlevel,maxlevel,fname]
dtopo_data.dtopofiles.append([3,4,4,'dtopo.tt3'])
dtopo_data.dt_max_dtopo = 0.2


# == setqinit.data values ==
rundata.qinit_data.qinit_type = 0
rundata.qinit_data.qinitfiles = []
# for qinit perturbations, append lines of the form: (<= 1 allowed for now!)
```

```
    #   [minlev, maxlev, fname]

    # == setfixedgrids.data values ==
    fixed_grids = rundata.fixed_grid_data
    # for fixed grids append lines of the form
    # [t1,t2,noutput,x1,x2,y1,y2,xpoints,ypoints,\
    #  ioutarrivaltimes,ioutsurfacemax]

    return rundata
    # end of function setgeo
    # ----------------------


if __name__ == '__main__':
    # Set up run-time parameters and write all data files.
    import sys
    rundata = setrun(*sys.argv[1:])
    rundata.write()
```

APPENDIX D

Tide gauge observations for AIC analysis

1570

Table D1: The simulated tide gauges corresponding to tsunami observations used in the 1570 AIC analysis

Gauge number	Set run longitude	Set run latitude	Original longitude	Original latitude	Type	Inferred min observed height	Inferred max observed height	AVG Height	Standev of inferred height	Weighted percentage based on standev
1014	-72.99914	-36.72784	-72.99081	-36.73617	Observed	4	5	4.5	0.5	2.00
1015	-73.16522	-36.77093	-73.17249	-36.76566	Inferred	3	5	4	1	1.00
1054	-73.54591	-38.34447	-73.48758	-38.34447	Inferred	2	5	3.5	1.5	0.67

1575

Table D2: The simulated tide gauges corresponding to tsunami observations used in the 1575 AIC analysis

Gauge number	Set run longitude	Set run latitude	Original longitude	Original latitude	Type	Inferred min observed height	Inferred max observed height	AVG Height	Standev of inferred height	Weighted percentage based on standev
1014	-72.99914	-36.72784	-72.99081	-36.73617	Inferred	3	5	4	1	1.00
1015	-73.16522	-36.77093	-73.17249	-36.76566	Inferred	3	5	4	1	1.00
1024	-73.54026	-37.89854	-73.54026	-37.89854	Inferred	4	6	5	1	1.00
1053	-73.53908	-38.32806	-73.53700	-38.32806	Inferred	2	9	5.5	3.5	0.29
1054	-73.54591	-38.34447	-73.48758	-38.34447	Inferred	2	9	5.5	3.5	0.29
1056	-73.46712	-38.71792	-73.47045	-38.71792	Inferred	4	12	8	4	0.25
1058	-73.42258	-38.78532	-73.42675	-38.78532	Inferred	4	12	8	4	0.25
1066	-73.41765	-39.88387	-73.42598	-39.88387	Inferred	3	10.5	6.75	3.75	0.27
1072	-73.72496	-41.63177	-73.67817	-41.57341	Inferred	4.1	10	7.05	2.95	0.34
1100	-74.01731	-41.88784	-74.00065	-41.84618	Inferred	4	6	5	1	1.00
1101	-74.04832	-42.06002	-74.04832	-42.06002	Inferred	7	10	8.5	1.5	0.67
1102	-74.12694	-42.63499	-74.12694	-42.63499	Inferred	5	7	6	1	1.00

1657

Table D3: The simulated tide gauge corresponding to tsunami observations used in the 1657 AIC analysis

Gauge number	Set run longitude	Set run latitude	Original longitude	Original latitude	Type	Inferred min observed height	Inferred max observed height	AVG Height	Standev of inferred height	Weighted percentage based on standev
1014	-72.99914	-36.72784	-72.99081	-36.73617	observed	7.5	8.5	8	0.5	2.00

1730

Table D4: The simulated tide gauges corresponding to tsunami observations used in the 1730 AIC analysis

Gauge number	Set run longitude	Set run latitude	Original longitude	Original latitude	Type	Inferred min observed height	Inferred max observed height	AVG Height	Standev of inferred height	Weighted percentage based on standev
1000	-71.63205	-33.03631	-71.63205	-33.03631	Observed	8.5	9.5	9	0.5	2.00
1001	-71.62859	-33.04365	-71.62942	-33.03948	Observed	9.5	10.5	10	0.5	2.00
1003	-71.59477	-33.03254	-71.60727	-33.04879	Observed	8.5	9.5	9	0.5	2.00
1011	-73.10445	-36.72057	-73.10445	-36.72474	Inferred	6	8	7	1	1.00
1014	-72.99914	-36.72784	-72.99081	-36.73617	Observed	7.5	8.5	8	0.5	2.00
1066	-73.41765	-39.88387	-73.42598	-39.88387	Inferred	5	8	6.5	1.5	0.67
1106	-71.49623	-32.75048	_-71.465166	-32.75595	Inferred	8	12	10	2	0.50

1751

Table D5: The simulated tide gauges corresponding to tsunami observations used in the 1751 AIC analysis

Gauge number	Set run longitude	Set run latitude	Original longitude	Original latitude	Type	Inferred min observed height	Inferred max observed height	AVG Height	Standev of inferred height	Weighted percentage based on standev
1008	-72.94457	-36.53788	-72.93624	-36.54621	Observed	3	4	3.5	0.5	2.00
1014	-72.99914	-36.72784	-72.99081	-36.73617	Observed	9.5	10.5	10	0.5	2.00
1028	-73.47727	-38.23294	-73.47727	-38.22961	Inferred	4	10	7	3	0.33
1029	-73.49290	-38.24237	-73.49290	-38.25070	Inferred	4	10	7	3	0.33
1052	-73.49333	-38.24531	-73.49333	-38.25364	Inferred	4	10	7	3	0.33
1053	-73.53908	-38.32806	-73.53700	-38.32806	Inferred	2	10	6	4	0.25
1054	-73.54591	-38.34447	-73.48758	-38.34447	Inferred	2	10	6	4	0.25

1822

Table D6: The simulated tide gauges corresponding to tsunami observations used in the 1822 AIC analysis

Gauge number	Set run longitude	Set run latitude	Original longitude	Original latitude	Type	Inferred min observed height	Inferred max observed height	AVG Height	Standev of inferred height	Weighted percentage based on standev
1002	-71.61034	-33.04254	-71.99600	-33.04271	Observed	3.1	4.1	3.6	0.5	2.00
1066	-73.41765	-39.88387	-73.42598	-39.88387	Inferred	0.5	2	1.25	0.75	1.33
1106	-71.49623	-32.75048	Ê-71.465166	-32.75595	Inferred	0.5	2	1.25	0.75	1.33

1835

Table D7: The simulated tide gauges corresponding to tsunami observations used in the 1835 AIC analysis

Gauge number	Set run longitude	Set run latitude	Original longitude	Original latitude	Type	Inferred min observed height	Inferred max observed height	AVG Height	Standev of inferred height	Weighted percentage based on standev
1002	-71.61034	-33.04254	-71.99600	-33.04271	Observed	0.1	1.1	0.5	0.5	2.00
1006	-72.41963	-35.31215	-72.41130	-35.31632	Observed	3	4	3.5	0.5	2.00
1008	-72.94457	-36.53788	-72.93624	-36.54621	Observed	23.5	24.5	24	0.5	2.00
1009	-72.96708	-36.63024	-72.96333	-36.61774	Observed	3.5	4.5	4	0.5	2.00
1010	-73.05687	-36.63735	-73.05999	-36.63735	Observed	8.5	9.5	9	0.5	2.00
1011	-73.10445	-36.72057	-73.10445	-36.72474	Observed	8.5	9.5	9	0.5	2.00
1012	-73.05561	-36.73054	-73.05561	-36.73471	Observed	14.5	15.5	15	0.5	2.00
1013	-73.15707	-36.72637	-73.16166	-36.73471	Inferred	3	9.5	6.25	3.25	0.31
1014	-72.99914	-36.72784	-72.99081	-36.73617	Inferred	3	9.5	6.25	3.25	0.31
1022	-73.15494	-37.03602	-73.15494	-37.03602	Inferred	3	9	6	3	0.33
1023	-73.42335	-37.23425	-73.42752	-37.23425	Inferred	3	8	5.5	2.5	0.40
1028	-73.47727	-38.23294	-73.47727	-38.22961	Inferred	4	8	6	2	0.50
1029	-73.49290	-38.24237	-73.49290	-38.25070	Inferred	4	8	6	2	0.50
1052	-73.49333	-38.24531	-73.49333	-38.25364	Inferred	4	8	6	2	0.50
1055	-73.87052	-38.37881	-73.86740	-38.37465	Inferred	6	8	7	1	1.00
1066	-73.41765	-39.88387	-73.42598	-39.88387	Inferred	3	6	4.5	1.5	0.67
1101	-74.04832	-42.06002	-74.04832	-42.06002	inferred	0.25	2	1.125	0.875	1.14

1837

Table D8: The simulated tide gauges corresponding to tsunami observations used in the 1837 AIC analysis

Gauge number	Set run longitude	Set run latitude	Original longitude	Original latitude	Type	Inferred min observed height	Inferred max observed height	AVG Height	Standev of inferred height	Weighted percentage based on standev
1002	-71.61034	-33.04254	-71.99600	-33.04271	Observed	0.5	1.5	1	0.5	2.00
1012	-73.05561	-36.73054	-73.05561	-36.73471	Inferred	3	5	4	1	1.00
1067	-73.39912	-39.89045	-33.39495	-39.89045	Observed	1.5	2.5	2	0.5	2.00
1066	-73.41765	-39.88387	-73.42598	-39.88387	Observed	1.00E-15	1.00E-14	1.00E-13	0.5	2.00
1072	-73.72496	-41.63177	-73.67817	-41.57341	Inferred	4.1	10	7.05	2.95	0.34
1100	-74.01731	-41.88784	-74.00065	-41.84618	Inferred	3	5	4	1	1.00
1101	-74.04832	-42.06002	-74.04832	-42.06002	Inferred	1.00E-15	1.00E-14	1.00E-13	0.5	2.00
1103	-74.19680	-42.86273	-74.19680	-42.86273	Inferred	3	7	5	2	0.50

1871

Table D9: The simulated tide gauge corresponding to tsunami observations used in the 1871 AIC analysis

Gauge number	Set run longitude	Set run latitude	Original longitude	Original latitude	Type	Inferred min observed height	Inferred max observed height	AVG Height	Standev of inferred height	Weighted percentage based on standev
1002	-71.61034	-33.04254	-71.61034	-33.04254	Observed	0.5	1.5	1	0.5	2.00

1871b

Table D10: The simulated tide gauge corresponding to tsunami observations used in the 1871b AIC analysis

Gauge number	Set run longitude	Set run latitude	Original longitude	Original latitude	Type	Inferred min observed height	Inferred max observed height	AVG Height	Standev of inferred height	Weighted percentage based on standev
1070	-72.95222	-41.48602	-72.96388	-41.48602	Observed	0.5	1.5	1	0.5	2.00

1898

Table D11: The simulated tide gauge corresponding to tsunami observations used in the 1898 AIC analysis

Gauge number	Set run longitude	Set run latitude	Original longitude	Original latitude	Type	Inferred min observed height	Inferred max observed height	AVG Height	Standev of inferred height	Weighted percentage based on standev
1012	-73.05561	-36.73054	-73.05561	-36.73471	Observed	0.2	1.2	0.7	0.5	2.00

1906

Table D12: The simulated tide gauges corresponding to tsunami observations used in the 1906 AIC analysis

Gauge number	Set run longitude	Set run latitude	Original longitude	Original latitude	Type	Inferred min observed height	Inferred max observed height	AVG Height	Standev of inferred height	Weighted percentage based on standev
1002	-71.61034	-33.04254	-71.99600	-33.04271	Observed	3.1	4.1	3.6	0.5	2.00
1004	-72.21120	-35.10968	-72.21120	-35.10968	Inferred	0.5	2	1.25	0.75	1.33
1005	-72.42500	-35.31588	-72.42500	-35.31588	Inferred	0.5	2	1.25	0.75	1.33
1006	-72.41963	-35.31215	-72.41130	-35.31632	Observed	0.5	1.5	1	0.5	2.00
1009	-72.96708	-36.63024	-72.96333	-36.61774	Observed	1	2	1.5	0.5	2.00
1011	-73.10445	-36.72057	-73.10445	-36.72474	Observed	0.9	1.9	1.4	0.5	2.00
1014	-72.99914	-36.72784	-72.99081	-36.73617	Observed	1	2	1.5	0.5	2.00
1022	-73.15494	-37.03602	-73.14661	-37.03602	Inferred	0.5	2.5	1.5	1	1.00
1107	-71.51217	-31.91211	-71.51158	-31.90929	Inferred	1	3	2	1	1.00

1920

Table D13: The simulated tide gauges corresponding to tsunami observations used in the 1920 AIC analysis

Gauge number	Set run longitude	Set run latitude	Original longitude	Original latitude	Type	Inferred min observed height	Inferred max observed height	AVG Height	Standev of inferred height	Weighted percentage based on standev
1011	-73.10445	-36.72057	-73.10445	-36.72474	Observed	0.9	1.9	1.4	0.5	2.00
1025	-73.48369	-37.99779	-73.47869	-37.99779	Observed	0.9	1.9	1.4	0.5	2.00
1026	-73.48082	-38.01159	-73.48082	-38.01159	Observed	0.9	1.9	1.4	0.5	2.00
1027	-73.46170	-38.08409	-73.46170	-38.08409	Observed	0.9	1.9	1.4	0.5	2.00

1927

Table D14: The simulated tide gauges corresponding to tsunami observations used in the 1927 AIC analysis

Gauge number	Set run longitude	Set run latitude	Original longitude	Original latitude	Type	Inferred min observed height	Inferred max observed height	AVG Height	Standev of inferred height	Weighted percentage based on standev
1104	-72.70921	-44.72976	-72.68421	-44.73059	Observed	2.3	3.3	2.8	0.5	2.00
1105	-72.84226	-45.40258	-72.82976	-45.40258	Inferred	3	5	4	1	1.00

1928

Table D15: The simulated tide gauges corresponding to tsunami observations used in the 1928 AIC analysis

Gauge number	Set run longitude	Set run latitude	Original longitude	Original latitude	Type	Inferred min observed height	Inferred max observed height	AVG Height	Standev of inferred height	Weighted percentage based on standev
1004	-72.21120	-35.10968	-72.21120	-35.10968	inferred	0.5	2.5	1.5	1	1.00
1006	-72.41963	-35.31215	-72.41130	-35.31632	observed	1	2	1.5	0.5	2.00

1943

Table D16: The simulated tide gauge corresponding to tsunami observations used in the 1943 AIC analysis

Gauge number	Set run longitude	Set run latitude	Original longitude	Original latitude	Type	Inferred min observed height	Inferred max observed height	AVG Height	Standev of inferred height	Weighted percentage based on standev
1107	-71.51217	-31.91211	-71.51158	-31.90929	Observed	0.5	1.5	1	0.5	2.00

1960

Table D17: The simulated tide gauges corresponding to tsunami observations used in the 1960 AIC analysis

Gauge number	Set run longitude	Set run latitude	Original longitude	Original latitude	Type	Inferred min observed height	Inferred max observed height	AVG Height	Standev of inferred height	Weighted percentage based on standev
1006	-72.41963	-35.31215	-72.41130	-35.31632	Observed	2	3	2.5	0.5	2.00
1011	-73.10445	-36.72057	-73.10445	-36.72474	Observed	4.6	5.6	5.1	0.5	2.00
1013	-73.15707	-36.72637	-73.16166	-36.73471	Inferred	3	5	4	1	1.00
1014	-72.99914	-36.72784	-72.99081	-36.73617	Inferred	3	5	4	1	1.00
1015	-73.16522	-36.77093	-73.17249	-36.76566	Inferred	3	5	4	1	1.00
1022	-73.15494	-37.03602	-73.14661	-37.03602	Observed	1.5	2.5	2	0.5	2.00
1023	-73.42335	-37.23425	-73.42752	-37.23425	Inferred	3	5	4	1	1.00
1024	-73.54026	-37.89854	-73.54026	-37.89854	Inferred	4	6	5	1	1.00
1028	-73.47727	-38.23294	-73.47727	-38.22961	Inferred	4	11	7.5	3.5	0.29
1029	-73.49290	-38.24237	-73.49290	-38.25070	Inferred	4	11	7.5	3.5	0.29
1052	-73.49333	-38.24531	-73.49333	-38.25364	Inferred	4	11	7.5	3.5	0.29
1053	-73.53908	-38.32806	-73.53700	-38.32806	Inferred	2	9	5.5	3.5	0.29
1054	-73.54591	-38.34447	-73.48758	-38.34447	Inferred	2	9	5.5	3.5	0.29
1055	-73.87052	-38.37881	-73.86740	-38.37465	Observed	24.5	25.5	25	0.5	2.00
1056	-73.46712	-38.71792	-73.47045	-38.71792	Observed	11	12	11.5	0.5	2.00
1058	-73.42258	-38.78532	-73.42675	-38.78532	Observed	11	12	11.5	0.5	2.00
1059	-73.28660	-39.12751	-73.28660	-39.12751	Inferred	4	8	6	2	0.50
1060	-73.23603	-39.28183	-73.24019	-39.28183	Observed	14.5	15.5	15	0.5	2.00
1061	-73.22780	-39.35852	-73.23197	-39.35852	Inferred	6	8	7	1	1.00
1062	-73.24635	-39.42700	-73.24635	-39.42700	Inferred	8	15	11.5	3.5	0.29
1066	-73.41765	-39.88387	-73.42598	-39.88387	Observed	9.5	10.5	10	0.5	2.00

Gauge number	Set run longitude	Set run latitude	Original longitude	Original latitude	Type	Inferred min observed height	Inferred max observed height	AVG Height	Standev of inferred height	Weighted percentage based on standev
1067	-73.39912	-39.89045	-33.39495	-39.89045	Observed	9.5	10.5	10	0.5	2.00
1068	-73.59558	-39.94386	-73.59558	-39.94386	Inferred	6	8	7	1	1.00
1069	-73.74307	-40.53544	-73.74327	-40.53536	Inferred	7	8	7.5	0.5	2.00
1072	-73.72496	-41.63177	-73.67817	-41.57341	Observed	9	10	9.5	0.5	2.00
1100	-74.01731	-41.88784	-74.00065	-41.84618	Observed	4.5	5.5	5	0.5	2.00
1101	-74.04832	-42.06002	-74.04832	-42.06002	Inferred	7	12	9.5	2.5	0.40
1103	-74.19680	-42.86273	-74.19680	-42.86273	Inferred	5	12	8.5	3.5	0.29
1104	-72.70921	-44.72976	-72.68421	-44.73059	Observed	2.3	3.3	2.8	0.5	2.00
1105	-72.84226	-45.40258	-72.82976	-45.40258	Observed	2.5	3.5	3	0.5	2.00

APPENDIX E

The following 17 figures each illustrate a specific overview of all source models in the AIC statistical analysis for a given earthquake event. Earthquake source models with lower Δ_i values were selected by the AIC equations as better matches to a specific event within the historical record based on the observations available.

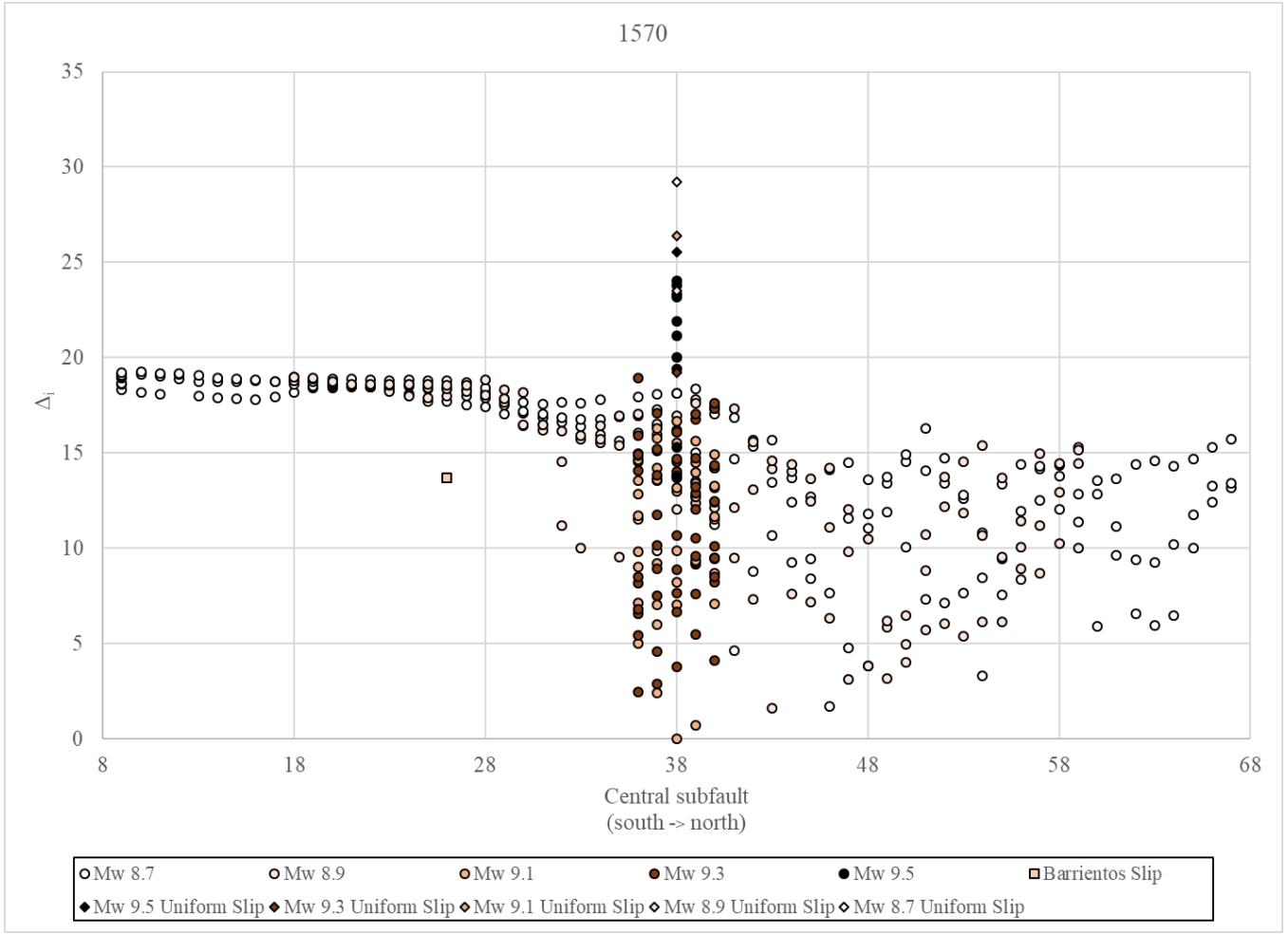

Appendix E_1: The Δ_i versus central subfault of rupture for all tsunami simulations relative to the lowest AIC value calculated from observations of the 1570 historical tsunami. Earthquake magnitude positively correlates to darker colored data points.

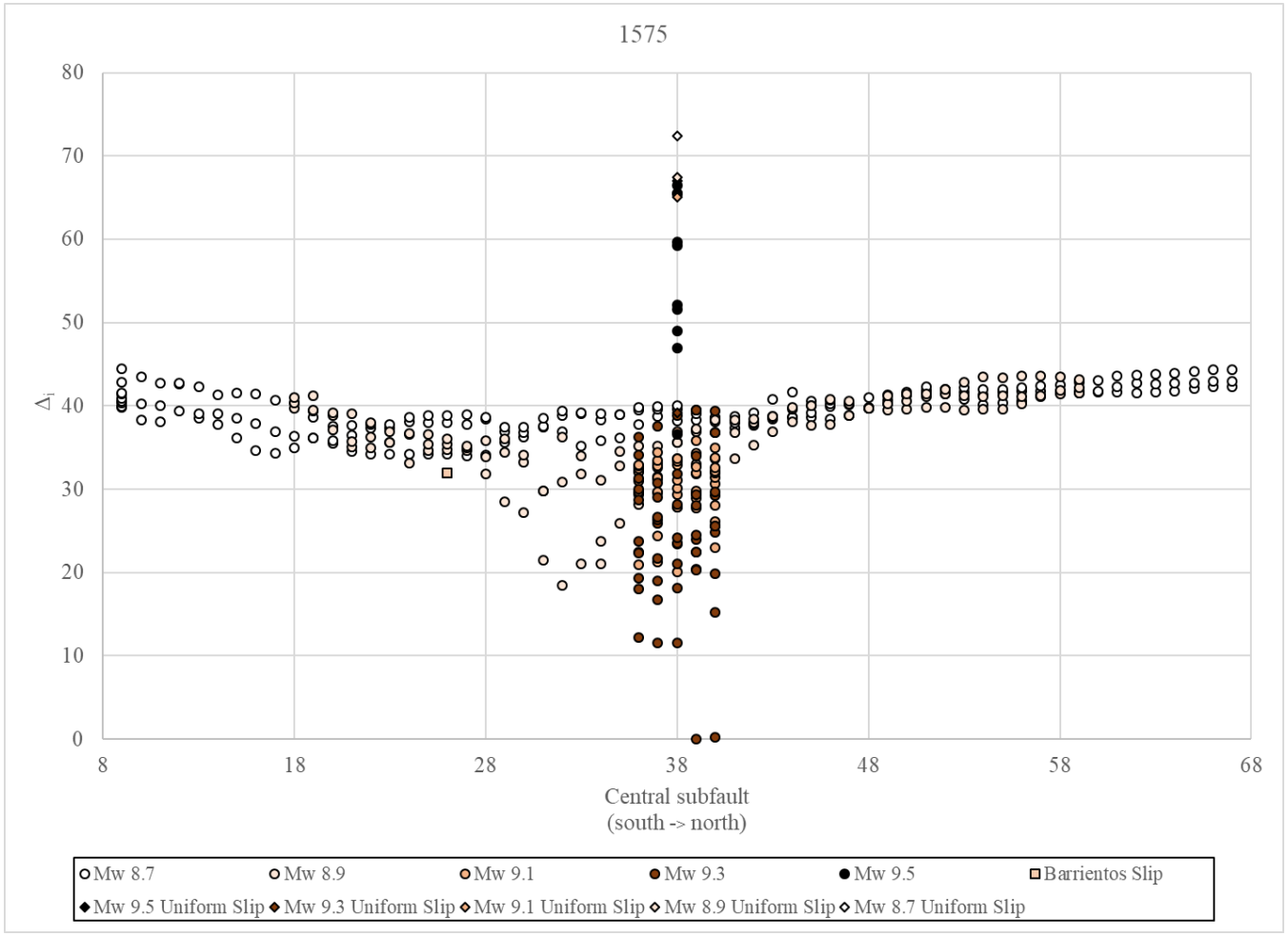

Appendix E_2: The Δ_i versus central subfault of rupture for all tsunami simulations relative to the lowest AIC value calculated from observations of the 1575 historical tsunami. Earthquake magnitude positively correlates to darker colored data points.

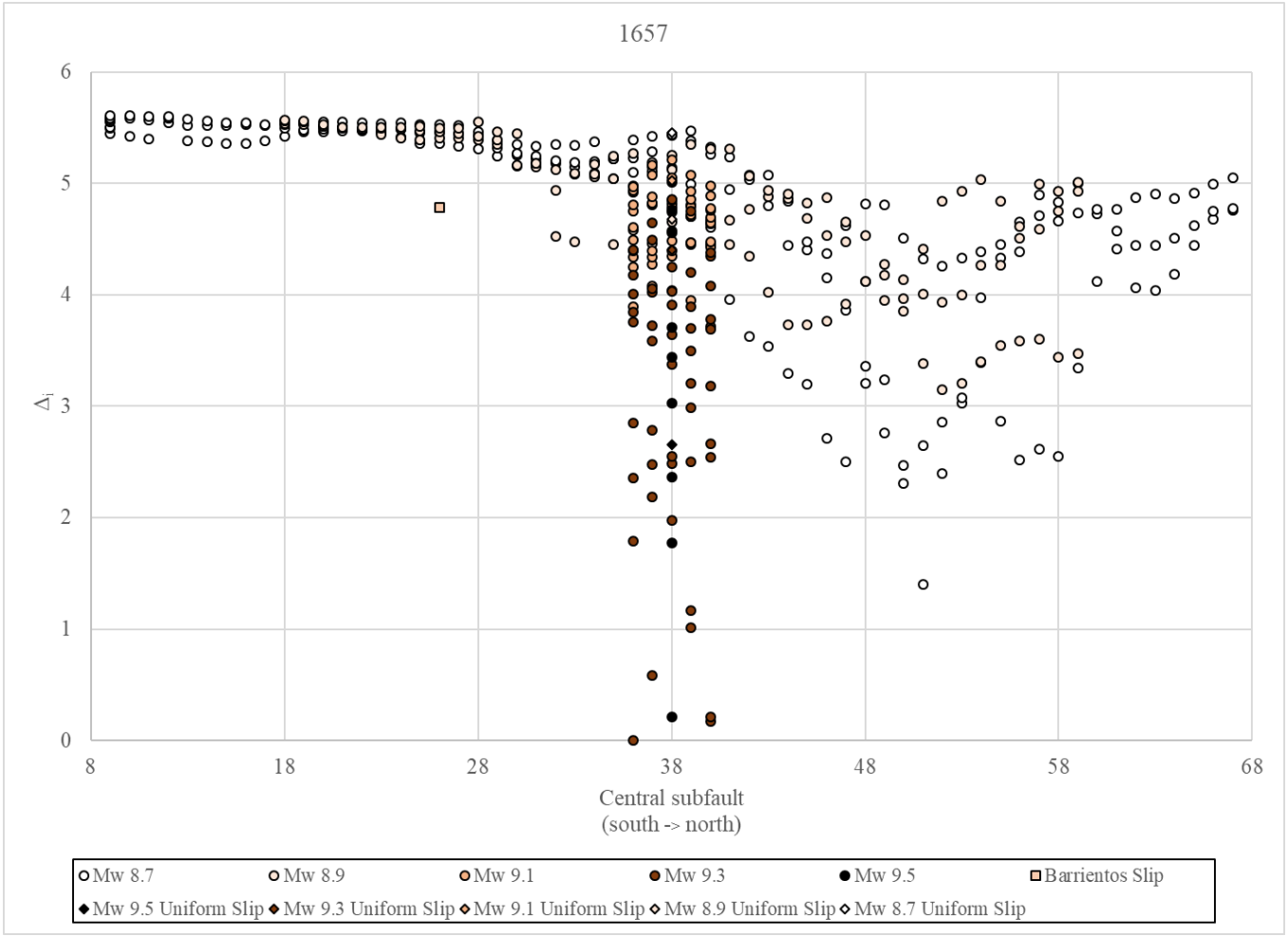

Appendix E_3: The Δ_i versus central subfault of rupture for all tsunami simulations relative to the lowest AIC value calculated from observations of the 1657 historical tsunami. Earthquake magnitude positively correlates to darker colored data points.

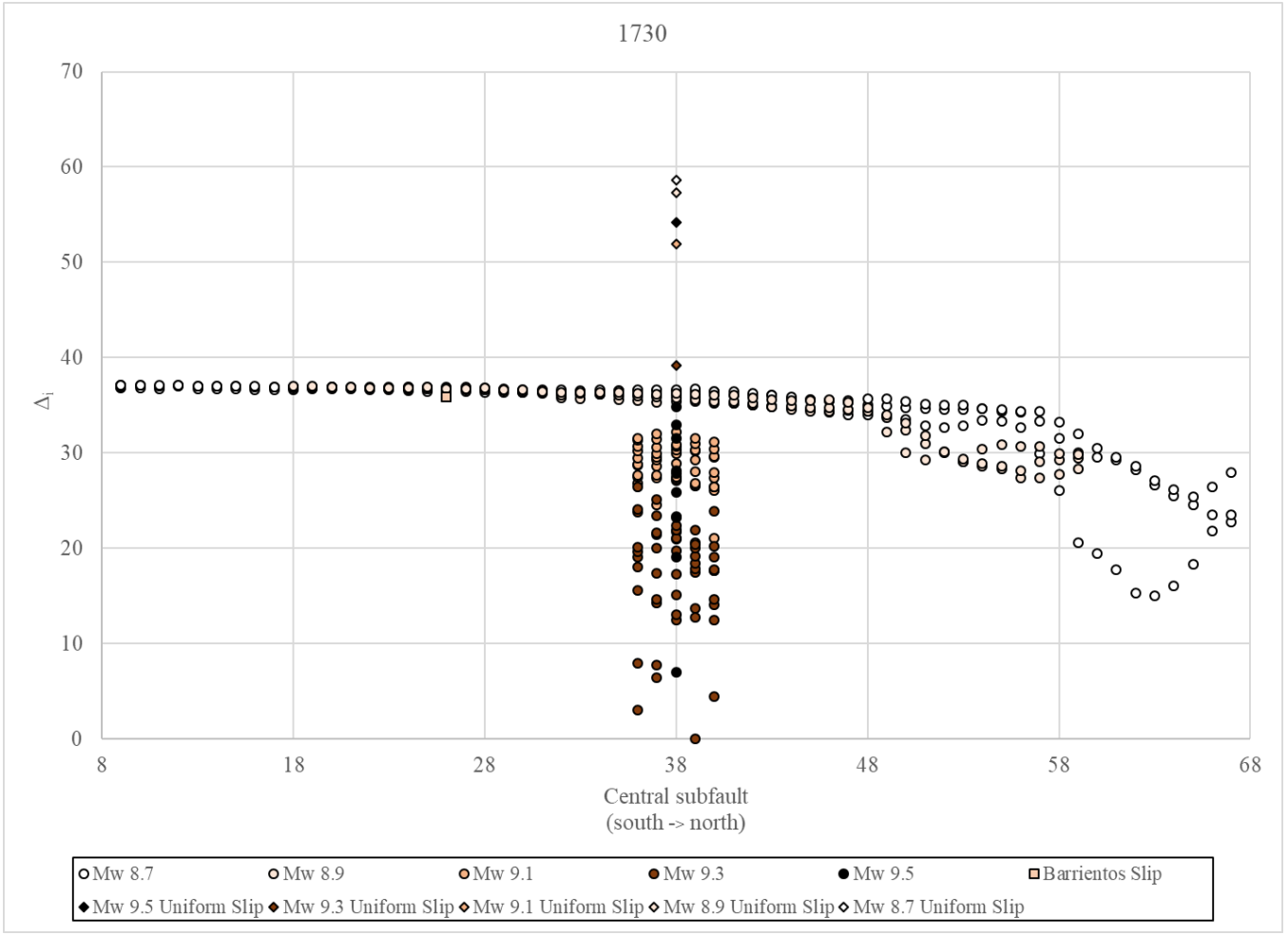

Appendix E_4: The Δ_i versus central subfault of rupture for all tsunami simulations relative to the lowest AIC value calculated from observations of the 1730 historical tsunami. Earthquake magnitude positively correlates to darker colored data points.

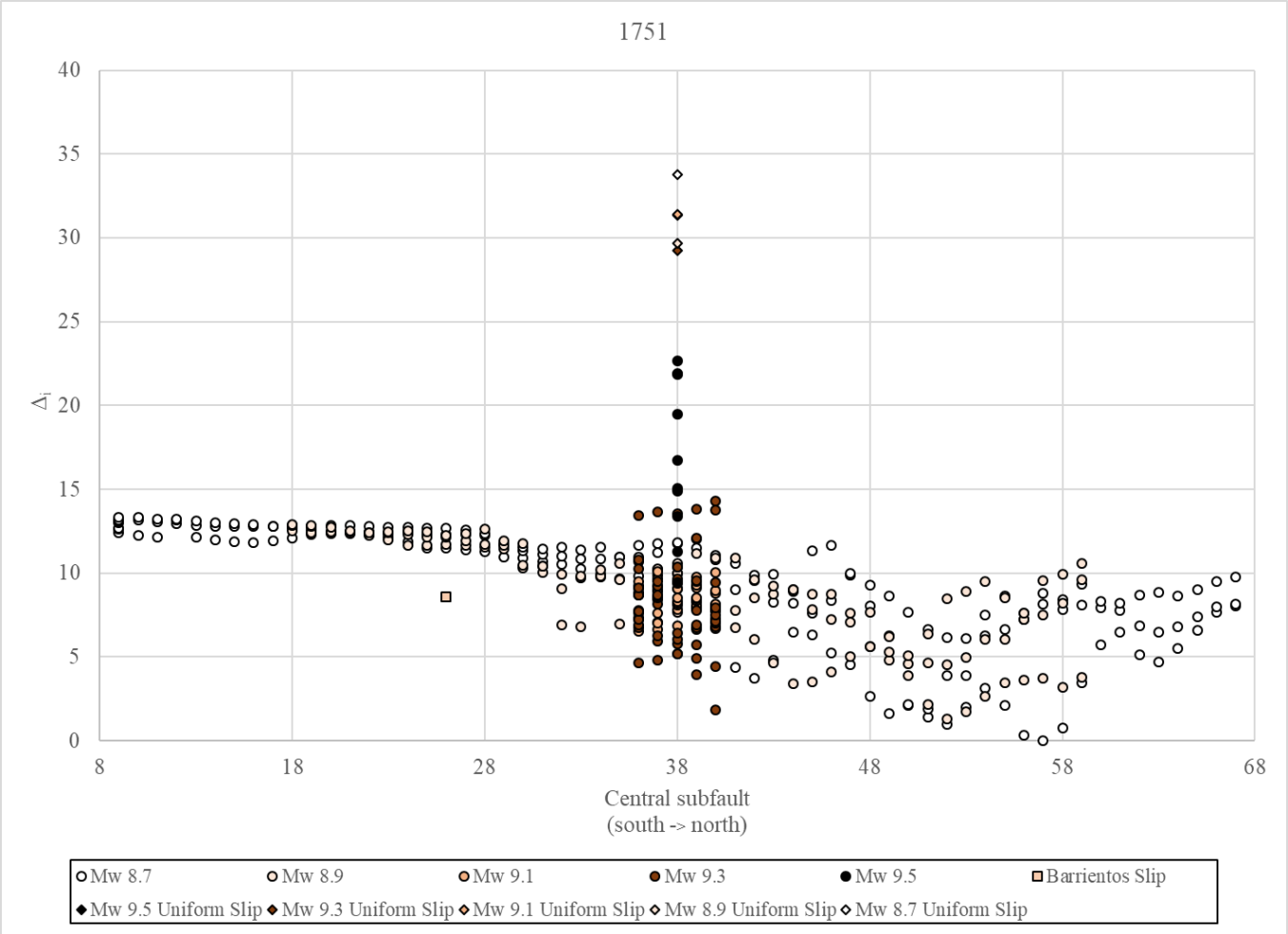

Appendix E_5: The Δ_i versus central subfault of rupture for all tsunami simulations relative to the lowest AIC value calculated from observations of the 1751 historical tsunami. Earthquake magnitude positively correlates to darker colored data points.

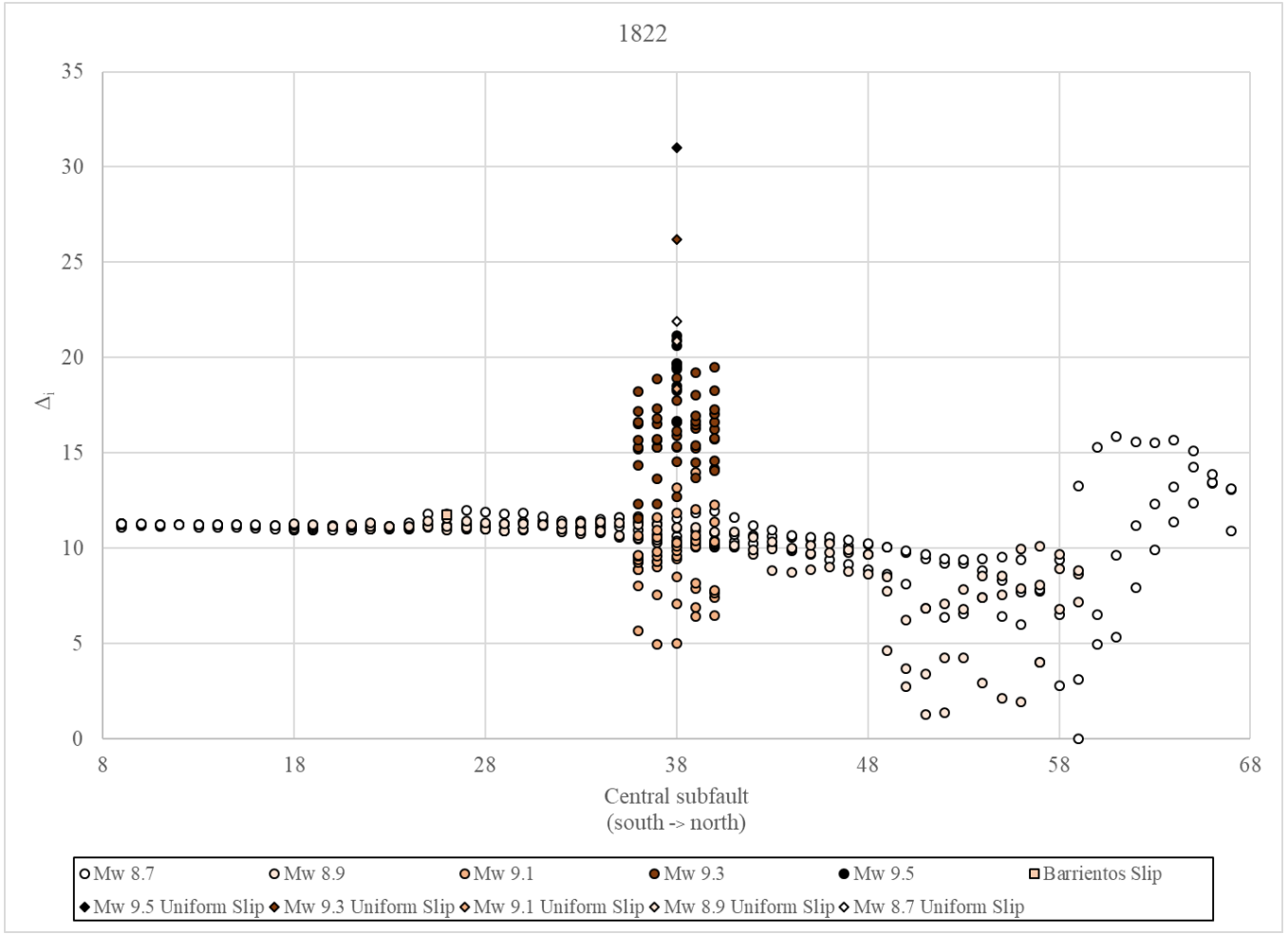

Appendix E_6: The Δ_i versus central subfault of rupture for all tsunami simulations relative to the lowest AIC value calculated from observations of the 1822 historical tsunami. Earthquake magnitude positively correlates to darker colored data points.

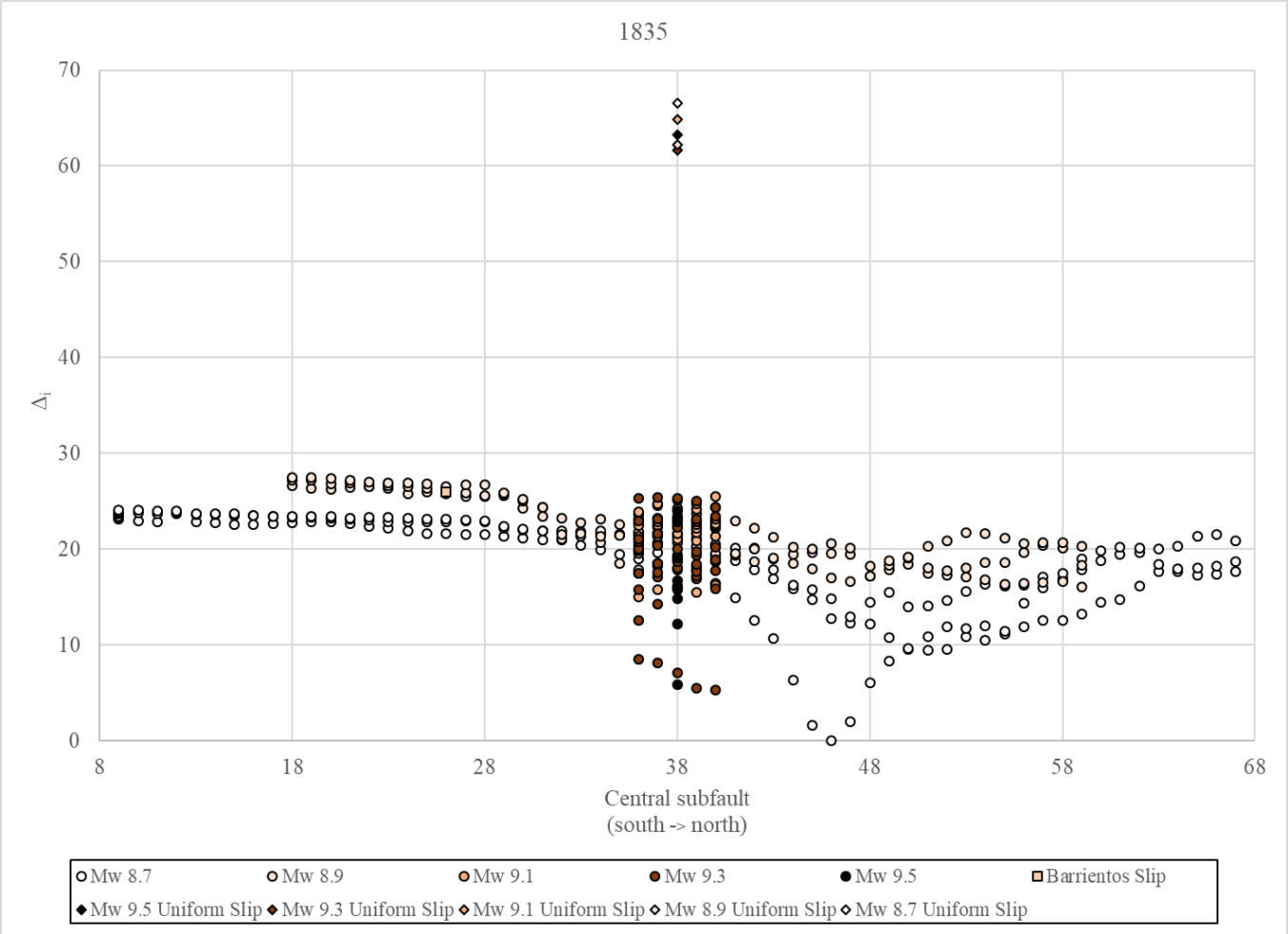

Appendix E_7: The Δ_i versus central subfault of rupture for all tsunami simulations relative to the lowest AIC value calculated from observations of the 1835 historical tsunami. Earthquake magnitude positively correlates to darker colored data points.

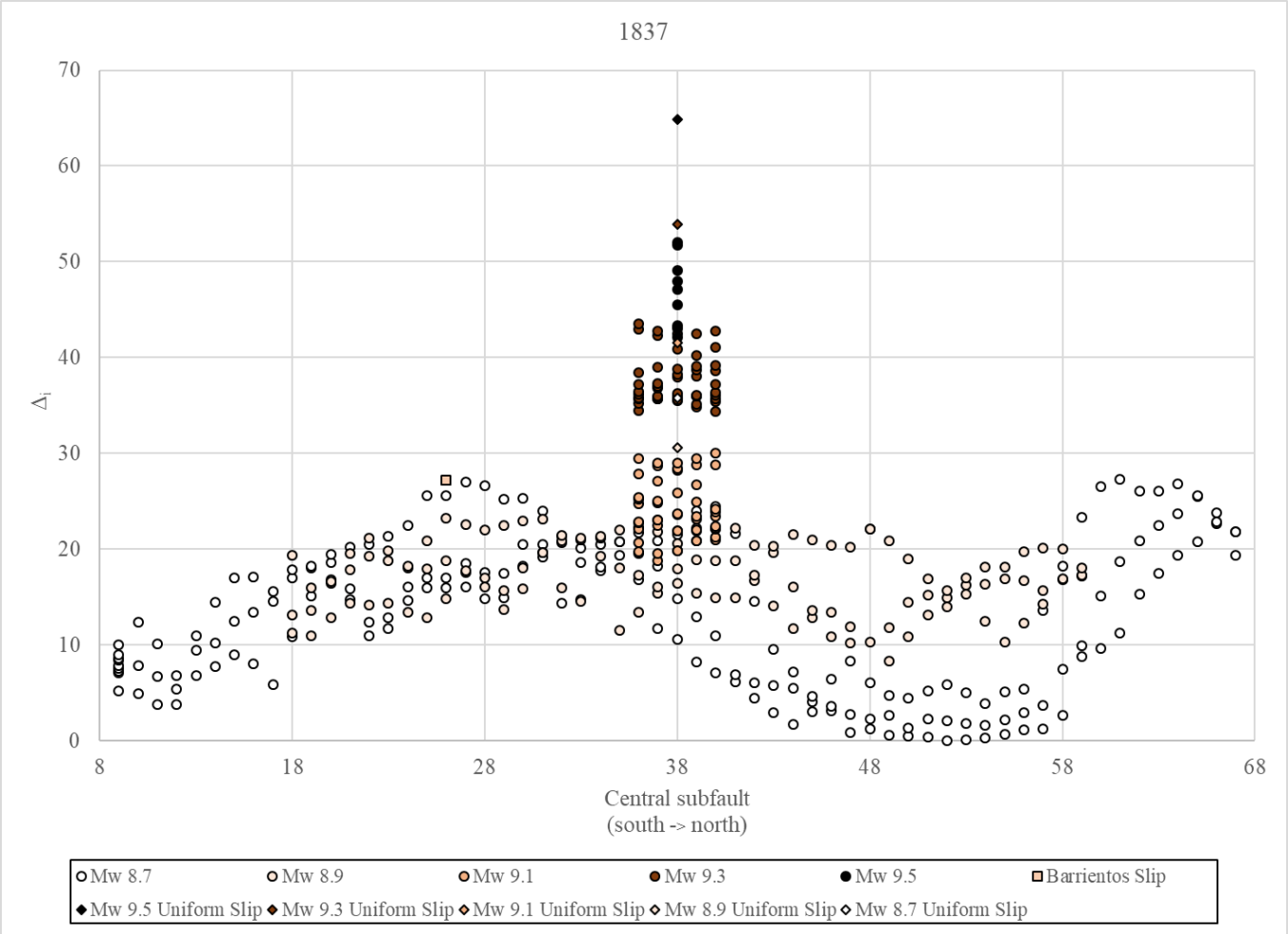

Appendix E_8: The Δ_i versus central subfault of rupture for all tsunami simulations relative to the lowest AIC value calculated from observations of the 1835 historical tsunami. Earthquake magnitude positively correlates to darker colored data points.

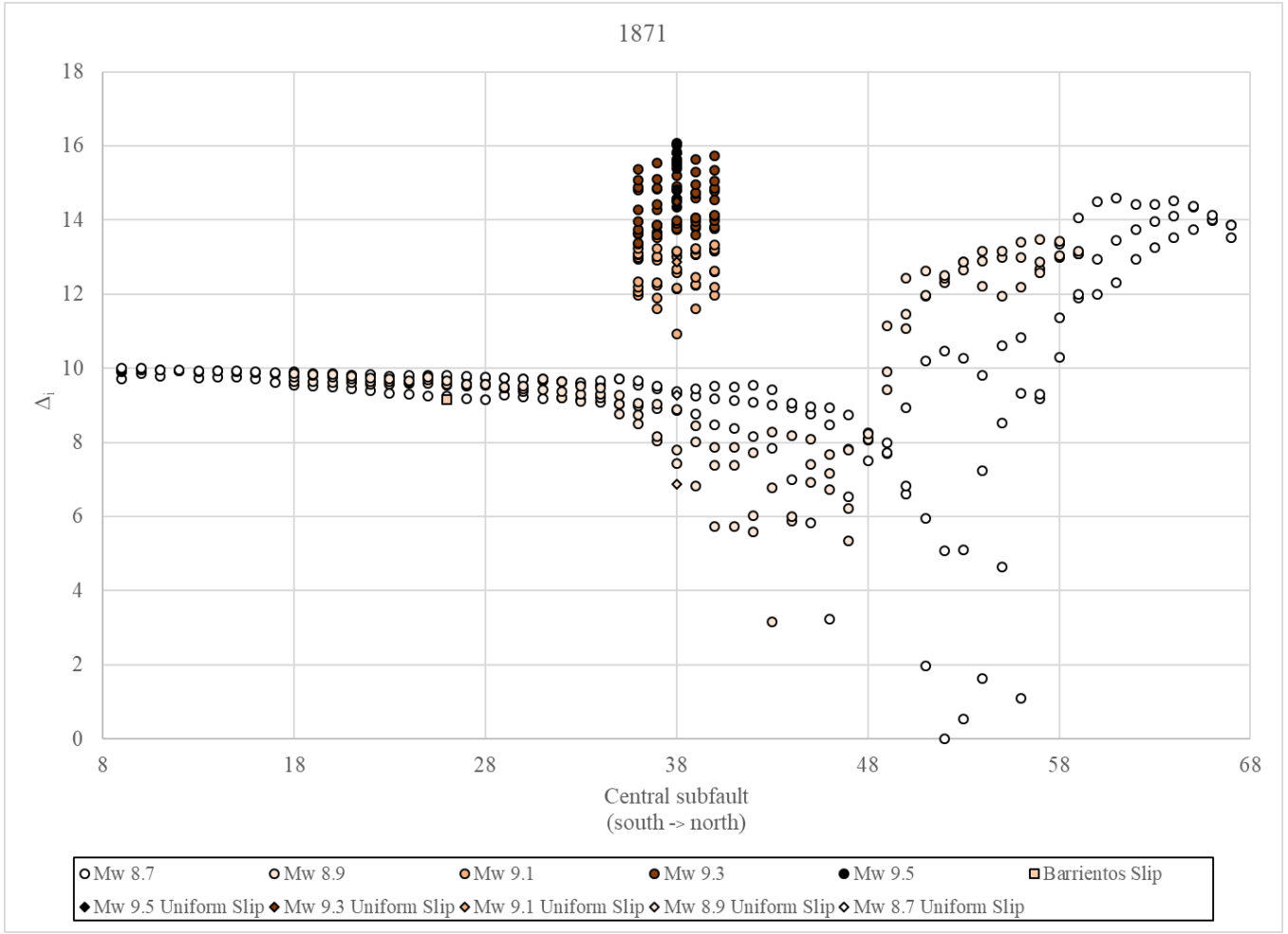

Appendix E_9: The Δ_i versus central subfault of rupture for all tsunami simulations relative to the lowest AIC value calculated from observations of the 1871 historical tsunami. Earthquake magnitude positively correlates to darker colored data points.

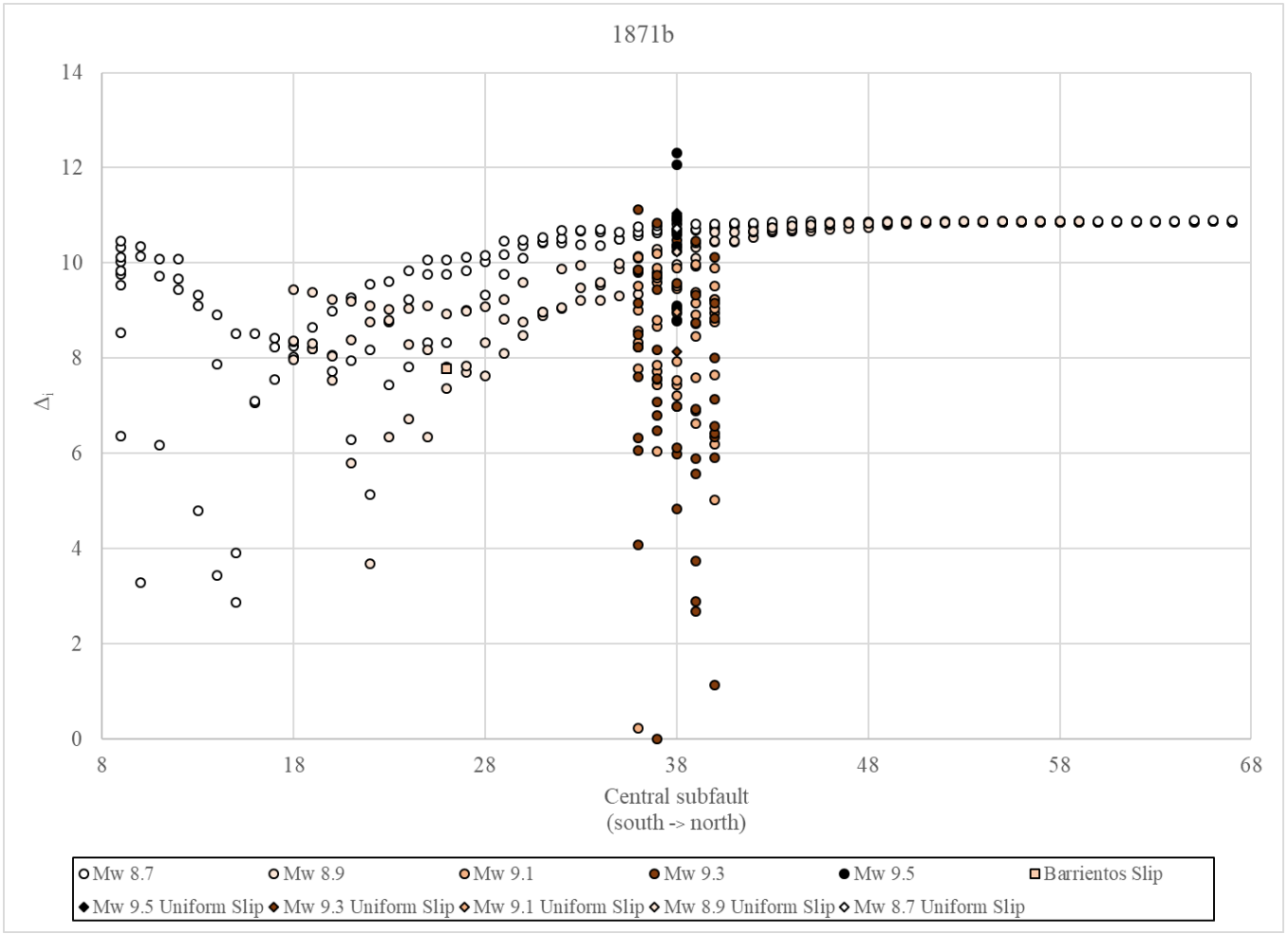

Appendix E_{10}: The Δ_i versus central subfault of rupture for all tsunami simulations relative to the lowest AIC value calculated from observations of the 1871b historical tsunami. Earthquake magnitude positively correlates to darker colored data points.

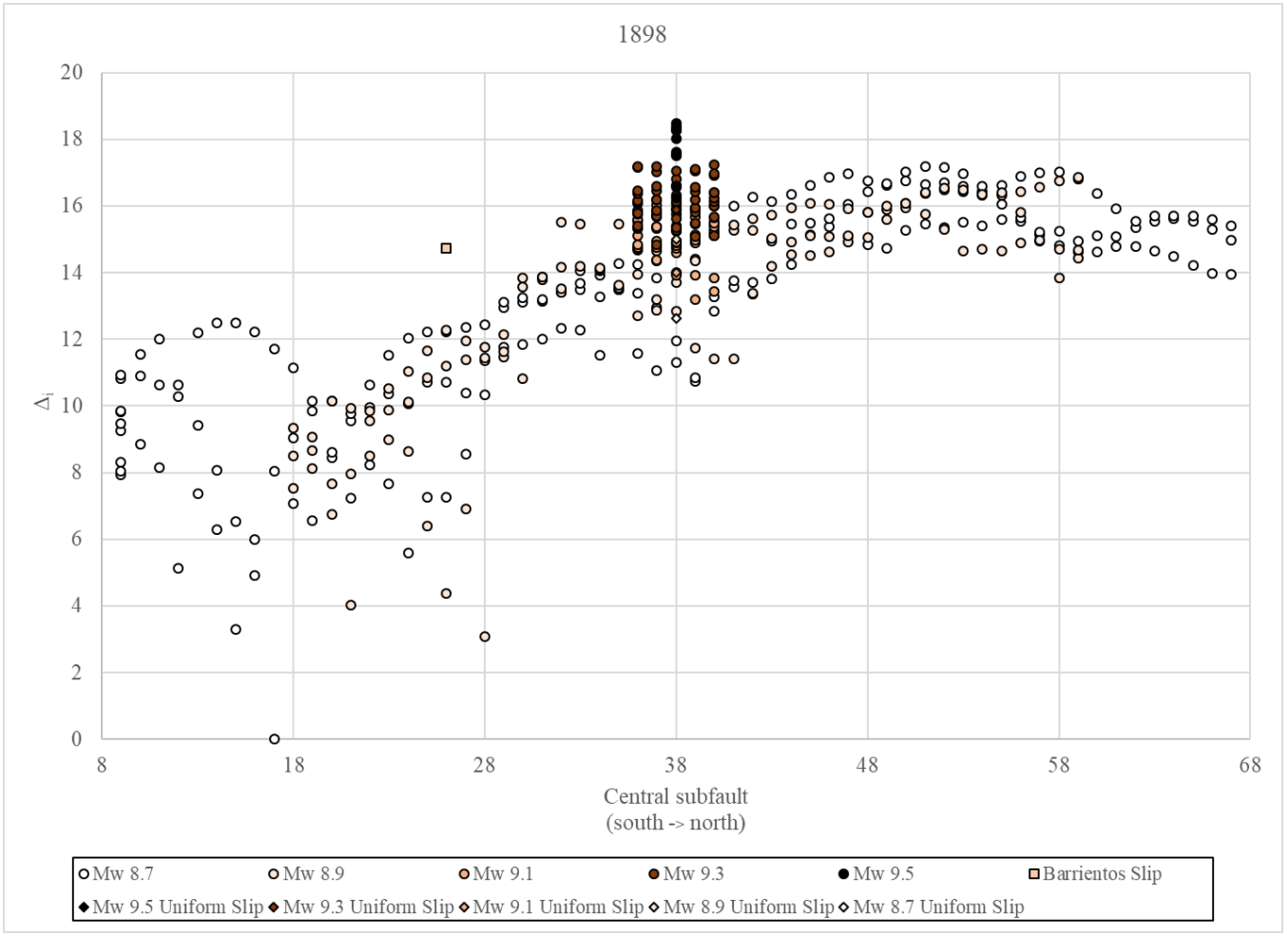

Appendix E_{11}: The Δ_i versus central subfault of rupture for all tsunami simulations relative to the lowest AIC value calculated from observations of the 1898 historical tsunami. Earthquake magnitude positively correlates to darker colored data points.

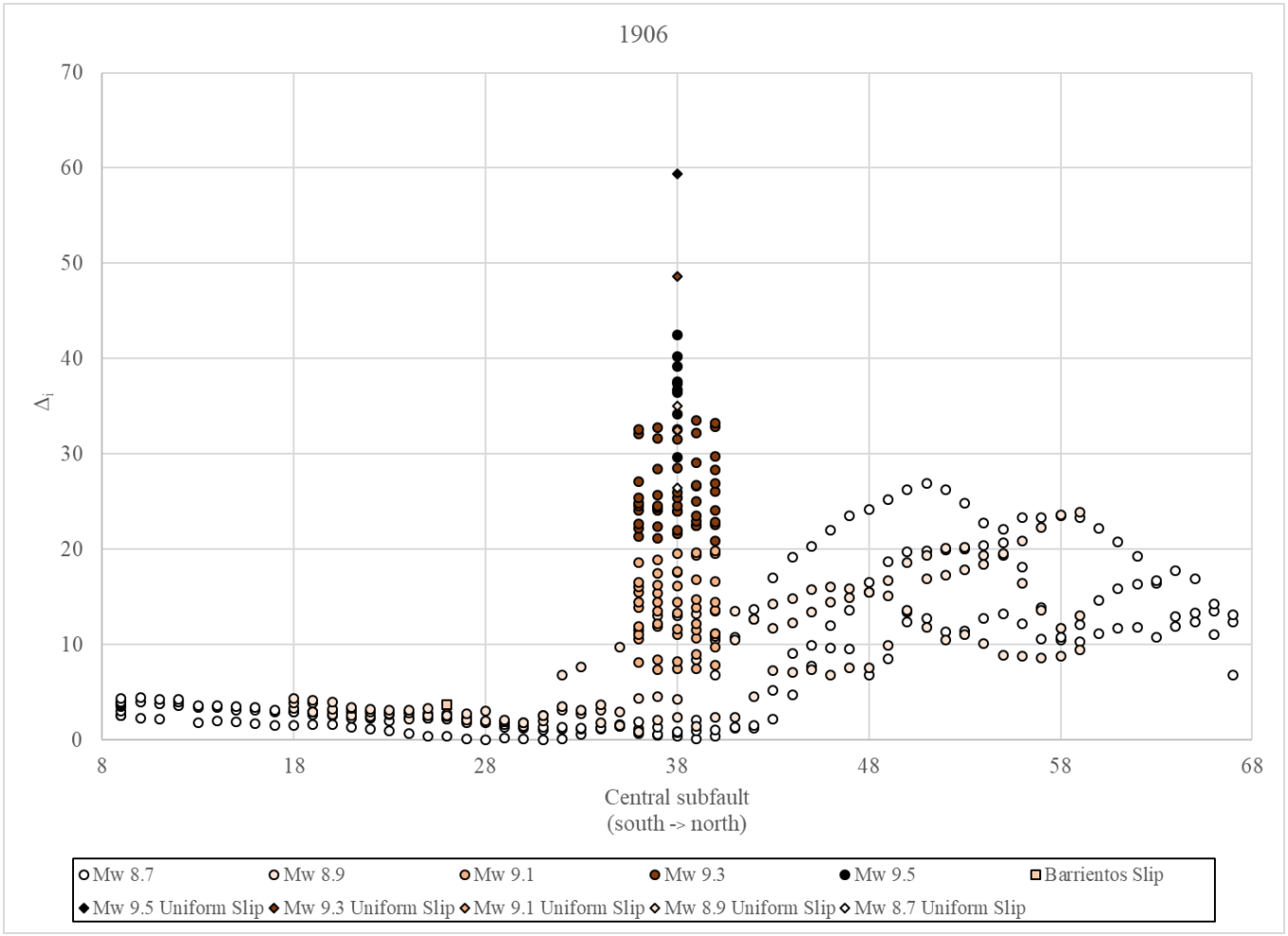

Appendix E_{12}: The Δ_i versus central subfault of rupture for all tsunami simulations relative to the lowest AIC value calculated from observations of the 1906 historical tsunami. Earthquake magnitude positively correlates to darker colored data points.

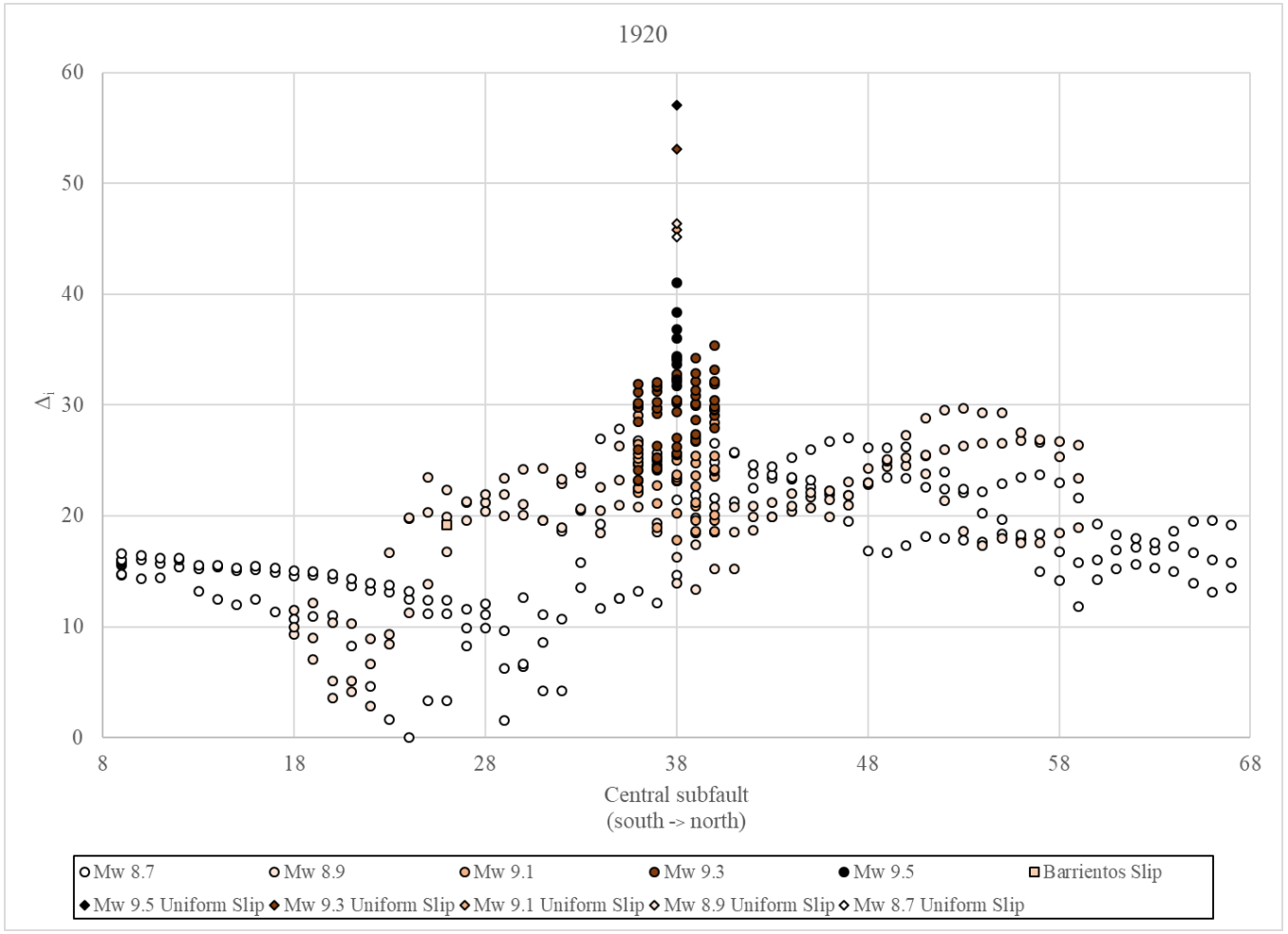

Appendix E_{13}: The Δ_i versus central subfault of rupture for all tsunami simulations relative to the lowest AIC value calculated from observations of the 1920 historical tsunami. Earthquake magnitude positively correlates to darker colored data points.

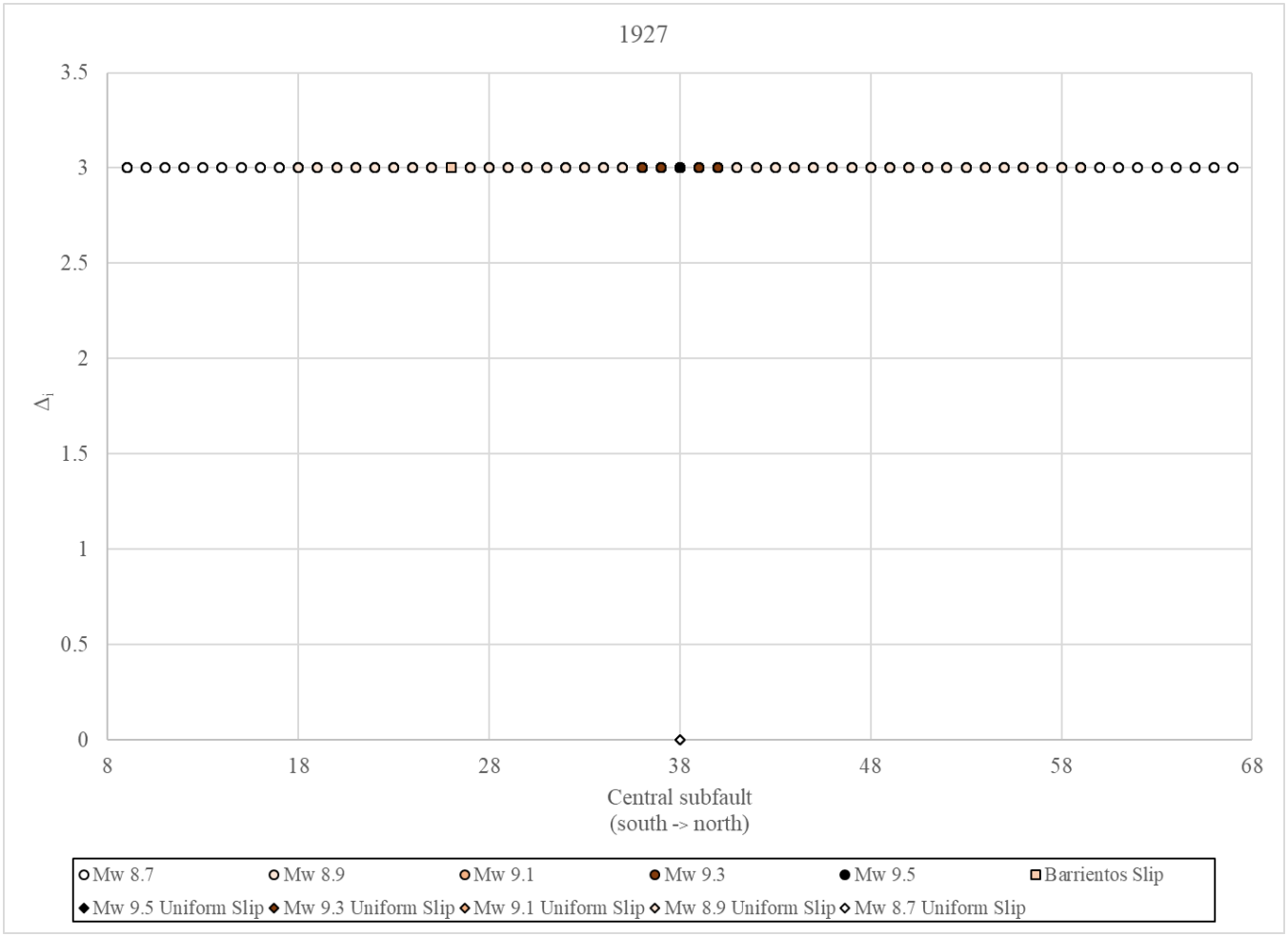

Appendix E_{14}: The Δ_i versus central subfault of rupture for all tsunami simulations relative to the lowest AIC value calculated from observations of the 1927 historical tsunami. Earthquake magnitude positively correlates to darker colored data points.

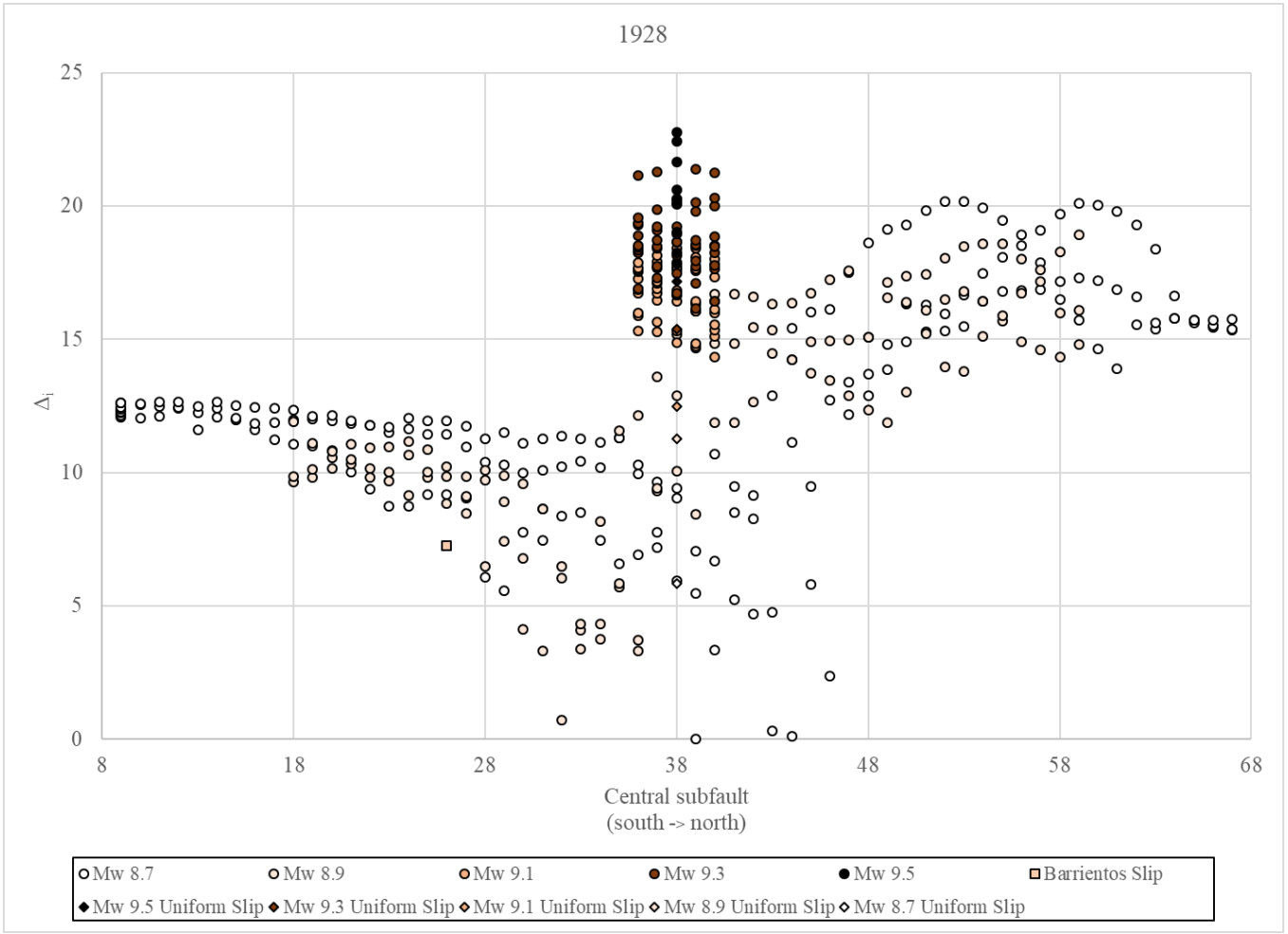

Appendix E_{15}: The Δ_i versus central subfault of rupture for all tsunami simulations relative to the lowest AIC value calculated from observations of the 1928 historical tsunami. Earthquake magnitude positively correlates to darker colored data points.

220

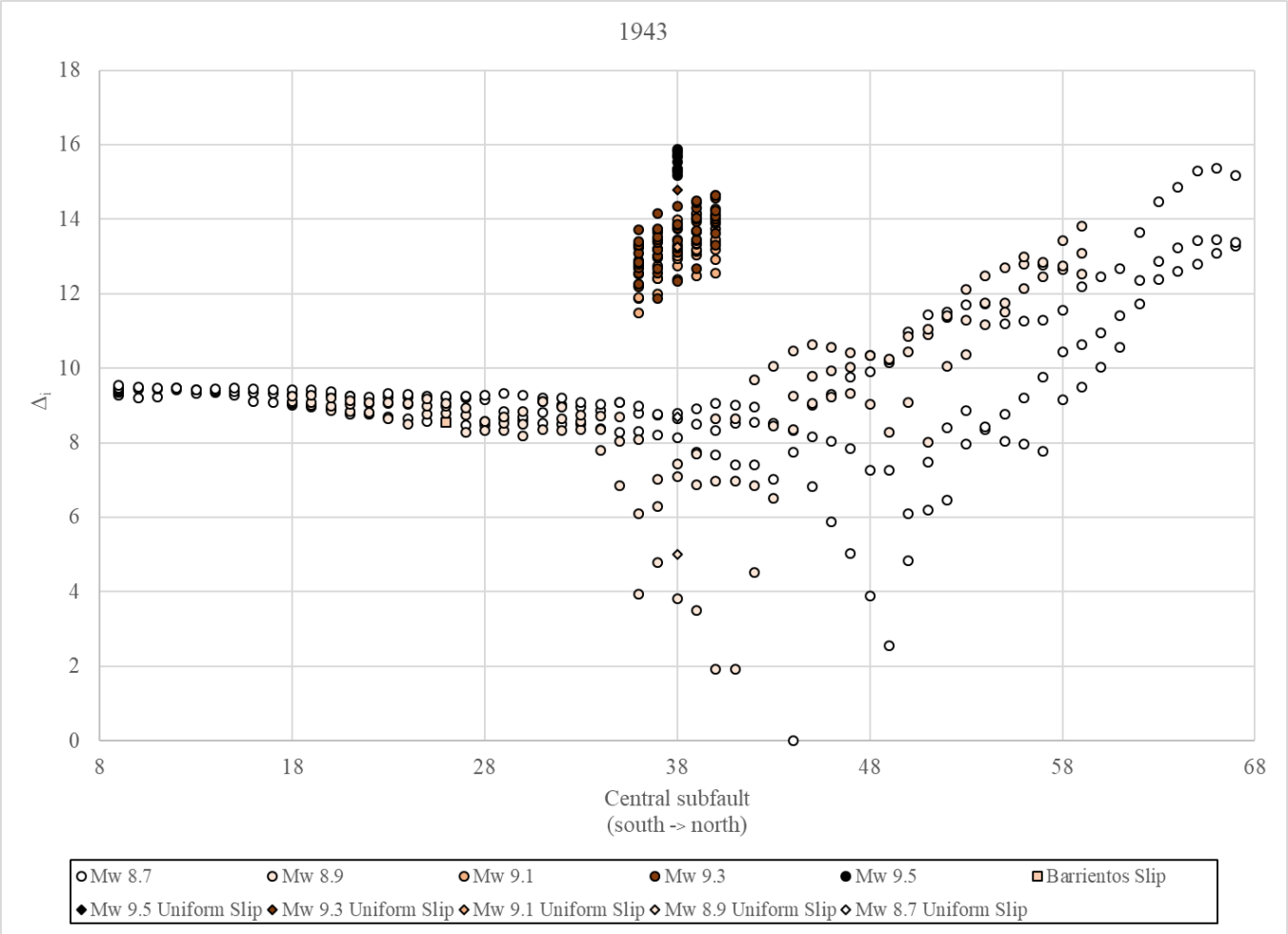

Appendix E_{16}: The Δ_i versus central subfault of rupture for all tsunami simulations relative to the lowest AIC value calculated from observations of the 1943 historical tsunami. Earthquake magnitude positively correlates to darker colored data points.

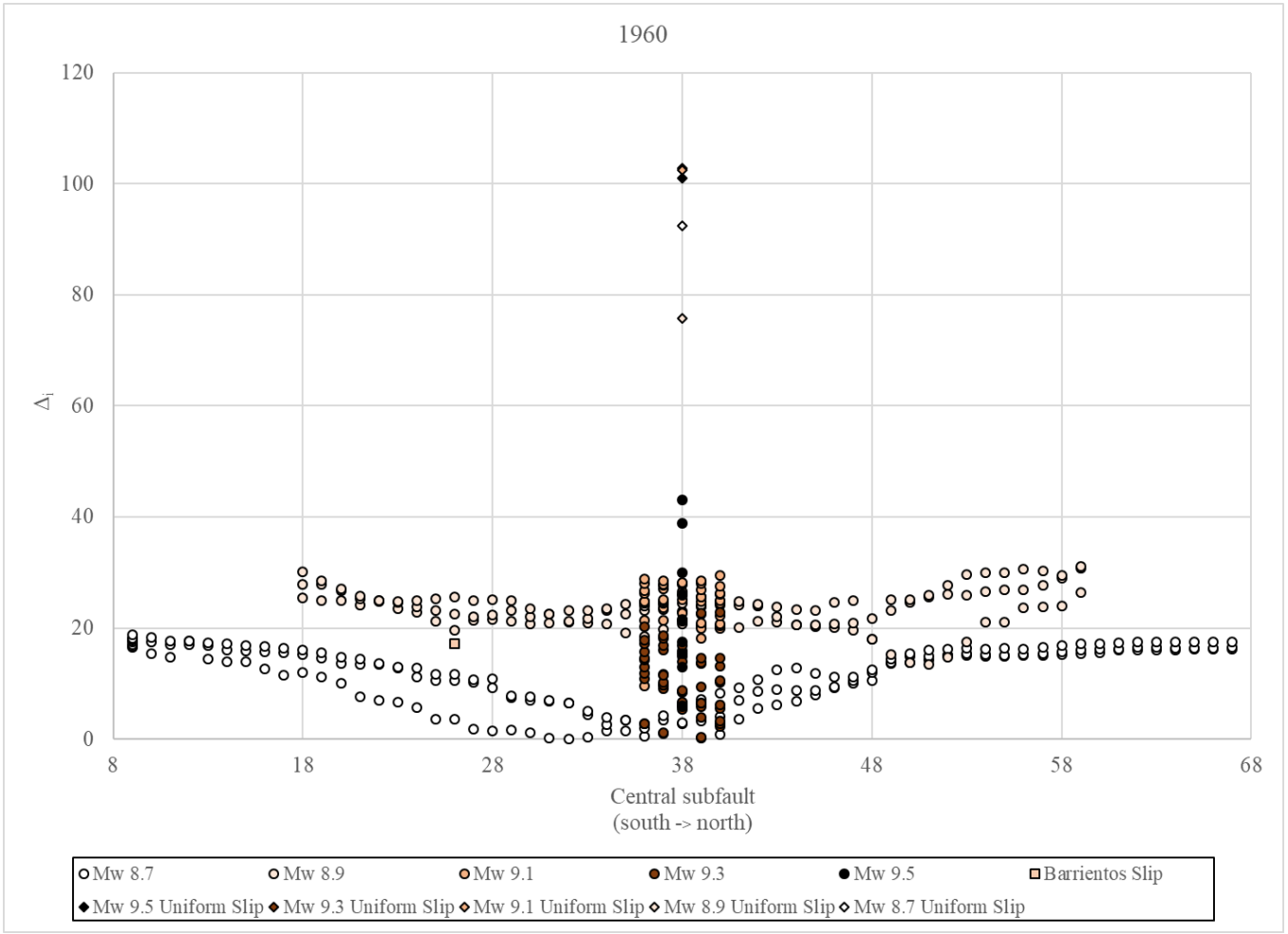

Appendix E_{17}: The Δ_i versus central subfault of rupture for all tsunami simulations relative to the lowest AIC value calculated from observations of the 1960 historical tsunami. Earthquake magnitude positively correlates to darker colored data point.